ISTANBUL TECHNICAL UNIVERSITY ★ GRADUATE SCHOOL

DEFORMATION BEHAVIOR OF THIN WALLED STRUCTURES FILLED WITH AUXETIC AND NON-AUXETIC CORE MATERIALS

Ph.D. THESIS

Fatih USTA

Department of Aeronautics and Astronautics Engineering

Aeronautics and Astronautics Engineering Programme

MARCH 2021

ISTANBUL TECHNICAL UNIVERSITY ★ GRADUATE SCHOOL

DEFORMATION BEHAVIOR OF THIN WALLED STRUCTURES FILLED WITH AUXETIC AND NON-AUXETIC CORE MATERIALS

Ph.D. THESIS

Fatih USTA
(511152102)

Department of Aeronautics and Astronautics Engineering

Aeronautics and Astronautics Engineering Programme

Thesis Advisor: Prof. Dr. Halit Süleyman TÜRKMEN
Thesis Co-Advisor: Prof. Dr. Fabrizio SCARPA

MARCH 2021

İSTANBUL TEKNİK ÜNİVERSİTESİ ★ LİSANSÜSTÜ EĞİTİM ENSTİTÜSÜ

ÖKZETİK VE ÖKZETİK OLMAYAN DOLGU MALZEMELİ İNCE CİDARLI YAPILARIN DEFORMASYON DAVRANIŞI

DOKTORA TEZİ

Fatih USTA
(511152102)

Uçak ve Uzay Mühendisliği Anabilim Dalı

Uçak ve Uzay Mühendisliği Programı

Tez Danışmanı: Prof. Dr. Halit Süleyman TÜRKMEN
Eş Danışman: Prof. Dr. Fabrizio SCARPA

MART 2021

Fatih USTA, a Ph.D. student of ITU Graduate School student ID 511152102 successfully defended the thesis/dissertation entitled “DEFORMATION BEHAVIOR OF THIN WALLED STRUCTURES FILLED WITH AUXETIC AND NON-AUXETIC CORE MATERIALS”, which he prepared after fulfilling the requirements specified in the associated legislations, before the jury whose signatures are below.

Thesis Advisor :	**Prof. Dr. Halit Süleyman TÜRKMEN** Istanbul Technical University	.....
Co-advisor :	**Prof.Dr. Fabrizio SCARPA** University of Bristol	.....
Jury Members :	**Prof. Dr. Zahit MECİTOĞLU** Istanbul Technical University	.....
	Prof. Dr. Fazıl Önder SÖNMEZ Boğaziçi University	.....
	Prof. Dr. Şenol ATAOĞLU Istanbul Technical University	.....
	Prof. Dr. Şafak YILMAZ Istanbul Technical University	.....
	Prof. Dr. Hasan KURTARAN Adana Alparslan Türkeş Science and Technology University	.....

Date of Submission : 26 February 2021
Date of Defense : 25 March 2021

This thesis is proudly dedicated to my family,

FOREWORD

First and foremost, I would like to begin by expressing my profound gratitude to my supervisor Prof. Dr. Halit S. TÜRKMEN for providing his supervision, convincing guidance, patience and endless support throughout the completion of Ph.D. thesis. Since the first day of working with him I have learned many things about doing research and regarding the working discipline without losing the motivation during my M.Sc. and Ph.D. research. I am sincerely indebted to my co-advisor Prof. Dr. Fabrizio SCARPA for hosting and guiding during my visiting research in University of Bristol and for providing supervision and sharing his profound knowledge during my Ph.D. research. I have benefited from his high-quality advices in a number of ways when exploring new ideas.

I desire to express my thanks to the jury members of my Ph.D., Prof. Dr. Zahit MECİTOĞLU, Prof. Dr. Fazıl Önder SÖNMEZ and Prof. Dr. Şenol ATAOĞLU for their profound contributions.

I was honored with the 2211/C Domestic Priority Areas Doctoral Scholarship by the Scientific and Technological Research Council of Turkey (TÜBİTAK) and with the YÖK 100/2000 Graduate Scholarship by the Council of Higher Education (YÖK) to have my Ph.D. degree. TÜBİTAK has also supported me for my visiting research in University of Bristol with its 2214-A International Research Fellowship Program. Hence, I would like to thank TÜBİTAK and YÖK for funding my studies during my Ph.D.

I would like to gratefully acknowledge the support of Turkish Aerospace Industries (TAI) for the project of DKTM 2015-1, TÜBİTAK for the project 115M465 related to this thesis study. I would also like to gratefully acknowledge the support Istanbul Technical University for the projects of Science Research Projects (BAP) MDK-2019-41879 and MGA-2018-41414 and Researcher Development Program (ITU-AYP-2015-1)

I also extend my gratitude and thankfulness to the special people in my life. I would like to thank my fiancée Dr. Eda KILINÇARSLAN, who is a theoretical physicist, for inspiring me to keep working hard and for her constant support throughout the entire process. I owe my deepest gratitude to my parents, Rüstem and Aysel USTA. I am forever indebted to them and it is a big pleasure to thank my brothers Hayati and Samet USTA.

I am thankful to the Faculty of Aeronautics and Astronautics at Istanbul Technical University and Bristol Composites Institute at University of Bristol for providing an excellent environment to perform my scientific research. Thank you to the technicians Müslüm ÇAKIR and Sefa BAŞALAN for their support in experiments in Composites and Structures Laboratory.

March 2021

Fatih USTA
(Aeronautical Engineer)

TABLE OF CONTENTS

Page

FOREWORD ..... **ix**
TABLE OF CONTENTS ..... **xi**
ABBREVIATIONS ..... **xv**
SYMBOLS ..... **xvii**
LIST OF TABLES ..... **xix**
LIST OF FIGURES ..... **xxi**
SUMMARY ..... **xxvii**
ÖZET ..... **xxxi**
1. INTRODUCTION **1**
1.1 Purpose of the Thesis 3
1.2 Literature Review 4
1.2.1 Thin-walled structures 4
1.2.2 Sandwich panels 5
1.2.2.1 Low-velocity impact 5
1.2.2.2 High-velocity impact 6
1.2.2.3 Doubly curved panels 9
1.2.3 Crash tubes 10
Filled tubes 11
1.2.4 Core and filler types 14
1.2.4.1 Foam filler 14
1.2.4.2 Auxetic Fillers 15
1.2.4.3 Architectural structures 16
1.3 Overview 17
2. NOVEL HIERARCHICAL UNIT CELLS HONEYCOMB AND MULTIPHASE LATTICE METAMATERIALS **19**
2.1 Purpose 19
2.2 Design Methodology and Manufacturing Processes 19
2.2.1 Unit cell designs 19
2.2.2 3D printing of the PLA plastic slotted samples 21
2.2.3 PLA-made hierarchical cellular honeycombs filled with hydrogel 22
2.2.4 PLA-made hierarchical cellular honeycombs filled with PUR foam 23
2.3 Material Properties of PLA Plastics and PUR Foam 24
2.3.1 Tensile tests of PLA plastics 24
2.3.2 Compression tests of PUR foam 24
2.4 Compression Tests 27
2.5 Finite Element Simulations 33
2.5.1 FE modeling of bulk thickness and slotted samples 33
2.5.2 Validation of bulk thickness and slotted samples 34
2.5.3 Deformation mechanism 36
2.5.4 FE modeling of hybrid samples 39
2.5.5 Validation of hybrid samples 40
2.6 Results and Discussion 41

2.6.1 Metrics for benchmark 41
2.6.2 Comparison of the specific compressive strength 42
2.6.3 MCF comparison 44
2.6.4 SEA comparison 45
2.6.5 Specific compressive modulus 46
2.7 Parametric Studies related to Hybrid Hierarchical Honeycombs 47
2.8 Conclusion 51
3. SANDWICH PANELS WITH AUXETIC OR NON-AUXETIC CORES 53
3.1 Purpose 53
3.2 Low-Velocity Impact Resistance of the Flat Composite Sandwich Panels 53
3.2.1 Cellular core designs 54
3.2.2 Sample preparation and material properties 56
3.2.2.1 Composite face sheets 57
3.2.2.2 PLA plastic cores 58
3.2.2.3 PUR foam core 59
3.2.3 Drop weight test set up 60
3.2.4 Finite element simulations 62
3.2.5 Results and discussions 65
3.2.5.1 Validation of the numerical models 65
3.2.5.2 Impact damage morphology 69
3.2.5.3 Impact resistance of samples at different energy levels 71
3.2.5.4 The effects of design parameters on the impact resistance 74
3.2.6 Conclusion 75
3.3 High-velocity Impact on the Doubly Curved Sandwich Panels 76
3.3.1 Design and manufacture methodology 76
3.3.2 Doubly curved PLA plastic core 77
3.3.3 Doubly curved PUR foam core 78
3.3.4 Doubly curved composite face sheets 79
3.3.5 Test set up 81
3.3.6 Impact tests on doubly curved sandwich panels 85
3.3.7 Finite element modeling 86
3.3.8 Results and discussion 87
3.4 Single and Doubly Curved Sandwich Panels- A parametric Analyses Under Projectile Impact 89
3.4.1 The geometry of single and doubly curved panels 90
3.4.2 Numerical analyses of single and doubly curved shells 90
3.4.3 Effects of the impact location on the impact resistance of the toroidal panel 92
3.4.4 Conclusion 94
3.5 Effects of Thickness and Curvature on Impact Behavior of Composite Panels 94
3.5.1 Problem definition 94
3.5.2 Material properties 96
3.5.3 Results and discussions 96
3.5.4 Conclusion 98
3.6 Optimization of Cylindrical Curved Composite Panels Using Response Surface Methodology and Genetic Algorithm 98
3.6.1 Problem definition 98
3.6.2 Material properties of UD Hexcel S2 glass fiber prepreg composite 99
3.6.3 Formulation of the optimization problem 100

3.6.4 Response surface models for optimization criteria 100
3.6.5 FE modeling and correlation of RSM and FE results 102
3.6.6 Results and discussions 105
4. THIN WALLED CRASH TUBES 107
4.1 Purpose 107
4.2 Impact Behavior of Triggered and Non-Triggered Crash Tubes with Auxetic Lattices 107
4.2.1 Material properties of AL6063 aluminum alloy 108
4.2.2 Material properties of ABSplus plastics 109
4.2.3 Finite element modeling 111
4.2.4 Tube designs 112
4.2.5 Results and discussion 114
4.2.5.1 The effects of length of the tubes on crashworthiness 114
4.2.5.2 Comparison triggered and non-triggered tube designs 116
4.2.5.3 The effects of using auxetic lattices on crashworthiness 117
4.2.5.4 Conclusion 118
4.3 Crushing Behavior Of Circular Aluminum Tubes with Square Prism Auxetic Filler 119
4.3.1 Manufacture of square prism auxetic filler 119
4.3.2 Manufacture of aluminum tubes 124
4.3.3 Low-velocity impact tests 125
4.3.3.1 Impact tests and analysis of empty tubes 125
4.3.3.2 Impact tests and FE analysis of auxetic core 127
4.3.3.3 Impact tests and FE analysis of aluminum tubes with auxetic core 127
4.3.4 Results and discussions 129
4.4 Experimental and Numerical Investigation of Impact Behavior of Nested Tubes with and without Honeycomb Filler 129
4.4.1 Nested tube structures and problem definition 130
4.4.2 Finite element modeling 133
4.4.3 Results 134
4.4.3.1 Single tube 134
4.4.3.2 Nested tubes (case A) 135
4.4.3.3 Nested tubes (case B) 139
4.4.4 Discussion 142
4.4.4.1 Collapse mechanism of samples 142
4.4.4.2 Effect of honeycomb filler 143
4.4.4.3 Effect of the number of tubes 144
4.4.4.4 Effect of tube lengths 145
4.4.5 Conclusion 147
4.5 Impact Behavior of Tapered Nested Tube Structures with and without Imperfection 148
4.5.1 Problem definition 149
4.5.2 Finite element modeling 150
4.5.3 Results and discussion 150
4.6 Crashworthiness Optimization of Nested and Concentric Circular Tubes Using Response Surface Methodology and Genetic Algorithm 152
4.6.1 Finite element model 153
4.6.2 Optimization procedure 155
4.6.3 Formulation of the optimization problem 155
4.6.4 Response surface models for optimization criteria 156

4.6.5 Solution of optimization problem 161
4.6.6 Conclusion..... 166
5. CONCLUSIONS..... 169
5.1 Recommendations and Suggestions for Future Research 172
REFERENCES..... 173
CURRICULUM VITAE..... 185

ABBREVIATIONS

ABS : Acrylonitrile Butadiene Styrene
ASTM : American Society for Testing Materials
BFGS : Broyden–Fletcher–Goldfarb–Shanno algorithm
DAH : Double arrow-head
DQM : Differential quadrature method
FDM : Fused Deposition Modeling
CFE : Crush Force Efficiency
CFRP : Carbon fiber reinforced epoxy
GA : Genetic Algorithm
MCF : Mean crushing force
NSGA : Non-dominated Sorting Genetic Algorithm
PLA : Polylactic Acid
PU : Polyurethane
RCA : Re-entrant chiral auxetic structures
RS : Response Surface
SEA : Specific Energy Absorption
UD : Unidirectional
WHO : World Health Organization

SYMBOLS

$\boldsymbol{\kappa_1, \kappa_2}$	**:** Principal curvatures
K	**:** Gaussian curvature coefficient
w	**:** deflection
σ	**:** Compressive stress
E	**:** Young's modulus
$\boldsymbol{\theta}$	**:** Cell wall angle
ρ	**:** Density

LIST OF TABLES

Page

Table 1.1 : A literature overview. **9**
Table 2.1 : Material properties of PUR foams. **26**
Table 3.1 : Properties of unidirectional CFRP composite..... **58**
Table 3. 2 : The FE analysis results of the DAH core sandwiches based on design parameters of face sheet and core structure. **75**
Table 3.3 : Penetration depth of the tested and analyses doubly curved sandwiches. **89**
Table 3.4 : Results of numerical analyses. **92**
Table 3.5 : Results of numerical analyses for toroidal sandwich panels..... **94**
Table 3.6 : Absorbed energy of the samples. **97**
Table 3.7 : Max contact forces on the master surfaces. **97**
Table 3.8 : Displacement at the centre of backplane, reaction forces on the boundaries and residual velocities. **97**
Table 3.9 : Properties of UD Hexcel S2 glass fiber prepreg composite..... **100**
Table 3.10 : Ranges of design variables used in DOE table. **102**
Table 3.11 : Comparison of the FE and optimization results of the best design..... 105
Table 4.1 : Mechanical properties and random errors of AL6063 aluminum alloy. **109**
Table 4.2 : Mechanical properties and random errors of ABSplus plastics. **110**
Table 4.3 : Crashworthiness parameters of tubes with auxetic filler. **117**
Table 4.4 : Crashworthiness parameters of tubes with and without auxetic filler. . **118**
Table 4.5 : FE analyses results of auxetic core structures in tubes. **123**
Table 4.6 : Comparison of the test results. **129**
Table 4.7 : Dimensions of single and nested tubes in case A (units: mm)..... **131**
Table 4.8 : Dimensions of nested tubes in case B (units: mm). **131**
Table 4.9 : Dimensions of samples. **150**
Table 4.10 : Results of FE analyses. **152**
Table 4.11 : Ranges of design variables used in the DOE table. **158**
Table 4.12 : DOE table used in creating RS models. **158**
Table 4.13 : Parameter specifications for the NSGA-II. **162**
Table 4.14 : Optimum values of design variables for concentric circular tubes. **163**
Table 4.15 : Comparison of single and optimum nested tube results. **165**

LIST OF FIGURES

Page

Figure 1.1 : Impact scenario chart for passenger airplane fuselage [3]. **2**
Figure 1.2 : Schematic illustration of a gas gun [25]. **7**
Figure 1.3 : Configuration of a yarn/fibre before and after transverse impact: (a)before impact; (b)–(d) after impact [26]. **8**
Figure 1.4 : The Gaussian curvature, K, relates to the structures on the slab surface as follows: (a) K > 0, (b) K = 0 and (c) K<0 [46]. 10
Figure 2.1 : a) Hexagonal, b) re-entrant, and c) asymmetric re-entrant designs. **20**
Figure 2.2 : Conventional and re-entrant honeycomb structures. **20**
Figure 2.3 : Bulk thickness, hierarchical (slotted), and composite (PUR foam and hydrogel) cells. **21**
Figure 2.4 : Raise N1 3D printer machine: 3D printing slicing of structures in IdeaMaker software and printed samples. **22**
Figure 2.5 : a) Hydrogel injection into the slots, b) $CaCl_2$ bath of the hexagonal slotted lattice. **23**
Figure 2.6 : Slotted re-entrant honeycomb filled with PUR foam. **23**
Figure 2.7 : Stress-strain curves of the PLA plastic. **24**
Figure 2.8 : Cubic PUR foam test samples. **25**
Figure 2.9 : Compression test of the PUR foam. **25**
Figure 2.10 : Comparison of average stress-strain curves of the foams at different strain rates. **26**
Figure 2.11 : Compression tests by using a) Instron test machine and b) Video gauge system. **27**
Figure 2.12 : Stress vs. strain curves of re-entrant samples under compression along the x-direction: Bulk thickness (black), Slotted (red), Multiphase (blue) and Hybrid (green). **28**
Figure 2.13 : Deformation mechanisms of hexagonal honeycombs along the *x*-direction. **29**
Figure 2.14 : Deformation patterns of the re-entrant honeycombs along the *x*-direction. **30**
Figure 2.15 : Deformation mechanisms of the AEC re-entrant honeycombs along the *x*-direction. **30**
Figure 2.16 : Deformation mechanisms of hexagonal honeycombs along the *y*-direction. **31**
Figure 2.17 : Deformation mechanisms of re-entrant honeycombs along the *y*-direction. **32**
Figure 2.18 : Deformation mechanisms of AEC re-entrant honeycombs along the *y*-direction. **32**
Figure 2.19 : FE modeling of the compression test. **33**
Figure 2.20 : Comparison between numerical and experimental results related to the bulk thickness cellular structures. **35**
Figure 2.21 : Comparison between numerical and experimental results related to the slotted cellular structures. **36**

Figure 2.22 : Deformation mechanisms of the samples under compression along the *X*-direction. **38**
Figure 2.23 : Deformation mechanism of the samples compressed along the *Y*-direction. **39**
Figure 2.24 : FE modeling of hybrid AEC re-entrant sample. **40**
Figure 2.25 : Specific compressive strength vs. strain curves of AEC re-entrant sample loading in the *x*-direction. **41**
Figure 2.26 : Specific compressive strength. **43**
Figure 2.27 : Mean crushing force (MCF). **44**
Figure 2.28 : Specific energy absorption (SEA). **46**
Figure 2.29: Specific compressive modulus. **47**
Figure 2.30 : Unit cell configurations of AEC re-entrant samples with and without radius of round by changing the number of slots. **48**
Figure 2.31 : The Specific compressive strength and modulus values of modified hybrid samples. **50**
Figure 2.32 : The SEA and MCF values of modified hybrid samples. **50**
Figure 2.33 : Deformed and non-deformed shapes of the optimum design: S4-rounded sample. 51
Figure 3.1 : Topologies of auxetic and non-auxetic cellular structures: Unit cell designs of (a) hexagonal, (b) re-entrant, (c) DAH (d) hexachiral honeycombs; 2D sketches of (e) hexagonal, (f) re-entrant, (g) DAH, (h) hexachiral honeycomb cores. **55**
Figure 3.2 : Schematic of the sandwich panel and manufactured CFRP sandwich panels. **56**
Figure 3.3 : Manufactured CFRP sandwich panels: non-auxetic (PUR foam, hexagonal lattice) and auxetic core (re-entrant, DAH, hexachiral). **57**
Figure 3.4 : Tension and compression test specimens of carbon fiber composites. . **58**
Figure 3.5 : Stress-strain curve of the PLA plastic. **59**
Figure 3.6 : Stress-strain curve of the PLA plastic. **60**
Figure 3.7 : INSTRON 9340 Drop Test Machine. **61**
Figure 3.8 : Manufactured specimens and deformed shapes. **62**
Figure 3. 9 : a) FE modelling of sandwich panels and b) boundary conditions. **63**
Figure 3.10 : Comparison between numerical and experimental results of sandwich panel PUR foam core. **66**
Figure 3. 11 : Comparison between numerical and experimental results related to sandwich panels with PLA cores. **68**
Figure 3. 12 : Deformation patterns of CFRP sandwich panels with hexachiral, DAH, re-entrant, hexagonal and PUR foam core from experiments and FE analysis **70**
Figure 3. 13 : Load vs. displacement curves of the sandwich panels with: PUR foam (black), hexagonal (red), re-entrant (brown), DAH (purple) and hexachiral (blue) at the 76 J impact energy. **70**
Figure 3. 14 : Relationship between impact energy and dent depth. **73**
Figure 3. 15 : Relationship between impact energy and peak load. **73**
Figure 3. 16 : Relationship between impact energy and dent depth. **74**
Figure 3.17 : Schematic of the doubly curved sandwich panel. **77**
Figure 3.18 : Specimen dimensions and position of strain gauges and impact point. **77**
Figure 3.19 : 3D printing of doubly curved re-entrant core. **78**
Figure 3.20 : CNC processing of doubly curved PUR foam core. **79**

Figure 3.21 : Manufactured spherical mould by using CNC machine..... **79**
Figure 3.22 : List of essential materials for wet/hand lay-up method..... **80**
Figure 3.23 : Vacuumed composite fabrics with mould (left) and a manufactured doubly curved composite. **81**
Figure 3.24 : Gas gun test machine a) safety box, barrel, gas tank, solenoid valve b) inner of safety box, and test specimen. **82**
Figure 3.25 : Kestamid and Delrin sabots. **82**
Figure 3.26 : Design of test frames and connection parts. **83**
Figure 3.27 : Design and manufacture of test frames and connection parts. **83**
Figure 3.28 : Composite panel (left) and test room (right). **84**
Figure 3.29 : Data acquisition system and strain gauge connection. **84**
Figure 3.30 : Top and sectional views of tested doubly curved sandwich panels with re-entrant core. **85**
Figure 3.31 : Top and sectional views of tested doubly curved sandwich panels with foam core. **86**
Figure 3.32 : Finite element models and damaged mechanism of the sandwich panels with re-entrant (left) and foam core (right). **87**
Figure 3.33 : Strain vs time curves of tested sandwich panels with re-entrant core. **88**
Figure 3.34 : Strain vs. time curves of tested sandwich panels with foam core. **88**
Figure 3.35 : Toroidal, ellipsoid and spherical surface. **90**
Figure 3.36 : FEMs of curved panels. **91**
Figure 3.37 : Impacted points on the toroidal sandwich panel. **93**
Figure 3.38 : Cross-section and isometric views of damaged sandwich panels. **93**
Figure 3.39 : a) Isometric view of 4 ply flat b) cross section view of 4 ply flat c) isometric view of 4 ply cylindrical d) cross section view of 4 ply cylindrical. **95**
Figure 3.40 : Isometric (left) and cross section (right) view of 4-ply flat panel. **96**
Figure 3.41 : Quasi static tensile and compression tests: a) 0^0 compression, b) 45^0 compression, c) 90^0 compression, d) 0^0 tension, e) 45^0 tension, f) 90^0 tension. **99**
Figure 3.42 : Flowchart of the optimization process. **101**
Figure 3.43 : FE analysis of a set of selected curved panels. **103**
Figure 3.44 : Fitted and actual values for backplane displacement. **104**
Figure 3.45 : Fitted and actual values for SEA. **104**
Figure 3.46 : Stress distribution in FE analysis of the best design. 105
Figure 4.1 : Tensile test specimens of AL6063 aluminum alloy. **108**
Figure 4.2 : Engineering stress and strain curve of AL6063 tube. **109**
Figure 4.3 : Tensile test specimens of ABSplus plastics. **110**
Figure 4.4 : Engineering stress and strain curve of ABSplus plastics. **111**
Figure 4.5: a) Schematic view of rigid impactor and tube, b) re-entrant honeycomb cell parameters. **112**
Figure 4.6 : NT-E and NT-A models. **113**
Figure 4.7 : CT-E and CT-A models. **113**
Figure 4.8 : LT-E and LT-A models. **114**
Figure 4.9 : Comparison of deformation and force response of NT-A models. **115**
Figure 4.10 : Comparison of deformation and force response of CT-A models. ... **115**
Figure 4.11 : Comparison of deformation and force response of LT-A models. **115**
Figure 4.12 : Comparison of force response of different samples with auxetic filler. **117**
Figure 4.13 : Dimensions of re-entrant unit cell. **120**

Figure 4.14 : Design of auxetic core in CATIA. **120**
Figure 4.15 : Desing of auxetic core structure by changing lattice parameters. **121**
Figure 4.16 : FE model and analysis of Model 1. ..... **121**
Figure 4.17 : FE model and analysis of Model 2. ..... **122**
Figure 4.18 : FE model and analysis of Model 3. ..... **122**
Figure 4.19 : FE model and analysis of Model 4. ..... **122**
Figure 4.20 : Deformation behavior of Model 4 in time. **123**
Figure 4.21 : Design and production of auxetic core. **124**
Figure 4.22: Manufacture of aluminum tubes. **124**
Figure 4.23 : INSTRON Drop Test Machine. **125**
Figure 4.24 : E-1, E-2 and E-3 test specimens and FE analysis. **126**
Figure 4.25 : Force-time response of E-1, E-2, E-3 test specimens and FE analyses. **126**
Figure 4.26 : AC (Auxetic core) impact test and analysis. **127**
Figure 4.27 : T-AC-1, T-AC-2 and T-AC-3 test specimens and FE analysis. **128**
Figure 4.28 : Force-time response of T-AC-1, T-AC-2 ve T-AC-3 test specimens and FE analyses. **128**
Figure 4.29 : Schematic representation of impact test. **132**
Figure 4.30 : Hexagonal unit cell of honeycomb filler. **132**
Figure 4.31 : a) Nested-4A and b) the Nested-4B samples with honeycomb filler. **133**
Figure 4.32 : FE model of nested aluminum tube with honeycomb filler with labeling mesh types, mesh sizes, boundaries, material types, impact velocity, and impact direction. **134**
Figure 4.33 : Single tube test and FE analysis results. **135**
Figure 4.34 : Experiment and FE analysis results: a) empty Nested-2A and b) Nested-2A samples with honeycomb filler. **137**
Figure 4.35 : Experiment and FE analysis results: a) empty Nested-3A and b) Nested-3A samples with honeycomb filler. **137**
Figure 4.36 : Experiment and FE analysis results: a) empty Nested-4A and b) Nested-4A samples with honeycomb filler. **138**
Figure 4.37 : Experiment and FE analysis results: a) empty Nested-5A and b) Nested-5A samples with honeycomb filler. **138**
Figure 4.38 : Experiment and FE analysis results: a) empty Nested-3B and b) Nested-3B samples with honeycomb filler. **140**
Figure 4.39 : Experiment and FE analysis results: a) empty Nested-4B and b) Nested-4B samples with honeycomb filler. **141**
Figure 4. 40 : Experiment and FE analysis results: a) empty Nested-5B and b) Nested-5B samples with honeycomb filler. **141**
Figure 4.41 : Comparison of crashed specimens obtained from FE analyses. **143**
Figure 4.42 : PCF values for all cases. **145**
Figure 4.43 : SEA values for all cases. **146**
Figure 4.44 : CFE values for all cases. **146**
Figure 4.45 : Schematic of the square tapered nested tube structure. **149**
Figure 4.46 : Undeformed and deformed the shape of optimum tube systems for different weight functions. **151**
Figure 4.47 : Concentric circular tri-tubular structure and FE model. **154**
Figure 4.48 : Comparison of experiment and numerical analysis (V = 4.22 m/s). . **154**
Figure 4.49 : Flowchart of the optimization process. **157**
Figure 4.50 : Steps of RSM. **157**
Figure 4.51 : Fitted and actual values for SEA. **160**

Figure 4.52 : Fitted and actual values for CFE. **161**
Figure 4.53 : Coupling of FE Analyses, RS models and GA for crashworthiness optimization. **161**
Figure 4.54 : Pareto frontier for nested and concentric circular tubes. **162**
Figure 4.55 : Undeformed and deformed shape of optimum tube systems for different SEA and CFE values. **164**
Figure 4.56 : Schematic views of nested and single tube structures. **166**

DEFORMATION BEHAVIOR OF THIN WALLED STRUCTURES FILLED WITH AUXETIC AND NON-AUXETIC CORE MATERIALS

SUMMARY

Air vehicles can be exposed to structural damages and disable integrity due to static and dynamic loads. Windshields of an airplane, i.e., fuselage or wing surfaces, can have a risk of these loads, and therefore, they should withstand these external loads. The skin shape of the air vehicle components, e.g., fuselage/wing/empennage of airplane and blade/canopy of the helicopter, can be considered as the combination of curved or flat panels. Likewise, thin-walled tubular structures, which can be utilized as the forms of landing gears or frames of aircraft, can possess curved or flat surfaces depending on cross-section types. This thesis proposes to increase the indentation and impact resistance of the air vehicles under low and high-velocity impact loading. The structural durability of the aircraft components under compressive loading has a key role in the protection of structural integrity during accidents. We mainly focus on enhancing mechanical performances of integrated structures, e.g., sandwich panels and thin-walled tubes with auxetic (i.e., negative Poisson's ratio) and non-auxetic core. In particular, we focus on the effects of curvature by examining flat, single, and doubly curved sandwich panels and then curved thin-walled tubes throughout the thesis studies. The results are compared in terms of compressive modulus, strength, and energy absorption metrics.

In the first part of this thesis, we develop novel auxetic open cell assemblies to provide high-performance core structures for integrated stuctures. We describe the behavior of a novel class of hierarchical slotted and asymmetrical edge cellular shapes honeycombs with auxetic and non-auxetic configurations subjected to edgewise compression. Hierarchical (slotted) and non-hierarchical specimens, including hexagonal, traditional re-entrant, and asymmetric re-entrant, are produced by the Fused Deposition Modeling (FDM) method, which is the most common method for additive manufacturing. The specimens are 3D printed by using Raise3D N1 3D machine and Polylactic acid (PLA) plastic filament, and then they are tested under edgewise compression along the in-plane directions. The number of cells is determined as 5x4, and dimensions of 122x105x10 mm^3 are kept constant for each design. A rigid mass is crushed through the top edge surface at an axial quasi-static speed of 3 mm/min by using an Instron Roell Amsler test machine. An Imetrum Video Gauge^{TM} system is also used to capture the images of the test samples during crushing and to determine the Poisson's ratio of the samples. The material properties of the PLA plastics are determined via tensile tests following the ASTM D638-14 test standard. FE analyses have been performed using the LS-DYNA code to benchmark force-displacement curves with the experimental results. The numerical models are validated by comparing the load-displacement responses with the experimental results for each sample. Linear elastic properties, crashworthiness, and energy absorption capability of the novel honeycomb structures are evaluated from the experimental and numerical standpoint. Specific metrics like normalized compressive modulus, compressive

strength, and specific energy absorption (SEA) are evaluated. The Poisson's ratio of the hierarchical honeycomb configurations is compared to the bulk ones.

In this section, we also introduce a novel type of composite open cells honeycombs with the PLA plastic reinforcements, hydrogel, and polyurethane foam over a hierarchical cellular platform. The first class is represented by a hybrid architecture combining a hierarchical honeycomb with polyurethane foam filler, while the second is a multiphase structure produced by injecting a sodium alginate hydrogel into the hierarchical voids of the honeycomb metamaterial. The hydrogel formulation consists of sodium alginate (alginate) and a non-ionic surfactant, Pluronic F127. Gel-containing PLA structures are immersed in a 100mM $CaCl_2$ bath prepared by dissolving calcium chloride powder in deionized water. The resulting gel structure is injected into the voids of PLA structures by using syringes. Semi-reticulated polyurethane rigid (PUR) foam blocks (density 69 kg m^{-3}) are processed by using a CNC machine in accordance with the dimensions of gaps in the architectural structures. Then twelve different auxetic and non-auxetic metamaterial architectures are subjected to edgewise compression loading at the same test speed. A parametric numerical analysis is also performed using validated FE models to identify the best metamaterial architecture configurations.

Second, we conduct the studies on flat, single, and doubly composite sandwich panels under low and high-velocity impact loading. Sandwich panels are composed of two thin stiff and strong face sheets and a thick lightweight core. The geometrical configuration has a key role to be able to absorb more energy and have more impact resistance. The interface angle, stacking sequence, ply orientation, ply thickness, and material type are the important parameters for manufacturing composite sandwich panels. Here we mainly focus on the effects of different types of auxetic and non-auxetic core structures and curvature of composite panels. In addition, the effects of thickness and stacking sequence of the composite panels are examined, and then an optimization study of the impact behavior of curved plates is performed by using multi-objective optimization techniques.

Impact resistance of composite sandwich panels with different types of auxetic (re-entrant, double arrowhead, and hexachiral) and non-auxetic core structures are investigated by using Instron 9340 drop test machine. In the experimental studies, sandwich panels are manufactured with the constituents of UD carbon fiber reinforced epoxy resin (CFRP) composite face sheets and PUR foam core and 3D printed PLA plastic cellular core. Composite face sheets consisting of three plies with the [0/45/90] stacking sequence are manufactured with wet/hand lay-up method. A Heatcon vacuum press test machine is used to cure the epoxy resin and ensure a uniform flatness on both sides of the face sheets. The material properties of the constituents have been determined via tensile and compression tests in accordance with the relevant ASTM test standards. The cellular core topologies are fixed to have the same dimension of wall thickness and number of cells (39x4 except hexachiral topology). A rigid striker with a hemispherical head tip is dropped on the specimens with a speed of 2.6 m/s. A set of numerical analyses with different impact energies are performed using validated FE models to identify the best core design.

Then, we indicate how an open cellular core topologies (re-entrant lattice) and a PUR lightweight foam core structures affect the high-velocity impact behavior of the doubly curved CFRP sandwich panels. Composite face sheets are manufactured with the dimensions of 250-mm radius, 30-mm core thickness, and 1.05-mm face sheet

thickness by using a doubly curved mould made of aluminum alloy. High-velocity impact tests are carried out by using an air gas gun test machine capable of maximum 40-bar compressed air. Frames and fasteners of the gas gun are renewed considering the connection surface of the specimens. Frames are designed and produced with the same radius of curvature of the sandwich panel. In the experimental studies, a 10-mm diameter spherical steel projectile is launched to the centre of the specimens with a speed of 100 m/s. The FE models are developed by using the LS-DYNA software to simulate the high-velocity impact behavior of the specimens. The strain values measured by using strain gauges are recorded via a data acquisition system. The penetration depth of the projectile is measured by using a digital caliper.

Moreover, the effects of curvature on the impact behavior of composite panels are examined by using numerical methods. The doubly curved surfaces are investigated and classified according to the Gaussian curvature coefficient. The impacted surface is extracted from the surfaces of torus, ellipsoids, spheres, and cylinders. We evaluate twelve different doubly and one single curved panels impacted by a spherical projectile at a velocity of 100 m/s. The results are firstly discussed by considering the effects of the curvature on the backplane displacement and the energy absorption of the panels. In addition to these, a multi-optimization study based on the Genetic algorithm and Response Surface method is carried out in order to determine the optimum designs of curved plates under high-velocity impact loading.

Third, we conduct the studies on crash tubes subjected to axially quasi-static compression and low-velocity impact loading. Crash tubes are important safety components used as thin-walled structures owing to their lightweight. Here we investigate the effects of filler types, curvature, tube numbers, cross-section, and imperfection on the single and multi-tube systems' crashworthiness performance. Re-entrant and hexagonal configurations are chosen as unit cell shapes of the filler. The numerical studies are conducted using LS-DYNA software. Material properties of tubes made of aluminum alloy and auxetic lattices utilizing Acrylonitrile butadiene styrene (ABS) plus and PLA plastics are determined by using tensile tests according to ASTM E8/E8M and ASTM D638-14 test standards.

The effects of imperfection on the tube and using auxetic filler on the crushing behavior of circular crash tubes are examined by using numerical methods. FE analyses are performed at 5 m/s impact velocity. Two different trigger shapes are suggested and compared to each other and discussed the advantages and disadvantages over non-triggered tubes. In order to indicate the effects of auxeticity, circular crash tubes with and without re-entrant lattices are examined under dynamic loads by using experimental and numerical techniques. The tubes in the specified length are cut from the extruded cylindrical aluminum profiles. Then, each specimen is placed in the special grooves on the aluminum plate and bonded using adhesive. Impact tests are conducted by using the Instron Dynatup 8150 test machine.

As a special case of integrated thin walled structures, nested tubes are also examined in this section. The effects of using hexagonal honeycomb filler, increasing the numbers of tubes, and changing the lengths of the tubes on the nested tube structures are examined both experimentally and numerically. In the experimental study, a mass is dropped at 2.75 m/s impact velocity onto the multi-tubular crash tubes by a drop test machine. The results of single, double, triple, quadruple, and quintuple tubular structures with and without the honeycomb filler are compared in terms of collapse mechanism and common crashworthiness indicators. Furthermore, the effects of taper

angle, imperfection, and cross-section types on the impact behavior of nested tubes are investigated numerically. Lastly, we present a crashworthiness optimization of nested and concentric circular tubes under impact loading which is performed by coupling FE model, Response Surface models, and Genetic algorithm. Length and thickness of three concentric tubes, as well as the radius of one tube, are adopted as design variables, which are effective parameters on crashworthiness and energy absorption. To reduce the computational cost of the optimization procedure, simple and computationally cheap Response Surface models are created to replace FE analyses in further calculations. The Non-dominated Sorting Genetic Algorithm –II (NSGAII) is applied to obtain the Pareto optimal solutions.

ÖKZETİK VE ÖKZETİK OLMAYAN DOLGU MALZEMELİ İNCE CİDARLI YAPILARIN DEFORMASYON DAVRANIŞI

ÖZET

Hava araçları uçuş esnasında veya yer hareketi sırasında karşılaşılan kazalardan dolayı yapısal hasarlara maruz kalmaktadır. Kazalar uçakların taksi yolundan veya aprondan çıkması, alan ihlalleri, kuş/dolu çarpması, yabancı madde hasarı (FOD), mekanik arızalanmalar gibi çeşitli nedenlerden dolayı oluşmaktadır. Kazalarda dinamik ve statik dış yüklemelere maruz kalan hava aracı komponentleri yapısal hasarlara maruz kalması aynı zamanda aracın yapısal bütünlüğünün bozulmasına neden olmaktadır. Kazalar esnasında uçakların kanat ve gövde üzerinde bulunan bölümlerinin dış yüklere karşı dayanıklılığını artırmak mühendislik açısından öneme sahiptir. Mekanik dayanımı yüksek komponentlerin tasarımı genellikle beraberinde ağırlık artışına neden olmaktadır. Ağırlık artışı ise taşıtların performansını azaltmakta ve yakıt sarfiyatını artırmaktadır. Dolayısıyla hem dayanıklı hem de hafif yapıların tasarımı için bugüne kadar birçok özgün tasarım ve yenilikçi malzeme türü geliştirilmiştir.

Ökzetik malzemeler negatif Poisson oranı değerine sahip malzemelerdir. Doğada nadiren karşılaşılan ökzetik malzemeler ağaç özü, mercan ve süngerlerin mikro yapılarında karşımıza çıkabilmektedir. Doğadaki pek çok yapının aksine ökzetik malzemeler basma yüküne maruz kaldığında enine kesitinde daralma meydana gelirken, çekme yüküne maruz kaldığında enine kesitinde genişleme meydana gelir. Bu özelliği sayesinde ökzetik yapılı ürünlerde yapısal hasarlar azaltılabilir. Yapay ökzetik malzemeler negatif Poisson oranına sahip olacak şekilde özel olarak geliştirilen meta-malzemelerdir ve mühendislik uygulamalarında kullanımı giderek yaygınlaşmaktadır.

Bu tez çalışmasında hava araçlarının düşük veya yüksek hızlı yüklemeler altında çarpma dayanımının artırılması amaçlanmıştır. Uçak kanat, gövde kuyruk takımı ile helikopter pali ve kanopisi gibi hava aracı yapılarının dış yüzeyleri düz veya eğrilikli panel geometrisine sahiptir. Bunun yanı sıra iniş takımları ile çeşitli takviye elemanları ince cidarlı içi boşluklu geometrilere sahiptir. Tez kapsamında bu yapıların dış yükler altında mekanik dayanımını artırmak için ökzetik ve ökzetik olmayan kafes yapılı çeşitli dolgular takviye edilerek entegre yapılar oluşturulması ve çarpma yüklerine karşı bu yapılarda eğrilik başta olmak üzere kalınlık, birim hücre geometrisi gibi tasarım parametrelerinin etkilerinin incelenmesi hedeflenmiştir.

İlk bölümde entegre yapılarda kullanılabilecek özgün ökzetik yapılı hücre tasarımları geliştirilmesi için çalışmalar yapılmıştır. Bu amaçla girintili (re-entrant) kafes yapılı hiyerarşik ökzetik tasarımlar geliştirilmiştir. Kalınlık boyunca dikdörtgen kesitli yarıklar içeren bu tasarımın simetrik ve asimetrik girintili kafes yapılı modelleri ile ökzetik olmayan balpeteği kafes yapılı modelleri PLA plastik malzemeli flamanlar kullanılarak en yaygın eklemeli imalat yöntemi olan FDM (Fuse Deposition Method) yöntemiyle Raise3D N1 isimli 3B yazıcıda üretilmiştir. Numunelerin hücre sayıları ve ebatları sırasıyla 5x4 ve 122x105x10 mm^3 olarak sabit tutularak 12 farklı model test edilmiştir. Testler Bristol Kompozit Enstitüsü laboratuvarında bulunan Instron Roell

Amsler servohidrolik test cihazı kullanılarak 3 mm/dk ezilme hızında gerçekleştirilmiştir. Ezilme testlerinde yer değiştirme, tepki kuvveti, hız verileri kaydedilmektedir. Bunun yanı sıra Imetrum Video Gauge^{TM} video kamera ölçüm cihazı kullanılarak deney numunelerinin düzlem içi deformasyon şekilleri kaydedilmiş ve numunelerin Poisson oranları hesaplanmıştır. PLA plastik malzeme özellikleri ASTM D638-14 test standardına göre çekme testleri yapılarak belirlenmiştir. Daha sonra LS-DYNA yazılımı ile her bir modelin aynı şartlarda sonlu eleman analizleri yapılarak elde edilen sonuçlar kuvvet-yer değiştirme eğrileri bakımından deneylerden elde edilen sonuçlarla karşılaştırılarak modeller doğrulanmıştır. Sonuçların incelenmesi için özgül enerji emilimi, basma dayanımı ve sıkıştırma modülü değerleri karşılaştırma parametreleri olarak kullanılmıştır.

Bu bölümde ayrıca bir başka özgün faaliyet olarak hiyerarşik modellerin boşluklu bölümlerine farklı yoğunluk ve faz yapısında malzeme takviyesi yapılarak yüksek performanslı özgün kompozit meta-malzemeler tasarlanmıştır. 3B yazıcıda üretilen PLA plastik malzemeli hiyerarşik modellere ayrı ayrı düşük yoğunluğa sahip rijit poliüretan köpük malzeme ve yarı akışkan (non-Newtonian) aljinat hidrojel malzeme takviyesi yapılarak hibrit yapılı numuneler üretilmiştir. Poliüretan köpük CNC test cihazı ile işlenerek istenilen boyut ve geometrilerde imal edilirken, aljinat hidrojel ise Bristol Biomedikal Fakültesi laboratuvarında özel olarak üretilip PLA plastik numunelere uygulanmıştır. Altı farklı hibrit ve altı farklı çok-fazlı kompozit metayapılı numunenin aynı şartlar altında ezilme testleri ve sonlu eleman analizleri yapılarak geleneksel balpateği ve girintili latis yapılara karşı avantaj ve dezavantajları gösterilmiştir. Poliüretan köpük malzeme özellikleri ASTM D1621-91 test standardına göre basma testleri yapılarak belirlenmiştir.

Ökzetik kafes yapıları genellikle sandviç panel veya ince cidarlı içi boş yapılarda dolgu yapısı olarak tercih edilmektedir. Örneğin uçak kanat ve gövde panellerinde yaygın olarak sandviç plakalar kullanılır. Balpeteği kafes yapılı açık hücreli dolgular ile kapalı hücreli köpük malzemeli dolgular hafif olmasının yanı sıra sandviç yapılarda mekanik dayanımı ve enerji emilimi artıran özelliklere sahiptir. Araştırmanın bu safhasında ezilme ve çarpma yüküne maruz kalan ökzetik ve ökzetik olmayan dolguların entegre yapılarda mekanik performansı artırmaya yönelik katkıları araştırılmıştır. Entegre yapılar iki bölüme ayrılarak ikinci bölümde kompozit sandviç paneller, üçüncü ve son bölümde metalik ince cidarlı yapılarda uygulamaları anlatılmaktadır.

İkinci bölüm faaliyetleri düz, tek eğrilikli ve çift eğrilikli sandviç panellerde düşük ve yüksek hızlı parçacık çarpması etkilerinin incelenmesi üzerinedir. Bu çalışmalarda başta girintili olmak üzere asimetrik (hexachiral) ve ok uçlu (arrowhead) kafes yapılı ökzetik yapılı dolgularla ökzetik olmayan altıgen balpeteği kafes yapılı ve köpük malzemeli dolgular sandviç panellere uygulanmıştır. Bunun yanı sıra panellerin eğrilik geometrisi, kompozit katman kalınlığı, katman dizilimi gibi tasarım parametrerinin mekanik dayanıma ve enerji emilim kapasitesine etkileri araştırılmıştır.

İlk olarak düşük hızlı kütle düşürme testlerinde girintili, asimetrik ve çift ok uçlu kafes yapılı ökzetik dolgular ile altıgen balpeteği kafes yapılı ökzetik olmayan dolgular karbon elyaf takviyeli kompozit plakalar arasında dolgu yapısı olarak kullanılmıştır. 3B yazıcıda üretilen açık hücreli PLA plastik dolgulu sandviç panellerin yanı sıra kapalı hücreli rijit poliüretan köpük dolgulu paneller test edilerek karşılaştırılmıştır. ASTM 7136 test standardına göre 150x100x20 mm^3 ebatlarında İTÜ UUBF Kompozit ve Yapı laboratuvarında üretilen düz sandviç panellerin sonrasında Sabancı Üniversitesi'nde Instron 9340 test cihazı kullanılarak düşük hızlı çarpma testleri

yapılmıştır. Karbon elyaf takviyeli kompozit, rijit poliüretan köpük ve PLA plastik malzemelerinin malzeme karakterizasyonları ilgili ASTM test standartlarına göre basma ve çekme testleri yapılarak belirlenmiştir. Yarıküresel uçlu rijit çarpan kütle 2.6 m/s çarpma hızında panellerin merkezine çarptırılmıştır. Sonlu eleman analizlerinde ise farklı çarpma enerjilerinde panellerin mekanik performansları parametrik olarak incelenmiştir. Bu faaliyette düz panellerde dolgu yapısı olarak farklı ökzetik kafes yapıları ile ökzetik olmayan açık ve kapalı hücreli çeşitli yapıların çarpma performansları karşılaştırılmıştır.

Daha sonra eğrilik etkisini incelemek için çift eğrilikli kompozit panellerde parçacık çarpma testleri ve analizleri yapılmıştır. Deneyler için tek kademeli sıkıştırılmış hava ile parçacık fırlatılan çarpma test düzeneği kurulmuş ve paneller üzerine küresel parçacık fırlatma testleri yapılmıştır. İlk olarak test düzeneği 250 mm çaplı küresel çift eğrilikli panellerin testlerini yapabilecek şekilde modifiye edilmiştir. Panellerin eğriliğine uygun şekilde bağlantı elemanlarının tasarımı, imalatı ve montajı yapılmıştır. Girintili kafes yapılı ökzetik dolgular PLA plastik malzemeli filaman kullanılarak 3B yazıcıda üretilmiştir. Ayrıca rijit poliüretan köpük CNC makinesinde işlenerek aynı eğriliğe sahip çift eğrilikli köpük dolgular elde edilmiştir. Karbon elyaf takviyeli kompozit panellerin imalatı içinse öncelikle belirlenen eğrilik geometrisine uygun alüminyum malzemeli kalıp üretilmiş ve ısıtmalı vakum masası kullanılarak elle yatırma yöntemiyle çift eğrilikli kompozit paneller imal edilmiştir. Kompozit paneller ile PLA malzemeli dolgu ve poliüretan dolguların temas yüzeylerine epoksi reçine ve sertleştirici karışımı uygulanarak kürleşme gerçekleşene kadar işkenceler ve ağırlıklar kullanılarak bağlantı yüzeylerinin teması sağlanmıştır. PLA plastic malzemeli ökzetik dolgu ile poliüretan köpük ökzetik olmayan dolgulu iki farklı sandviç panel için tekrar testleri de dikkate alınarak üçer adet numune üretilip yüksek hızlı çarpma testleri gerçekleştirilmiştir. 40 bara kadar hava sıkıştırma kapasitesine sahip test düzeneğinde 100 m/s çarpma hızında 10 mm çaplı küresel çelip bilye kullanılarak fırlatma testleri yapılmıştır. Deneylerde, kronograf ile namlu çıkış hızı ve gerinim pulları ile panellerin arka yüzeylerinde belirlenen noktalarda gerinim değerleri ölçülmüştür. Deneylerden sonra çarpan cismin panel içindeki penetrasyon uzunlukları ölçülerek daha sonra sonlu eleman analizlerinden elde edilen değerlerle karşılaştırılmıştır. Sonlu eleman yöntemleri ile dolgu ebatları ve birim kafes yapıları aynı olacak şekilde düz sandviç panellerin analizleri yapılarak eğrilikli panellerle karşılaştırılmış ve çalışmanın sonunda eğrilik etkisi incelenmiştir.

Panellerin çarpma davranışına eğrilik etkisinin incelenmesi için bir başka faaliyette ise sonlu eleman yöntemleri farklı eğrilik ölçülerine sahip modeller karşılaştırılmıştır. Gaussian eğrilik katsayısı değerinin pozitif, negatif ve sıfır olması koşullarına göre her durum için farklı eğriliklerde panel geometrileri belirlenerek sonlu eleman modelleri kurulmuştur. Silindirik, toroid, katenoid, elipsoid ve küresel eğrilikli karbon elyaf takviyeli kompozit panellerin 100 m/s çarpma hızında parçacık çarpması analizleri yapılarak mekanik performansları karşılaştırılmıştır. Daha sonra girintili ökzetik dolgulu çift eğrilikli bir sandviç panelin merkezi ve kenarları arasında farklı noktalara çarpma analizleri yapılarak ökzetik dolgulu panellerde merkez dışındaki noktalardaki çarpma yüklerinde performans değişimi parametrik olarak incelenmiştir. Bir başka çalışmada ise 50 m/s çarpma hızında karbon elyaf takviyeli kompozit panellerde panel eğriliği, katman dizilimi ve sayısının etkileri incelemiştir. Son olarak Hexcel cam elyaf kompozit malzemeli panellerin eğrilik tasarım parametresine ideal tasarımlarının belirlenmesi için çok amaçlı optimizasyonu yapılmıştır. Belirlenen sınırlar dahilinde azami dayanımı ve enerji emilim kabiliyeti olan optimum tasarımları belirleyebilmek

için Genetik algoritma ve Yanıt Yüzey yöntemi (RSM) çok amaçlı eniyileme probleminin çözümünde kullanılmıştır. Modellerin tasarımları CATIA, sonlu eleman analizleri LS-DYNA ve optimizasyonu ise MATLAB yazılımları kullanılarak yapılmıştır.

Üçüncü ve son bölümde ise tez araştırmasındaki ikinci entegre yapı olarak ele alınan ince cidarlı yapılarda ökzetik kafes yapılı dolguların deneysel ve sayısal uygulamaları gerçekleştirilmiştir. İdeal ince cidarlı tüplerin tasarımı için çarpma yükü altında tepe kuvveti değerinin düşük olması ve tepe kuvveti ile diğer tepki kuvvetleri arasındaki farkın düşük olması beklenir. İdeal ince cidarlı yapılar hem yüksek enerji soğurma kapasiteli hem de düşük atalet etkileri ile iyi bir sönümleyici yapı elemanı olmalıdır. Bu bölümde sanki-statik ezme yükleri ile düşük hızlı dinamik çarpma yükleri tüplerin kesitine dik doğrultuda uygulanarak eğrilik, dolgu kafes yapısı, iç içe tüp kullanımı, kesit geometrisi ve tüpler üzerinde oluşturulan çeşitli modifikasyonların numunelerin mekanik performansına etkileri araştırılmıştır. Dolgu kafes yapısı olarak girintili ve altıgen balpeteği konfigürasyona sahip dolgular 3B yazıcılarda üretilmiştir. Tüpler alüminyum, dolgular ise PLA ve ABSplus plastik malzemelerden imal edilmiştir. Bu faaliyetlerde kullanılan AL6063 alüminyum alaşım ile PLA ve ABSplus plastik malzemelerinin malzeme özellikleri ASTM test standartlarına göre belirlenmiştir.

İlk olarak dairesel kesitli tüplerde girintili ökzetik dolguların ve tüp üzerinde uygulanan modifikasyonların 5 m/s çarpma hızında çarpma dayanımına etkileri sonlu eleman yöntemleriyle incelenmiştir. Tüplerin 2 mm kalınlık, 70 mm çap ve 100 mm boya sahiptir. Tüpler üzerinde yükseklik boyunca girintili hücre sayısına eşit sayıda zigzag şeklinde modifikasyon tanımlanarak katlanma mekanizmasının kontrol edilmesi öngörülmüştür. Bu faaliyette ökzetik dolgulu ve dolgusuz standart tüpler ile, iki farklı modifiye edilmiş tüpün mekanik performansları karşılaştırılmıştır.

Daha sonra ökzetik dolgu kullanımının deneysel olarak incelenmesi için 3 mm/dak ezme hızında statik ezme testleri ve 2.5 m/s çarpma hızında dinamik testleri yapılmıştır. Alüminyum tüplerin imalatı için dairesel kesitli AL6063 malzemeli borular temin edilmiş ve belirlenen boyutlarda kesilmiştir. ABSplus plastik kare kesitli ökzetik dolgular ise Dimension Elite 3B yazıcı cihazı kullanılarak üretilmiştir. Test numunelerinin deney esnasında kaymasını önlemek için numuneler alüminyum bir plaka üzerinde CNC ile işlenen kanallara yerleştirilerek sabitlenmiştir.

İnce cidarlı entegre yapılı tüplerde ayrıca iç içe kademeli değişen boylara sahip çoklu tüpler de incelenmiştir. ABSplus plastik malzemeli altıgen balpeteği dolgular dairesel kesitli alüminyum tüplerin iç boşluklarına yerleştirilerek tüplerin sayısı 1-5 arasında değişen ve tüp boyları içten dışa artan ve azalan şekilde numuneler üretilmiştir. Bu çalışmada dolgu kullanımı, tüp boyları ve sayısının değişiminin ince cidarlı iç içe tüplerde düşük hızlı çarpma yüklerine karşı etkileri incelenmiştir. Çarpma testleri 2.75 m/s çarpma hızında darbe test cihazı kullanılarak yapılmıştır. Sonlu eleman analiz sonuçları ile deney sonuçları karşılaştırılarak sonlu eleman modelleri doğrulanmıştır. Daha sonra sonlu eleman analizleri ile iç içe kademeli tüplerde kesit geometrisi, incelen kesit kullanımı ve tüplerin yanal yüzeylerinde oluşturulan modifikasyonların etkileri incelemiştir. Son olarak iç içe üçlü tüpler için boy, çap ve kalınlık tasarım değişkenlerine göre enerji absorbe kapasitesi ve mekanik dayanımı artırmayı amaçlayan çok amaçlı optimizasyon algoritmaları ile en iyi performansa sahip tasarımlar belirlenmiştir. Genetik algoritma ve Yanıt Yüzey yöntemi (RSM) çok amaçlı eniyileme probleminin çözümünde kullanılmıştır.

1. INTRODUCTION

Thin-walled structures are extensively used in the automotive, aerospace, and military industries due to their energy absorption capacity and their lightweight for the protection of the passengers, drivers, and electronic devices of the vehicle. Herein, panels and tubes are the most common thin-walled structures used as a structural component of vehicles.

Air vehicles can be exposed to structural damages and disable integrity due to static or dynamic loads. Several airplane accidents due to flying debris impact during high wind events to hail impact or bird strike have been recorded and statistically investigated their catastrophic results and frequencies so far. The number of bird strikes reported in 2014 is six times more than that of the year 1990, according to the FAA [1]. According to the analysis of bird strike data collecting by ICAO since 1965, one bird strike occurs in 2,000 flights [2]. Hail or debris impacts are rare and have less potential damages on the components, but they could be risky in particular for the performance of control equipment and engines. Although the majority of the damages do not present safety risks, they generate high costs due to maintenance and repair services.

Windshields of an airplane, e.g., fuselage or wing surfaces, can have a risk of these impact loads [3] and therefore, they should withstand these external loads in order to protect not only its shape integrity but also the performance of other components connected with them (Figure 1.1). For this purpose, manufacturers have striven to increase safety lengths of vehicles, and researchers have tried to improve the strength and reduce the sensitivity of the exterior parts against indentation and impact loading. They have tested and compared various configurations, material types of structural components of the vehicles.

The shape of the outer surfaces of the vehicles can be considered as a combination of curved and flat panels. They are skin structures of fuselage/wing/empennage of an airplane, blade/canopy of a helicopter, windshield of a spacecraft vehicle, etc. Therefore debris, bullet, hail impact, or bird strike of these components have more

importance for the protection of structural integrity. Increasing strength, energy absorption, and reducing the weight of these components are among the primary aims of engineering. The usage of sandwich panels has become popular in aeronautics and aerospace industry, marine/offshore industries, ground transportations, and military applications thanks to its lightweight, high specific strength, stiffness, tailorability, and stability properties against impact loading [4-10]. Foams and cellular honeycombs are extensively used as core material for sandwich structures.

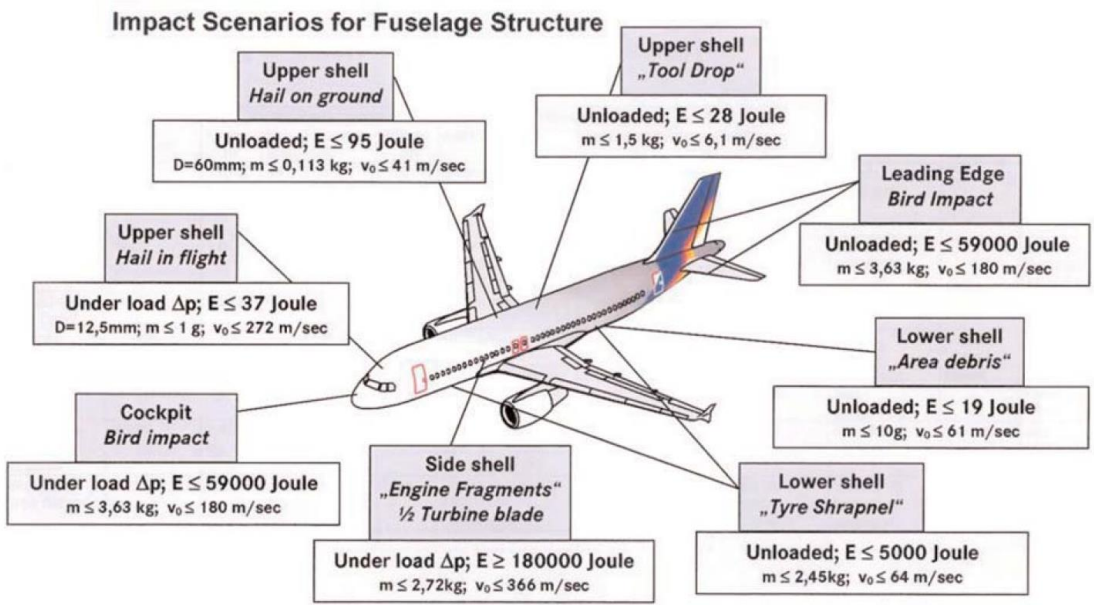

Figure 1.1 : Impact scenario chart for passenger airplane fuselage [3].

Likewise, thin-walled tubular structures may have curved or flat surfaces according to cross-section types. They can be utilized as the forms of landing gears or frames of aircraft. They are also generally used as crash boxes in the automotive industry. Converting some amount of kinetic energy during a collision to the plastic energy prevents passengers and devices from squeezing. Besides, inertial loads can be harmful for passengers during dynamic crash. The frontal and rear sides of vehicles are the typical regions subjected to impact loads; therefore, crumple zones are used to absorb crash energy in these areas. Crash tubes are one of the significant safety components used as thin-walled structures owing to their lightweight. Similar to sandwich panels, lightweight structures such as foams and honeycombs are implemented into the thin-walled tubes to increase mechanical performance under crushing loads.

Many natural solids like woods, coral, sponge, and bone are made of cellular microstructures. Man-made cellular structures inspired by the shape of these natural

solids are widely used in engineering applications that require lightweight structural components, energy absorption, heat insulation, high stiffness and high strength. Honeycombs are between the most common and promising cellular structures used as core materials, and numerous studies have clarified the relation between the global mechanical properties of these lattices and the geometrical features of their unit cells. Common materials exhibit positive Poisson's ratio – i.e., when the material is subjected to tensile loading, it deforms by stretching along the axial direction and shrinks transversely. Auxetics instead become larger transversely to the tensile pulling direction. In recent years, the interest in auxetic metamaterials has increased remarkably.

1.1 Purpose of the Thesis

This thesis proposes to increase the resistance of the air vehicles under dynamic and static loading. We mainly focus on enhancing mechanical performances of flat and curved sandwich panels and thin-walled tubes, which are the common configurations for aircraft design. The effects of curvature and core/filler configuration of these structures are investigated. The core and filler configurations are chosen as auxetic and non-auxetic cellular shapes

In the first part of the thesis, we study on the mechanical performances of hierarchical slotted and asymmetrical edge cellular shapes honeycombs with auxetic and non-auxetic configurations subjected to edgewise compression. Auxetic materials are very special kinds of materials that exhibit negative Poisson's ratio (NPR) under tensile or compressive loading across a wide range of materials. Several cellular shape of auxetic metamaterials have been developed and used in several engineering applications thanks to its superior properties over traditional ones. Differently from existing auxetic lattice designs, this thesis introduces a set of novel hierarchical auxetic metamaterials with re-entrant cellular configurations which have higher compressive stiffness, strength and specific energy absorption capabilities over traditional ones.

Then, low and high-velocity impact behavior of flat and doubly curved sandwich panels with and without auxetic core is investigated by conducting the following studies:

- Low-velocity impact behavior of composite sandwich panels with different types of auxetic and non-auxetic core structures are described.
- High-velocity impact behavior of doubly curved sandwich panels is described by using a gas gun test machine.
- A parametric analysis of single and doubly curved sandwich panels with auxetic core under projectile impact.
- Thickness and curvature effects on high-velocity impact behavior of flat and cylindrical panels are investigated numerically.

Moreover, the deformation behavior of thin-walled tubes with and without auxetic fillers are investigated by conducting the following studies:

- Circular crash tubes with and without auxetic lattices are examined under dynamic loads.
- Quasi-static and dynamic crushing behavior of circular aluminum tubes with square prism auxetic filler
- The effects of using honeycomb filler, increasing the number of tubes, and changing the length of tubes on nested tube structures under dynamic impact loading.
- Cashworthiness optimization of nested and concentric circular tubes under impact loading.

None of the listed studies above are found in the pertinent literature. Therefore, this thesis proposes to develop novel auxetic lattice configurations, sandwich panels, and tubular structures and provide valuable knowledge to the research community.

1.2 Literature Review

1.2.1 Thin-walled structures

Thin-walled structures can be applied as shells, plates, or beams (column or rod) in constructions and have a growing and important proportion in the engineering profession for not just the aircraft, spfacecraft, missiles, vessels, or land-based vehicles but also warehouses, bridges, storage racks, etc. Therefrom the knowledge of the deformation behavior of thin walled structures when they are exposed to vibration,

impact, shock, or any kind of environmental loads becomes substantial for engineering to improve the sustainability of the vehicle components or infrastructures [11-12]. In this study, the thin-walled structures in the form of sandwich panels and cylindrical tubes are considered.

1.2.2 Sandwich panels

Composite panels have a wide range of uses in engineering applications due to their lightweight characteristics, acoustic insulation, high strength, high stiffness, corrosion resistance and wear resistance, etc. Increasing strength, energy absorption, and reducing the weight of the structural components simultaneously are among the primary aims of engineering. The usage of composite face sheets in sandwich structures has become popular in aeronautics and aerospace industry, marine/offshore industries, ground transportations, and military applications thanks to its high specific strength, stiffness, tailorability, and stability properties against impact loading [4-10]. Sandwich panels are made of two thin stiff and strong skin layers and a low-density core material. Skin layers can be various types of aluminum, steel, composites, etc. Core materials are considered as foams and honeycombs made of low density materials. They can protect structural integrity while absorbing large amounts of impact energy.

Generally speaking, impacts can be classified as low, high, and hypervelocity in several studies [13]. Although there is a debate about representing the quasi-static indentation test and impact event [14], the low-velocity impact can vary from the speed of quasi-static indentation tests to the order of tens [15]. The impact velocities of equal or greater than 100 m/s may represent the high-velocity impact event. The hypervelocity impact event can vary in the range of 2-10 km/s [16].

1.2.2.1 Low-velocity impact

Low-velocity impact protection has a particular interest in engineering applications. It induces more localized damage than quasi-static compression and less localized damage than high-velocity impact loading [13]. The deformation mechanism under high and low-velocity impact conditions is likely to be governed by localized material damage rather than global buckling. The energy absorption of the brittle composites laminates is mainly governed by elastic deformation. The deformation mechanism and

transverse damage resistance are poor due to a lack of reinforcement through the thickness direction [17]. Particularly, carbon fiber/epoxy resin (CFRP) composites can absorb energy by material damage such as fiber breakage, matrix cracking, delamination rather than yielding [18]. The geometrical configuration has a key role to be able to absorb more energy and have more impact resistance. The stacking sequence, ply orientation, ply thickness, and material type are the important parameters for manufacturing composite laminates. Strait et al. [19] indicated that the stacking sequence has a significant effect on the impact resistance by comparing the energy to maximum load response of the cross-ply, quasi-isotropic, and [0/+-45] layups. Wang et al. [20] showed composite laminates with angle-ply stacking sequences can keep greater residual tensile strength than cross-ply stacking sequences. In addition, the relatively small thickness of laminates is prone to buckling under compression loading due to elastic instabilities [21].

1.2.2.2 High-velocity impact

Fragment impacts at high velocities can lead to fatal results on structures. Therefore, investigation of the response of structures under impact loading is very important. For this purpose, panel structures made of different materials (aluminum, steel, composite, etc.) have been examined experimentally and numerically so far. For example, López-Puente et al. [22] demonstrated that oblique impact caused a larger deformed zone compared to the normal impact on the backplane of the composite panel for projectile velocities close to the ballistic limit. Wambua et al. [23] tested and compared different kinds of composites panels made of flax, hemp, and jute fabric reinforced polypropylene. Flax composites gave better energy absorption capability. Gower et al. [24] sought the effect of the nose shape of projectiles on the ballistic behavior of the laminated composite panels impacted at velocities between 130-250 m/s. They carried out experimental and numerical studies using conical and hemispherical nose shapes. Also, failure mechanisms of the composites such as delamination, shear plugging, petaling, and matrix cracking were investigated numerically, experimentally, and analytically by other researchers [24-26].

Ahmadi et al. [25] investigated the impact resistance of the GLARE (Glass Laminate Aluminum Reinforced Epoxy) composite panels in terms of ballistic limit and perforation energy regarding to different thicknesses ratios. Experiments were

implemented by using a gas gun machine with 50 bar of compressed helium. The length of the barrel was 2.5 m, and the projectile was spherical steel. The velocity of the projectile was measured by using a chronograph. The schematic view of the test system is shown in Figure 1.2. The ballistic limit was measured by comparing the test results. The ballistic limit means that the minimum velocity of the projectile to perforate the panel.

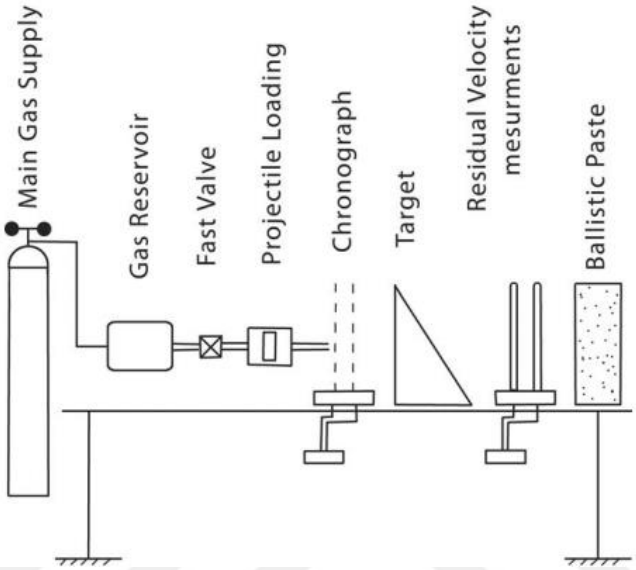

Figure 1.2 : Schematic illustration of a gas gun [25].

Vlot et al. [27] investigated the low and high dynamic impact and quasi-static crushing performance of the monolithic aluminum panel and GLARE and ARALL (Aramid-Reinforced Aluminium Laminate) hybrid composite panels by using numerical and experimental methods. Samples were tested at 10 m/s and 100 m/s impact velocities. Okafor [28] studied the spherical steel projectile impact behavior on the composite panels at different impact velocities by using a gas gun with compressed nitrogen gas. Aktay et al. [29] studied the high dynamic impact behavior of composite panels by using concrete projectile at 60 m/s impact velocity. They considered that concrete debris impact on the aircraft could be encountered during landing, taking off, and taxiing on the runway. Projectiles were located in sabots.

In another study, the dynamic impact behavior of fabric composite panels was examined in 2-D analytical formulations, and then the analytical results were compared with the experimental results [26]. Fracture mechanics of targeted panel, velocity/mass and dimensions of the projectile were taken into consideration for comparison studies. The cone formation on the back face of the panel, stresses on the

primary fiber, deformation of the secondary fibers, delamination, matrix cracking, shear plugging, and friction during penetration were discussed and evaluated. The thickness of the square panel was 2 mm, and the edge length is 125 mm. Ballistic limit, interaction duration, the radius of cone formation, radius of the deformed zone on the surface were determined analytically and obtained good coherence with the experimental results. In Figure 1.3, the cone formation of the panel is shown [26].

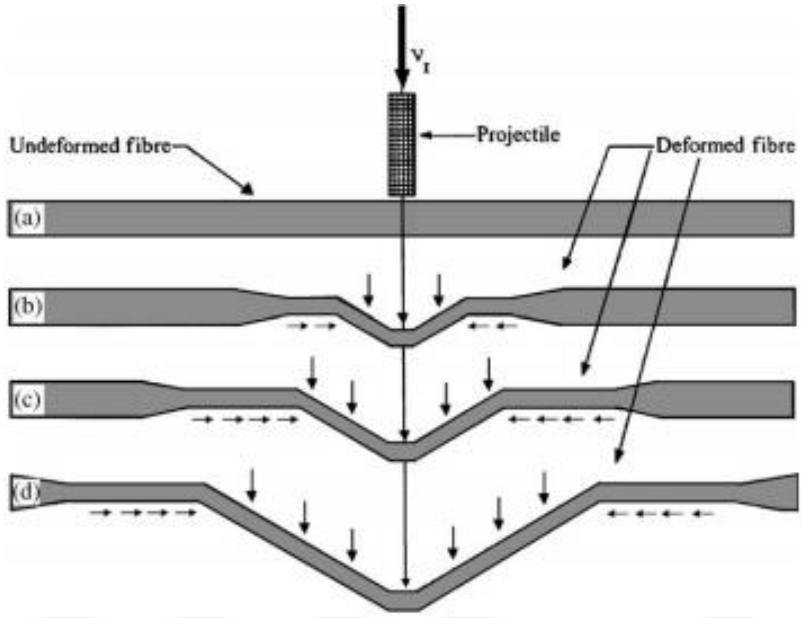

Figure 1.3 : Configuration of a yarn/fibre before and after transverse impact: (a)before impact; (b)–(d) after impact [26].

Sun and Potti [30] considered the composite laminates that have higher-order nonlinearity during interaction and penetration by using different analytical methods. The circumferential length of the Graphite epoxy was 305x305 mm. The results showed that the local/global deformation, the damage initiation, and progression in the target lead to complexity.

The literature review indicates that LS-DYNA, Abaqus, PAM CRASH, and AUTODYN software programs are generally preferred for Finite Element analyses. In most of the studies, a quarter of the target panel was modeled to reduce the computation cost. Besides, the mesh size of the impacted zone was selected lower to reduce the computation time. These referenced articles could also provide a general overview of experimental studies of composite panels by using a gas gun test machine. Besides the target panel, determining material types, dimensions, configuration, mass, and ejection angle of the projectile has an important place for the experimental studies. Rigid and spherical steel projectiles are most likely encountered in these articles within

the range of 1-20 gr masses. Based on the literature review, several studies related to high-velocity impact are listed according to their published year and technical content in Table 1. In Table 1, software programs, mass, diameter, shape, and impact velocity of bullets used in researches are given in detail.

Table 1.1 : A literature overview.

Published year	Mass of Projectile (g)	Velocity of Projectile (m/s)	Configuration of Projectile	Diameter of Projectile (mm)	Circumferential Length of Target (mm)	Thickness of Target (mm)	Pressure Capacity (Bar)
2012 [25]	14.0	100-180	Cylindrical	8.7	150x150	1.75-7.25	50
2006 [26]	2.8	150	Cylindrical	5.0	125x125	2.0	-
2001 [31]	4.0	900-1500	-	5.59	120x120	-	-
2007 [32]	-	65-129	Spherical	12.7 20	200x200	1.5-6.0	
2009 [33]	18.8	<500	Semi-Spherical	20	300x300	4.8	250
2008 [22]	1.73	70-531	Spherical	7.5	80x80	2.2	300
2001 [34]	1.0 3.0	250	Spherical	6.3 12.7	70x70 120x120 50x200 80x200	2 and 6	-
2008 [24]	-	130-250	Conical Cylinder Spherical	7.5 9.0	304.8x304.8 254x304	-	-

1.2.2.3 Doubly curved panels

The majority of the works on doubly curved panels are about the determination of the mode shapes free vibration and their natural frequencies [35-37]. In these studies, doubly curved panels were discretized using finite element methods and investigated analytically. Reddy and Chandrashekhar [38] have examined the effects of the nonlinearity of the geometry and shear deformation on cylindrical/doubly curved shells. Kapania [39] developed a formulation for the buckling analyses of the doubly curved structures. Ganapathy and Rao [40] performed the failure analyses of the cylindrical and spherical panels. In recent years, Tornabene and Viola [41-45] have published several papers on doubly curved panels. In these papers, free vibrations of

the doubly curved panels were solved by using the generalized differential quadrature method (DQM). Mode shapes were determined under static and dynamic loading.

Two principal curvatures are used to define the local shape of a point on a surface. One of them is characterized by the rates of maximum and minimum bending of the surface and its tangent directions. These principle curvatures are estimated according to the Euler Formula in equation (1.1).

$$\kappa = \frac{\frac{\partial^2 w}{\partial x^2}}{\left[1 + \left(\frac{\partial w}{\partial x}\right)^2\right]^{3/2}} = \frac{1}{\rho} \tag{1.1}$$

$\kappa_1$and κ_2 represent the principal curvatures of the surface. Gaussian curvature is estimated by using equation (1.2).

$$K = \kappa_1 \kappa_2 \tag{1.2}$$

According to sign of the K, various types of doubly curved surfaces can be obtained, seen in Figure 1.4.

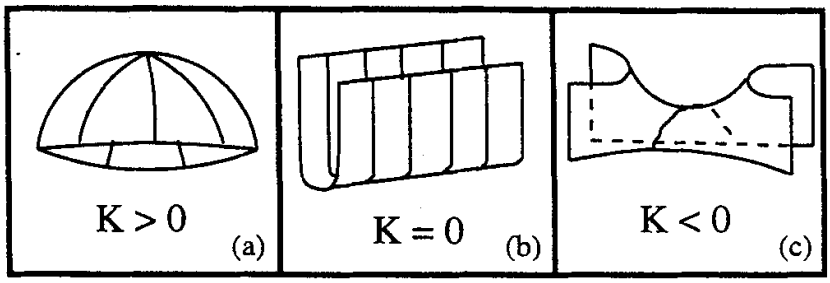

Figure 1.4 : The Gaussian curvature, K, relates to the structures on the slab surface as follows: (a) K > 0, (b) K = 0 and (c) K<0 [46].

1.2.3 Crash tubes

According to the World Health Organization (WHO) report, traffic accidents in 2013 resulted in the deaths of over one million people worldwide, with even more seriously injured [47]. Therefore, manufacturers strive to increase safety lengths of vehicles against crash loads to protect passengers and drivers. The frontal and rear sides of vehicles are the typical regions subjected to impact loads; therefore, crumple zones are used to absorb crash energy in these areas. Crash tubes are one of the most primary safety components used as thin-walled structures owing to their lightweight.

An effective crash tube design has a higher energy absorption capability and exhibits lower peak crash force (PCF) when subjected to crash loads. To date, a number of studies have been conducted to obtain better crash tube designs by changing the geometry and material properties, amongst other factors. Aluminum alloys are typically used materials for crash tubes owing to their lightweight, easy processing, and higher energy absorption capabilities.

In recent years, a number of studies have been conducted to increase crashworthiness and energy absorption of thin-walled tubes. For this purpose, geometrical modifications on tubes, various cross-section types, and material types have been examined to obtain better designs. For example, Usta et al. [48, 49] studied on stepped and concentric circular crash tubes under axial impact loading by using numerical, experimental, and optimization techniques. Eyvazian et al. [50] investigated the effects of corrugations on the deformation behavior, energy absorption, and failure mode of circular aluminum tube and showed that corrugated tubes provided higher crashworthiness characteristics. Lee et al. [51] analyzed metallic tubes, including grooves at folding sites where could be pre-estimated by FEA analysis. Triggering improved the energy absorption performance, and the half-dented tube was more effective than the full-dented tube. On the contrary, energy absorption could be worsened by using triggering without consideration of the peak location of the folding wave and inhomogeneous deformation. The geometry of the trigger mechanism could be optimized by using various methods [52]. El-Hage et al. [53] investigated various types of trigger mechanisms of metallic tubes, such as chamfering, triangular hole pattern, and geometric imperfection. Force displacement response and folding mechanism could be controlled by changing trigger types.

Filled tubes

Using foam filler is one of the most preferred methods of increasing the energy absorption and strength of crash tubes. They are classified as open-cell foam if the faces are solid and sealed and closed-cell foam if the foam includes open faces and is connected to the cell edges [54]. Duarte et al. [55] reported a hybrid foam model containing both open and closed-cells as fillers of thin-walled aluminum tubes. Googarchin et al. [56] reported a theoretical expression representing the mean crush load of tapered multi-cell tubes with closed-cell foams. Liu et al. [57] investigated the

effects of Poisson's ratios of foams on energy absorption capacity. They reported that interaction between the foam and tubes has a significant effect on the energy absorption capacity. They proposed that double tubes with mixed types of foam with negative and positive Poisson's ratio had greater specific energy absorption (SEA).

Li et al. [58] compared the quasi-static crushing test results of square and circular empty tubes and various ex-situ-filled tube types. They reported that the mean crush force, SEA, energy absorption per stroke, and effectiveness factors of circular tubes were greater than those of the square tubes because of the compact deformation modes. In terms of crush force efficiency and SEA, foam-filled single and double circular tubes were recommended. Taherishargh et al. [59] fabricated foam-filled tubes by an in-situ infiltration process and obtained superior mechanical properties of the foam-filled tubes owing to the interaction between the foam and tubes. Hussein et al. [60] reported that tubes filled with polyurethane foam and aluminum honeycomb combinations exhibited considerable increases in terms of mean crush force, energy absorption, and SEA compared to empty tubes. The increases were greater than the sum of the mean crush forces of the polyurethane foam, aluminum honeycomb, and empty tubes.

In the open literature, open-cell foams were typically investigated by changing the geometry of the unit cells. The most common type was the hexagonal honeycombs. Usta et al. [61] reported the impact behavior of tubes with auxetic honeycomb core by considering various types of trigger mechanisms. Luo and Fan [62] compared thin-walled and sandwich walled tubes and tube thicknesses in terms of mean crushing force (MCF). They reported that thick sandwich walled tubes crushed progressively and thin sandwich walled tubes bent globally and that both were superior to thin-walled tubes. Nia and Parsapour [63] reported that multicell tubes had greater energy absorption capacities than single tubes by testing and analyzing triangular, square, hexagonal, and octagonal sectional tubes.

In numerous studies, the design of multicell tubes has been determined by implementing optimization techniques. Tran and Baroutaji [64] optimized triangular multicell tubes with different cross-sections subjected to both axial and oblique impact loads. Fang et al. [65] reported the crashworthiness of multicell tubes under multiple loading by using optimization techniques. Xie et al. [66] described polynomial response surfaces of peak crushing and MCF considering variations in lengths and

thickness of different multicell square tubes and reported that the geometrical optimization parameters have a significant influence on energy absorption. Chen et al. [67] compared the crashworthiness of a new type of five-cell profile with existing multicell tubes and investigated the effects of corner cell sizes and wall thickness. They reported an increase of 11.6% in SEA values using multi-objective particle swarm optimization and response surface method combinations. Usta et al. [68] reported the crashworthiness optimization of tri-tubular nested tube structures by combining finite element (FE) models, Response Surface (RS) methods, and Genetic Algorithms to reduce the computational cost by using SEA and crush force efficiency (CFE) indicators.

Studies on nested tubes have also significantly increased over the past number of years. Niknejad et al. [69] reported a novel longitudinal grooved tube with a special cross-section type subjected to lateral compression loads. Empty, foam filled, and nested tubes produced using various materials were investigated. Their novel design of nested tubes had advantages in terms of energy absorption capability over the tube designs in previous studies. Tasdemirci et al. [70] were inspired by the geometry of a balanus, a type of SEA creature whose bi-tubular structure comprised one outer shell and one conical inner core. Altın et al. [71] optimized nested tubes, which were filled with foam material, according to taper angle, the thickness of tubes, and foam density, considering both axial and lateral foam filling. Wang et al. [72] applied a theoretical model to analyze internally nested circular tubes under lateral loading. Nia and Chahardoli [73] tested four different types of nested tube structures under quasi-static compression and reported that the nested tubes provided better energy absorption than single tubes by maintaining constant height, thickness, and mass. They also [74] performed an optimization study to determine an optimal design of tri-tubular nested tube structures considering different thicknesses and heights. The optimization study indicated that greater energy absorption and lower peak forces could be obtained by changing the thickness and height of nested tubes. In addition, the difference between the lengths of nested tubes should be shorter for more continuous load-displacement curves. Esa et al. [75] investigated nested tubes triggered by holes at the top edges that could manipulate the damage level and reduce total weight. Usta et al. investigated the effects of the number of tubes [49] and cross-section types [48] of nested tube structures parametrically by using LS-DYNA software. The crushing behavior of

nested tube structures was also investigated under lateral loading conditions, and parametrical studies were performed to obtain higher energy-absorbing structures [76]. Morris et al. [77] tested and analyzed the nested tube structures with vertical and inclined constraints under compression loading. Tran et al. [78] derived a theoretical model to obtain PCF values of multi-cell tubes and verified the theoretical results of multi-stage nested two and three square tubes by comparing the experimental and numerical results.

1.2.4 Core and filler types

1.2.4.1 Foam filler

Foams and cellular honeycombs are extensively used as core material for sandwich structures under impact loading [6]. The impact response of the foam core sandwich constructions is mostly related to the density and modulus of foam [7]. Heavier cores increase the local rigidities, which can annihilate the potential advantages of the core under the low-velocity impact. Sharma et al. [8] noted that PU core failure was governed by shear strain and delamination between the face sheet and core. The core material increased the support surfaces for bonding with the face sheets. Zhang et al. [9] used a hybrid core material with the constituents of PU foam and pyramidal truss members to enhance the impact resistance and energy absorption of composite panels. The load-carrying capacity of the foam-filled sandwich structures with truss members has developed thanks to the synergistic effects of the core constituents. Njuguna et al. [10] examined the impact response of PU core sandwich panels by filling the core with nanoparticles. This way increased the number of PU cells with the smaller dimensions and anisotropy index and led to higher peak loads. Crupi et al. [79] compared the low-velocity impact response of honeycomb and foam for the aluminum sandwiches and observed different collapse mechanisms. The collapse mechanism of honeycomb sandwiches was represented by the buckling of cells, while foam core sandwiches collapsed for the foam crushing. The impact resistance and energy absorption capacity of the foam core were strongly related to foam quality, while the performance of the honeycomb core tended to cell size. Jiang and Hu [80] fabricated a novel multilayer orthogonal structural composite with auxetic effect consisting of PU foam and reinforcement structures and then compared low-velocity impact performance with the

non-auxetic one. They exhibited an auxetic composite that could provide better energy absorption.

1.2.4.2 Auxetic Fillers

Cellular honeycombs can be classified as auxetic and non-auxetic according to the sign of Poisson's ratio. Mechanical metamaterials and auxetics have a wide range of use in engineering applications due to their lightweight characteristics, large energy absorption, heat insulation, tailorable stiffness, and strength. Several pioneering studies related to auxetic cellular structures have shown advantages superiority over classical cellular configurations in terms of mechanical properties, which results from the interplay between the geometry of the unit cells of those lattices and the characteristics of their core materials [81-90]

Auxetic materials exhibit negative Poisson's ratio (NPR) under tensile or compressive loading and are represented across a wide range of materials, which include cellular solids, microporous polymers, composites, and molecular assemblies. Typical unit cell configurations of auxetic materials are the re-entrant [61, 82, 91-95], arrowhead

[95-99], chiral [94], rhombic [97-100], star-shaped [101] and tetra-petals [102] configurations. Here we focus on re-entrant, arrowhead, and chiral honeycombs, which are the most common unit cell configurations of auxetic materials. The butterfly shape morphology is based on arranging the inclined rib if the hexagonal honeycomb at a negative angle [81]. Sarvestani et al. [103] presented the re-entrant configurations could get higher energy absorption capacity over hexagonal and rectangular cellular cores. Yang et al. [104] exhibited the re-entrant auxetic sandwich panels could achieve higher impact performance considering the combination of a reduction in peak load and an increase in energy absorption capacity comparing to the hexagonal, rhombic, and octahedral sandwich panels. The material of re-entrant honeycomb core flowed into the impact region and caused material concentration due to negative Poisson's ratio effect, which increased the impact resistance of the sandwich panels[105, 106].

Larsen et al. [107] first proposed the auxeticity of the double arrow-head (DAH) honeycombs. The interest in DAH honeycombs has increased thanks to their auxetic properties remarkably so far. Wang et al. [108] indicated that the stiffness and auxeticity of DAH auxetic structure increased with the increase of compression strain. The deformation pattern of the DAH configuration was governed by the bending of

the ribs rather than axial and shear deformation[109, 110]. Lim [111] exhibited the Poisson's ratio of DAHs could be controlled by changing linkage lengths or half angles. Similar to the re-entrant and DAH configurations, hexachiral auxetic structures have also drawn increasing attention in recent years [112-119]. Prall and Lakes [112] first proposed hexachiral honeycomb on the basis of the theoretical expressions under small deformation. The deformation mechanism of the chiral honeycombs could be identified by rotation of cylinders and flexing of ligaments [113].

1.2.4.3 Architectural structures

Recent works have shown that specific architectures of unit cells can enhance the mechanical properties and energy absorption capacity of cellular structures. Tan et al. [120] investigated two re-entrant hierarchical honeycombs, including unit cells with regular hexagon and equilateral triangle substructures. Chen et al. [121] showed that hierarchical cellular configurations created by replacing cell walls with triangular lattices provided progressive failure modes, higher energy absorption, and stiffness under uniaxial loading. Ingrole et al. [82] developed a new hybrid-auxetic-strut structure combining re-entrant auxetic and regular honeycomb unit cells. The configuration showed an improved energy absorption capacity and strength under compression loading and reduced stress concentration under large deformations because of the custom struts designs. Alomarah et al. [122] investigated the compressive properties of re-entrant chiral auxetic structures (RCA) combining topological features of re-entrant and chiral honeycombs. The RCA structure could provide more specific energy absorption and strength than other types of honeycombs, depending upon the loading direction.

All types of materials can display auxetic behavior if they take the shape of any auxetic cellular form, and mechanical properties can be improved by arranging dimensions or shapes. In addition to this, auxetic structures with a combination of two or more materials can provide another solution to enhance the overall mechanical properties. Studies on auxetics composite materials have significantly increased over the past decade [123]. Ge et al. [124] numerically investigated the compression behavior of 3D auxetic textile structures composing of weft, yarn, and stitch yarns reinforcements. Jayanty et al. [125] reported auxetic behavior of some polymer nanocomposites with carbon nanofibers. Jopek and Strek [126] investigated the thermomechanical behavior

(geometry of fiber and thermal effects on materials) of auxetic composites built from two constitutive materials. Previously, composites made of auxetic lattices as reinforcement and surrounding viscoelastic matrix were developed by Scarpa et al. [127] and Gandhi's Group [128, 129]. Viscoelastic inserts bridging segments of the honeycomb cell walls were also used to increase damping and energy dissipation [130, 131]. Sloan et al. [132] discussed the effects of the starting angle of a wrap fiber, diameter ratio of the wrap to core fibers, and the inherent Poisson's ratio of the fibers on their novel auxetic textile composites. Quan [133] showed that continuous fiber-reinforced thermoplastic composite auxetic honeycomb had extremely high compressive stiffness and energy absorption capacity than the pure polylactic acid (PLA) re-entrant honeycomb. Subramani et al. [134] investigated the mechanical behavior of five different auxetics by changing the structural cell angle and using core reinforced braided composite rods. Xu et al. [135] have shown that non-Newtonian fluid could improve low-velocity impact and compression resistance of composite structures. Shear thickening fluids provide for example, a synergistic effect with auxetic warp-knitted spacer fabrics and could increase energy absorption of the composites due to the shear thickening transition. Large energy absorption under impact has also been recently observed when shear thickening (Non-Newtonian) fluids have been used as through-the-thickness fillers in hexagonal honeycomb sandwich panels [136].

1.3 Overview

The thesis study is organized as five chapters to answer the research questions and is easy to follow for the reader. The introduction chapter contains a general overview, the purpose of the thesis, literature review, and organization of the thesis. Chapter 2 focuses on developing novel hierarchical auxetic metamaterials with re-entrant cellular configurations. Chapter 3 covers the studies on sandwich panels, such as the effects of implementing different types of auxetic cores ve effects of curvature under projectile impact loading. Chapter 4 presents the deformation behavior of curved tubes with and without auxetic fillers by introducing novel nested and triggered crash tube designs. The last chapter expresses the conclusion and recommendations for future studies.

2. NOVEL HIERARCHICAL UNIT CELLS HONEYCOMB AND MULTIPHASE LATTICE METAMATERIALS

2.1 Purpose

The work introduces a novel type of auxetic open cell assembly with asymmetrical unit cells along the two edge sides and a new architectural design with modified thickness of unit cells. Differently from existing auxetic lattice and composite designs, this study also introduces a novel type of composite open cells honeycombs with the PLA plastic reinforcements, hydrogel, and polyurethane rigid (PUR) foam over a hierarchical cellular platform. The cellular structures evaluated in this study are subjected to unidirectional edgewise compression. We describe the design, manufacturing, characterization, and mechanical compression of these novel multifunctional auxetic structures. Effective compressive stiffness, strength, and specific energy absorption capabilities of the structures are here discussed. The advantages and disadvantages of our novel designs are also evaluated. The experimental results of the hybrid and multiphase types of the new composite hierarchical structures are compared with the analogous results from samples with their internal configuration made of full solid materials.

2.2 Design Methodology and Manufacturing Processes

2.2.1 Unit cell designs

The baseline cell architectures considered in this work are re-entrant configurations with asymmetrical units along the edges and the perforated rib lattice configuration based on controlled porosity of the 3D printing process. Figure 2.1 shows the different bulk thickness honeycomb configuration evaluated in this work in uniaxial in-plane compressive loading. The conventional hexagonal (non-auxetic) and re-entrant (auxetic) cellular configurations are indicated in Figure 2.1a and Figure 2.1b, respectively. The novel asymmetric edge cellular re-entrant configuration is shown in Figure 2.1c. In the novel designs, asymmetric cells are aligned at the right and left side

of the re-entrant cells. The number of cells chosen for the Finite Element and experimental tests was 5x4, dimensions of 122x105x10 mm^3 kept constant for each design.

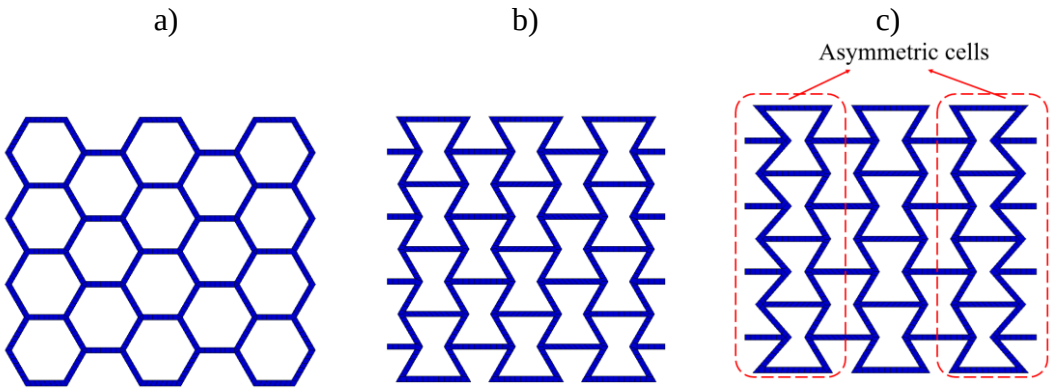

Figure 2.1 : a) Hexagonal, b) re-entrant, and c) asymmetric re-entrant designs.

In terms of unit cell geometry, our designs are classified as hexagonal, re-entrant, and asymmetric re-entrant. The design parameters of the unit cell are the height *H*, the thickness *t* of the struts, the length *l* of the inclined strut, the internal cell angle *θ*, and the out of plane thickness *b* of the struts (Figure 2.2). The dimensions of those parameters used for the 3D printed samples are *h*=30 mm, *t*=3 mm, *l*=15 mm, *θ*=60°, and *b*=20 mm. Dimensions and number of cells in each specimen are the same, except for the case of the asymmetric unit cells in which the length of the rib is *l*=16.96 mm, and the inclined angle of the edge side facing outwards is 50°.

The hierarchical (slotted) structures are designed by leaving two small gaps along the thickness of the ribs. The thickness of the struts in the slotted cells is 0.8 mm.

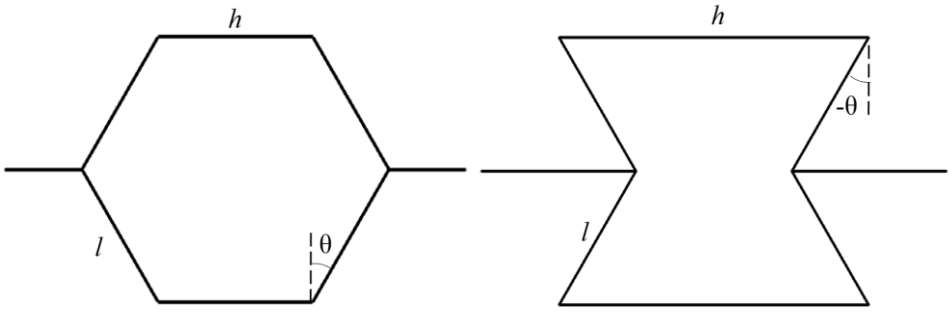

Figure 2.2 : Conventional and re-entrant honeycomb structures.

We consider here two types of multiphase material architectures for the ribs of those lattice configurations. The first combines a solid slotted (deterministic porosity) made of PLA and filled with a non-Newtonian gel (hydrogel). The type of hydrogel used here is alginate gel. The second is related to a type of hybrid structure made of PUR

foam added into slots (deterministic pores) of the PLA-made samples. Figure 2.3 shows unit cells with bulk (fully filled ribs) thickness, slotted, and composite cellular structures are listed considering hexagonal and symmetric/asymmetric re-entrant types.

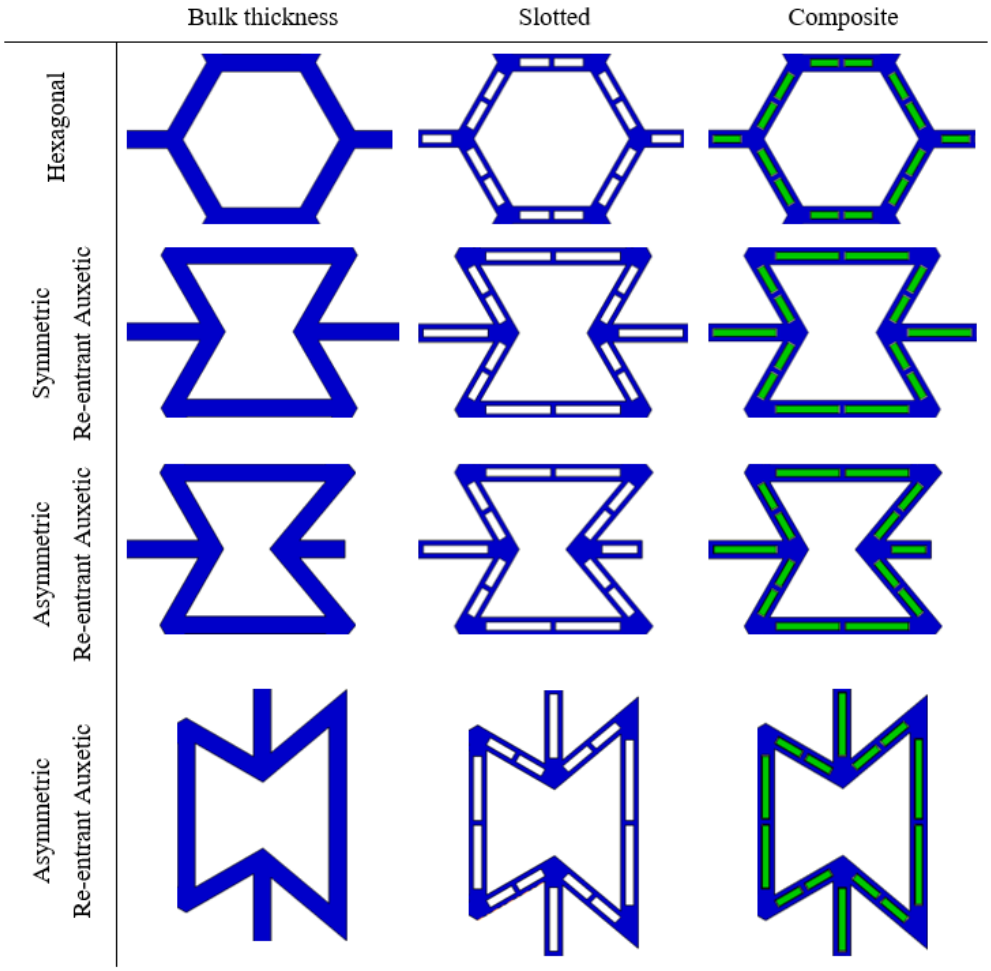

Figure 2.3 : Bulk thickness, hierarchical (slotted), and composite (PUR foam and hydrogel) cells.

2.2.2 3D printing of the PLA plastic slotted samples

The PLA-made slotted samples have been printed using a Raise3D N1 3D machine based on fused deposition modeling. The CAD stl design was imported into the Ideamaker 3D printer slicing software. This software converted the stl into a gcode file by selecting two outer shells, 100% filling ratio, and ±45^{o} infill angles. Specimens consisting of 5 x 4 (width x height) number of unit cells have been printed at 225 °C of extruder temperature, with 65 °C of heated bed temperature and 0.2 mm layer height. A couple of samples are printed with different infill ratio to see the porosity effects, seen in Figure 2.4.

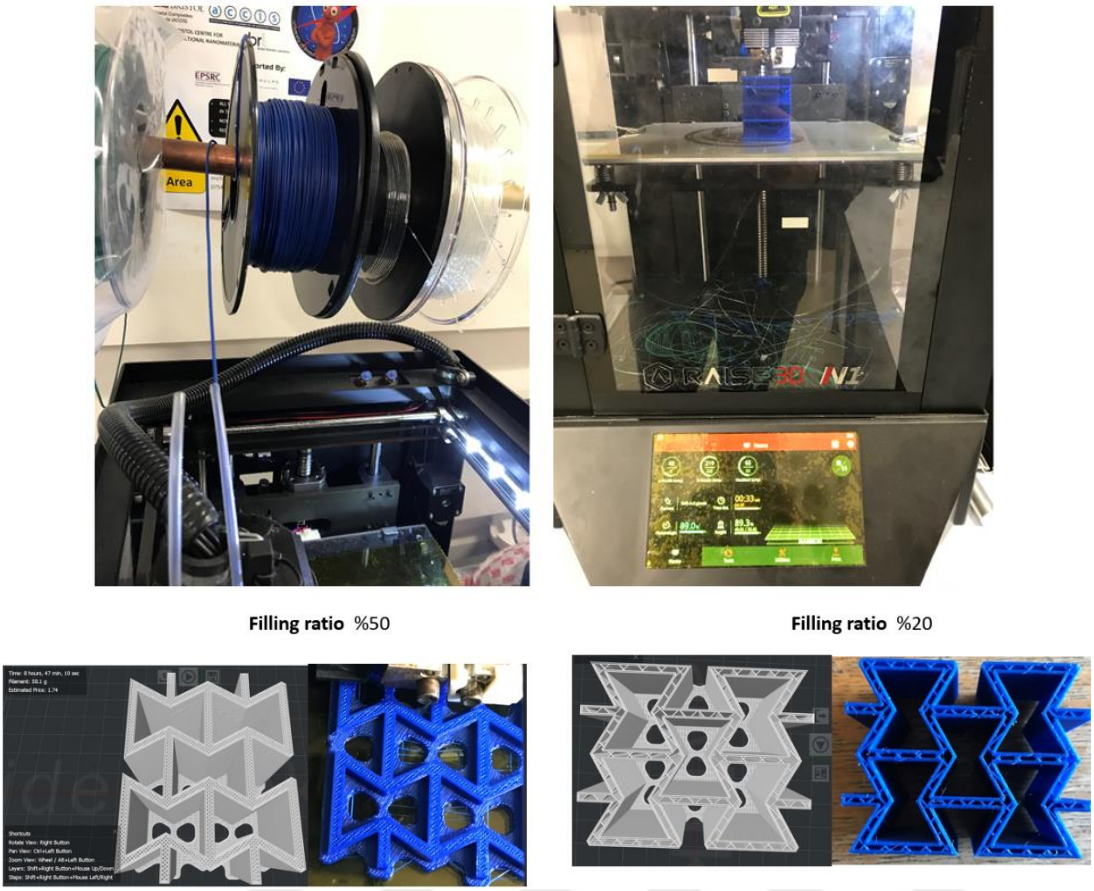

Figure 2.4 : Raise N1 3D printer machine: 3D printing slicing of structures in IdeaMaker software and printed samples.

2.2.3 PLA-made hierarchical cellular honeycombs filled with hydrogel

Hydrogels have been used as core constituents within the auxetic and hierarchical lattice configurations to stabilize the whole deformation of the lattices during large geometric and material nonlinear loading and also to verify the potential increase in terms of energy absorption.

Characterization and preparation of the hydrogel used have been previously described [137]. Briefly, the hydrogel formulation consists of sodium alginate (alginate) and a non-ionic surfactant, Pluronic F127 (F127). A 10 wt% alginate solution was prepared through centrifugation of sodium alginate powder (Sigma Aldrich, UK) with Dulbecco's Modified Eagle's Medium (DMEM, Sigma Aldrich, UK), using a dual asymmetric centrifuge (DAC 150.1 FV, SpeedMixer, UK) at 3500 RPM for 5 minutes. A 40 wt% solution of F127 in Phosphate Buffered Saline (PBS, Sigma Aldrich, UK) was autoclaved at 121 °C for 40 minutes, then cooled to 4 °C and stored for up to a week before use. The working gel formulation was 6 wt% alginate,

13 wt% F127, and was achieved by mixing alginate and F127 solutions with a DAC at 3500RPM for 30 seconds. Gels were transferred to 20ml syringes (Terumo Corporation, Japan) after mixing and injected into slots within PLA structures (Figure 2.5a). Then, gel-containing PLA structures were immersed in a 100mM $CaCl_2$ bath for 10 minutes (Figure 2.5b), prepared by dissolving calcium chloride powder (Sigma Aldrich, UK) in deionized water. The $CaCl_2$ bath crosslinked the alginate gel component, whilst allowing the F127 component to dissolve and diffuse out of the gel structure. The resulting gel structure is a macroporous alginate hydrogel.

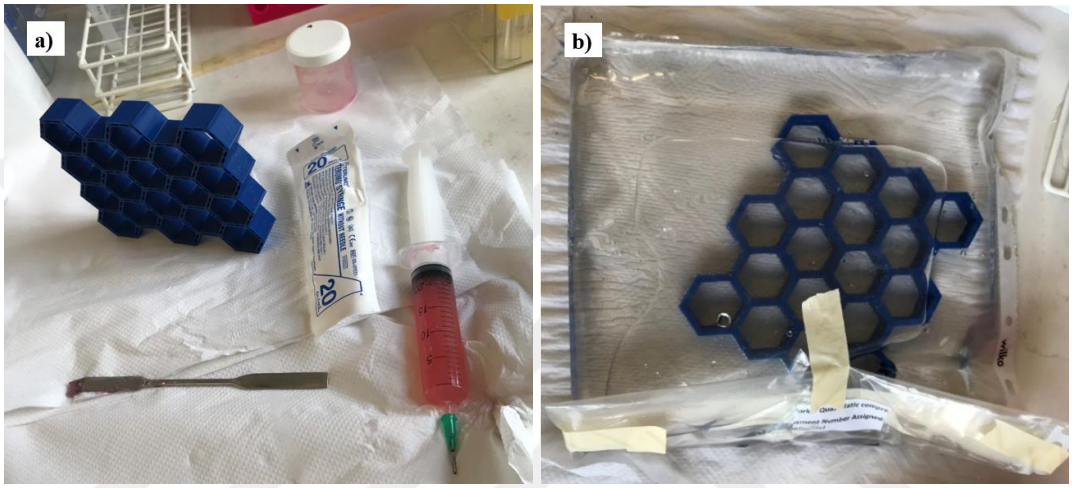

Figure 2.5 : a) Hydrogel injection into the slots, b) $CaCl_2$ bath of the hexagonal slotted lattice.

2.2.4 PLA-made hierarchical cellular honeycombs filled with PUR foam

PUR foam blocks (density 69 kg m^{-3}) were cut by using a CNC machine in accordance to the dimensions of gaps in the architectural structures. The foam cuts were then manually positioned into the gaps one by one. Each PLA-made sample contains 150 gaps, and the size of these gaps can differentiate according to the position of ribs in the unit cell and configuration types. An example of a filled slotted re-entrant lattice is shown in Figure 2.6.

Figure 2.6 : Slotted re-entrant honeycomb filled with PUR foam.

2.3 Material Properties of PLA Plastics and PUR Foam

2.3.1 Tensile tests of PLA plastics

Six dogbone specimens have been printed following the ASTM D638-14 test standard [138] by using a Raise3D N1 machine. Tensile tests have been performed using an Instron 25 kN test machine. Stress-strain curves of the samples have been obtained, and the Poisson's ratio was measured from the in-plane displacements of target points recorded with a video gauge system. The average Young's modulus of the PLA samples is 4.6 ±0.1 GPa, the ultimate strength is 49±1 MPa, the yield strength is 45±2 MPa, the density is 1.45 gr/cm^{3,} and the Poisson's ratio is 0.36 ±0.02. The engineering stress-strain curves of the specimens are plotted in Figure 2.7.

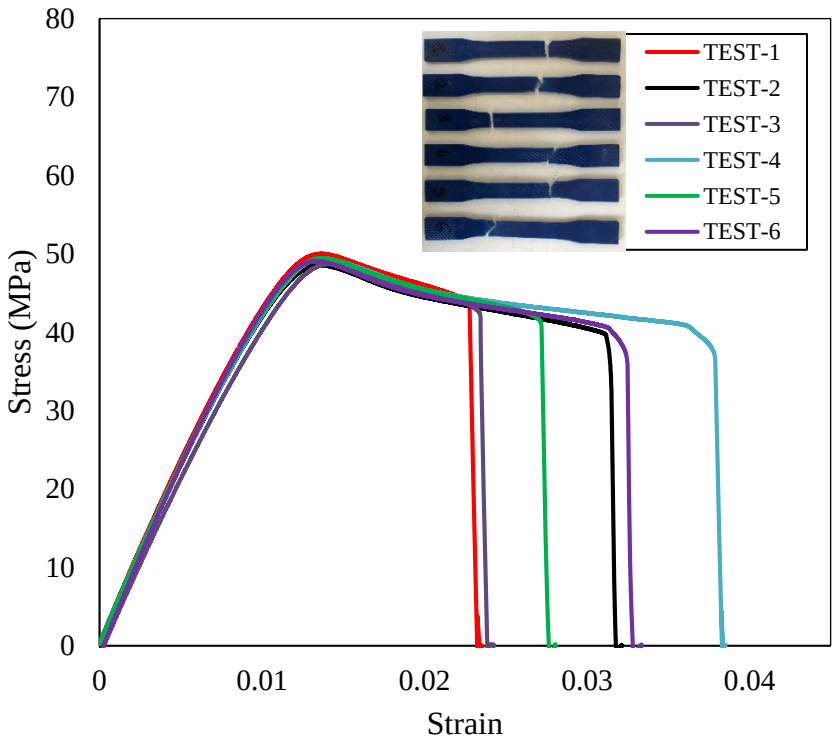

Figure 2.7 : Stress-strain curves of the PLA plastic.

2.3.2 Compression tests of PUR foam

Compression tests on the PUR semi-reticulated cell foam with the components organic resins of polyol and isocyanate (ESPOL Sponge and Chemical Industry Ltd. Co., Turkey) have been performed on cubic samples (5x5x5 cm) prepared in accordance to the ASTM D1621-91 standard [139] by using an MTS Universal test machine (Figure 2.8). Compression tests in displacement control mode were carried out parallel to the

three axis-directions with crosshead speeds of 2.5, 25 and 100 mm/min corresponding to the strain rates of $8.33x10^{-4}$, $8.33x10^{-3}$ and $3.33x10^{-2}$ s^{-1} in order to investigate the anisotropy of the foam material and its strain rate dependency [140]. Each case was repeated by testing 5 identical test specimens at different strain rates and different loading directions. 45 cubic foam were tested in order to determine the mechanical properties of PUR foam.

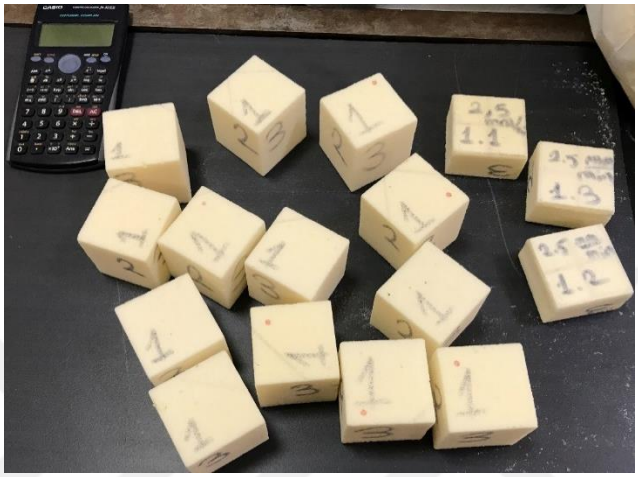

Figure 2.8 : Cubic PUR foam test samples.

Loading directions were coded as 1, 2 and 3 on the surfaces of samples, which represented material directions of cubic test samples (Figure 2.9).

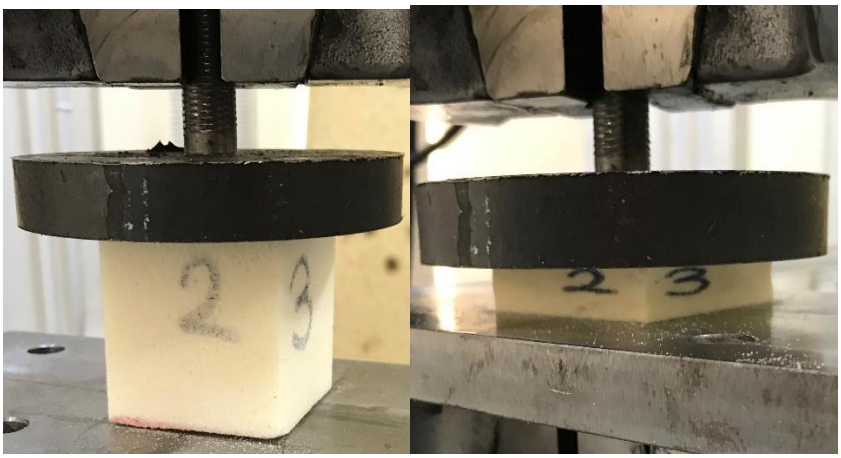

Figure 2.9 : Compression test of the PUR foam.

The average stress-strain curves of the specimens are plotted according to different strain rates and loading directions in Figure 2.10. The results show that each curve contains typically three distinct regions (as expected): a linear elastic and a plateau followed by densification.

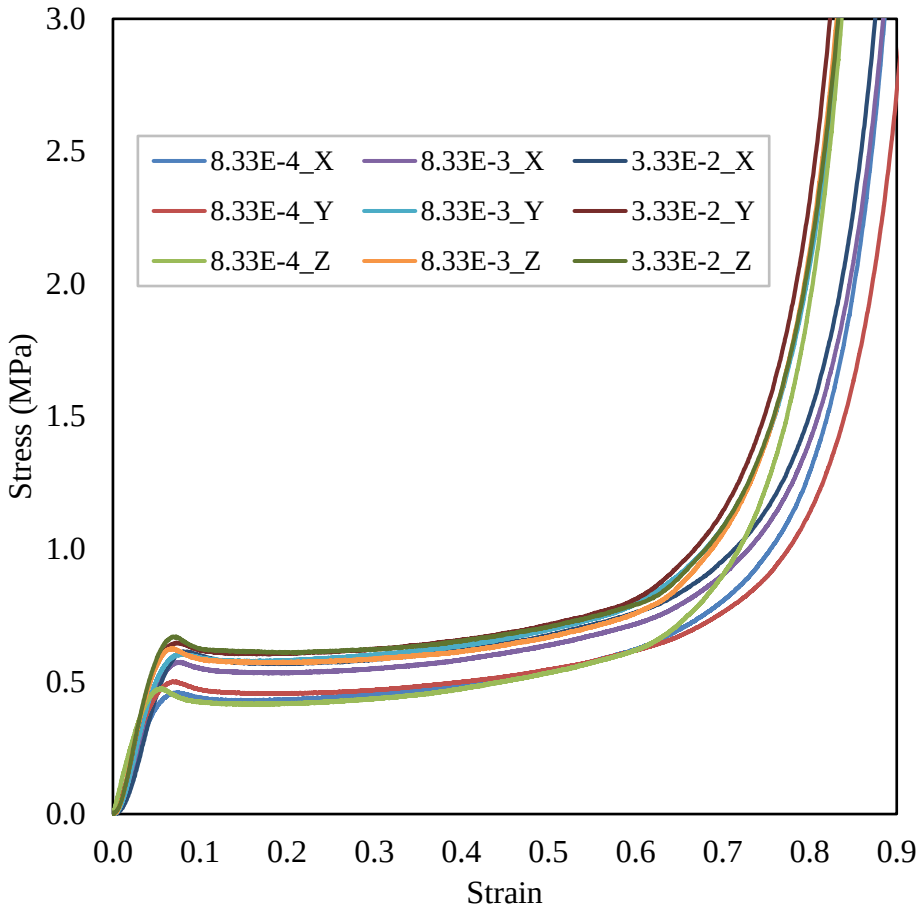

Figure 2.10 : Comparison of average stress-strain curves of the foams at different strain rates.

The linear elastic properties of each test were determined according to stress vs. strain curves in Figure 2.10. Young's modulus, plateaus onset stress, and corresponding strains are shown in Table 2.1.

Table 2.1 : Material properties of PUR foams.

	ε	E (MPa)	ε	σ_{pl} (MPa)
2.5-X	0.069	10.294	0.073	0.459
2.5-Y	0.005	10.278	0.073	0.499
2.5-Z	0.005	11.381	0.067	0.474
25-X	0.004	10.338	0.084	0.574
25-Y	0.006	10.966	0.084	0.604
25-Z	0.006	11.294	0.083	0.626
100-X	0.006	11.060	0.085	0.613
100-Y	0.026	11.807	0.083	0.647
100-Z	0.019	11.509	0.085	0.670

Table 2.1 clearly indicates that there is no remarkable difference between the values of the Young's moduli, no matter which loading direction or strain rate is considered. The stress corresponding to the plateau onset is however strain-rate dependent, with a maximum discrepancy of ~ 41% between the analogous values along the z-direction when passing from 25 mm min-1 to 100 mm min-^{1}. For the continuation of our study, we have adopted the results of the samples tested at 2.5 mm/min.

2.4 Compression Tests

The compression tests were performed using an INSTRON Roell Amsler Test Machine with a 25 kN load cell, as illustrated in Figure 2.11a. The largest crosshead displacement was 100 mm and reached with a velocity of 3 mm/min. A flatwise part was located between the top surface of test specimens and crosshead to fully overlap with the compressed surface of the sample and provide uniformly distributed loads. A video gauge system was also used to capture the images of the test samples during crushing and to determine the Poisson's ratio of the samples (Figure 2.11b). Four selected points were traced on the central area of specimens. Axial and transverse displacements of these points were recorded, and average true strains (ε_{axial} and $\varepsilon_{transverse}$) in both the axial and transverse directions were calculated. The Poisson's ratio of the samples was calculated by using equation (2.2):

$$\nu_{xy} = -\frac{\varepsilon_{transverse}}{\varepsilon_{axial}} \tag{2.1}$$

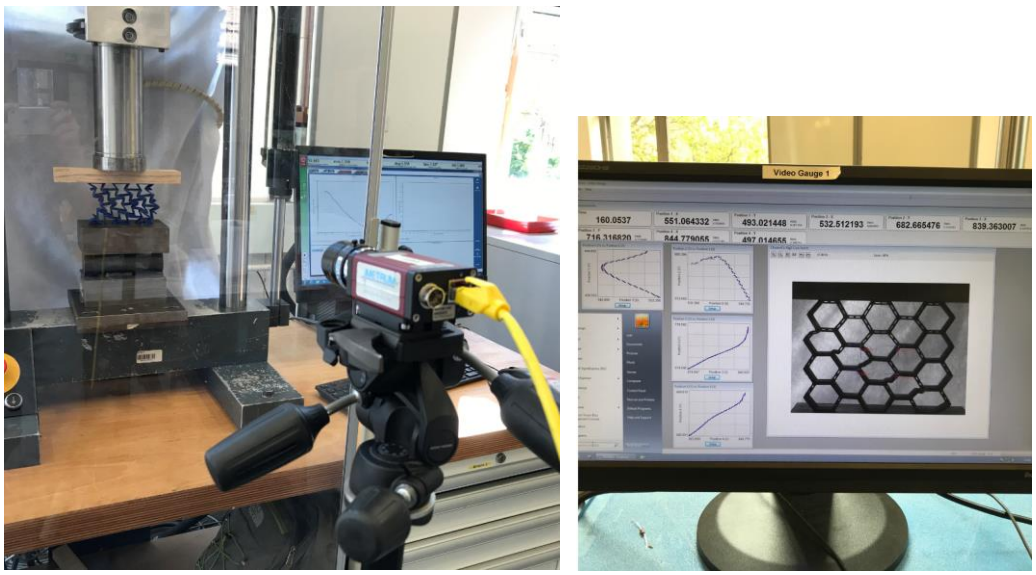

Figure 2.11 : Compression tests by using a) Instron test machine and b) Video gauge system.

The representative normalized stress vs strain curves of AEC re-entrant samples are indicated in Figure 2.12.

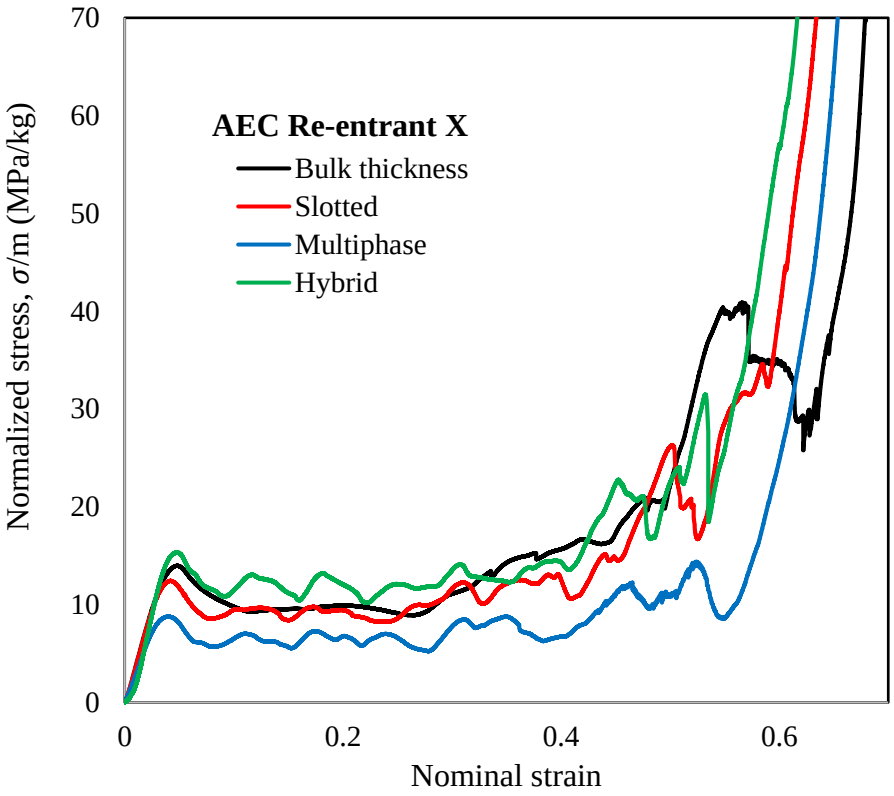

Figure 2.12 : Stress vs. strain curves of re-entrant samples under compression along the x-direction: Bulk thickness (black), Slotted (red), Multiphase (blue) and Hybrid (green).

During the tests, no out-of-plane displacements were observed. An Imetrum Video Gauge™ system was used to capture images of the in-plane deformations. Figures 2.13-2.18 show the deformation patterns related to the bulk thickness, slotted, multiphase and hybrid samples. The specimens are related to lattice configurations (hexagonal, re-entrant and AEC re-entrant), both loaded along the *x* and *y*-directions. The deformation mechanism of the bulk thickness and slotted structures are dominated by the inclined ribs in the case of samples crushed along the *x*-direction. In a similar manner, the deformation mechanism of the multiphase and hybrid samples appears to be dominated by the inclined ribs when loading along the same direction. Microbeams belonging to the first yielding cells of the multiphase and hybrid samples fail where the strain reaches a critical limit, and densification starts at the strains of 0.708, 0.701, 0.508, 0.521, 0.601 and 0.580 for the hexagonal, re-entrant and AEC re-entrant multiphase and hybrid samples, respectively. The results indicate that all the hexagonal

types possess similar collapse mechanisms, except for the bulk thickness samples that do not feature microcracks on the ribs.

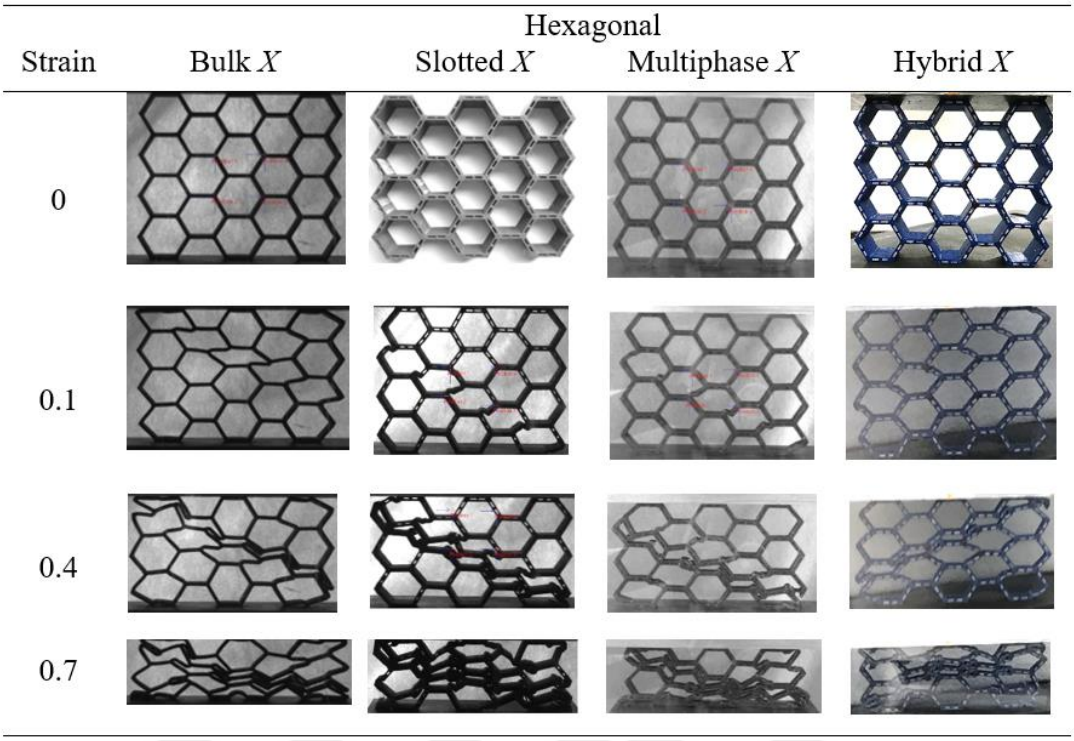

Figure 2.13 : Deformation mechanisms of hexagonal honeycombs along the *x*-direction.

As expected, the auxetic structures (re-entrant and AEC re-entrant) show negative Poisson's ratio behaviors during the elastic deformation under compression loading along the *x*-direction. When stresses reach the onset of plateau stress, the deformation assumes a global buckling behavior due to the rotation of cells around the failed ribs. Figure 2.14 and Figure 2.15 show that slotted lattices possess advantages over bulk thickness configurations because of the reduction of global rotations during the deformation. This has also been observed in hierarchical lattice configurations evaluated by Chen et al. [121] and Yin et al. [141]. It is evident from observing Figure 2.14 that multiphase structures reduce the global rotation of the samples significantly during the collapse and assume a more stable and progressive deformation because of the presence of the hydrogel. This is also valid and even more evident for the AEC re-entrant configurations shown in Figure 2.15, with the multiphase lattice-type showing a clear progressive and almost parallel front of collapse without global rotations of the samples.

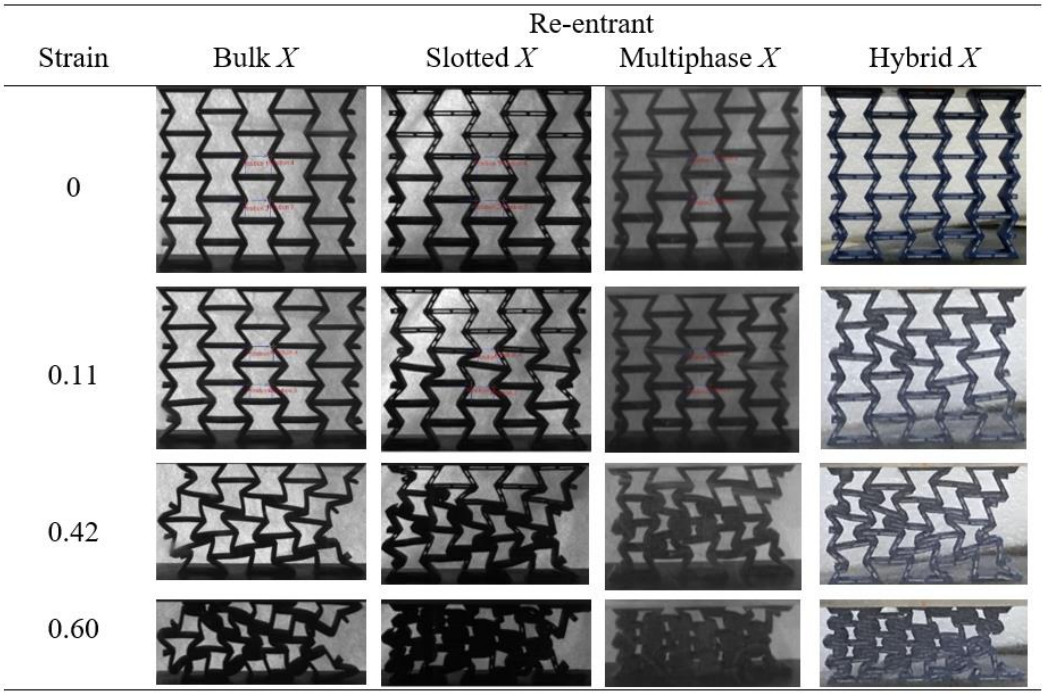

Figure 2.14 : Deformation patterns of the re-entrant honeycombs along the *x*-direction.

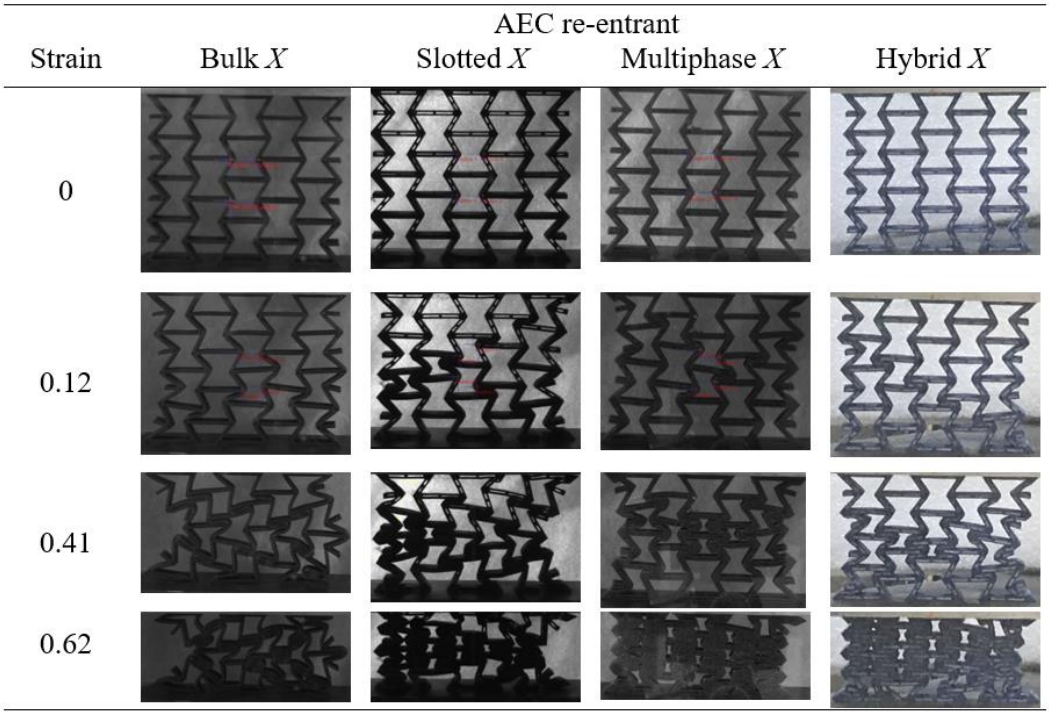

Figure 2.15 : Deformation mechanisms of the AEC re-entrant honeycombs along the *x*-direction.

In the case of loading along the *y*-direction, the deformations of the vertical and inclined ribs both contribute to the global deformation of the honeycombs. Figure 2.16-2.18 show that elastic buckling, plastic collapse and brittle failure are all mechanisms present during the deformation of the bulk thickness and slotted

hexagonal samples. Multiphase and hybrid samples exhibit similar deformation modes (Figure 2.16). Multiphase specimens seem here to feature a collapse front on cells close to the lower platen, while all the other samples tend to show the onset of the presence of this front towards the top of the specimen. This is an overall indication that the multiphase hexagonal samples appear to provide a more uniform transfer load during quasi-static crushing compared to the other configurations (bulk thickness included). In the re-entrant samples (Figure 2.17), the cells in the second and fourth rows of the slotted, multi-phase and hybrid samples tend to deform by beam buckling and brittle failure, while the bulk thickness samples tend to collapse by providing first a global rotation of the sample. Multiphase samples also fail by the progressive front of buckling failure of the vertical ribs, but the overall compressive deformation towards densification is more uniform than the other configurations.

The collapse mechanism of the AEC re-entrant samples is different from the ones of the re-entrant samples when loading *y*-direction because of the presence of the edge asymmetric cells (Figure 2.18). The vertical ribs of asymmetric cells along the left and right sides are longer than those belonging to the internal cells. This AEC topology avoids the onset of an earlier plastic deformation of the second and fourth rows of the lattices, compared to the other configurations.

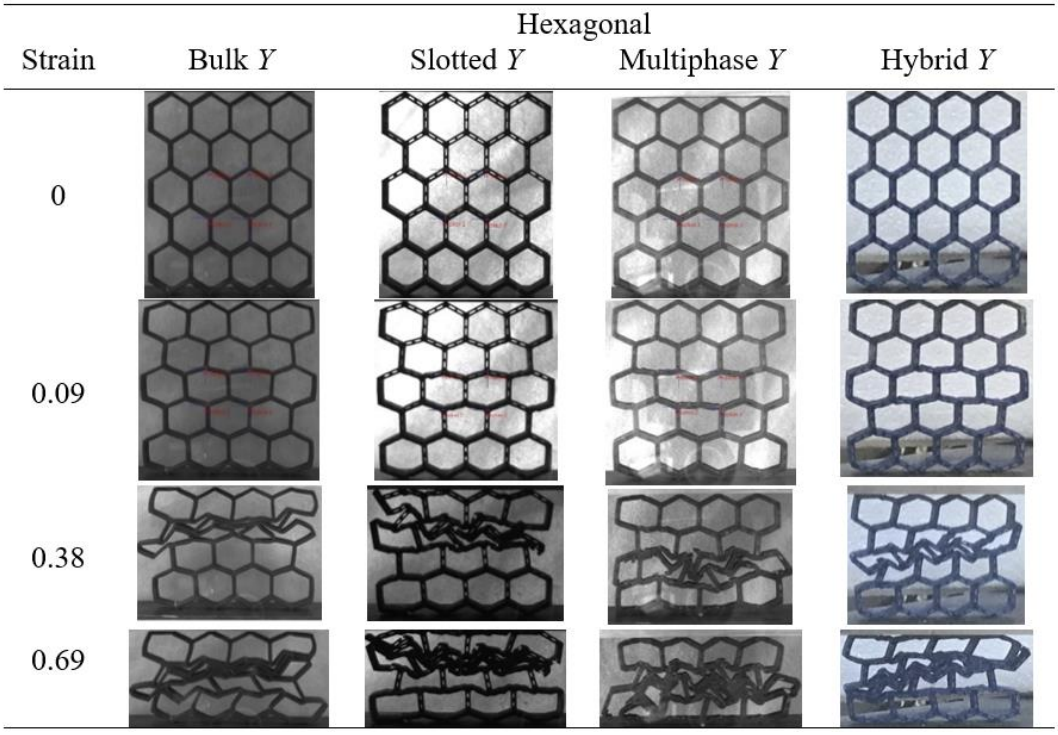

Figure 2.16 : Deformation mechanisms of hexagonal honeycombs along the *y*-direction.

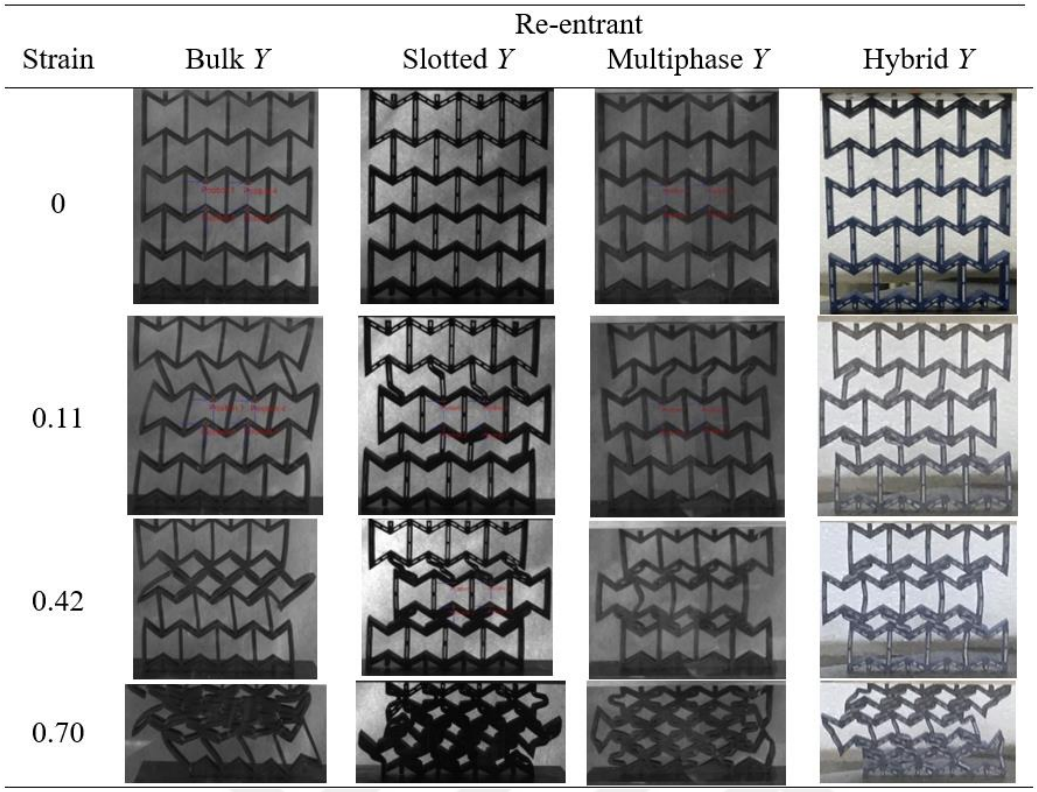

Figure 2.17 : Deformation mechanisms of re-entrant honeycombs along the *y*-direction.

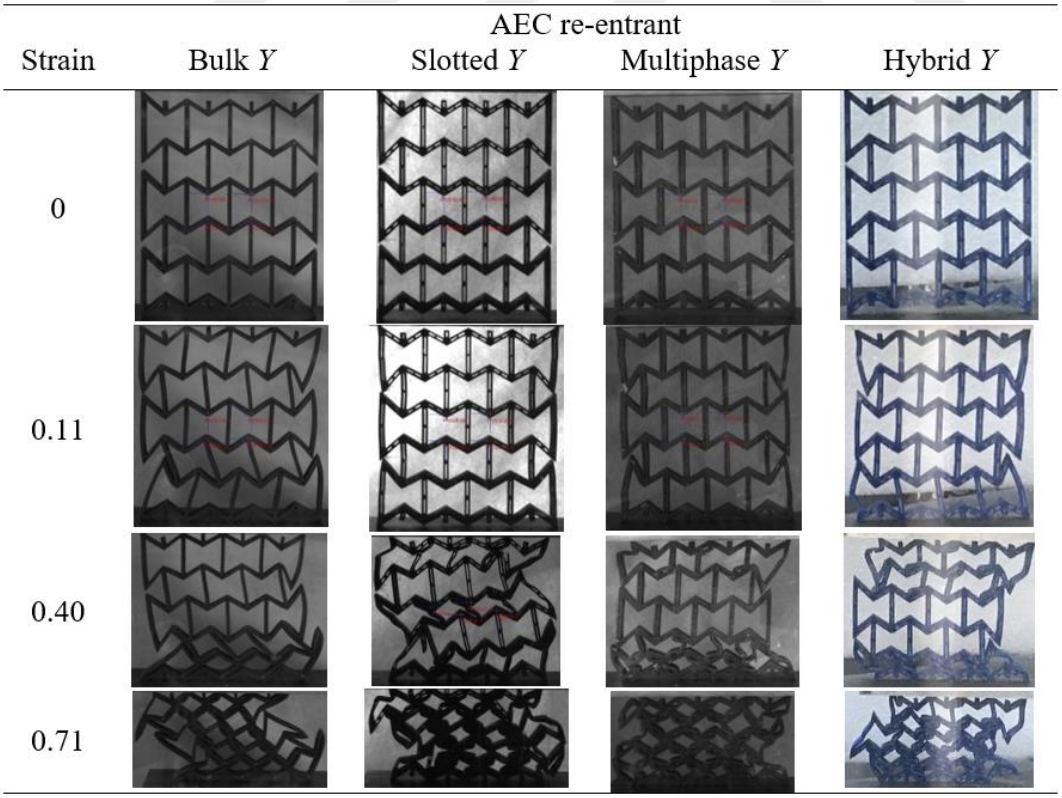

Figure 2.18 : Deformation mechanisms of AEC re-entrant honeycombs along the *y*-direction.

2.5 Finite Element Simulations

2.5.1 FE modeling of bulk thickness and slotted samples

The FE analyses were performed using LS-DYNA software. A rigid mass was crushed through the top edge surface at an axial quasi-static speed of 3 mm/min (Figure 2.19). Prescribed motion rigid model constraints were added. The nodes at the bottom of the cellular structure were fixed and the out of plane rotations and displacements of the nodes at the front and rear surfaces were also blocked.

The PLA-made structures were modeled by using ELFORM 1 (element formulation option 1) based on constant stress solid elements. A mesh convergence study was performed to identify an adequate balance between accuracy and mesh quality. Hexagonal lattice with bulk thickness is modeled with five different mesh qualities of 3x3, 2.5x2.5, 2x2, 1.5x1.5 and 1x1 mm. According to the comparison of results in terms of force-displacement response, the optimum element size was found as 1x1 mm. Automatic single surface contact algorithms were used for each individual part. In addition, automatic surface-to-surface contact interfaces were also defined between the surfaces of the cellular structure and the rigid mass. The friction coefficients are chosen as 0.2 for each contact definition [82]. The MAT24 piecewise linear plasticity material model was used to define the material properties of the cellular structures. The elastic material properties of the cellular structure calculated from the tensile tests were implemented in this material model. Finite element analyses were performed by using ANSYS-LS-DYNA solver with 2 s of fixed time stepping. EQ 2: Nonlinear with Broyden–Fletcher–Goldfarb–Shanno algorithm (BFGS) updates was implemented as solution method for implicit analyses.

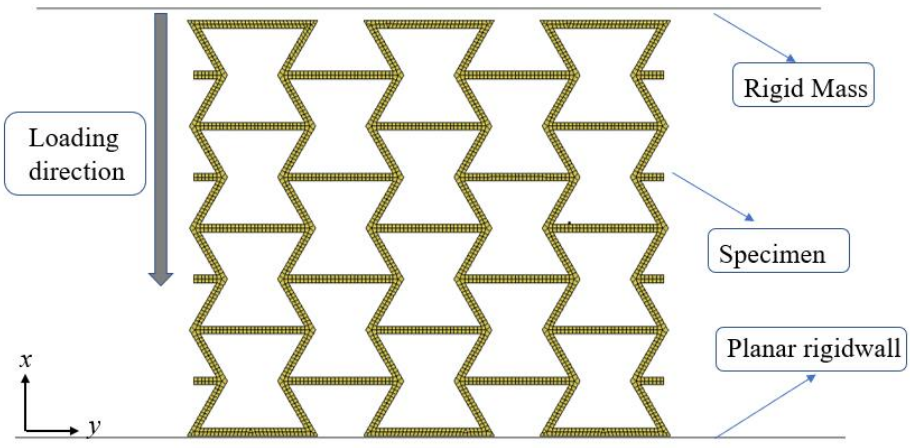

Figure 2.19 : FE modeling of the compression test.

2.5.2 Validation of bulk thickness and slotted samples

The numerical models were validated by comparing the load-displacement responses with the experimental results for each sample. The comparisons between the numerical and experimental results of bulk and slotted samples are shown in Figure 2.20 and Figure 2.21. One can observe (in accordance to the general behavior of cellular solids under compression) the presence of three stages within the load-displacement response: a linear elastic one, a plastic collapse plateau and a final densification region [85]. There is a general good agreement between experimental and simulations concerning the linear elastic response, the onset of yielding, the plastic collapse plateau and the starting point of the densification. The most general discrepancy between the numerical and experimental results was observed shortly before the densification points. The main reason of this could be the increase of the complexity of the deformation due to a large number of contact surfaces between the cell ribs, and also the presence of cracks observed during the experiments during the large deformations phase.

The slotted samples show the presence of a series of small force peaks in the experimental results probably due to local non-uniform deposition of the material. Slotted cells consist of various microbeams that are weaker than the bulk ones [87]. The reason of the instantaneous rise and fall of the peak values of slotted re-entrant and asymmetric re-entrant samples under compression along the *Y* direction is likely linked to the failure of those microbeams.

The loading direction and the geometries of the single unit cells also have an important role in the results. Vertical ribs dominate the crushing response for the compression along the *Y* direction. The densification of re-entrant samples starts earlier, and contact forces increase because of the auxetic type of deformation. The difference between the experimental and numerical results of the samples with re-entrant cellular shapes loaded along the *Y* direction could be affected by these aspects. Nevertheless, the discrepancies between the numerical and experimental results are acceptable from an engineering perspective.

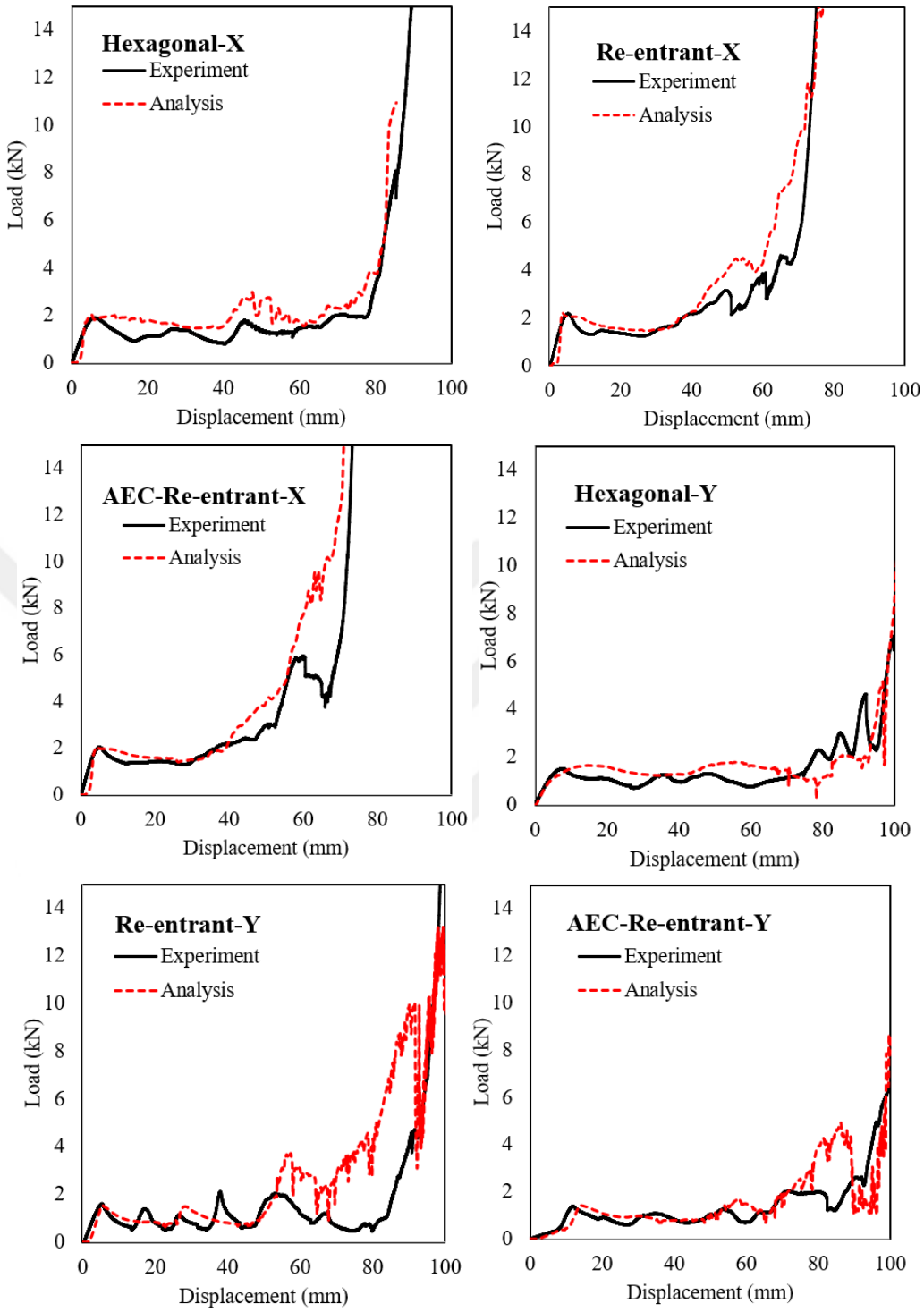

Figure 2.20 : Comparison between numerical and experimental results related to the bulk thickness cellular structures.

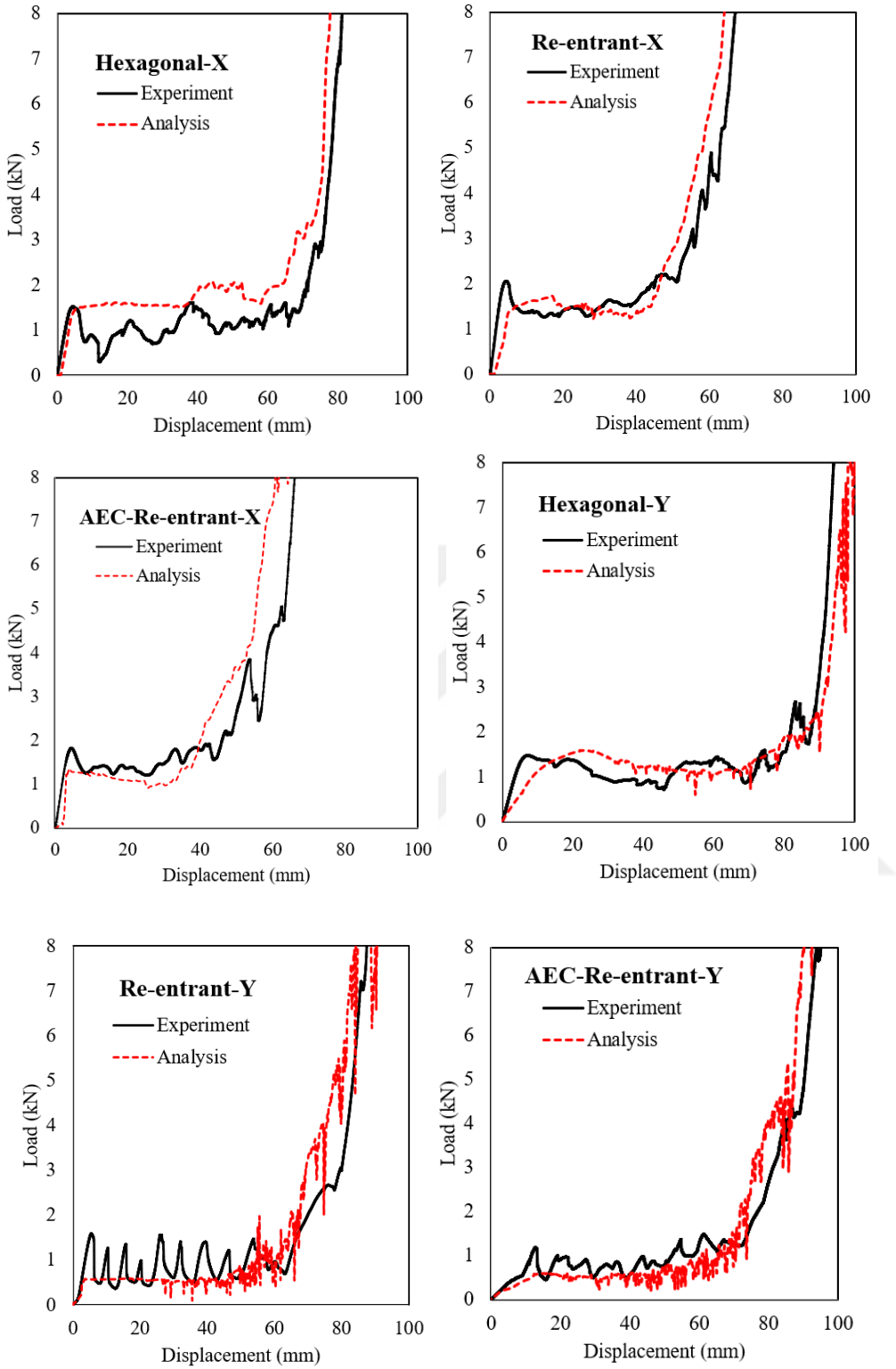

Figure 2.21 : Comparison between numerical and experimental results related to the slotted cellular structures.

2.5.3 Deformation mechanism

The planar deformations of the crushed samples were recorded by using an Imetrum's Video Gauge™ point tracking camera system. The deformed shapes of the samples

were obtained by taking screenshots at different stages of the compression. Figure 2.22 exhibits the deformation patterns of bulk thickness and slotted samples loaded along the *X* direction, while Figure 2.23 is related to the same lattices loaded along *Y*.

The deformation mechanism is dominated by the inclined ribs in the case of samples crushed along the *X*-direction. Plastic yielding of the bulk and slotted honeycombs is initiated in single arranged cells from the top left to the bottom right. In bulk thickness honeycombs, all cells are subjected to bending before plastic yielding, and the cells then start to deform by elastic buckling, plastic collapse and brittle failure. On the other hand, the slotted lattices feature a collapse mechanism defined by the deformation of adjacent cells around the initially yielded region, after reaching the critical strain. The cells away from the yielding zone remain undeformed because of the strong localization of the deformations. Slotted honeycomb tends to densify around the first yielding cells and the internal microbeams tend to break due to brittle failure.

The bulk thickness, slotted and asymmetric re-entrant samples contract in the transverse direction due to auxetic properties of the unit cells. After reaching the critical yielding point, the lattices show a global rotation that is of lower magnitude in the case of the slotted samples. Even though the latter tend to exhibit a global rotation, the material densification around the collapse region causes a progressive deformation of the samples middle section due to the failure of the microbeams of the neighboring cells around the densified region. The slotted re-entrant and asymmetric samples are therefore more stable under compression along the *X*-direction. The modified cells increase the stability of the structure because of the lower cell angles at the edges.

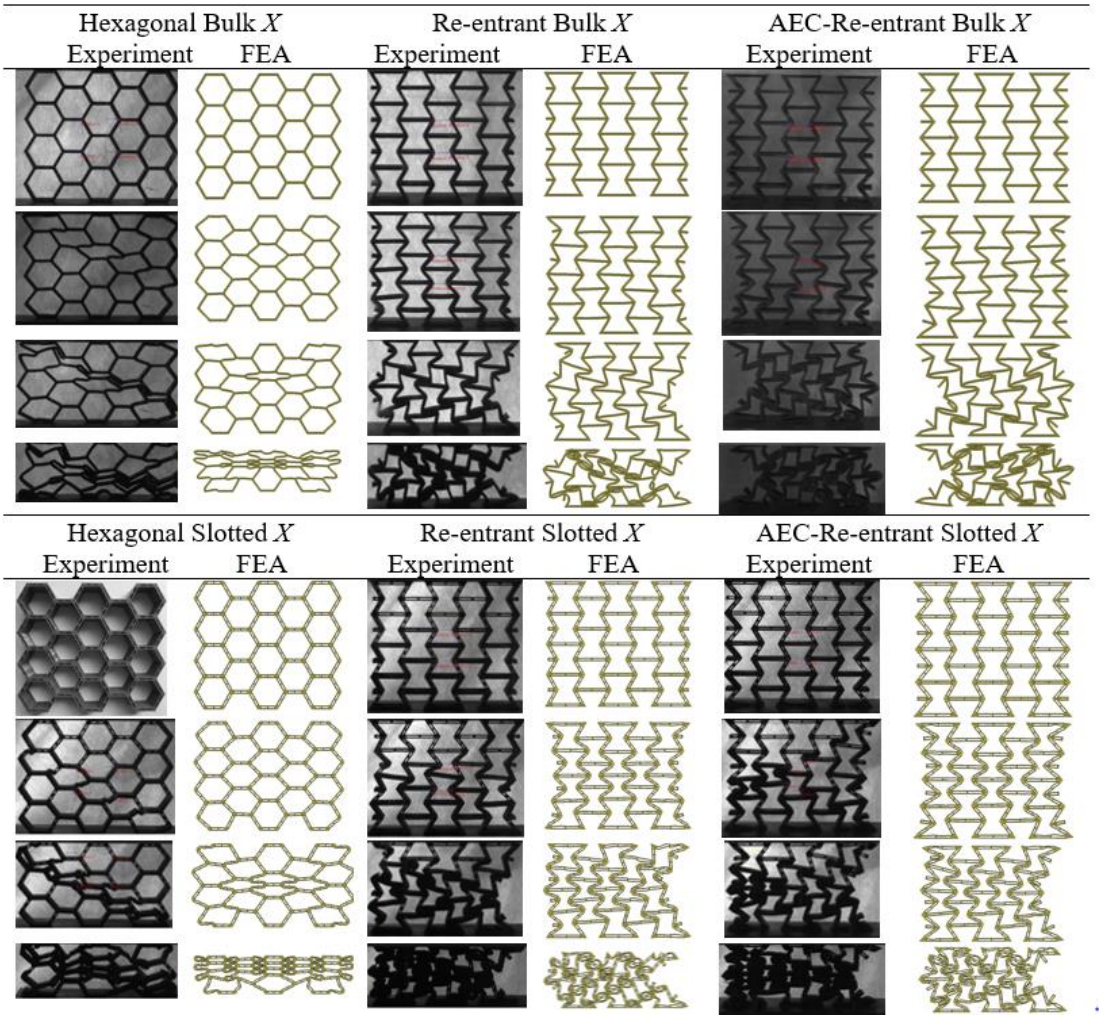

Figure 2.22 : Deformation mechanisms of the samples under compression along the *X*-direction.

The deformation mechanism of the same samples loaded along the *Y*-direction is very different from the previous ones and is shown in Figure 2.23. Both the vertical *h* and inclined *l* ribs have, in this case, a large effect on the deformation behavior of hexagonal and re-entrant samples. In hexagonal samples, the inclined ribs exhibit initially the onset of elastic buckling, followed by plastic collapse and brittle failure; the vertical ribs remain, however, almost undeformed for small/medium compressive strains. In the re-entrant samples, the deformation mechanisms appear mainly to be dictated by the rotation of the oblique ribs, as if a plastic hinge is present at the connecting cell walls. It is also worth noticing that the center points of the oblique ribs also behave as plastic hinges in the slotted re-entrant samples, unlike in the case of the bulk thickness ones.

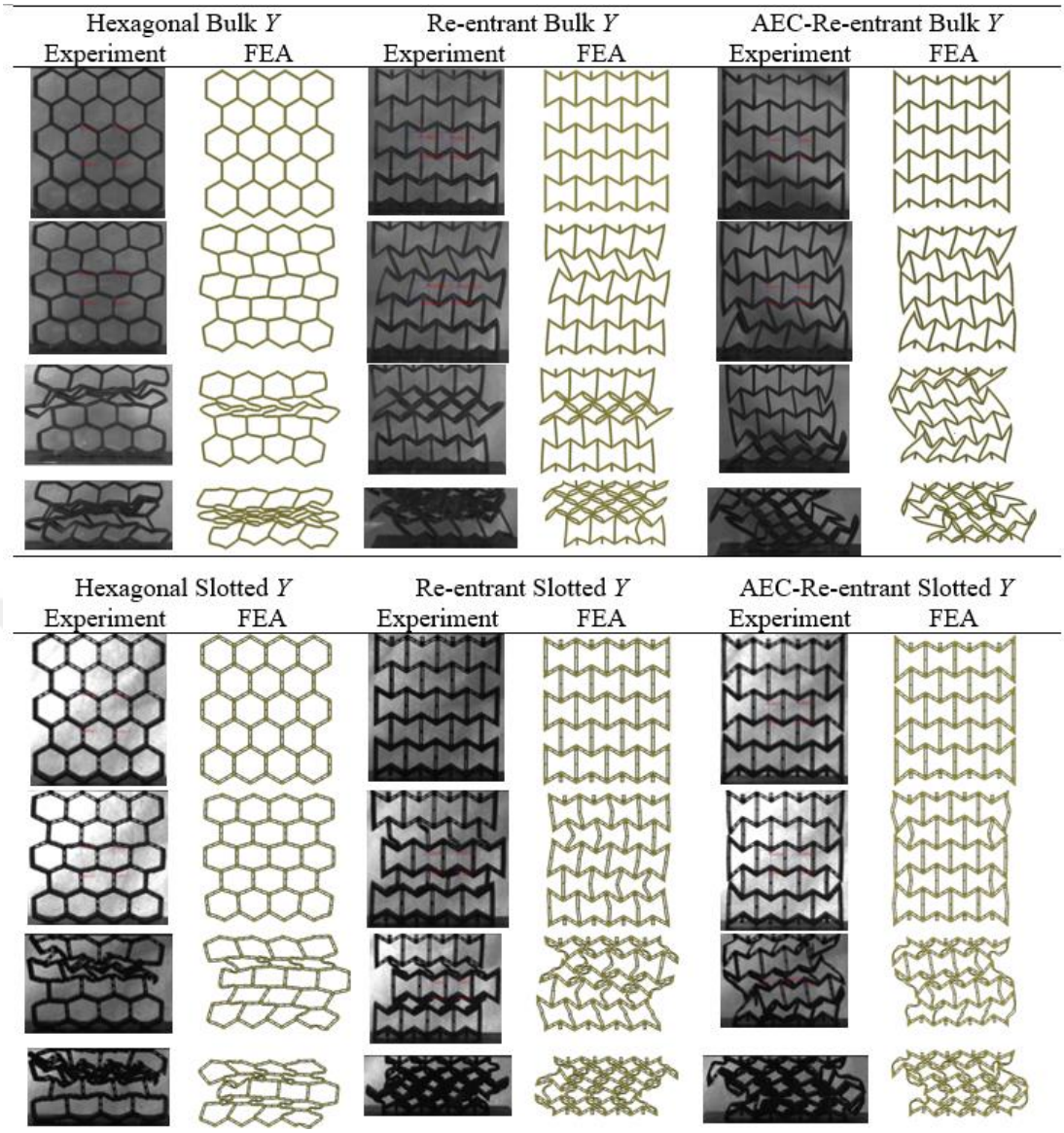

Figure 2.23 : Deformation mechanism of the samples compressed along the *Y*-direction.

2.5.4 FE modeling of hybrid samples

Figure 2.24 shows a 3D view of the FE model of a hybrid sample. The material properties of the PUR foam have been implemented from the experimental material characterization into the 'MAT63 crushable foam' material card. Rate sensitivity via the damping coefficient has been defined as 0.5. The interactions between the PUR foam and the PLA-made lattice and between the rigid wall and the honeycomb have been defined by using automatic surface-to-surface contact interfaces. Automatic single surface contact algorithms have also been used for each individual foam part and PLA-made lattice with a coefficient of 0.2.

A mesh convergence study was performed to identify an adequate balance between accuracy and mesh quality. Hybrid samples with foams were modeled using 5 different mesh densities. In these five models, the number of elements used were 8853, 10044, 12894, 16305 and 18189. Numerical results have shown that convergence in terms of force versus displacement response was achieved with the finer meshes. The FE modeling of the hybrid sample with a large number of parts (150 foams and a PLA-made lattice), however, restricted the minimum element size. A trade-off has been identified with 18189 elements.

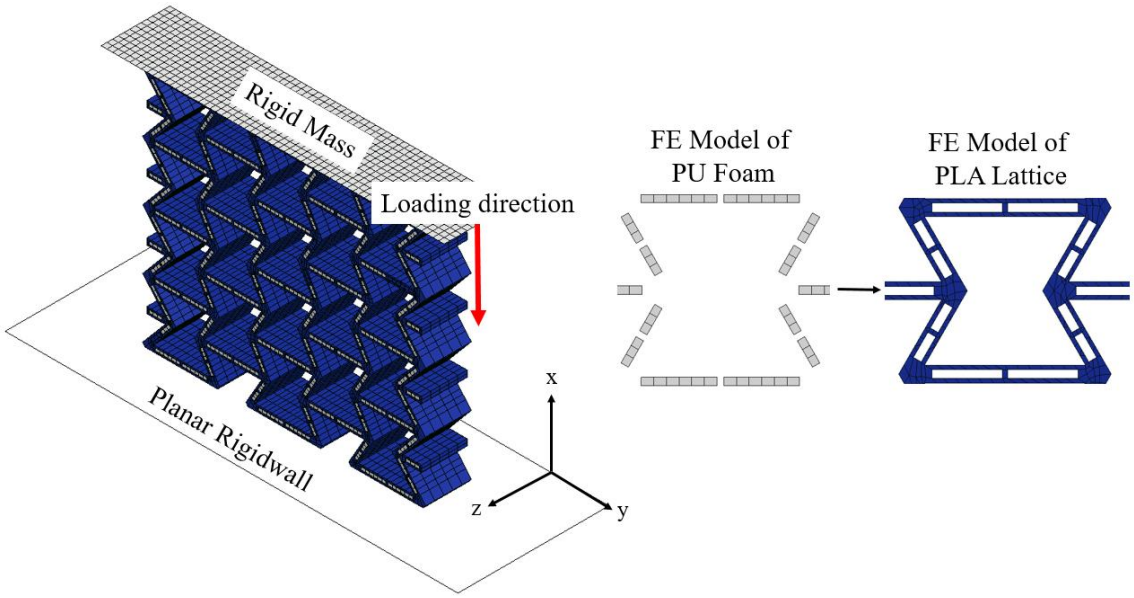

Figure 2.24 : FE modeling of hybrid AEC re-entrant sample.

2.5.5 Validation of hybrid samples

An additional benchmark of the modeling approach has been carried out in this work related to the hybrid structures proposed, and the results are shown in Figure 2.25. Good agreement can be observed between numerical and experimental results for the three stages of stress-strain curves: linear elastic, plastic collapse plateau, and the final densification.

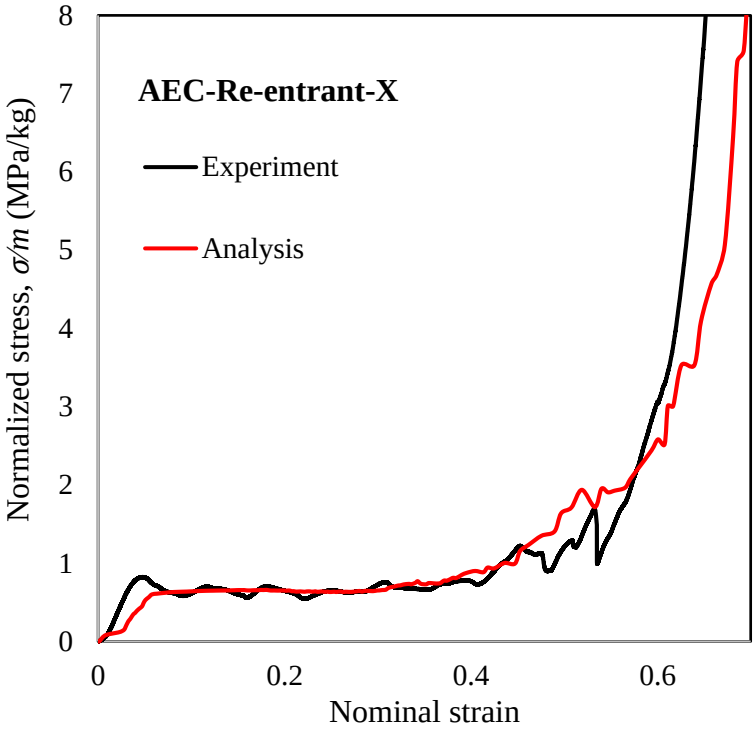

Figure 2.25 : Specific compressive strength vs. strain curves of AEC re-entrant sample loading in the *x*-direction.

2.6 Results and Discussion

2.6.1 Metrics for benchmark

The results of compression tests were compared in terms of specific compressive modulus, strength, specific energy absorption, and mean crushing force metrics defined in equations (2.2)-(2.5):

Specific compressive strength: $$\frac{Compressive\ stress}{Mass} = \frac{\sigma}{m} \quad (2.2)$$

Mean crushing force (MCF) $$\frac{Absorbed\ Energy}{Displacement} \quad (2.3)$$

Specific energy absorption (SEA): $$\frac{Absorbed\ energy}{Mass} \quad (2.4)$$

Specific compressive modulus $$\frac{Compressive\ modulus}{Mass} = \frac{E}{m} \quad (2.5)$$

Specific compressive strength has been calculated as the ratio between the compressive strength and the total mass. The use of the total mass as normalizing

quantity is a convenient method to compare samples consisting of two or more materials. Both the compressive strength and the compressive modulus were determined by using the stress-strain curves of the crushed samples. The average compressive stress was calculated by dividing the reaction force between the rigid wall and the sample by the top surface area of the sample. The ratio of the displacement to the sample height is the strain, and the slope of the stress-strain curve in the elastic region has been used for the compressive modulus. On average the elastic strains are varied in the range of 0.02-0.03 strains.

Mechanical performances and energy absorption capabilities of the cellular structures are based on the densification strain at which the plateau regime ends and a sharp increase starts in stress-strain curves. Here, the intersection point of these regions were determined by drawing a straight line for the plateau regime and the slope of the densification region. Specific compressive strength, MCF and SEA were determined from the average data points at densification in the range of 0.7, 0.5, 0.5 strains for the hexagonal, re-entrant and AEC re-entrant, respectively. Compressive strength and absorbed energy were determined from the average data points at densification in the range of 0.705, 0.514, 0.591 strains for the hexagonal, re-entrant and AEC re-entrant, respectively.

2.6.2 Comparison of the specific compressive strength

The regular re-entrant honeycombs possess higher compressive strength than the hexagonal configurations, and the introduction of hierarchies in the re-entrant lattice could increase the strength of these structures [82, 121]. Our hybrid lattice configurations allow the improvement of the compressive strength by modifying the unit cell topologies and adding lightweight materials. Figure 2.26 shows that hybrid samples provide the highest specific compressive strength compared to the other classes of specimens, no matter which lattice configuration and loading direction are considered. The results also show that the specific compressive strength significantly increases by using very low-density material in hybrid structures. In comparison with the hexagonal samples, the hybrid configurations show a 30% and 34% increase in specific compressive strength over the bulk thickness samples when loading along the x and y-directions, respectively. Hybrid configurations also provide 12% and 24% more specific compressive strengths than the slotted ones. Hybrid structures with re-

entrant and AEC re-entrant shapes display compressive strength efficiencies of 7%, 17% (along the *x*-direction) and 35% and 53% (in the *y*-direction) greater than those shown by the bulk samples. They also display compressive strength efficiencies of 6%, 8% (along the *x*-direction) and 15%, 25% (in the *y*-direction) larger than the slotted samples. The discrepancies of the results related to the compressive strength along the *x* and *y*-directions stem from the different deformation modes [88], which also affect stiffness and the SEA [142].

Multiphase samples show however the worst performance because the hydrogel was squeezed out along the out-of-plane direction during testing. In addition, hybrid structures with re-entrant shape feature an enhanced performance compared to analogous hexagonal configurations; the AEC re-entrant topologies also have the highest specific compressive strengths of 37.2 and 41.5 MPa/kg when loading along the *x* and *y*-directions (Figure 2.26). These results show that the novel designs with PUR foams inserts are interesting from an engineering perspective when the specific compressive strength needs to be maximized.

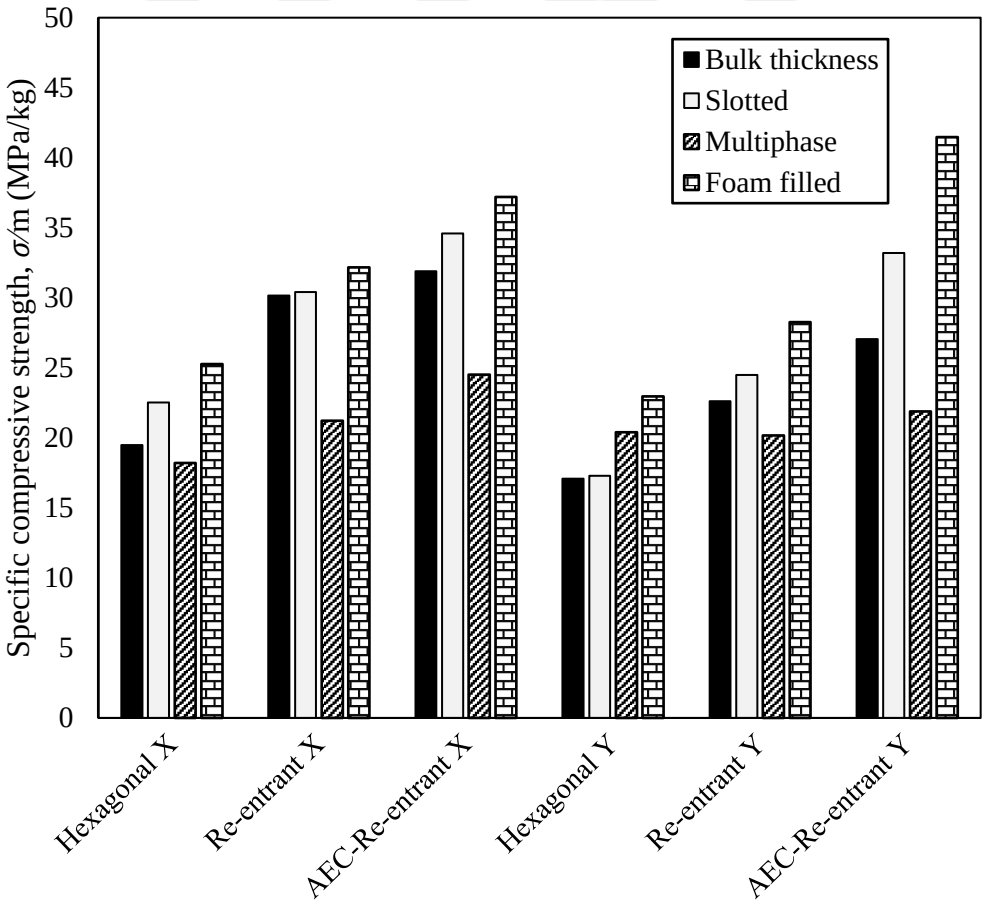

Figure 2.26 : Specific compressive strength.

2.6.3 MCF comparison

Zhou et al. [143] found that re-entrant honeycombs provide higher mean crushing forces than initial peak crushing forces; this allows larger energy absorbing capacities. Tan et al. [120] indicated that the MCF of their re-entrant hierarchical honeycombs was improved by up to 298% and 108% compared with conventional re-entrant honeycombs. The MCF performance of the configurations considered here and loaded along the different directions is shown in Figure 2.27. The re-entrant and AEC re-entrant samples show ~35% increase in MCF performance compared to hexagonal samples along the *x*-direction. There is however no noticeable difference in the MCF performance between the different configurations along the *y*-direction, and this could be explained by the specific deformation modes acting along that direction [88].

The hybrid configurations have larger MCF efficiencies (~5% to 35%) than the slotted and hydrogel-filled samples along the *x* and *y*-directions. The MCFs of hybrid samples with hexagonal, re-entrant and AEC re-entrant shapes are also 13%, 18% and 14% larger than the ones related to the bulk thickness samples along the loading *y*-direction, respectively.

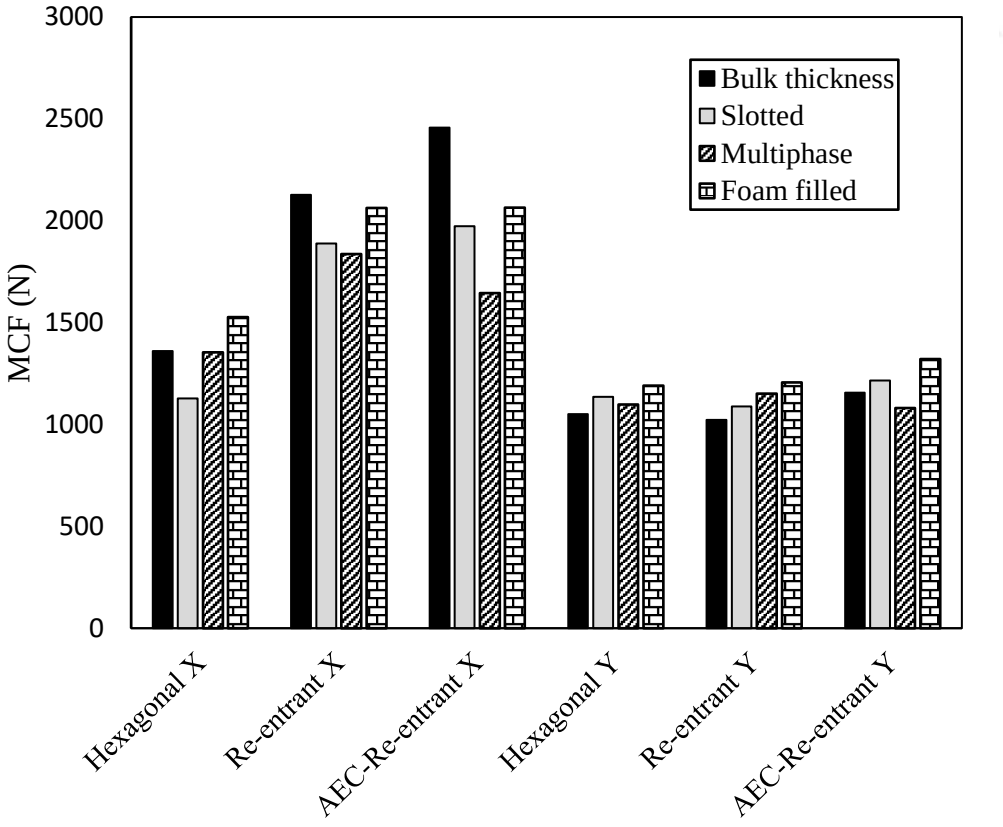

Figure 2.27 : Mean crushing force (MCF).

2.6.4 SEA comparison

Ingrole et al. [82] indicated that re-entrant honeycombs could absorb ~27% more energy than the hexagonal configurations. In addition, the energy absorption capacity could be improved by introducing hierarchies into the re-entrant (e.g., by up to 292% [120]) and hexagonal honeycombs (e.g., by up to 750% [121]). The present study highlights that the proposed hybrid structures can be effective to enhance the energy absorption performance of hierarchical configurations. The SEA performance of the samples with different unit cell configurations loaded along different directions is shown in Figure 2.28. Bulk thickness samples with the AEC re-entrant topologies compressed along the *x*-direction had the best energy absorption capacity within the whole family of cellular structures considered here. Multiphase samples had however the lowest specific energy absorption performance due the leaking of hydrogel during quasi-static crushing. Hybrid samples absorb more specific energy than the slotted and hydrogel samples along the *x* and *y*-directions; the SEA of hybrid samples with hexagonal, re-entrant and AEC re-entrant shape features is also 19%, 4% and 6% larger than the one of bulk thickness samples along the loading *y*-direction, respectively. Hybrid configurations also improve the SEA by 6% compared to the bulk thickness samples with hexagonal cellular structures when loaded along the *x*-direction.

Another important result is that the auxeticity causes a reduction of the SEA capacity in hybrid samples compared to the hexagonal ones, and this is due to a ~37% increase of mass. Although re-entrant honeycombs [82] are known to possess more energy dissipation over hexagonal configurations, they have larger densities than the regular topologies, and those could dominate the SEA behavior. Asymmetrical configurations appear to be better than conventional re-entrant configuration in terms of the SEA.

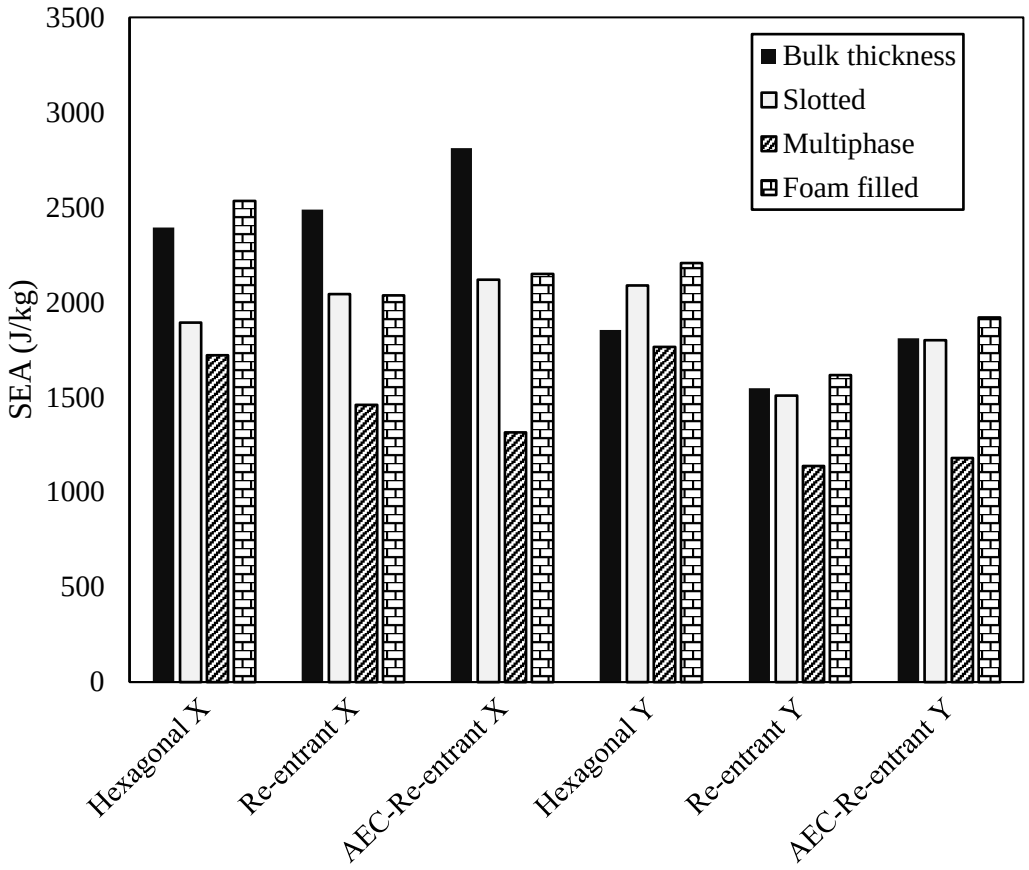

Figure 2.28 : Specific energy absorption (SEA).

2.6.5 Specific compressive modulus

Figure 2.29 shows that both slotted and hybrid samples have superior specific modulus compared to the other configurations. This is consistent with similar findings in [120], [121] regarding hierarchical structures. The compressive modulus of hybrid samples along the *x*-direction is increased by 14 % and 11% compared to bulk thickness configurations with hexagonal and re-entrant cellular structures. Out-of-plane leaking of the hydrogel in multiphase samples have likely caused the decrease of the specific stiffness. The specific modulus of both multiphase and hybrid samples decreases when passing from hexagonal to AEC re-entrant configurations, both for the values associated to the *x* and *y*-directions. The increase in mass is also a likely reason for this reduction. The specific compressive modulus of hybrid samples with re-entrant cellular shapes is ~4% and 2% lower than the one featured by hexagonal cells along the loading *x* and *y*-directions. The samples with AEC re-entrant topologies show ~13% and 59% lower performances. This indicates that the reduction of the cell wall angle θ could be more influential on the stiffness performance of the samples than the resulting increase of mass [142].

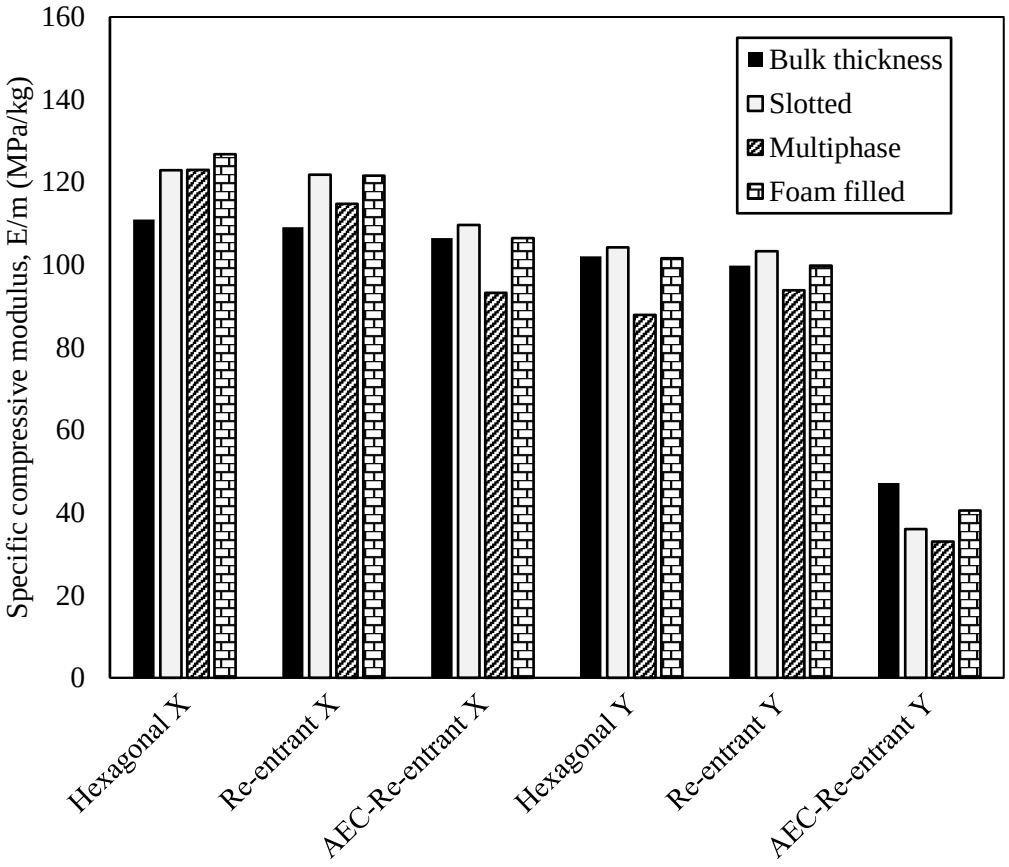

Figure 2.29: Specific compressive modulus.

2.7 Parametric Studies related to Hybrid Hierarchical Honeycombs

The experimental studies showed that the hybrid samples possess a superior compressive crashworthiness performance compared to the other configurations. The combination of an additive manufactured polymeric structure and the inclusions of a lightweight porous solid provide an increase of mechanical properties of the lattices, especially the ones with auxetic topology. The most common parametric analyses for these cellular structures involve the variation of the internal cell angles [88, 93, 142, 144, 145] and aspect ratios of the cell ribs [93, 97, 146-148]. Apart from those more traditional parameters, we have also previously observed the effects of the hierarchical configurations on the quasi-static crushing performance of the metamaterials presented here. Therefore, the parametric analysis is here focused on the hybrid topologies with varying geometry of the hierarchies in unit cell, but with constant lengths, cell wall angle, and thickness of the ribs. The AEC re-entrant topology has been selected as the most mechanically efficient honeycomb configuration; the design parameters consisted of the number of slots present in one rib and the rounding of the corners of

both slots in the PLA-made structure and the PUR foam. These modifications were conducted via finite element modeling by taking into consideration the difficulties existing in the manufacturing processes. In the first case, the number of slots on a single rib is varied from 1 to 4 (Figure 2.30). In the second case, the corners of the slots and foam parts were rounded with a radius of 0.4 mm. The FE simulations indicated that the effect of the radius of rounded corner on the quasi-static crushing performance becomes more visible when the radius is equal or greater than 0.4 mm. Stress concentrations at the sharpened edges of rectangular slots can reduce the strength of the structure under compression loading, and this is the main rationale behind the investigation of the rounding [149]. The reduction in stress concentrations provided by the rounded corners would also help to reduce the onset of failure due to debonding in the weaker parts of the lattice.

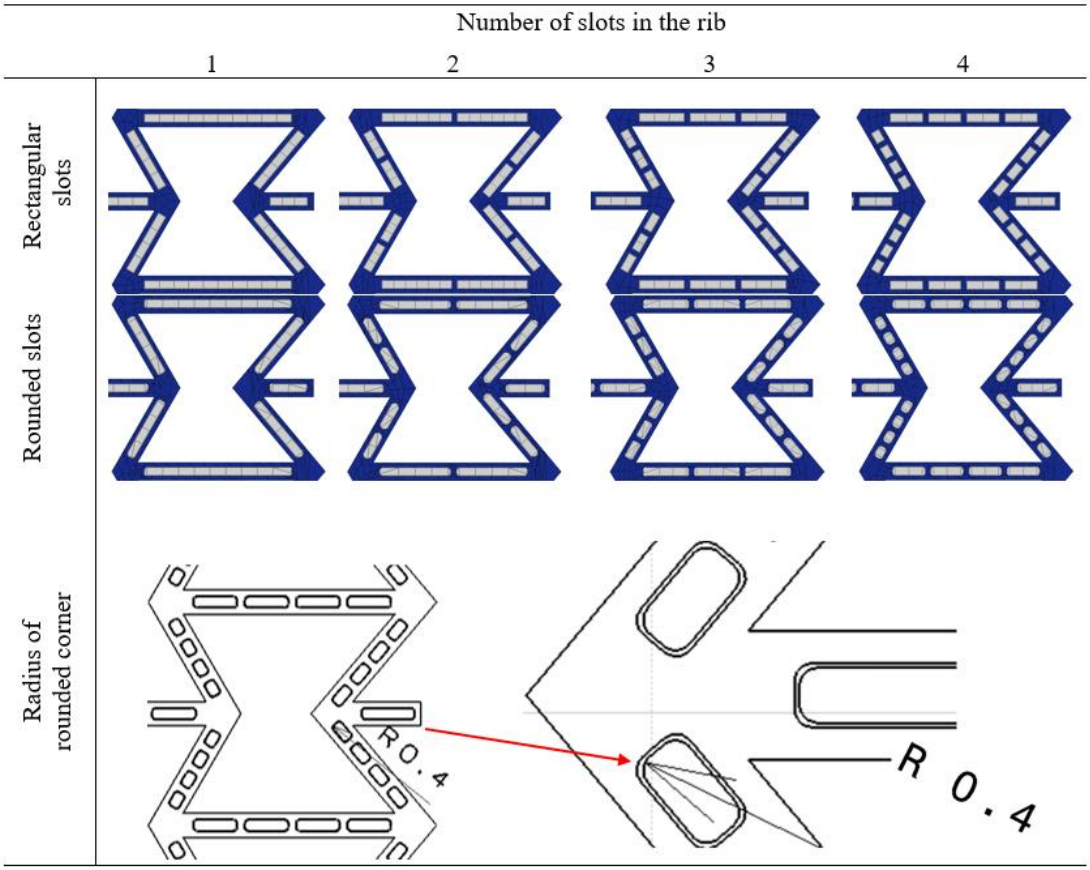

Figure 2.30 : Unit cell configurations of AEC re-entrant samples with and without radius of round by changing the number of slots.

Finite element analyses of eight different hybrid samples have been performed, and SEA, MCF, specific strength and stiffness are calculated. Figure 2.31 and Figure 2.32 illustrate the results related to each crashworthiness indicator. The MCF, SEA,

Specific compressive modulus and strength values are in the range of 92-2789 N, 61-1650 J/kg and 41-598 MPa/kg and 8-36 MPa/kg, respectively. The results show that the number of slots and the rounded corners of the same slots has remarkable effects. The relative stiffness, SEA and MCF values increase for rising numbers of slots, both in the rectangular and rounded corner cases. Normalized stresses also show an increasing trend when the number of slots is augmented, however, the results of samples having 2, 3 and 4 slots are quite close to each other. It is also important to notice that almost all samples with rounded corners have higher specific compressive strength, stiffness, the SEA and the MCF values, except for the case of the S1 samples in terms of specific compressive strength. The deformation mechanism of the rounded S1 sample exhibits a larger global rotation than the rectangular one due to instabilities in the deformation mechanism. The performance of the S1 samples is very reduced compared to those of samples having 2, 3 and 4 slots (more than 300% reduction in any case). The weakness and failure of the ribs of the S1 samples could be the reason of this peculiar behavior in terms of specific compressive strength. Unlike the case of the S1 samples, the adjacent cell walls of the slots and the corner of the unit cells tend to behave as plastic hinges under compression, which reduces the instabilities during the quasi-static crushing. The superiority of the samples with rounded corners over rectangular ones becomes more evident with the increase of the number of slots. The combination of the large number of slots per rib, the rounding of their corners, and the filling of the slots with foam appears to increase significantly the crashworthiness of the hybrid structures developed in this study. Deformed and non-deformed shapes of the S-4 rounded sample having the best performance are indicated in Figure 2.33.

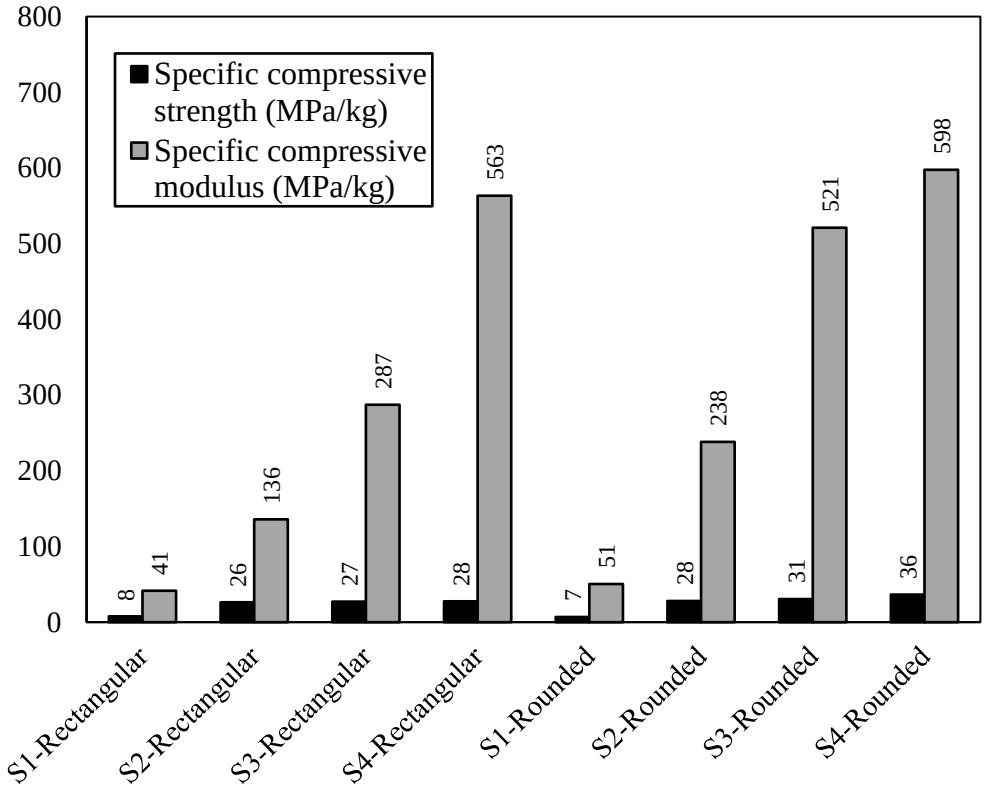

Figure 2.31 : The Specific compressive strength and modulus values of modified hybrid samples.

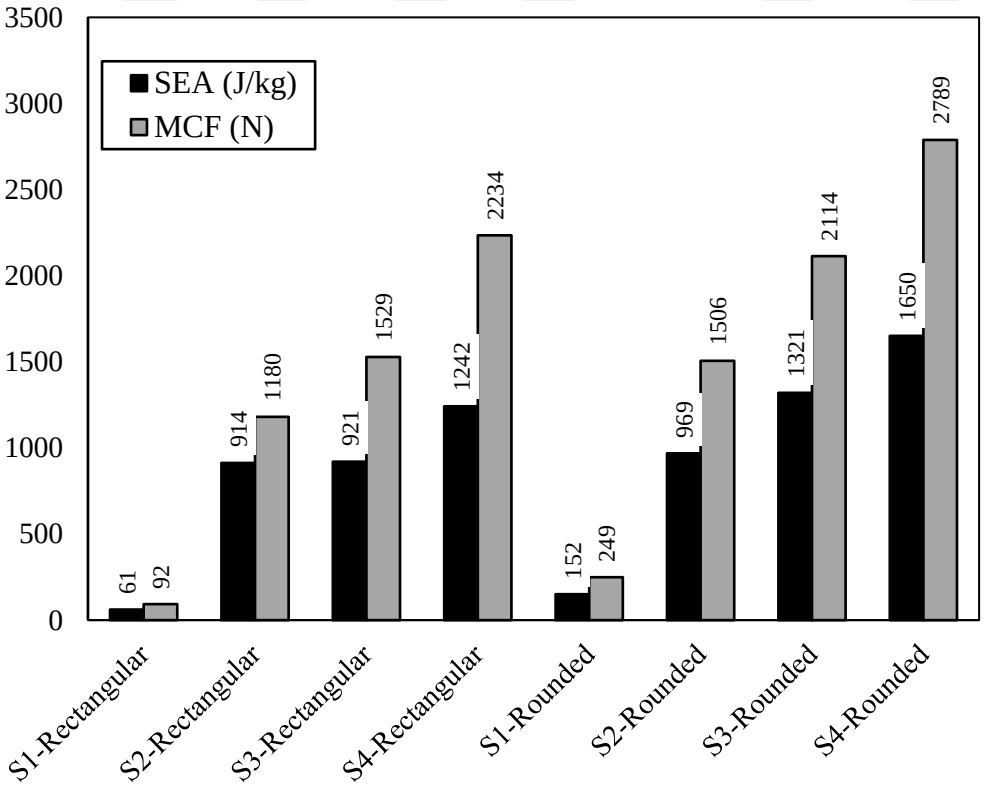

Figure 2.32 : The SEA and MCF values of modified hybrid samples.

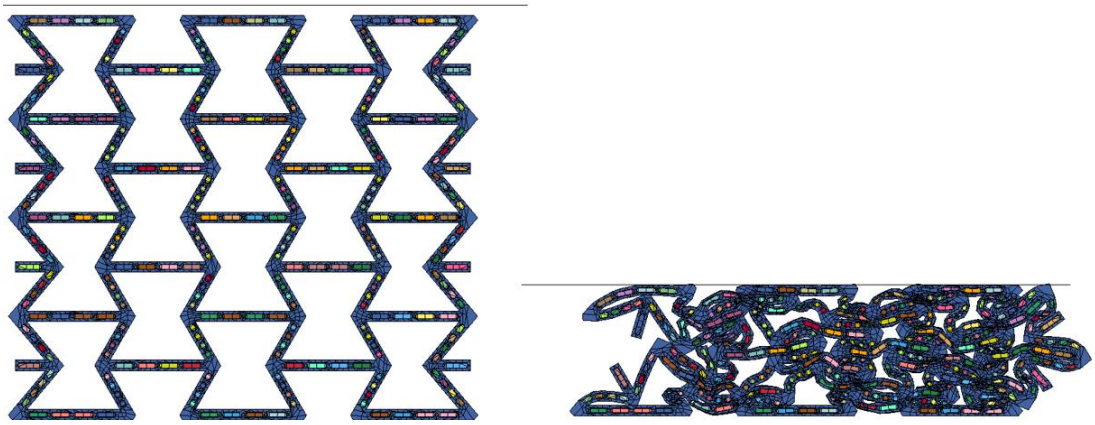

Figure 2.33 : Deformed and non-deformed shapes of the optimum design: S4-rounded sample.

2.8 Conclusion

This work has focused on the compression and energy absorption capabilities of auxetic and non-auxetic cellular metamaterials with two different ribs architectures and hybrid cells and introduced two novel composite hierarchical cellular shape honeycomb metamaterial designs for crashworthiness applications. The two configurations include the presence of slots in the cell ribs; in one case, those slots are filled with PUR foam and in the second case with injected hydrogel. The work has included numerical and experimental results. We have looked at the specific compressive strength, stiffness and energy absorption capabilities of these metamaterial configurations made of auxetic and non-auxetic cellular structures (re-entrant, AEC re-entrant and hexagonal).

The results show that the use of asymmetric cells on the edges of the lattices in re-entrant configurations provides higher Poisson's ratio values. The slotted structures appear in general to possess a higher specific compressive modulus compared to the bulk thickness ones. Asymmetric edge cells increase the specific compressive modulus when the lattices are compressed along the two principal directions of the plane compared to the hexagonal and re-entrant honeycombs. The slotted cells also increase the specific strength of the samples compared to bulk thickness configurations; however, they absorb less specific energy than the bulk samples in most cases. The use of asymmetric cells provides higher specific strength in all cases and higher SEA values in the majority of the configurations considered.

Experimental tests have been carried out to compare the performance of the novel designs with slots, but also bulk thickness configuration. The multiphase hierarchical samples showed that the non-Newtonian phase filler helps to reduce the instabilities during large deformations of the re-entrant honeycombs under quasi-static crushing. The overall crashworthiness performance of the multiphase samples is worse than the one from the other cases because of the leakage of the hydrogel along the out-of-plane direction. If improvements in the manufacturing process are identified, the stabilization of the deformation mechanism during compressive loading could be however an important aspect for the design of crashworthiness devices.

The results of hybrid samples filled with PUR foam have shown that the specific strength, stiffness and energy absorption of these hybrid structures are higher than those provided by the other configurations (auxetic and non-auxetic). The auxetic configurations (re-entrant and AEC re-entrant) also featured the highest values of specific strength.

The explicit FE parametric analyses performed in this work were made using models related to the hybrid configuration and benchmarked by experimental results. The parameters (number of slots in the ribs and round on the corner of those slots) reflect some aspects of the manufacturing constraints provide by state-of-the-art 3D printing techniques based on FDM. The results showed that those parameters do affect the quasi-static crushing performance, with higher specific stress, stiffness, the SEA and the MCF values increasing in the case of both rectangular and rounded slots. The samples with rounded corners also possess the highest specific stiffness, stress, SEA and MCF values, in particular when auxetic configurations are considered. The crashworthiness of the hybrid metamaterial configurations shown in this work can be improved with the combination of the larger number of slots in the ribs and the rounding of their corners.

Overall, this study has shown that strength, stiffness and energy absorption of cellular metamaterials can be increased by using slotted unit cells and asymmetric cells along the edge of the lattice assemblies and composite open cells honeycombs with the PLA plastic reinforcements, hydrogel and polyurethane rigid (PUR) foam. Our new designs also contribute to tailor the deformation mechanism of the lattices under compression and provide more stable and predictable deformation patterns under crushing.

3. SANDWICH PANELS WITH AUXETIC OR NON-AUXETIC CORES

3.1 Purpose

This chapter consists of the studies on sandwich panels under low and high-velocity impact loading. We mainly focused here on the effects of different types of auxetic and non-auxetic core structures and curvature of panels on the composite sandwich panels. In addition, the effects of thickness and curvature on the composite plates are examined, and an optimization study on the curved plates has been performed.

In Section 3.2, the impact resistance of composite sandwich panels with different types of auxetic (i.e., negative Poisson's ratio) and non-auxetic core structures have been investigated by using a drop test machine. In Section 3.3, open cellular core topologies (re-entrant lattice) and semi-reticulated polyurethane lightweight foam core structures are studied. This work proposes to indicate how they affect the high-velocity impact behavior of the doubly curved CFRP sandwich panels. In Section 3.4, we examine the impact behavior of single and doubly curved structures with auxetic cores by using numerical methods. We have evaluated twelve different doubly and one single curved panels impacted by a spherical projectile. In Section 3.5, the thickness and curvature effects on high-velocity impact behavior of flat and cylindrical panels are investigated numerically. In the last section of Chapter 3, an optimization study is carried out in order to determine the optimum designs of curved plates under high-velocity impact loading.

3.2 Low-Velocity Impact Resistance of the Flat Composite Sandwich Panels

This work describes the low-velocity impact behavior of composite sandwich panels with different types of auxetic (negative Poisson's ratio) and non-auxetic prismatic core structures. Sandwich panels have been manufactured with carbon/fiber epoxy composite face sheets, polyurethane rigid foam core or 3D printed PLA plastic cellular honeycombs head (hexagonal, re-entrant, hexachiral and arrowhead). The material properties of the constituents have been determined via tensile and compression tests.

The cellular core topologies have the same wall thickness and number of cells (39x4, except for the hexachiral topology). A rigid striker with a hemispherical head tip is dropped on the specimens with a speed of 2.6 m/s. Explicit finite element (FE) models are validated by the experimental results. Parametric numerical analyses using the validated FE have been carried out with different impact energies of 10J, 20J, 30J, 40J, 50J, 60J and 76 J to identify the best core designs. The results show that non-auxetic cores could have advantages over the auxetic ones at small deformation (impact energy is equal to 10 J) thanks to the larger contact surface and higher thickness of the cellular structure. The auxetic core, however, provide greater impact resistance and energy absorption capability as the impact energy increases due to the larger densification and lower indentation during the collapse. The arrowhead-based panels in particular, possess 25%, 13% and 11% larger crash efficiency than the other samples for impacts with 50, 60 and 76 J. The hexachiral lattice provides the best performance at 10, 20 and 30 J, and also possesses advantages over the other cellular configurations (except for the arrowhead core) in the case of 40, 50, 60 and 76 J impact loading. As a result, the arrowhead and hexachiral configurations are those mostly recommended for applications involving impacts under large deformations.

3.2.1 Cellular core designs

Here, four types of open cellular core topologies (hexagonal, re-entrant, arrowhead, and hexachiral lattice) and semi-reticulated cellular foam core structures were studied. This work proposes to indicate how they affect the low-velocity impact resistance of the CFRP sandwich panels. Open cellular core topologies were fixed to have the same dimension of wall thickness and number of cells (39x4 except hexachiral topology). 3D CAD models and unit cell designs with the topology parameters of the auxetic and non-auxetic core structures are depicted in Figure 3.1a-h. The design parameters of the hexagonal and re-entrant unit cells are as the thickness t of the struts, the length l of the inclined strut, the length h of the horizontal strut and the cell wall angle θ (Figure 3.1a-b). The dimensions of those parameters used for the 3D printed samples are h=5 mm, t=0.7 mm, l=2.5 mm, and θ= 60°. The relative densities of the hexagonal and re-entrant honeycombs are calculated as 0.26 and 0.43 by equation (3.1) [54, 85].

$$\frac{\rho^*}{\rho_s} = \frac{t/l(h/l+2)}{2cos\theta(h/l+sin\theta)} \tag{3.1}$$

The unit cell of the double arrowhead topology can be defined by three parameters *l*, θ_1, and θ_2 where they are the horizontal distance between vertices A and B, with the respective half re-entrant angles of struts AB and BC, respectively (Figure 3.1c). The dimensions of *l*, θ_1, and θ_2 used for the 3D printed samples are 3.76 mm, 63.3° and 33.5°. The relative density of the structure is calculated as 0.56 by using equation (3.2) [109].

$$\frac{\rho^*}{\rho_s} = \frac{t(sin\theta_1 + sin\theta_2)}{lsin(\theta_1 - \theta_2)} \tag{3.2}$$

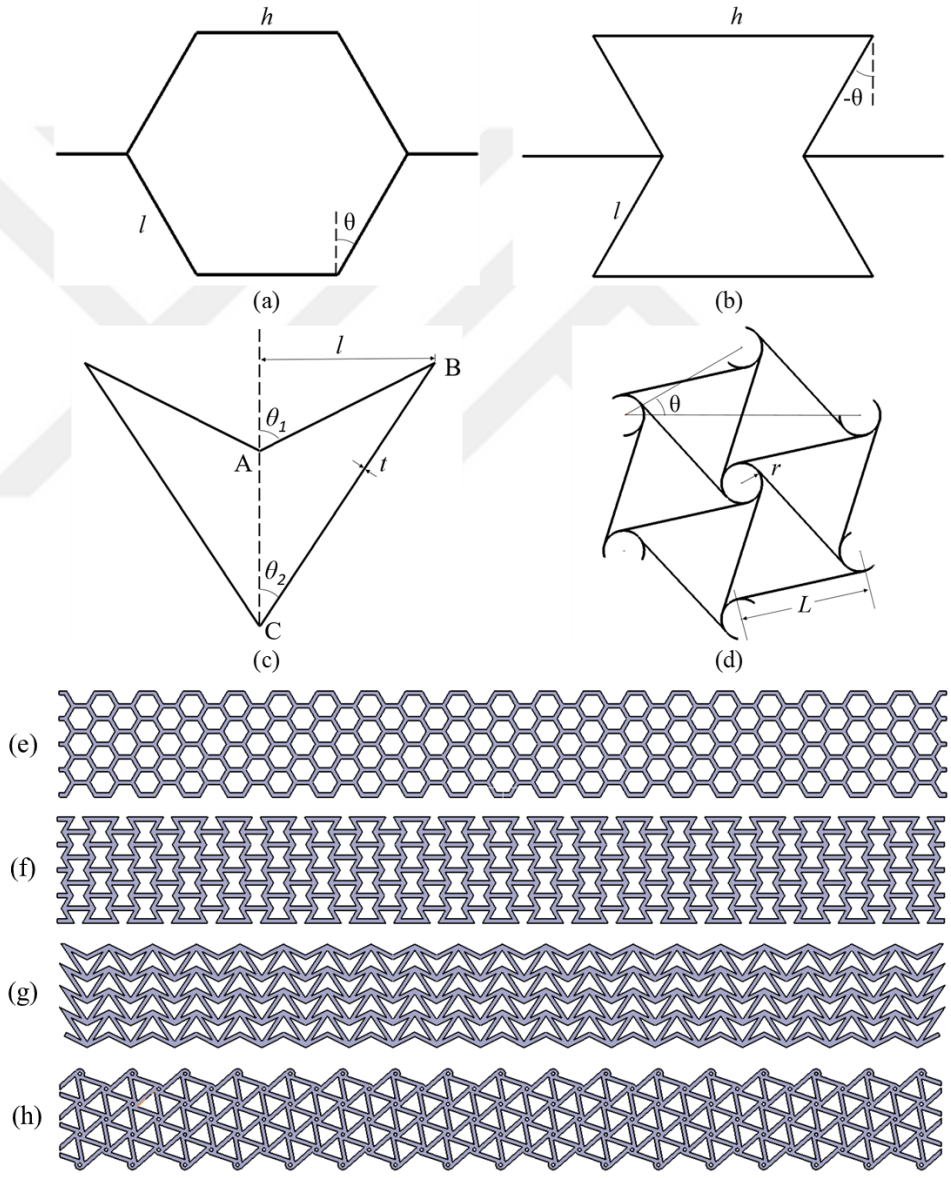

Figure 3.1 : Topologies of auxetic and non-auxetic cellular structures: Unit cell designs of (a) hexagonal, (b) re-entrant, (c) DAH (d) hexachiral honeycombs; 2D sketches of (e) hexagonal, (f) re-entrant, (g) DAH, (h) hexachiral honeycomb cores.

The chiral honeycomb consists of cylinders or nodes connected by ribs [50]. For hexachiral honeycombs, *L* and *r* represent the length of the ribs and the radius of nodes in Figure 3.1d. The dimensions of *L* and *r* are 4.65 and 0.575 mm. The relative density of hexachiral honeycomb is calculated as 0.60 by using equation (3.3) [115].

$$\frac{\rho^*}{\rho_s} = \frac{t(4\pi r + 6L)}{4\pi r^2 + 3L^2 sin\theta} \tag{3.3}$$

3.2.2 Sample preparation and material properties

The specimen preparation can be divided into four processes: 1) manufacturing composite face sheets, 2) 3D printing PLA plastic core designs, 3) preparation PUR foam core, 4) bonding face sheets and core structures. The resulted sandwich structures were manufactured with the dimensions of 150-mm long, 100-mm wide, and 20-mm thick compatible with the ASTM 7136-C test procedure (Figure 3.2) [150].

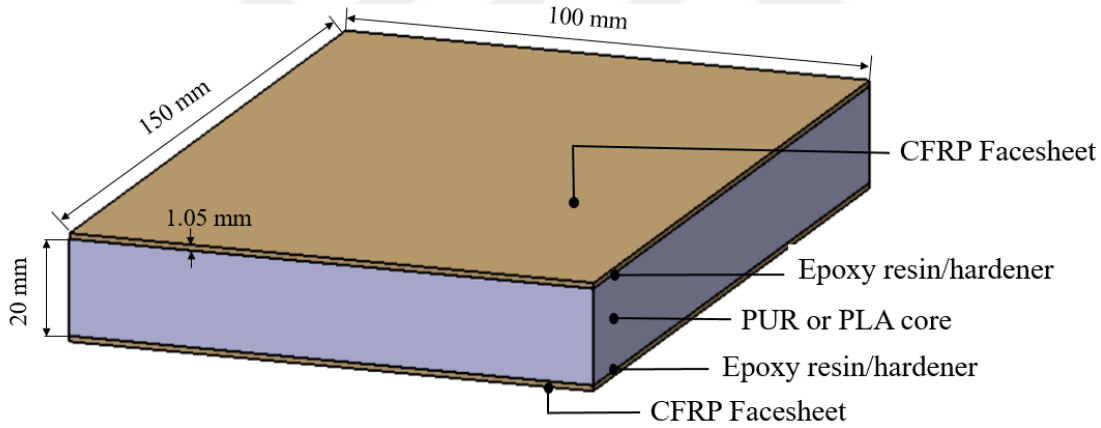

Figure 3.2 : Schematic of the sandwich panel and manufactured CFRP sandwich panels.

The types of core structures used here are classified as auxetic (re-entrant, DAH and hexachiral lattices) and non-auxetic (PUR foam and hexagonal lattice). The hexagonal, re-entrant, DAH and hexachiral cellular structures are made of PLA plastic. The PUR foam is made of rigid polyurethane foam. The manufactured composite sandwich panels with five different core designs are shown in Figure 3.3. The carbon skins and the cores were bonded by using the mixture of MSG lamination epoxy resin and hardener.

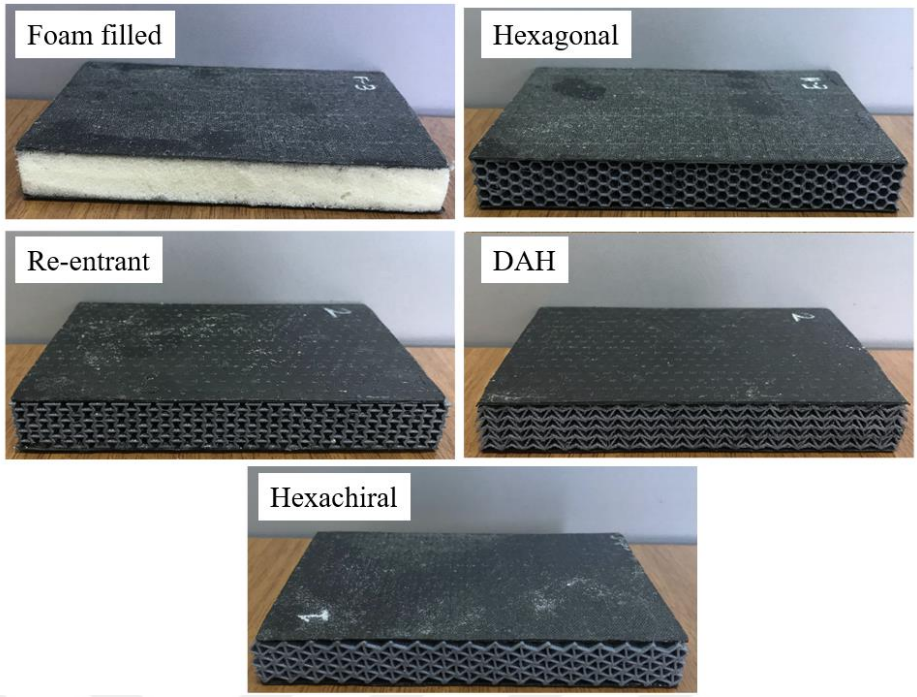

Figure 3.3 : Manufactured CFRP sandwich panels: non-auxetic (PUR foam, hexagonal lattice) and auxetic core (re-entrant, DAH, hexachiral).

3.2.2.1 Composite face sheets

Composite face sheets made out unidirectional (UD) carbon fiber fabrics of 300 gr/m2 were manufactured with the wet/hand lay-up method. Each face sheet consists of 3 plies with the [0/45/90] stacking sequence. Carbon fiber fabrics were cut by using the Robuso EC cutter. The mould release chemical liquid was spread on the mould, and then composite fabrics were placed on the mould. The carbon fiber fabrics were impregnated with the MGS® L285 lamination epoxy resin of 1.13 gr/cm3 and H285 hardener of 0.95 gr/cm3 with a mix ratio of 2:1 by weight, and peel plies were laid on the fabrics to provide clean and smooth surfaces. Heatcon vacuum press test machine was used to cure the epoxy resin and ensure a uniform flatness on both sides of the face sheets. Vacuuming and blanket drained the residue of epoxy resin. The curing stage was carried out at 45 C^0 temperature for 16 h. The cured panels with a thickness of 1.05 mm and a fiber volume fraction of 59 % were used as top and bottom face sheets of sandwich structures seen in Figure 3.4. After curing the laminated composites, carbon skins and the cores were bonded using the same resin system.

Material properties of UD carbon fiber composite panels have been determined following ASTM D3039/3039M-14, ASTM D6641/D6641M-14 and ASTM D3518/D3518M-13 test standards [151-153]. The baseline panels with a thickness of

2 mm were manufactured with wet/hand lay-up method, and then tension (250 mm x 20 mm) and compression (140 mm x 20 mm) test specimens were extracted from the surfaces of the baseline panels by using water jet machine. Biaxial strain gauges were glued onto the surface of the test specimens, and then tensile and compression tests were performed by using the MTS Universal test machine. According to the test results, the material properties of CFRP were listed in Table 3.1.

Figure 3.4 : Tension and compression test specimens of carbon fiber composites.

Table 3.1 : Properties of unidirectional CFRP composite.

Property	Value	
Density, ρ (gr/cm^3)	1.5	±0.1
Longitudinal stiffness, E_1 (MPa)	160000	±5000
Transverse stiffness, E_2 (MPa)	6500	±300
Poisson's ratio, v_{12}	0.12	±0.01
In-plane shear modulus, G_{12} (MPa)	5680	±240
Longitudinal tensile strength, X_t (MPa)	1020	±50
Longitudinal compressive strength, X_c (MPa)	650	±20
Transverse tensile strength, Y_t (MPa)	70	±6
Transverse compressive strength, Y_c (MPa)	100	±5
Transverse shear strength, S (MPa)	80	±4

3.2.2.2 PLA plastic cores

Auxetic and non-auxetic cellular cores were printed by using a 3DTurk machine based on the fused deposition modelling method. The CAD stl design was imported into the Repetier 3D printer slicing software. This software converted the stl into a gcode file by selecting two outer shells, 100% filling ratio. Specimens were printed at 215 ^{0}C extruder temperature 0.2 mm layer height. The FDM 3D printing method can induce anisotropy in the material properties of the components due to layerwise manufacturing. In the slicing software, the toolpath was defined as ± 45^0 at every two

layers and support walls; this was to reduce the material anisotropy. After that, the material properties of PLA have been determined by performing the tensile test of the five identical 3D printed dogbone specimens following the ASTM D638-14 test standard [138]. The stress-strain curves of the samples were obtained, and the Poisson's ratio was measured from the in-plane displacements of target points recorded with strain gauges (Figure 3.5). The average Young's modulus of the PLA samples is 1.9 ±0.2 GPa, the ultimate strength is 12.8±0.5 MPa, the yield strength is 16.1±0.7 MPa, the density is 1.4±0.2 gr/cm3, and the Poisson's ratio is 0.36 ±0.02.

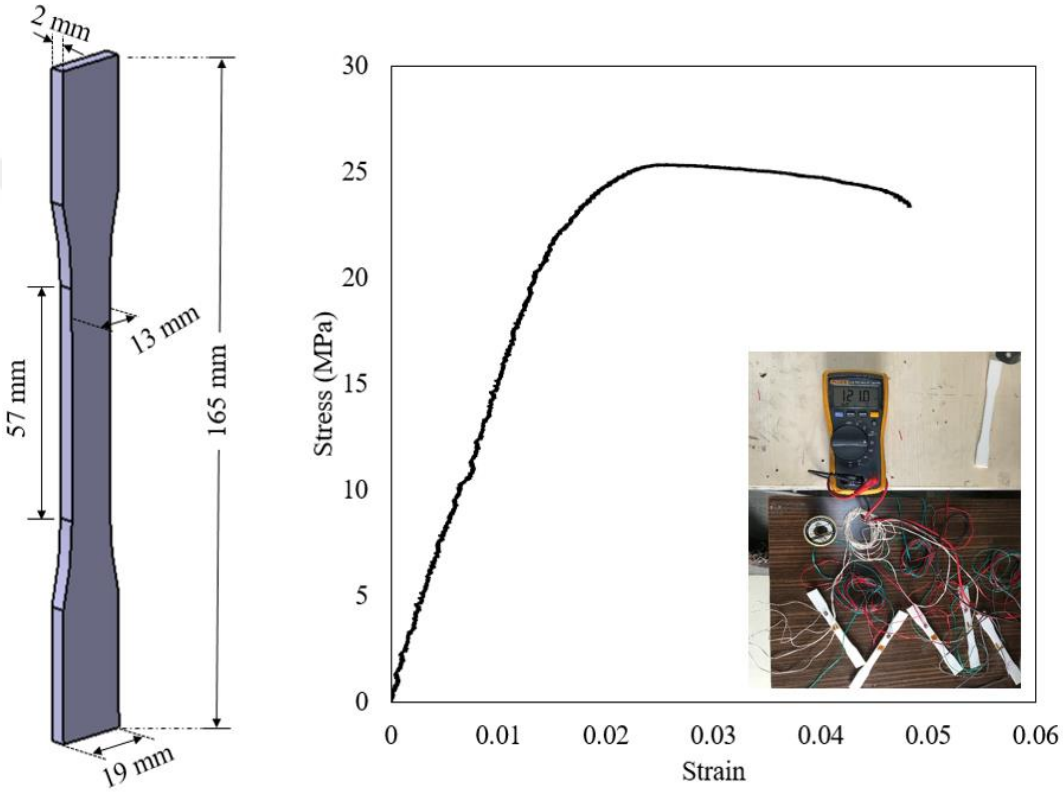

Figure 3.5 : Stress-strain curve of the PLA plastic.

3.2.2.3 PUR foam core

Polyurethane rigid foam studied in this research is an ideal core material thanks to its great energy absorption ability and lightweight, which is a semi-reticulated cellular rigid foam. The PUR foam with the components of organic resins of polyol and isocyanate (ESPOL Sponge and Chemical Industry Ltd. Co., Turkey) were processed by using the CNC 3-axis milling machine. The rectangular PUR foam cores were processed at 2000 rpm rotational speed of the milling machine to ensure smooth surfaces. The material properties are determined by performing compression tests on cubic samples (5x5x5 cm) prepared in accordance with the ASTM D1621-91 standard

[139] shown in Figure 3.6. The average Young's modulus of the PUR foam is 11.5 ±0.2 MPa, the plateaus onset stress is 0.65±0.02 MPa, the density is 69 kg m^3.

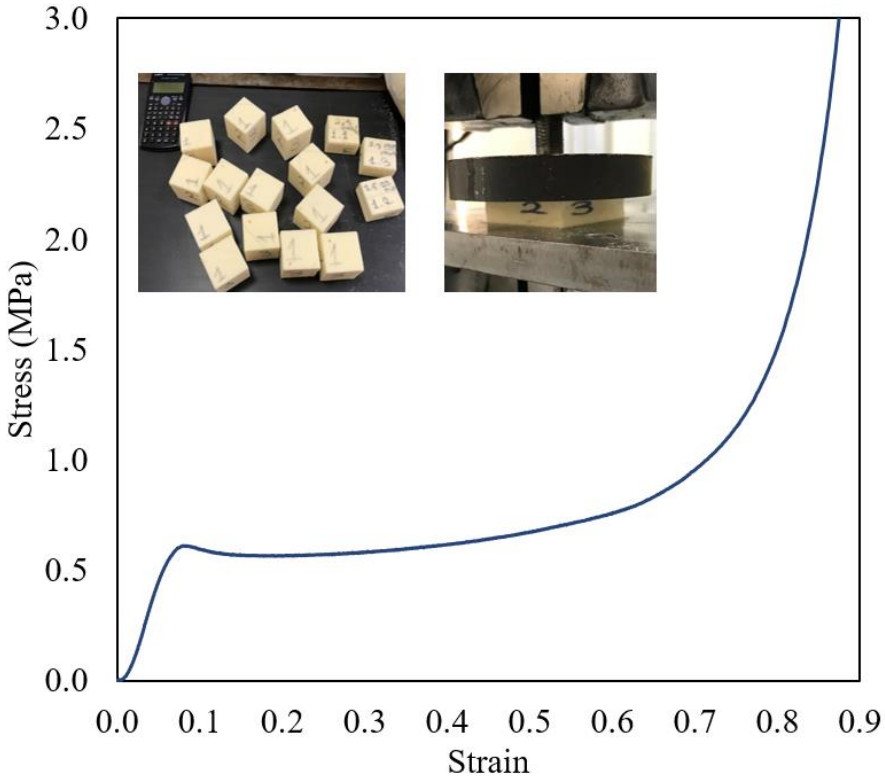

Figure 3.6 : Stress-strain curve of the PLA plastic.

3.2.3 Drop weight test set up

The low-velocity impact tests were performed by using INSTRON 9340 Drop Test Machine shown in Figure 3.7. Either the impacting mass or the dropping height was arranged to obtain the necessary amount of kinetic energy. The sandwich panels manufactured in this study have different damage tolerances for full perforation that is determined by performing the samples at various impact energies. The FE results showed that the impact energy of 76 J is quite enough to investigate the impact resistance of different samples under large deformation. The impactor with a hemispherical striker tip has a diameter of 20 mm and a mass of 22.5 kg (2.5 kg of the holder and 20 kg of additional weights) that follows ASTM 7136 [150]. The instrumented dropped-weight impactor was dropped to the specimens at the speed of 2.6 m/s. The specimens were fixed by using toggle clamps at each corner with the force of 890 N and located at the center of the impactor.

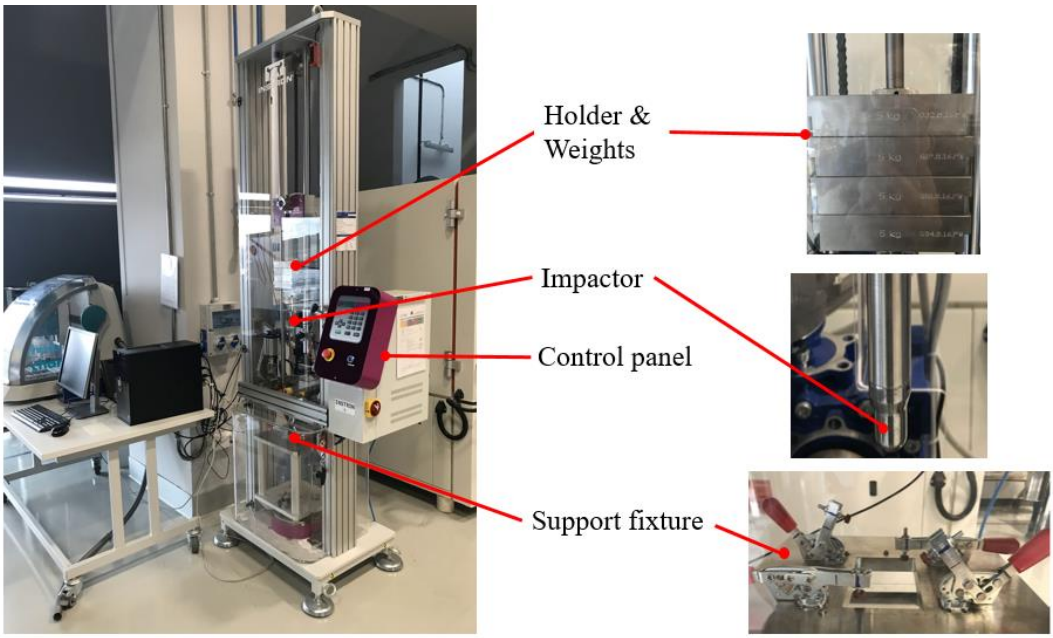

Figure 3.7 : INSTRON 9340 Drop Test Machine.

In the experiment, composite face sheets and PU foams were also tested in order to see the deformation behavior of constituents one by one. Then sandwich panels with different types of core structures were tested. Three identical specimens for each individual case were tested at the same conditions. Figure 3.8 indicates the manufactured specimens and deformation patterns.

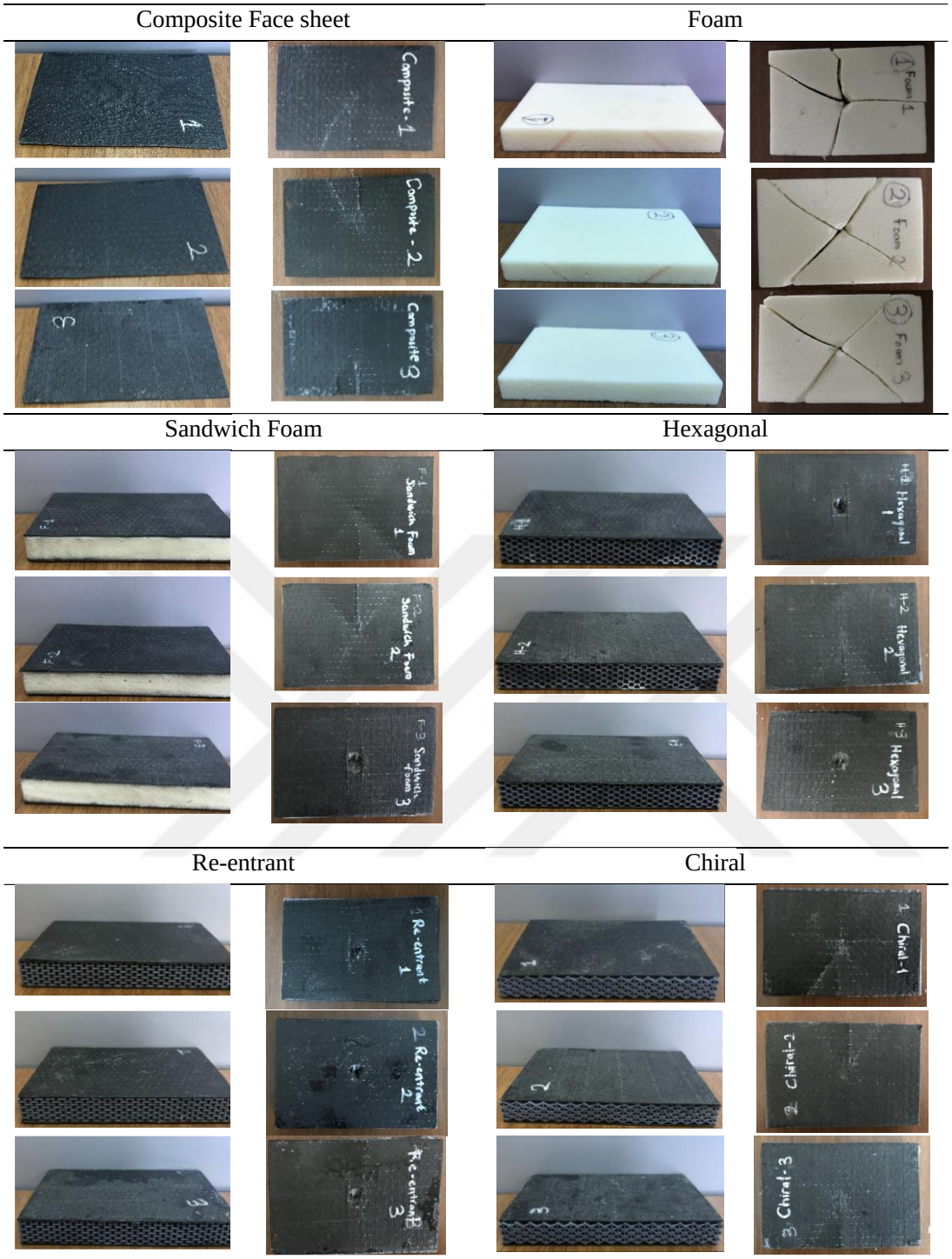

Figure 3.8 : Manufactured specimens and deformed shapes.

3.2.4 Finite element simulations

The FE models were developed by using the LS-DYNA software to simulate the low-velocity impact behavior of the specimens. The dimensions of the FE models were designed to be identical to those of the experimental ones shown in Figure 3.3. A rigid mass with a hemispherical head was dropped on the specimens with a speed of 2.6

m/s. Boundary conditions could significantly affect the impact performance of the sandwich panel when the surface area of the sandwich structure is not large compared to the impactor diameter, as used here. The boundary conditions (see Figure 3.9) were therefore defined following the standard ASTM test procedure. In the modelling, the boundary conditions (BCs) of the selected nodes at the upper and lower face of the sandwich panels were defined as clamped boundaries considering the interaction points of toggle clamps and upper face sheet (BC1) and the interaction surfaces of the support fixture and lower face sheet (BC2). The motion of the rigid impactor was allowed only along the loading direction (BC3).

The eroding surface-to-surface contact interfaces were implemented to define the interaction between the rigid impactor, composite faces and core. The automatic single surface contact algorithms were also used for each individual part by means of self-interaction.

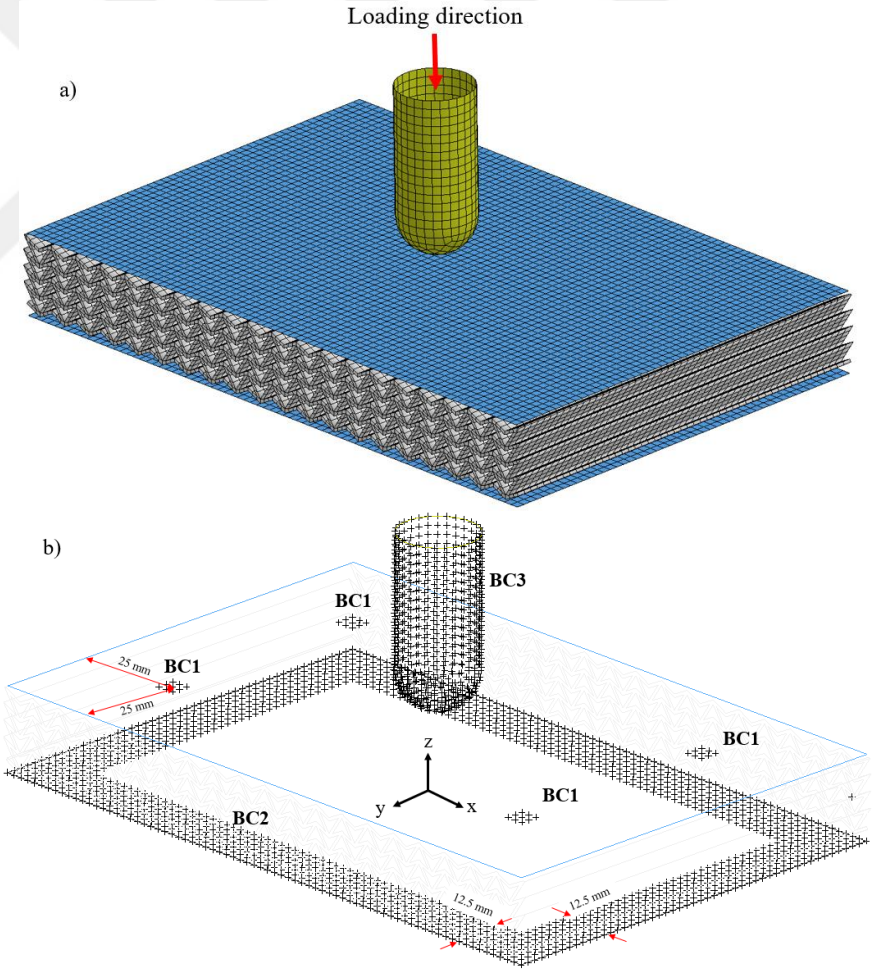

Figure 3. 9 : a) FE modelling of sandwich panels and b) boundary conditions.

The material properties of the hemispherical striker were implemented into the 'MAT20 rigid material model, where the material belonged to a rigid body. The

'MAT24 piecewise linear plasticity' material model was used to define the material properties of the PLA-made lattices. The material model describes an elastoplastic material with arbitrary stress as a function of the strain curve and failure based on a plastic strain obtained from the coupon tests. The true stress vs. effective plastic strain curve obtained from the coupon tests was implemented in this material model. The effective plastic strain values inputs are calculated by using equation (3.4):

$$\bar{\varepsilon}^p = {\varepsilon_{total}}^T - \frac{\sigma^T}{E} \tag{3.4}$$

where $\bar{\varepsilon}^p$ is the effective plastic strain, ${\varepsilon_{total}}^T$ is the total true strain and σ^T is the true stress. The Young's modulus, density, Poisson's ratio and failure strain inputs of the PLA-made lattices are given in Section 3.2.2.2.

Similarly, the material properties of the PUR foam obtained experimentally were implemented into the 'MAT63 crushable foam' material card. The PLA-made lattices and the PUR foam were modeled by using ELFORM 1 (element formulation option 1) based on constant stress solid elements. Belytschko-Tsay explicit shell elements consisting of 5 DOF in local coordinate system yield globally 6 DOF were adopted to the CFRP composite panels. The MAT54 'Enhanced Composite Damage' in LS-DYNA was utilized to simulate damage progression of composite panels under dynamic loading. The material properties in the elastic region were implemented by using experimental results (Table 3.1). Beyond the elastic region, MAT54 is based on the Chang-Chang failure criterion [154] as indicated in equations (3.5)-(3.8). The failure flags for the material direction 1 and 2 are represented by ε_f, ε_c , ε_d and ε_m which are called as tension and compression for the fiber direction, and tension and compression for the matrix direction. The 1-direction is the fiber direction, while the 2-direction is the matrix direction.

Tensile fiber mode where $\sigma_{11} \geq 0$

$$\varepsilon_{\mathrm{f}}^2 = \left(\frac{\sigma_{11}}{X_T}\right)^2 + \beta\left(\frac{\sigma_{12}}{S_C}\right) - 1 \quad \begin{Bmatrix} \geq 0 \text{ failure} \\ < 0 \text{ elastic} \end{Bmatrix} \tag{3.5}$$

Compressive fiber mode where $\sigma_{11} \geq 0$

$$\varepsilon_{\mathrm{c}}^2 = \left(\frac{\sigma_{11}}{X_C}\right)^2 - 1 \quad \begin{Bmatrix} \geq 0 \text{ failure} \\ < 0 \text{ elastic} \end{Bmatrix} \tag{3.6}$$

Tensile and compressive matrix mode where $\sigma_{22} \geq 0$

$$\varepsilon_{\mathrm{m}}^{2} = \left(\frac{\sigma_{22}}{\mathrm{Y_T}}\right)^{2} + \left(\frac{\sigma_{12}}{\mathrm{S_C}}\right)^{2} - 1 \quad \left\{ \begin{matrix} \geq 0 \text{ failure} \\ < 0 \text{ elastic} \end{matrix} \right\} \tag{3.7}$$

Compressive matrix mode where $\sigma_{22} \leq 0$

$$\varepsilon_{\mathrm{d}}^{2} = \left(\frac{\sigma_{22}}{2\mathrm{S_C}}\right)^{2} + \left[\left(\frac{\mathrm{Y_C}}{2\mathrm{S_C}}\right)^{2} - 1\right]\frac{\sigma_{22}}{\mathrm{Y_C}} + \left(\frac{\sigma_{12}}{\mathrm{S_C}}\right)^{2} - 1 \quad \left\{ \begin{matrix} \geq 0 \text{ failure} \\ < 0 \text{ elastic} \end{matrix} \right\} \tag{3.8}$$

A mesh convergence study was performed to identify an adequate balance between accuracy and mesh quality. The sandwich panel with double arrowhead core was modelled using 5 different mesh densities that consist of 36112, 41250, 49525, 57453 and 63664 elements. The numerical results have shown that convergence in terms of load-displacement curves was achieved with the increase of the mesh density. A model with 63664 elements has then been used during the validation, and the same mesh density was also found acceptable for the other samples.

3.2.5 Results and discussions

3.2.5.1 Validation of the numerical models

The FE models were validated by comparing the load-displacement responses with the experimental results for each sample. The impact force measured experimentally by using the sensor mounted on the impactor and the numerical force value is calculated using boundary conditions of the finite element model. The load vs. displacement and load vs. time histories from the FE simulation and experimental results of sandwich panels with auxetic and non-auxetic core are shown in Figures 3.11 and 3.12. There is a reasonable agreement between experimental and simulations concerning the peak load and the general trend in force response.

One can observe the sandwich panel with the PUR core has two different peak forces at the displacements of 5 mm and 25 mm, unlike the other sandwiches with PLA-made cellular cores. The main reason is that the impact resistance of the PUR foam is very low comparing to CFRP panels due to low stiffness and lightweight. When the hemispherical striker perforated the top composite face sheet and started to penetrate into foam core, load values decreased rapidly from 3 kN to 0.5 kN and remained on that level up to the onset of the lower face sheet deformation. The difference between

the first and second peak forces at 7.5 and 25 mm of displacement indicates how the synergy between the CFRP face sheets, and the foam core with their failure modes affects the load response of the sandwich panel. The first peak load stems from the upper face and core compression crushing. The peak is indicative of the full perforation of the upper face sheet. In the second region, core crushing and core shear failure have been observed, and the average load in that region is ~0.5 kN. The shear deformations of the polyurethane foam core could have a significant contribution to the deflections of the CFRP skinned sandwich panels [67]. Face/core debonding and lower face sheet crushing is observed where the average load response is 2.5 kN. The discrepancy shown in Figure 3.10 after 25 mm displacement results from differences in terms of predicted and experimental failure modes of the lower skin. The lower face deformation was dominated by the global bending and it is not localized, unlike within the FE simulations. This particular behavior could result from the low thickness of the face sheets. The manufacturing and the specimen preparation could also potentially cause premature defects in the test specimens

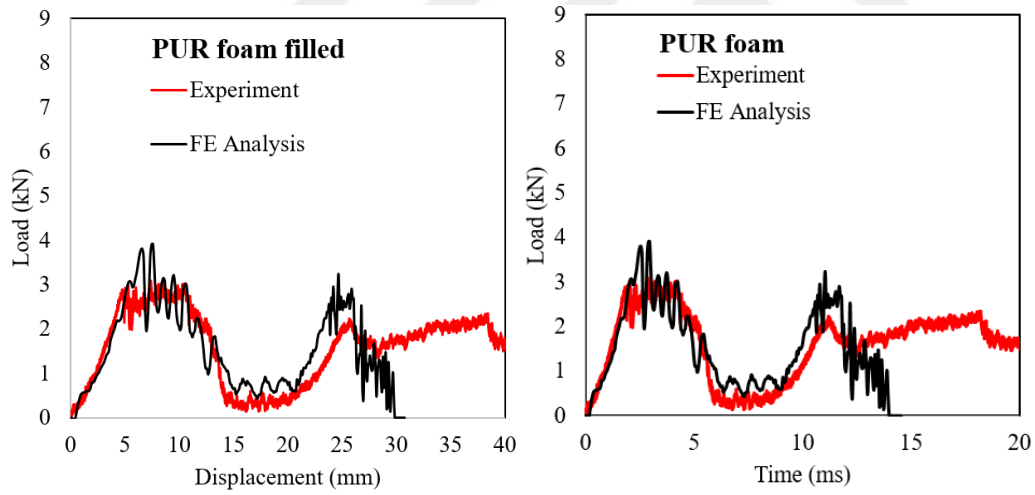

Figure 3.10 : Comparison between numerical and experimental results of sandwich panel PUR foam core.

Unlike foam core sandwich panel, cellular core designs densified earlier at around perforated regions thanks to its higher stiffness. They also provided a synergistic effect with the CFRP face sheets, which increased the resistance against the penetration of the striker. The most general discrepancy between the numerical and experimental results was observed shortly before the deformation of the lower face sheets. The main reason for this could be ascribed to manufacturing defects in the composite face sheets. Other aspects that could be source of defects are the additive manufacturing and

discontinuous bonding surfaces between the face sheets and the core. In the elastic regions, the load-displacement response of each sample are however, in good agreement between experiments and numerics, in particular in terms of peak forces. A difference could be observed in the load-displacement curves of the sample with a hexagonal core, which starts after the linear elastic deformation. In the experiment, the fibers belonging to the upper face started to crack where the strain reached the critical level. A sharp drop is seen afterward in the load response at 5 mm displacement. The force then starts to increase again due to synergistic effects between foam core and composite faces until the upper skin is fully perforated. This event can be seen in the samples with auxetic cores, but the discrepancy between the experimental and the FE results there are lower than in the case of the honeycomb sandwich panel in that region, which seems to contradict the rest of the load response shown in Figure 3.11. This is likely the effect provided by an imperfect bonding between the upper face and core that reduces the synergistic effects when the upper face fibers start to crack in the experiment. A similar discrepancy can be observed in the hexachiral sample. Both the re-entrant and DAH core samples, however, show a good agreement between FE simulations and experiments.

Another discrepancy between the numerics and the tests could be ascribed to the build orientation of the FDM parts and the failure criteria used in the simulation. The damage model for the PLA-made lattices is isotropic. The specimens were printed layer by layer along a different orientation to reduce the dependency of the mechanical properties on the build orientation. In addition, the element deletion option used in the simulations affects the load-displacement response. The results of the numerical model provide a visible region between the first and second peak loads, which is governed by core damage. In the experiment, this region is not evident to notice because the failed elements are not deleted and this leads to densification. Nevertheless, the discrepancies between the numerical and experimental results are acceptable to assess the overall performance from an engineering perspective.

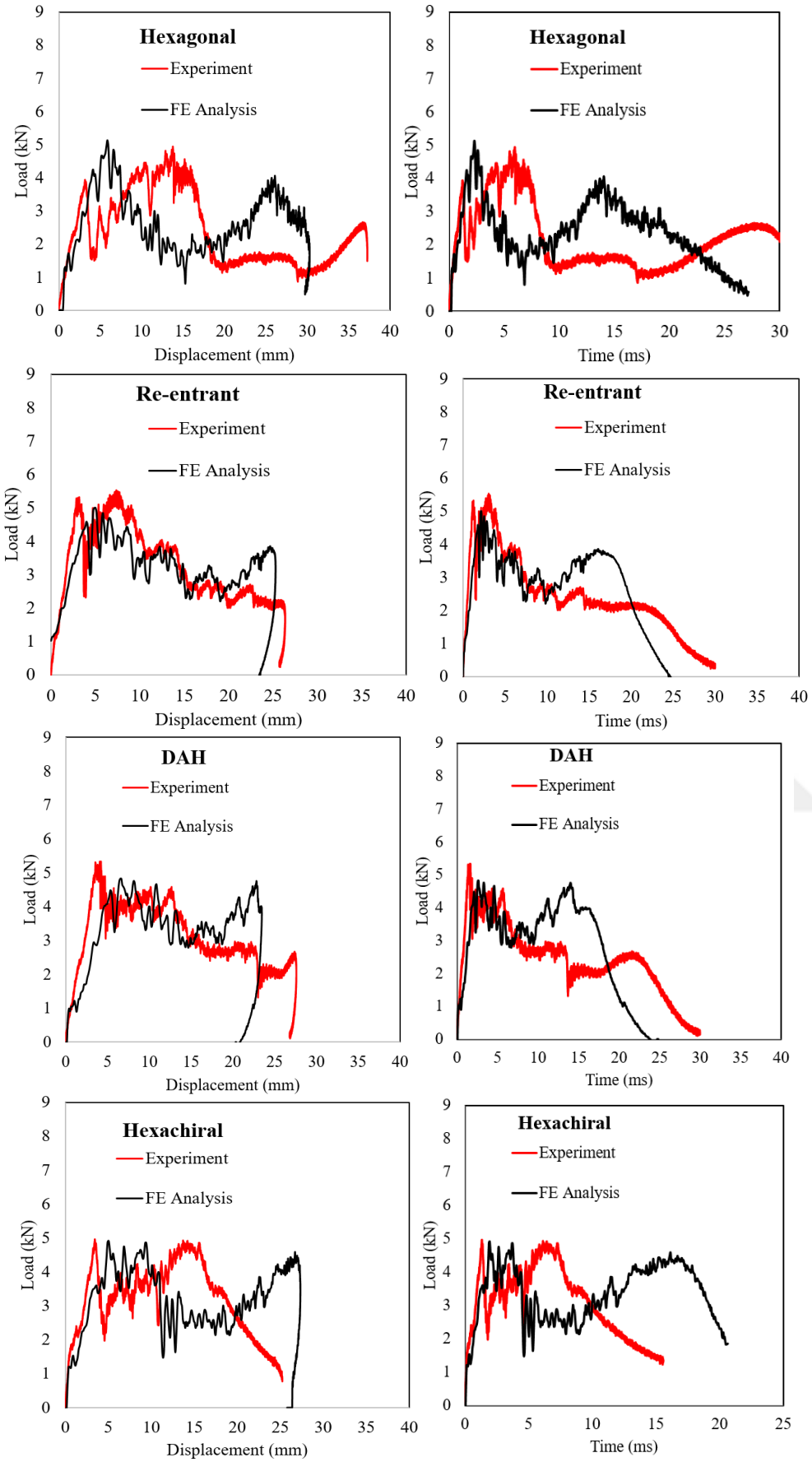

Figure 3. 11 : Comparison between numerical and experimental results related to sandwich panels with PLA cores.

3.2.5.2 Impact damage morphology

Figure 3.12 shows the top views of crushed samples. Deformed shapes of the samples in the FE analyses are similar to the ones in experiments, and the upper face sheet of each sample was perforated except the sample with the hexachiral lattice. The sample was not perforated during the experiment, while the striker penetrated up to the lower face sheet in the FE analysis. This happened because of the debonding of the composite skin surface out of the impacted zone. The core and the upper skin bonded along the line on the cylinders of the hexachiral unit cells. The epoxy resin used here does not seem to provide enough load transfer to withstand tensile loads, resulting in the region out of the impacted surface being debonded. Wrinkling failure appears in each direction on the upper skin due to the small thickness of the composite face sheet. Wrinkling induced the global deformation mechanism on the upper surface and prevented the perforation during the experiment.

The dent depth, force response, and deformation mechanism of the remaining samples were in agreement with the experimental results. Composite skins and cores of the samples (except one hexachiral core) were not debonding, and the impact damage was localized at the impacted zone. The failures were dominated by the fractures of the face sheets, shear, and crushing of foam core, buckling and breaking of the walls of the honeycomb cores.

Figures 3.10-3.12 show that sandwich panels with the PUR foam and hexagonal PLA lattice are fully perforated rather than the ones with auxetic lattices. The indentation depth of the sandwich panels with the hexagonal, re-entrant, DAH, and hexachiral cellular cores are 28.6, 23.6, 22.4, and 23.9 mm, respectively. It is evident from Figures 3.11 and 3.12 that auxeticity gives rise to an increase of the impact resistance of the sandwich samples because of higher densification and lower indentation depth during the collapse.

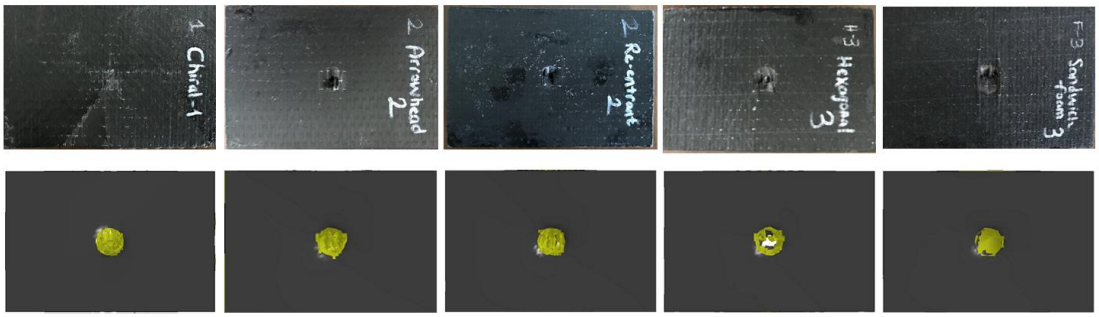

Figure 3. 12 : Deformation patterns of CFRP sandwich panels with hexachiral, DAH, re-entrant, hexagonal and PUR foam core from experiments and FE analysis.

The strength of the composite skins dominates the peak loads in the load-displacement curves. Figure 3.13 indicates that the change of the unit cell configuration does not provide a significant effect on the peak loads. The critical load, where the sandwich panel fails, therefore mostly depends on the strength of the composite skins. In addition, the peak load per unit displacement (crash efficiency - CF) could be another important indicator of the performance of the sandwich panel for impact resistance. Figure 3.13 shows that the average load-displacement between two peak loads can be classified in terms of increasing magnitude as: PUR foam, hexagonal, hexachiral, re-entrant and DAH core sandwiches. Conversely, the indentations are sorted in descending order in the same manner. The results indicate that cores have a significant role as much as the composite skins on the impact resistance of the sandwich panels considered in this work.

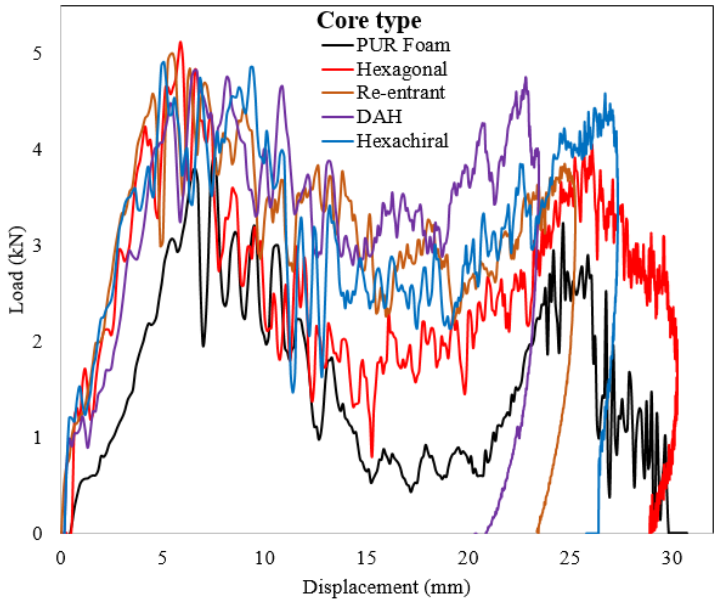

Figure 3. 13 : Load vs. displacement curves of the sandwich panels with: PUR foam (black), hexagonal (red), re-entrant (brown), DAH (purple) and hexachiral (blue) at the 76 J impact energy.

3.2.5.3 Impact resistance of samples at different energy levels

The results of the impact analysis were compared in terms of indentation depth, peak load, and efficiency metrics. The indentation depth and the peak load were determined by using the load-displacement curves of the impacted samples. Section 5.2 has shown that the peak load was dominated by the composite skins - unlike the indentation that depended on damage mechanisms belonging to both the core and the composite skins. The higher peak load and the lower indentation depth during impact are essential aspects for the design of crashworthiness devices. Therefore, the crash efficiency of the sandwich panel has been calculated as the ratio between the peak load and indentation depth in equation (3.9):

$$\text{Crash Efficiency (CE)} = \frac{Peak\ Load}{Dent\ depth} \tag{3.9}$$

The parametric analysis here focused on impact energies between 10-76 J on samples with the same relative densities of the sandwich panels with PLA-made honeycomb cores. The wall thicknesses of the hexagonal, re-entrant, DAH and hexachiral cells are chosen as 0.86, 0.65, 0.62, and 0.70 mm for obtaining the same relative density. The rest of the design variables are the same of those present in the tested specimens. Each sample was then simulated at 10, 20, 30, 40, 50, 60 and 76 J of impact energy in order to investigate the impact resistance at different deformation patterns. The results of those simulations are shown in Figures 3.14-3.16.

The PUR foam core has a great advantage over the other cellular core structures in accordance with lightweight. The sandwich panels with cellular core show ~60% increase in mass compared to the ones with foam core. However, the results show that the panels with cellular configuration could withstand impact without perforation for the cases at 10, 20, 30 and 40 J impact energies. In that cases, those panels feature the lower impact resistance in terms of peak load (3.56, 3.74, 3.79, 3.73 kN) and penetration depth (6.01, 9.66, 20.01 and 24.78 mm). The presence of the foam core does not seem to affect the peak load shown in Figure 3.15. The results show that the foam core could provide the better choice for sandwich panels in the case of lower impact energies, in comparison with the PLA-made cellular core ones. However, the PUR foam core used here does not seem to possess an adequate impact resistance over the PLA-made cellular cores due to low density.

The peak loads of any case do not show a noticeable difference with the increase of impact energy, except for the case of 10 J. Figure 3.15 shows that the peak load of the sandwich panel with the hexagonal core is larger than the one provided by the other samples with auxetic honeycombs; this is due to the larger cell wall thickness and contact surface with the composite skins. The peak loads increased when the upper face sheet was perforated (impact energy is equal or greater than 20 J), and the hexagonal core presented higher peak loads, except for the case of the arrowhead lattice. It is evident here that NPR samples do not always possess higher impact resistance in terms of peak load. The peak load is highly dependent on the contact surface and thickness of the cellular structure. One can say that the hexagonal lattice could represent a good choice instead of re-entrant and hexachiral cores when it concerns a larger impact force at lower impact energy. The indentation depth becomes lower for each auxetic sample when impact energy increases. Compared to the hexagonal lattice, the auxetic cores seem to enhance the impact resistance of the sandwich panels under large deformations. The results also show that the sandwich panel with the hexagonal core is almost fully perforated with a 29.5 mm penetration depth. This is further evidence that the hexagonal core may not meet the energy absorption capability under higher impact loads, which is also consistent with similar findings in [27, 29 and 30].

The results show the presence of a reducing crash efficiency for the sandwich panels, and the sample with the hexagonal core loses its superiority over the other cellular lattice structures in terms of crash efficiency as the impact energy increases. The impact resistance of the cellular structures is strongly related to the auxeticity, which becomes apparent under large deformations [37, 38]. In comparison with the other auxetic cores, the re-entrant lattice samples show, however, the worst crash efficiencies. Re-entrant honeycombs could be recommended instead of hexagonal lattices, but only in cases related to large deformations. The arrowhead lattice possesses the maximum rate of increase of the crash efficiency as the impact energy becomes large (Figure 3.16). Arrowhead-based panels possess 25%, 13% and 11% greater crash efficiency than the remaining samples for the case of 50, 60 and 76 J. As a result, the arrowhead core is the configuration mostly recommended for applications involving impacts with large deformations. In the case of the hexachiral core, the results show that this lattice provides the best performance at 10, 20 and 30 J, and also

possesses advantages over the other cellular configurations (except for the arrowhead core) in the case of 40, 50, 60 and 76 J impact loading.

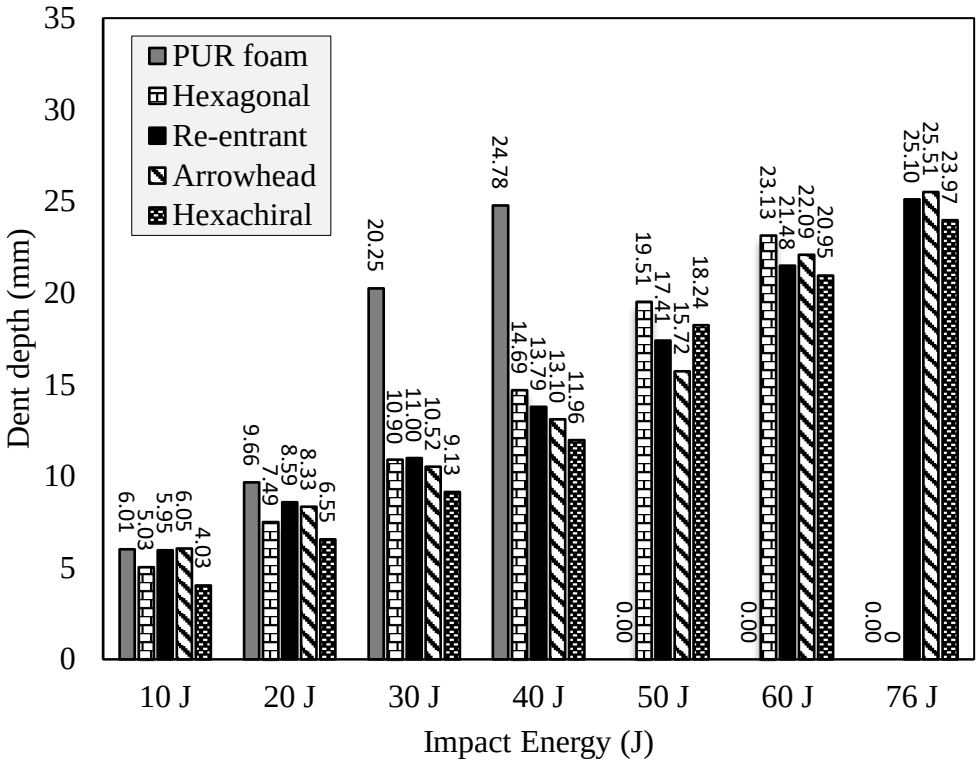

Figure 3. 14 : Relationship between impact energy and dent depth.

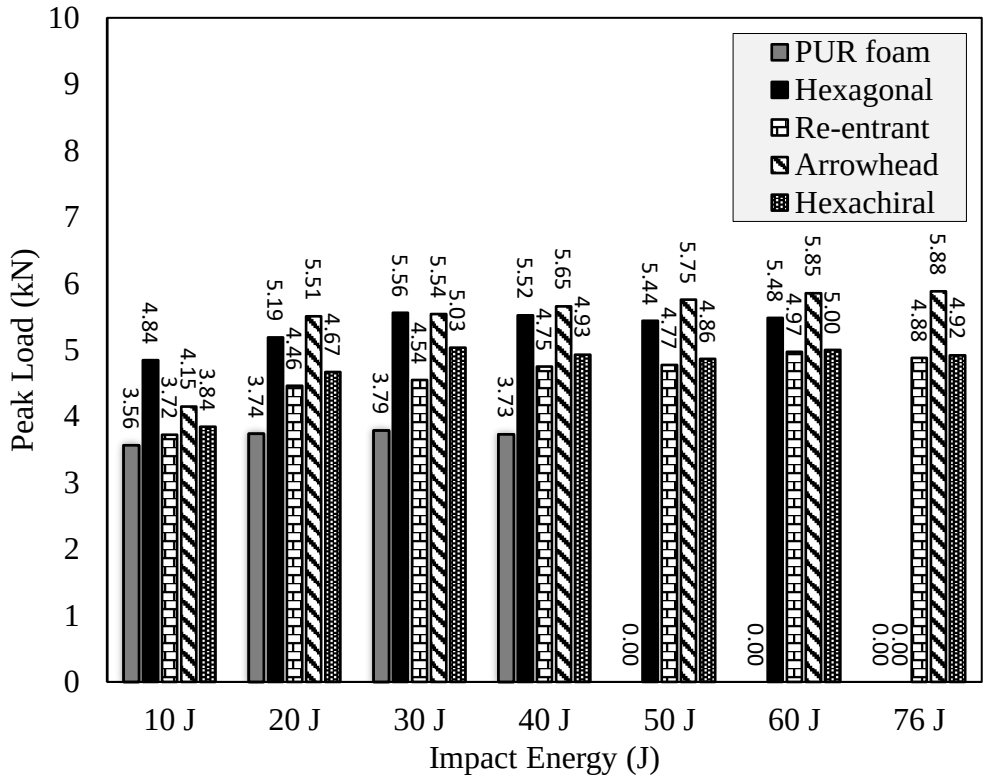

Figure 3. 15 : Relationship between impact energy and peak load.

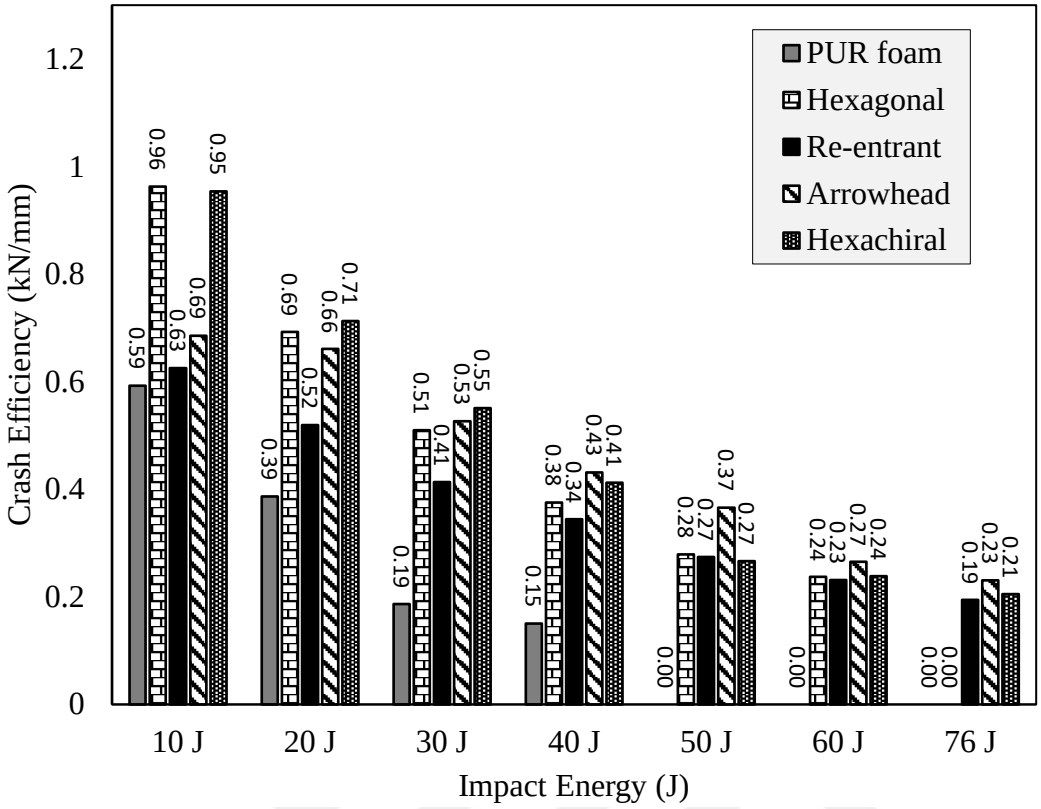

Figure 3. 16 : Relationship between impact energy and dent depth.

3.2.5.4 The effects of design parameters on the impact resistance

The comparison of impact resistance performances at different impact energy levels shows that the DAH core sandwiches possess a superior compressive crashworthiness performance compared to the other configurations. Therefore, the parametric analysis was here focused on the sandwich panel with the DAH core with varying the thickness of laminates and stacking sequences of the face sheets and the half re-entrant angles of the struts AB and BC in Figure 3.1c. The FE analyses were performed at impact energy of 50 J where the crash efficiency of the DAH core over the other cores becomes noticeable (~25% larger). The results were listed in Table 3.2. The stacking sequences of the laminates are chosen as [0/45/90], [45/90/0] and [90/0/45] where the crash efficiencies were calculated as 0.96, 0.94 and 0.91 from the simulations. The results show that changing the stacking sequence of the composite skins could have partially effective on the low-velocity impact resistance. The crash efficiency metric was divided by the relative densities of the sandwich panels to take into consideration weight discrepancies. In Table 3.2, it is seen that the normalized crash efficiencies of the sandwich panel with the laminate thickness of 0.35, 0.40 and 0.45 were are 0.96, 1.02 and 1.19 where the rate of increases in efficiency are 6% and 18%, respectively.

Then the effects of design parameters of the DAH core were investigated by varying θ_2 (28.5^0, 31^0, 33.5^0, 36^0 and 38.5^0), which affects the Poisson's ratio. The crash efficiencies of the sandwich panel with DAH core show a reducing trend (0.98, 0.95, 0.96, 0.86, 0.84) when θ_2 increases due to lower relative density.

Table 3. 2 : The FE analysis results of the DAH core sandwiches based on design parameters of face sheet and core structure.

θ_2	t (mm)	Stacking Sequence	Normalized Crash Efficiency (kN/mm)
28.5	0.35	[0/45/90]	0.98
31.0	0.35	[0/45/90]	0.95
33.5	0.35	[0/45/90]	0.96
36.0	0.35	[0/45/90]	0.86
38.5	0.35	[0/45/90]	0.84
33.5	0.35	[45/90/0]	0.94
33.5	0.35	[90/0/45]	0.91
33.5	0.40	[0/45/90]	0.94
33.5	0.45	[0/45/90]	1.19

3.2.6 Conclusion

In this work, we have presented the low-velocity impact resistance of composite sandwich panels with different types of auxetic and non-auxetic cellular prismatic lattices in experimental and numerical view. The results were compared with the impact resistance of a foam core sandwich panel. CFRP composite face sheets, PUR foam and PLA-made cellular cores with the hexagonal, re-entrant, DAH and hexachiral unit cell topologies have been manufactured, and their material properties determined by using tensile and compression tests. Drop weight tests were carried out at an impact speed of 2.6 m/s and impact energy of 76 J. FE models were also developed and their results validated with the experiments. Impact damage morphologies of each sample were observed and discussed by considering the effects of the deformation mechanisms on the impact resistance of the panels.

The impact resistance of the sandwich structures was parametrically simulated at impact energies of 10 J, 20 J, 30 J, 40 J, 50 J, 60 J and 76 J. The results were compared in terms of peak load, indentation depth and crash efficiency. The effects of the stacking sequence of the face sheet, laminate thickness and cell wall angle of the core were evaluated. The main conclusions that we can draw from this work are:

- A composite sandwich panel with a PUR foam core could provide a good choice for a lightweight structure in the case of lower impact energy considered in this

study. However, this type of sandwich panel could not withstand the full penetration of the striker when the impact energy increases. This is due to the lower impact resistance of the PUR foam core.

- Sandwich panels with hexagonal honeycombs also possess advantages in terms of impact resistance at lower impact energy levels (impact energy is equal to 10 J). This is particularly true when comparing their performance against re-entrant and DAH core panels. However, in the case of higher impact energies, the sandwich panels with auxetic configurations provide a greater resistance under large deformation because of the increasing amount of material flowing into the impact region and local densification.
- The DAH core composite sandwich panels possess the maximum rate of crash efficiency as the impact energy increases. Besides, the hexachiral core is the configuration that provides the best topology to work at small deformations. Only the arrowhead works better than the hexachiral at large deformations.
- The impact resistance of the best core design could be improved by changing other design parameters, such as the face sheet stacking sequence, laminate thickness and cell wall internal angle of core.

3.3 High-velocity Impact on the Doubly Curved Sandwich Panels

This work proposes to indicate how they affect the high-velocity impact behavior of the doubly curved CFRP sandwich panels. Here, open cellular core topologies (re-entrant lattice) and polyurethane lightweight foam core structures have been studied.

3.3.1 Design and manufacture methodology

In this study, spherical doubly curved sandwich panels were manufactured with the dimensions of 250-mm radius, 30-mm core thickness, 1.05-mm face sheet thickness, and 150x150 mm planar surface seen in Figure 3.17. The test specimens were clamped with 200x200 mm spherical frames by screwing on the corners to the test rig. Two strain gauges located 75 mm from the panels lateral edges were used for the lower surface of sandwich panels with the impact loading in order to determine the small deformation pattern seen in Figure 3.17. In the experiments, CFRP face sheets were bonded with two different cores that are PLA plastic cellular auxetic and PUR semi-reticulated non-auxetic foam structures. The specimen preparation can be divided into

four processes: 1) manufacturing composite face sheets, 2) 3D printing PLA plastic core designs, 3) preparation PUR foam core, 4) bonding face sheets and core structures.

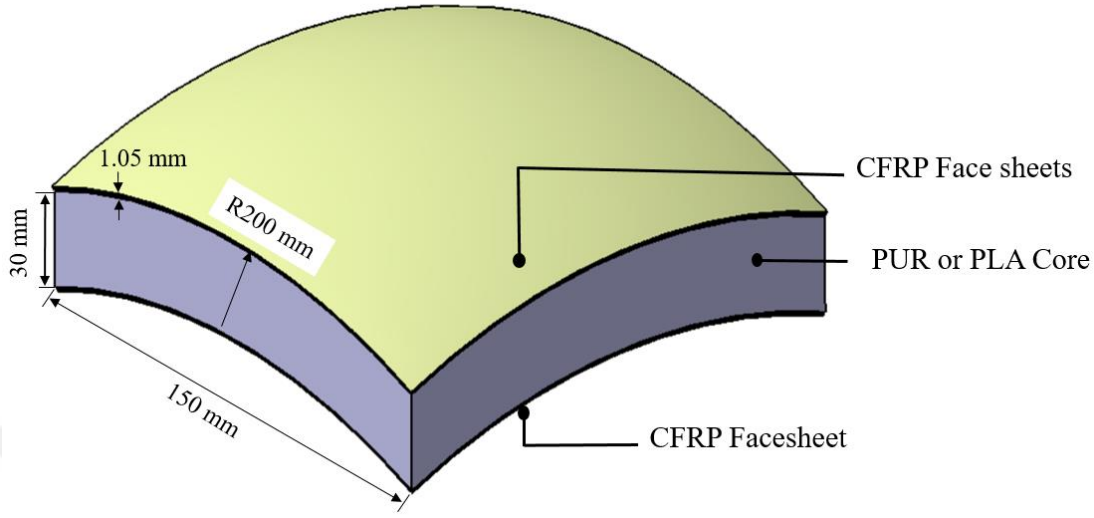

Figure 3.17 : Schematic of the doubly curved sandwich panel.

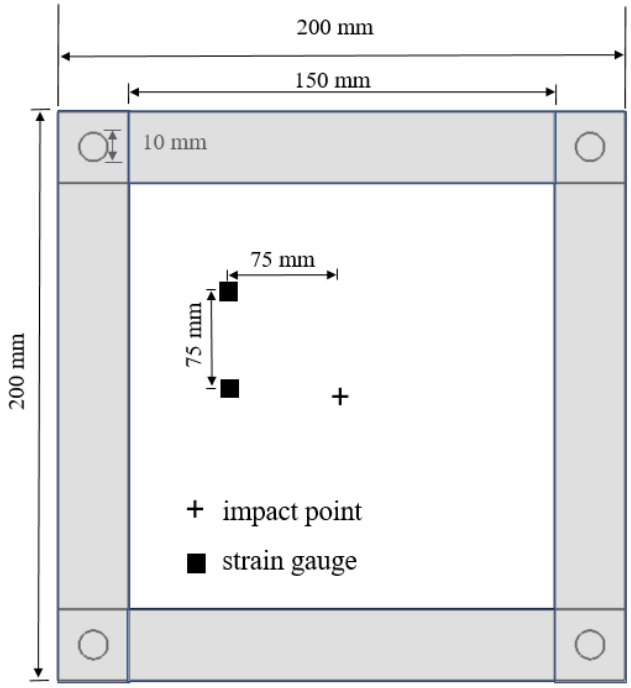

Figure 3.18 : Specimen dimensions and position of strain gauges and impact point.

3.3.2 Doubly curved PLA plastic core

Doubly curved re-entrant cores were printed by using a 3DTurk machine based on the fused deposition modeling method (Figure 3.19a). The CAD model in Figure 3.19b was imported into the Repetier 3D printer slicing software. This software converted

the stl into a gcode file by selecting two outer shells wit 100% filling ratio. Specimens were printed at 215 ^{0}C extruder temperature 0.2 mm layer height.

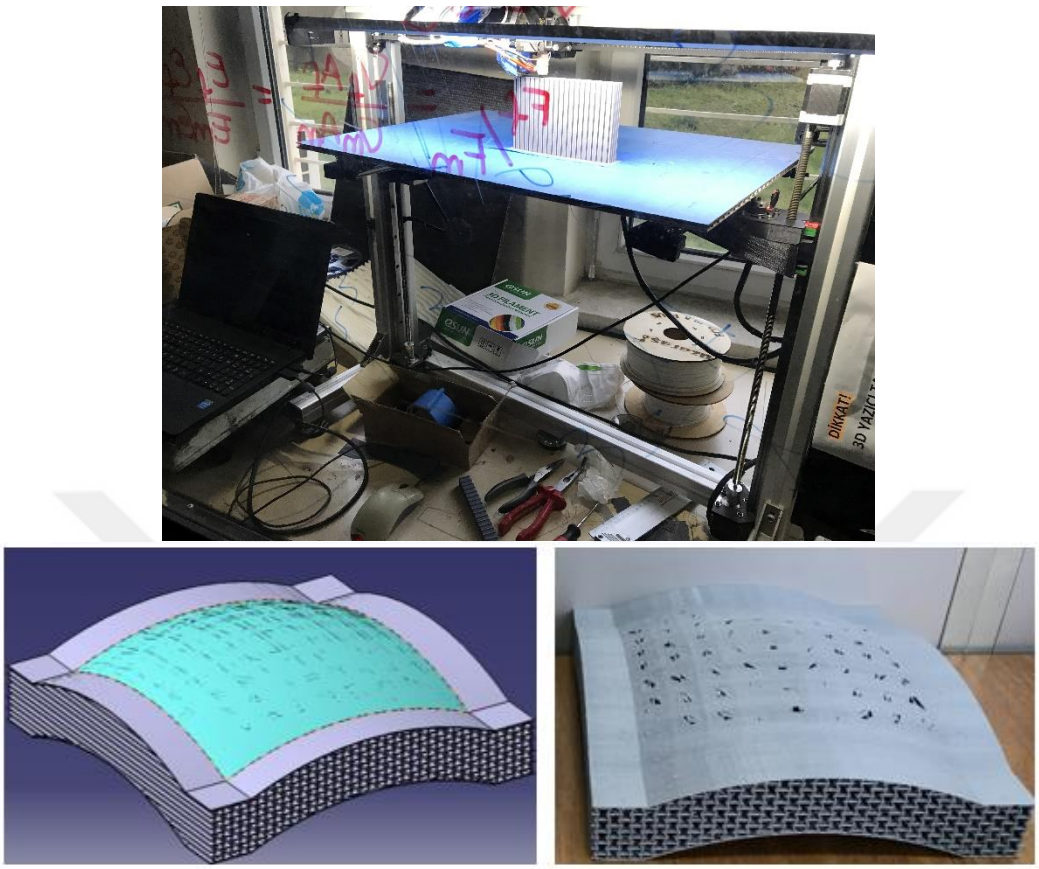

Figure 3.19 : 3D printing of doubly curved re-entrant core.

The design parameters of the re-entrant unit cells are as the thickness t of the struts, the length l of the inclined strut, the length h of the horizontal strut, and the cell wall angle θ (Figure 3.1a and Figure 3.1b). The dimensions of those parameters used for the 3D printed samples are h=6 mm, t=0.7 mm, l=3.9 mm, and θ= 30°. The relative density of the honeycomb and re-entrant unit cell is given by equation (3.1) [54, 85].

3.3.3 Doubly curved PUR foam core

Semi-reticulated cellular rigid polyurethane foam is an ideal core material thanks to its great energy absorption ability and lightweight. The PUR foam with the components of organic resins of polyol and isocyanate (ESPOL Sponge and Chemical Industry Ltd. Co., Turkey) were processed by using the CNC 3-axis milling machine shown in Figure 3.20. The rectangular PUR foam cores were processed at 2000 rpm rotational speed of the milling machine to ensure smooth surfaces.

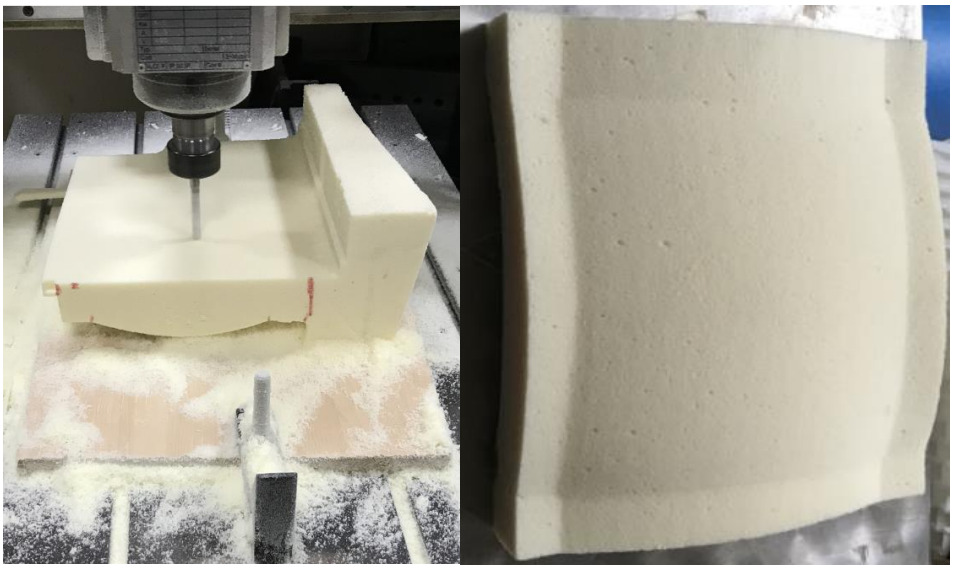

Figure 3.20 : CNC processing of doubly curved PUR foam core.

3.3.4 Doubly curved composite face sheets

Composite face sheets were manufactured with the wet/hand lay-up method, and the doubly curved mould made of aluminum alloy with the same radius were processed by using the CNC machine. The edges of mould were tempered to the assembly of face sheets onto the gas gun test system seen in Figure 3.21. The Planar area of the target surface is 150x150 mm, and the remaining parts at four edges with a width of 25 mm were considered for the connection of the specimens to the test system.

Figure 3.21 : Manufactured spherical mould by using CNC machine.

In Figure 3.22, essential materials are listed for wet/hand lay-up manfacturing process as below:

1. peel ply
2. nylon
3. blanket
4. carbon fiber fabric
5. ROBUSO EC Cutter
6. MSG lamination epoxy hardener
7. MSG lamination epoxy resin
8. brush
9. stirring rods

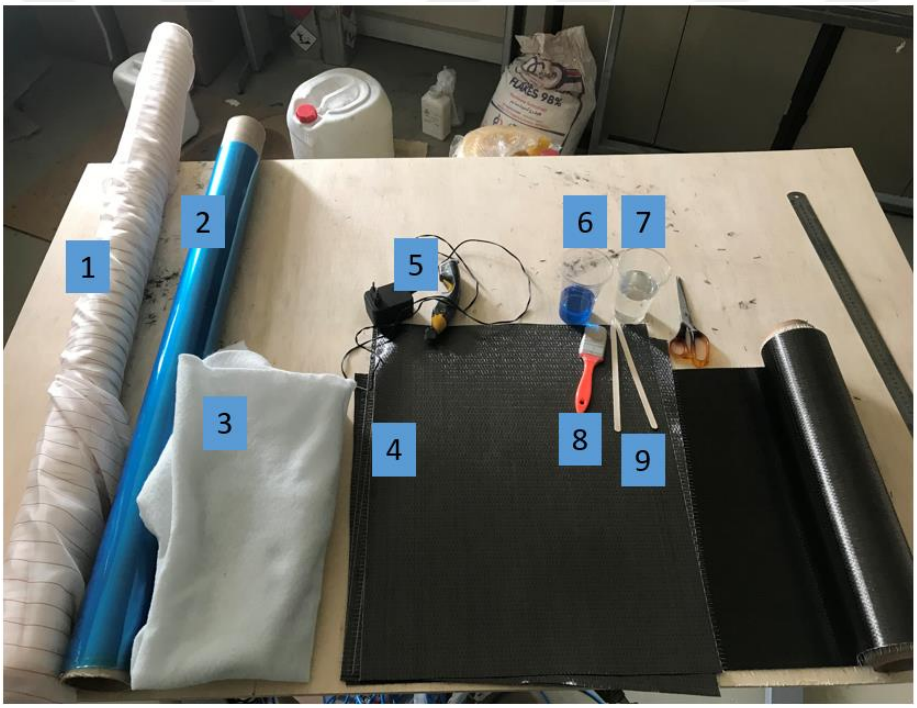

Figure 3.22 : List of essential materials for wet/hand lay-up method.

Carbon fiber fabrics were cut by using the Robuso EC cutter. The Raku tool AC9102 wax based mould release agent were implemented on the dry and polished surface of mould and then composite fabrics were placed on the mould. The carbon fiber fabrics were impregnated with the epoxy resin by hand, and peel plies were laid on the fabrics to provide clean and smooth surfaces. The Heatcon vacuum press test machine was used to cure the epoxy resin and ensure a uniform flatness on both sides of the face sheets. Vacuuming and blanket drained the residue of epoxy resin in Figure 3.23. The

curing stage was carried out at 45 ^{o}C temperature for 16 h. The cured panels with a thickness of 1.05 mm and a fiber volume fraction of 57% were used as top and bottom face sheets of sandwich structures. Each face sheet consists of three plies with the [0/45/90] stacking sequence.

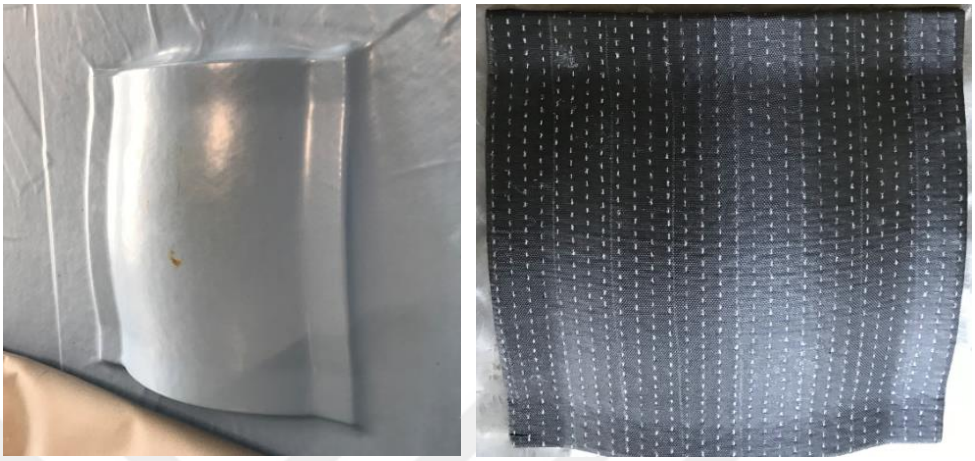

Figure 3.23 : Vacuumed composite fabrics with mould (left) and a manufactured doubly curved composite.

3.3.5 Test set up

High-velocity impact tests were carried out by using an air gas gun machine capable of 40-bar compressed air. The main components of our machine are pressure tank, solenoid valve, compressor, chronograph, data acquisition system, frames, safety box, barrel, barrier, computer etc. in Figure 3.24. It is actuated with a high-speed solenoid valve used for ballistic tests. The data acquisition system consists of 48 channels, and each has a 24-bit A/D converter, 12 bit / 50 mA bipolar sensor supply outlet, and 25000 Hz sampling rate capability. Shooting Chrony Alpha Chronograph is used to detect the speed of the projectile at the exit of the barrel. It consists of two sensors and the capacity to measure the speed in the range of 30 – 7000 fps with less than 0.5% error margin. The 10-mm diameter of spherical steel projectiles were located into the sabots in order to reduce the bullet deviation and prevent the structural damages of the barrel during the test. Therefore, sabots were preferred here as Kestamid (Cast Nylon-Cast Polyamide-PA6G) and Delrin® acetal homopolymer (Polyoxymethylene POM). Both were examined at the same test conditions. Comparing to test results, we decided to use kestamid as sabot material, which can enable axisymmetric deformation patterns and less bullet deviation, unlike delrin ruptures in Figure 3.25.

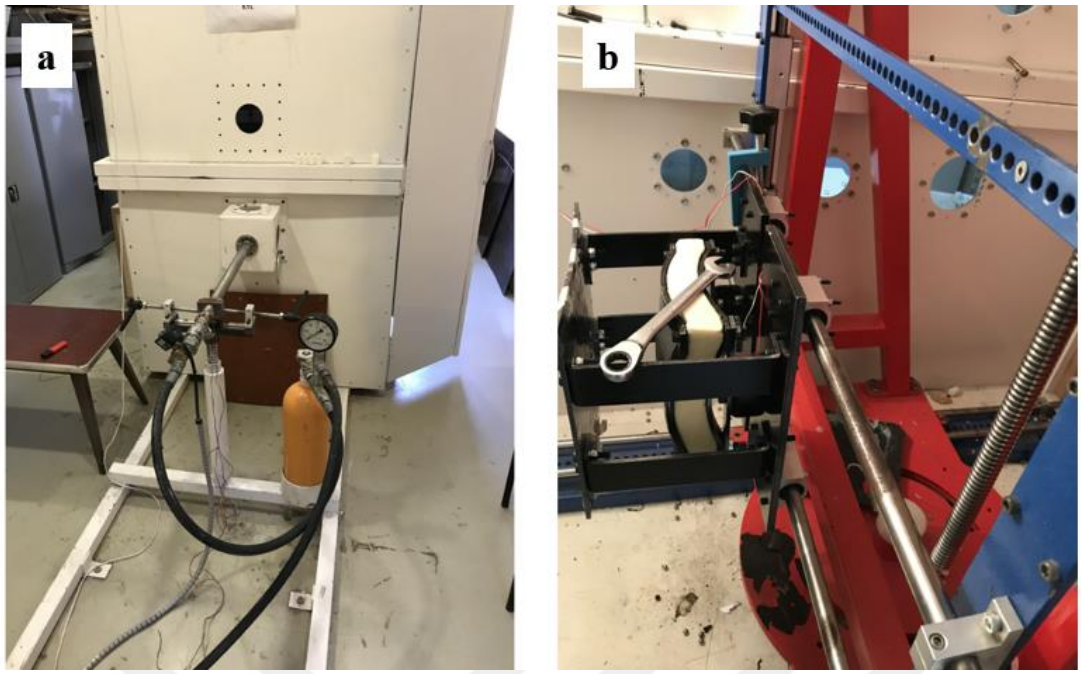

Figure 3.24 : Gas gun test machine a) safety box, barrel, gas tank, solenoid valve b) inner of safety box, and test specimen.

Figure 3.25 : Kestamid and Delrin sabots.

Frames and fasteners of the gas gun were renewed considering the connection surface of the specimens. Frames were designed and produced with the same radius of curvature of the sandwich panel. The connection parts were also reproduced to keep the test specimens in the desired position. A barrier was placed 100 mm far from the front-end of the specimen by screwing on four plates that are connected to the test rig (see, Figure 3.26). 20 mm of the hole was drilled on the center of the barrier, which eliminates the test if the projectile path deviates from the impact location in Figure 3.27.

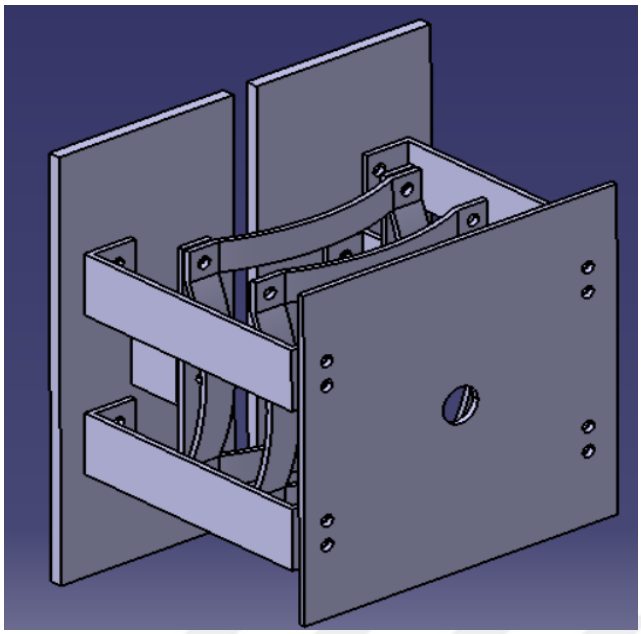

Figure 3.26 : Design of test frames and connection parts.

Figure 3.27 : Design and manufacture of test frames and connection parts.

To connect the specimen to the test rig, first, the specimen and test frames are compressed with dog wrenches, and corners of the panels were drilled by using an upright drilling machine. Then they were screwed on the test rig seen in Figure 3.28a. Figure 3.28b indicates the test room before the impact test of a foam core sandwich panel.

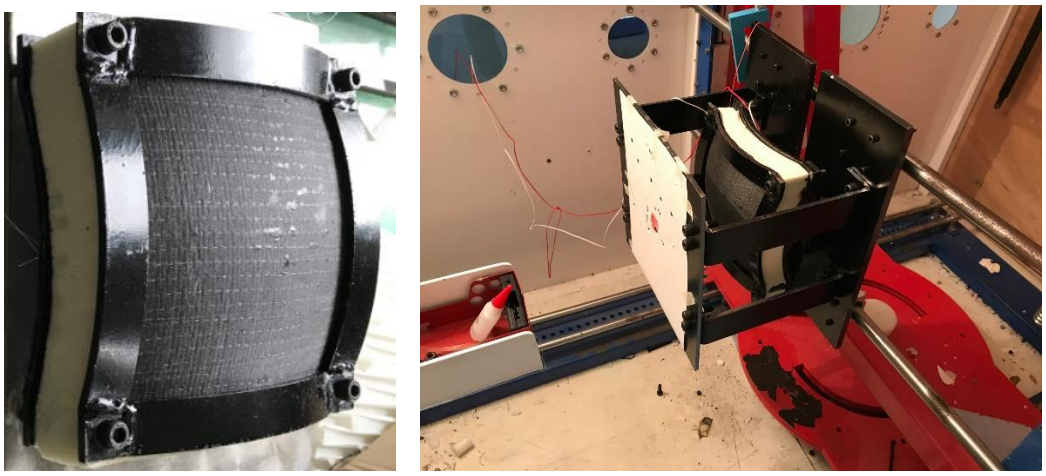

Figure 3.28 : Composite panel (left) and test room (right).

BF series of biaxial strain gauges with a 120-ohm resistance (TML, Tokyo Measuring Instruments Laboratory Co., Ltd) were connected on the back surface of the sandwich panels. Before wiring for the connection of strain gauges and data acquisition system, the resistance of cables were checked by using voltmeter in Figure 3.29.

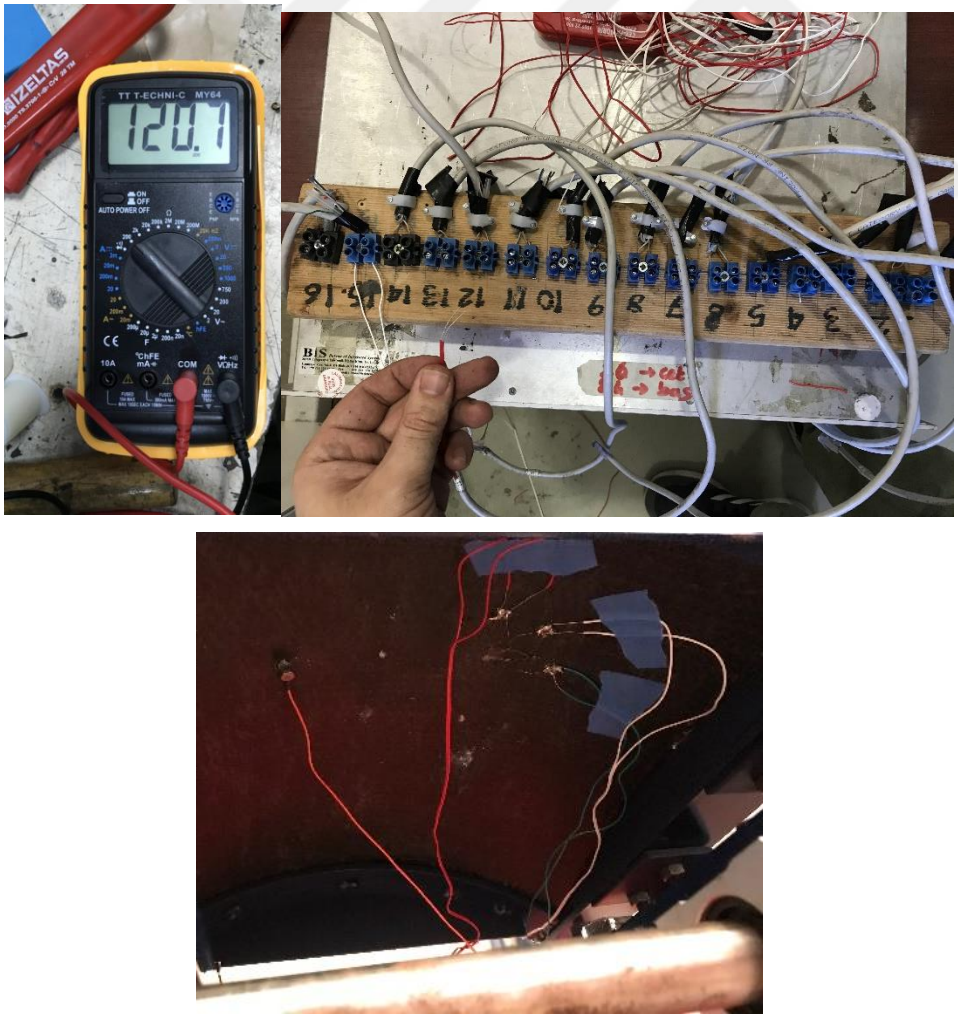

Figure 3.29 : Data acquisition system and strain gauge connection.

3.3.6 Impact tests on doubly curved sandwich panels

In the experimental studies, a 10-mm diameter spherical steel projectile was launched to the center of the specimens with a speed of 100 m/s. The pressure tank was charging with 17-bar compressed air before the tests and released via the solenoid valve. Three identical specimens for PLA and PUR core sandwich panels were tested at the same conditions. The deformed shapes of the specimens were shown in Figure 3.30 and Figure 3.31. Projectile penetrated into the specimens with localized in-plane deformation.

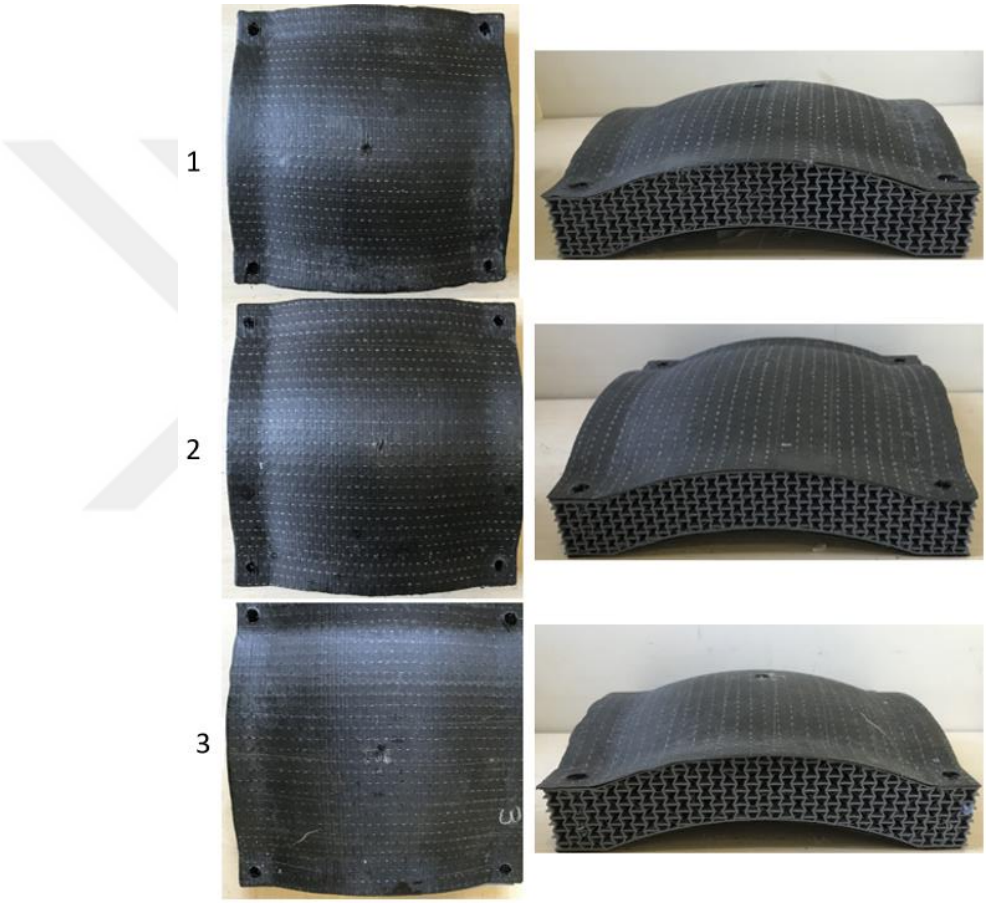

Figure 3.30 : Top and sectional views of tested doubly curved sandwich panels with re-entrant core.

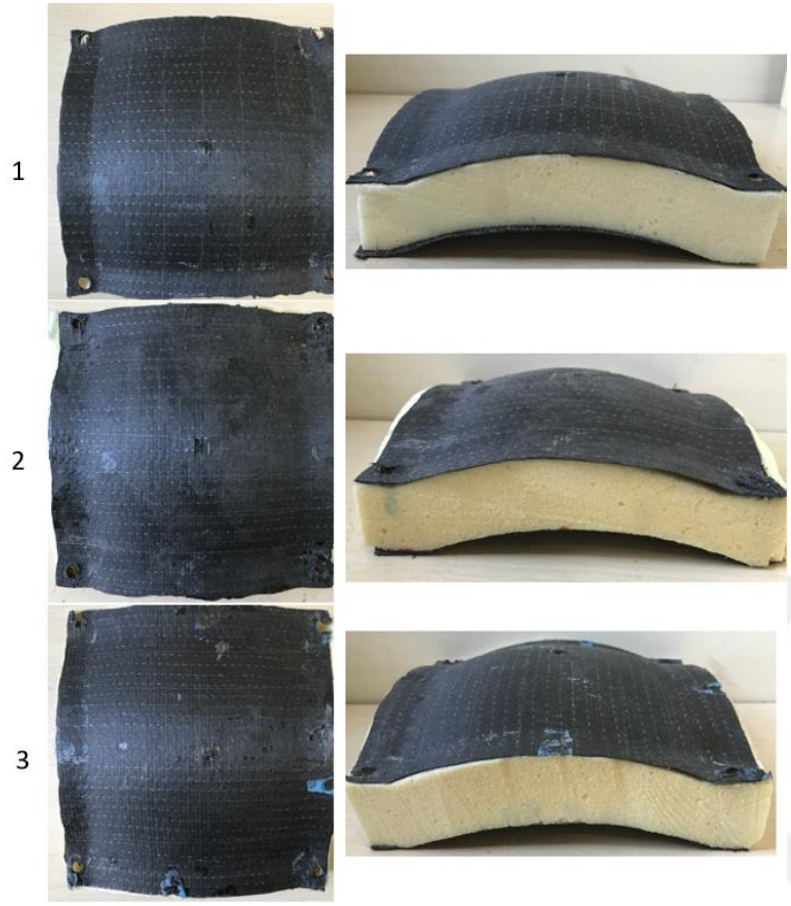

Figure 3.31 : Top and sectional views of tested doubly curved sandwich panels with foam core.

3.3.7 Finite element modeling

The FE models were developed by using the LS-DYNA software to simulate the high-velocity impact behavior of the specimens. The spherical steel projectile was impacted on the center of specimens with a speed of 100 m/s. In the modeling, the nodes on the corners of the sandwich panels were selected as boundaries. The material properties of the projectile were implemented into the 'MAT20 rigid material model. The 'MAT24 piecewise linear plasticity' material model was used to define the material properties of the PLA-made lattices. Similarly, the material properties of the PUR foam obtained experimentally were implemented into the 'MAT63 crushable foam' material card. Belytschko-Tsay explicit shell elements consisting of five DOF in local coordinate system yield globally 6 DOF were adopted to the CFRP composite panels. The MAT54 'Enhanced Composite Damage' in LS-DYNA was utilized to simulate damage progression of composite panels under dynamic loading. FE element models of doubly

curved sandwich panels with re-entrant and foam core structures were indicated in Figure 3.32.

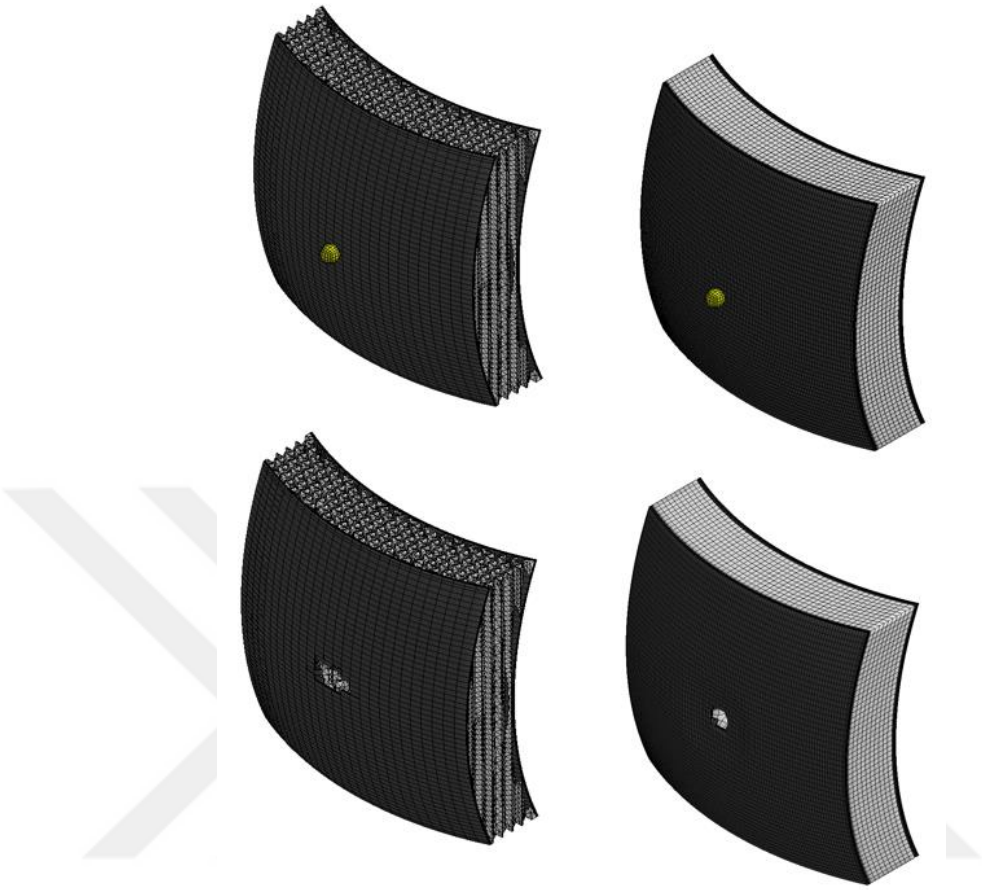

Figure 3.32 : Finite element models and damaged mechanism of the sandwich panels with re-entrant (left) and foam core (right).

3.3.8 Results and discussion

The strain values measured by using strain gauges were recorded via the data acquisition system. The strain changes in time were plotted for each test considering two directions of bi-axial gauges. Figure 3.33 indicates that the results of re-entrant core sandwich panels are between 6-20 strains. Figure 3.34 indicates that the peak strains of the foam core sandwich panels were between 10-60 strains. The cable connection of the Test-3_X was failed during the test. The results showed that there are significant discrepancies between the identical tests comparing to strain values. The foam core sandwich panels have greater strains than re-entrant sandwich panels due to larger penetrations.

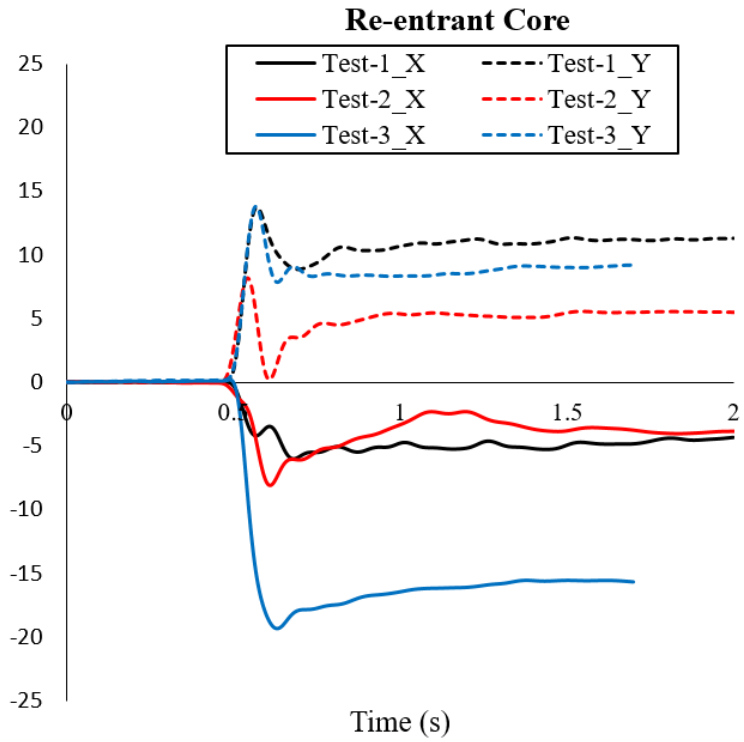

Figure 3.33 : Strain vs time curves of tested sandwich panels with re-entrant core.

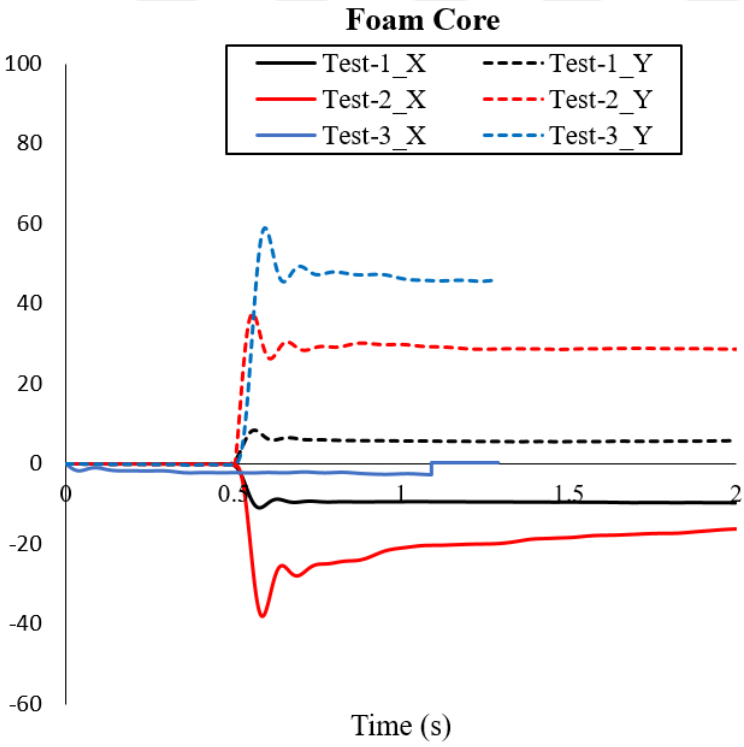

Figure 3.34 : Strain vs. time curves of tested sandwich panels with foam core.

The penetration depth of the projectile was measured by using caliper in the experiments. Then, flat and doubly curved sandwich panels possessing the same core materials, unit cells, and thickness were analyzed by using LS-DYNA in order to show

the effects of curvature. Impact speed and penetration depth of the projectile from the tests and FE analyses are listed in Table 3.3. The results show that the penetration depth of the re-entrant core sandwich panel is greater than flat re-entrant sandwich panel, unlike flat foam core sandwich cores are fully perforated and doubly curved foam core sandwich panels are not.

Table 3.3 : Penetration depth of the tested and analyses doubly curved sandwiches.

Core Type		Impact speed (m/s)	Penetration depth (mm)
Doubly curved Re-entrant	Test 1	101.2	16.06
"	Test 2	100.8	16.12
"	Test 3	99.3	15.90
"	FE model	100.0	18.83
Flat Re-entrant	FE model	100.0	15.96
Doubly curved Foam	Test 1	100.9	23.15
"	Test 2	102.5	27.93
"	Test 3	101.9	36.35
"	FE model	100.0	33.48
Flat Foam	FE model	100.0	Fully perforated

3.4 Single and Doubly Curved Sandwich Panels- A parametric Analyses Under Projectile Impact

In this work, we examine the impact behavior of single and doubly curved structures with auxetic cores by using numerical methods. We have evaluated twelve different doubly and one single curved panels impacted by a spherical projectile at a velocity of 100 m/s. The results are firstly discussed by considering the effects of the curvature on the backplane displacement and the energy absorption of the panels. A selected toroidal configuration is then modeled as the sandwich structure with an auxetic (re-entrant) core and a spherical projectile is shot on different locations from the center to edge. The sandwich structure is made by carbon fiber/epoxy laminates, while the re-entrant core is represented with ABSplus plastic. It is found that the damaged area of the auxetic core differs from a traditional honeycomb under impact loading, and this is mainly due to its negative Poisson's ratio. The investigation of the dynamic impact behavior of doubly curved sandwich panels with auxetic core and carbon/epoxy face sheets has not been presented before in open literature.

3.4.1 The geometry of single and doubly curved panels

The doubly curved surfaces are investigated and classified according to Gaussian curvatures. The impacted surface is extracted from the surfaces of torus, ellipsoids, spheres and cylinders. Twelve different doubly curved panels and one single curved panel are analyzed by using LS-DYNA software. The results of the analyses are compared in terms of maximum backplane displacement and absorbed energy of the panels subjected to a spherical steel projectile.

The work here is focused mainly on the geometry of the torus in Figure 3.35. Ten different doubly curved panels extracted from the surface of the torus are classified according to negative and positive Gaussian curvatures coefficients expressed in equations (1.1)-(1.2). Catenoidal (negative Gaussian curvature) and toroidal panels (positive Gaussian curvature) are modeled by selecting path radiuses between 500 and 2500 mm and keeping constant the profile radius as 250 mm. Ellipsoid paraboloid panel is extracted from the surface of an ellipsoid shell geometry as shown in Fig. 1. A, B and C represent the radius of the ellipsoid in three principal axes. The radii of curvatures of A and B are 250 mm and C is 200 mm. The radius of curvature of the spherical panel.

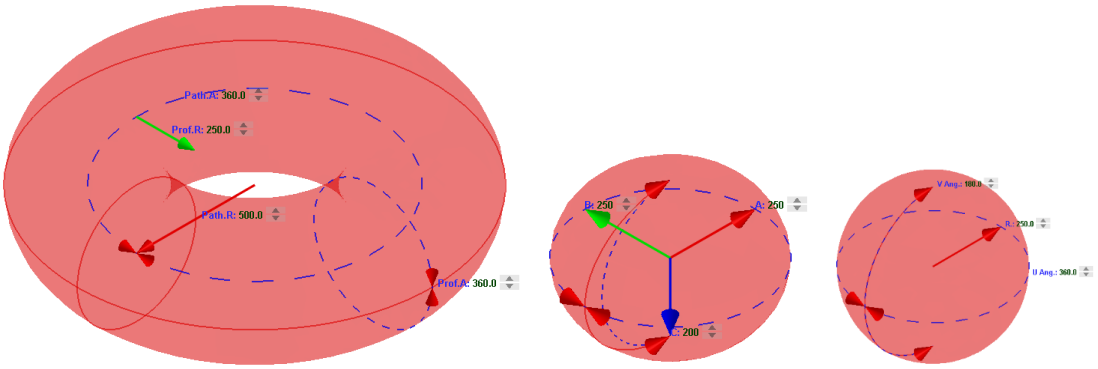

Figure 3.35 : Toroidal, ellipsoid and spherical surface.

3.4.2 Numerical analyses of single and doubly curved shells

In Figure 3.37, the extracted surfaces are indicated. The plan view for each panel is 300x300 mm and thickness is 2.8 mm.

The amount of SEA values and backplane displacements are obtained from the results of numerical analyses in Table 3.4. The results show that the SEA values increase, and the backplane displacements reduce as the radius of curvature is increased.

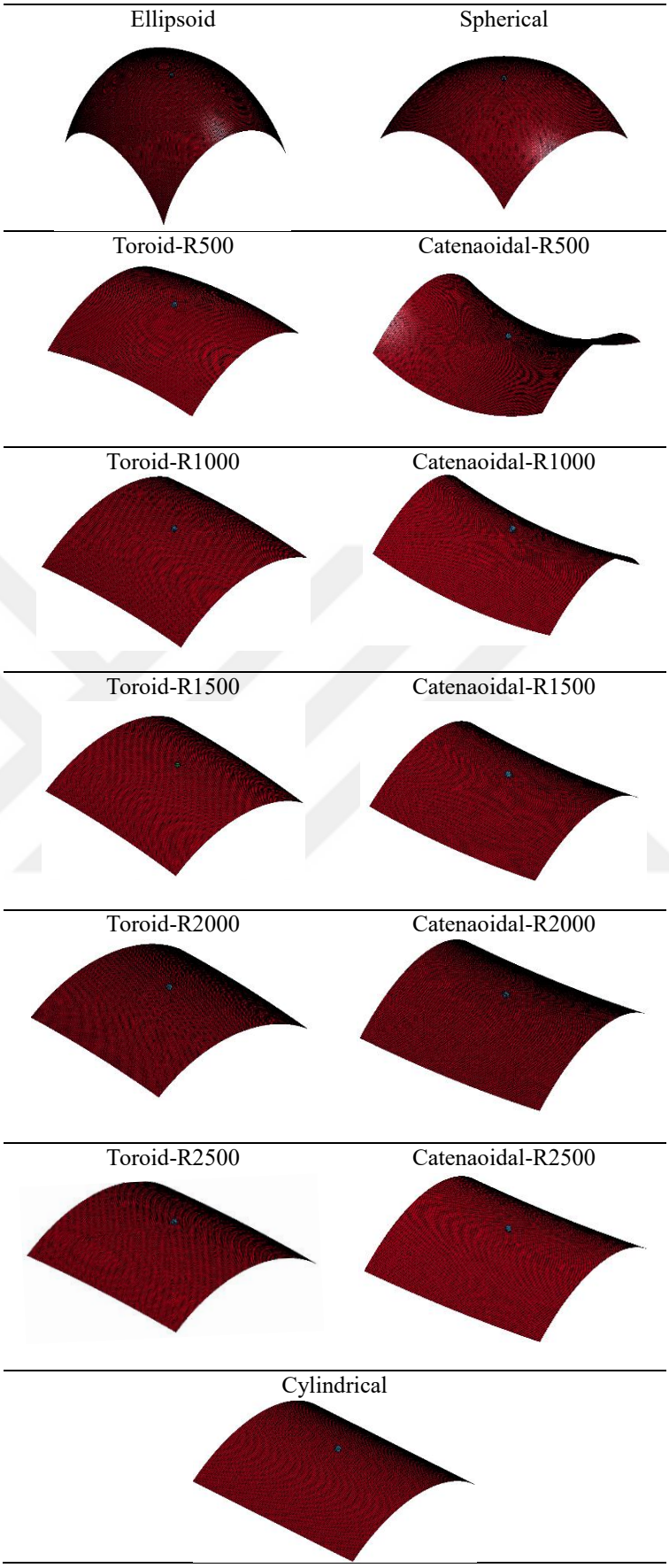

Figure 3.36 : FEMs of curved panels.

Table 3.4 : Results of numerical analyses.

	Mass (kg)	SEA (kg/J)	Displacement (mm)
Ellipsoid	1.231	9.79	15.49
Spherical	1.083	7.84	18.80
Toroidal-500	1.010	9.84	8.33
Toroidal-1000	0.997	9.09	7.58
Toroidal-1500	0.996	12.78	6.55
Toroidal-2000	0.995	14.52	4.60
Toroidal-2500	0.995	13.30	4.57
Cylindrical	0.995	14.75	3.58
Catenoidal-500	1.057	8.97	5.88
Catenoidal-1000	1.001	10.52	4.87
Catenoidal-1500	0.997	12.71	5.47
Catenoidal-2000	0.996	10.29	6.93
Catenoidal-2500	0.995	14.28	3.61

3.4.3 Effects of the impact location on the impact resistance of the toroidal panel

The impact response of a toroidal sandwich panel with the auxetic core is analyzed for a 300 m/s impact velocity of the rigid spherical projectile. Clamped boundary conditions are applied to all nodes at the four edges. The face sheets of the panel are made of four-layers composite CFRPs with $0^0/90^0$ fiber orientations. Automatic surface to surface tie-break contact and Eroding surface to surface contact types are defined between the plies. The profile and path radii of the toroidal panel are 250 and 500 mm, respectively.

The effects of the impact location are investigated by considering nine different impact points. In the first analysis, the center point of the sandwich panel is impacted. After that, four points on the right side of the center and four points on the vertical side of the same center are selected as seen in Figure 3.38. The distance between the two impacted points is 30 mm. The center point is abbreviated as “C”, the points on the right side are abbreviated as “R”, and the points on the vertical side are denominated as “V”. The numbers indicate the distances of the single points from the center of the panel.

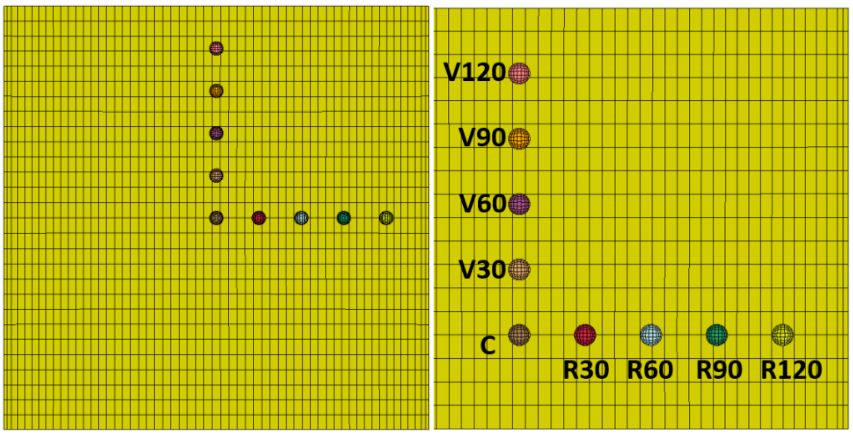

Figure 3.37 : Impacted points on the toroidal sandwich panel.

After performing numerical analyses, the views of the deformed sandwich panels are recorded for each model. Figure 3.38 shows the damaged zones and indentations of the projectiles into the sandwich panels. The indentation size of the projectile is higher for the center, V90, V120 and R120 impact points. The indentation resistance of the toroidal panel on these points is lower than the other configurations.

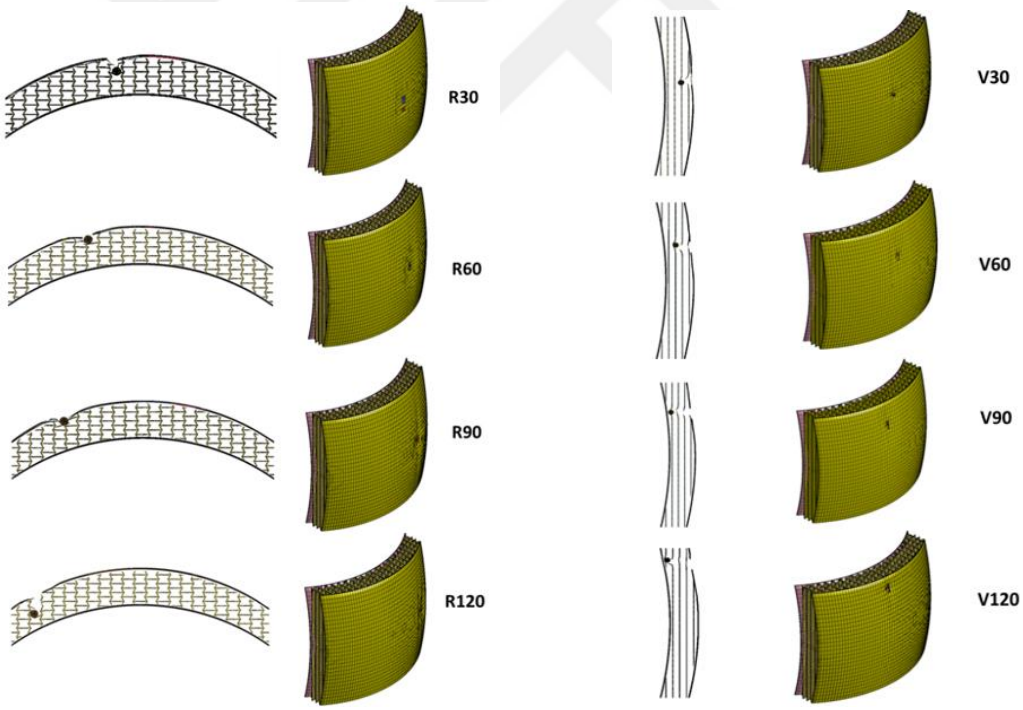

Figure 3.38 : Cross-section and isometric views of damaged sandwich panels.

The absorbed energies of the auxetic core, composite face sheets, total absorbed energy and the indentation of the projectile are shown in Table 3.5. The majority of the kinetic energy is absorbed by the auxetic core structure rather than the composite face sheets. The results show that there is no significant relationship between the amount of absorbed energy and indentation.

Table 3.5 : Results of numerical analyses for toroidal sandwich panels.

Impact Point	Auxetic Core (J)	Composite Face Sheets (J)	Total Absorbed Energy (J)	Projectile Indentation (mm)
Center	97.63	6.37	104.00	35.43
R30	74.39	8.09	82.48	28.32
R60	67.30	17.01	84.31	24.03
R90	80.32	11.27	91.59	20.28
R120	107.30	3.69	110.99	33.55
V30	84.91	13.05	97.96	25.36
V60	88.35	9.35	97.70	33.52
V90	95.06	6.37	101.43	43.66
V120	106.50	7.45	113.95	45.19

3.4.4 Conclusion

In this study, the impact behavior of doubly curved structures is examined by using the LS-DYNA code. First, thirteen different single and doubly-curved shells are analyzed to understand the effects of their curvature. The increase of the radius of curvature of these structures brings a higher resistance against the damage from a projectile impact. A selected toroidal sandwich panel is then parametrically analyzed by impacting the projectile on different points of its surface. The results show that the indentation resistance of the impacted location is lower on the center point and on locations close to the clamped edges. Most of the impact energy is absorbed by the auxetic core rather than by the composite face sheets.

3.5 Effects of Thickness and Curvature on Impact Behavior of Composite Panels

In this study, thickness and curvature effects on high-velocity impact behavior of flat and cylindrical panels are investigated numerically. Four different samples are analyzed by using LS-DYNA software and the results are compared with regard to the absorbed energy, contact force, reaction force on the boundaries, displacement at the center of the backplane surface and residual velocity of the impacting object.

3.5.1 Problem definition

Impact response of flat and cylindrical panels for clamped boundary conditions are analyzed for 50 m/s impact velocity of the projectile. The effects of thickness and layer

number on dynamic responses are investigated. Two different thickness values of 1 mm and 2 mm and two different layer number of 4-layer and 8-layer are considered. 4-layer and 8-layer plate and panel structures have $0^0/90^0$ fiber orientations. In Finite Element (FE) modeling of impact, 'Automatic surface to surface tie-break contact' and 'Eroding surface to surface contact' are defined between plies. The impacted projectile is a 10 mm diameter spherical steel. Panels are made of CFRP material. For the cylindrical panel, the radius is 2000 mm, and the circumferential length is 400 mm. For the flat panel, the circumferential length is 400 mm. The isometric and cross-section view of the FE model of the 4-ply flat and cylindrical panels are shown in Figure 3.39.

Five different mesh sizes are used to determine the proper mesh size. Values of displacements at the center of the rear surface are 4.15, 4.14, 4.13, 4.36 and 4.32 mm for mesh sizes of 6, 5, 4, 3 and 2.5 mm, respectively. According to the mesh sensitivity study, 2.5 mm mesh size was selected for the following FE analysis.

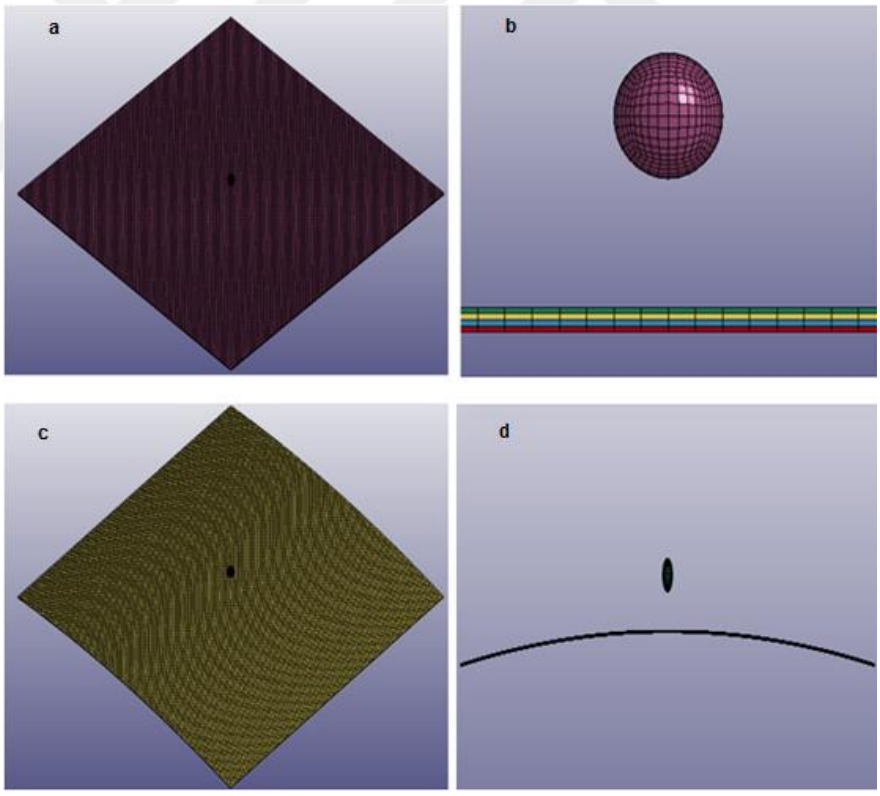

Figure 3.39 : a) Isometric view of 4 ply flat b) cross section view of 4 ply flat c) isometric view of 4 ply cylindrical d) cross section view of 4 ply cylindrical.

3.5.2 Material properties

Material properties of the target panels using in MAT_55 in LS-DYNA are given in the [155]. The CFRP laminates are manufactured from Hexcel's AS4 carbon fibers and 3501-6 epoxy. The material model used for the CFRP laminate is based on the Tsai-Wu failure criterion, which is widely used in the literature. A rigid material model through MAT_20 material card is used for the spherical steel projectile. It requires no calculation of stresses and strains and reduces the computation time.

3.5.3 Results and discussions

The isometric (left side) and cross-section views (right side) of deformed shapes of the 4-ply flat panel are shown in Figure 3.40. The deformed area is localized at the impacted area that looks like a cone shape. The same study is implemented for the other three models. Non-perforated images are obtained from all analyses. To determine the backplane displacement, sixteen nodes at the center of the impacted area are selected, and the displacement values in the normal direction to the panel surface are compared. Results of the analysis are compared with regard to absorbed energy of plies, reaction forces of the nodes selected as boundaries, contact forces between the plies and backplane displacements. The results are close to each other for 4-ply panels. The absorbed energies of the top and bottom plies are higher than the interior plies expressed in Table 3.6. The results of the 8-ply flat panel are different from the other models. The absorbed energy of the 8-ply flat panel model is too low than the others because vibration has a significant effect on the absorbed energy of the other three models.

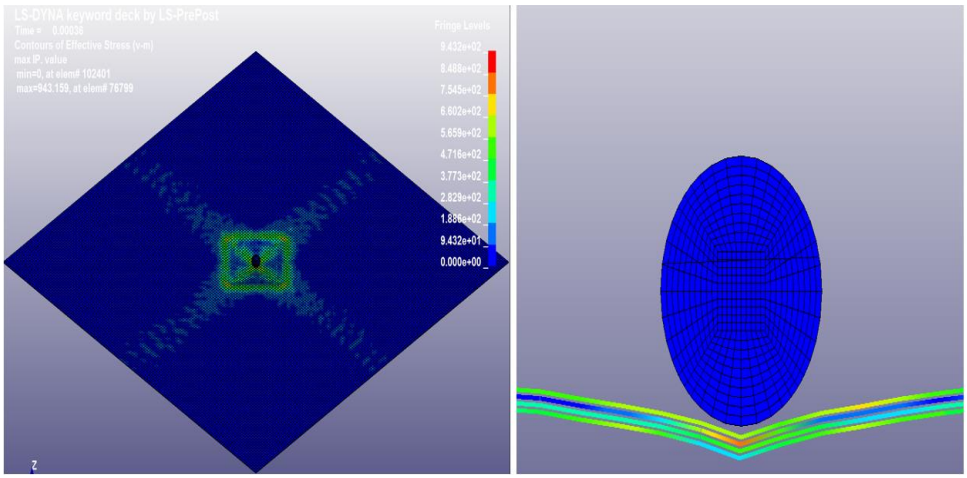

Figure 3.40 : Isometric (left) and cross section (right) view of 4-ply flat panel.

Table 3.6 : Absorbed energy of the samples.

Ply No	4-Ply Flat (J)	4-Ply Cyl. Curved (J)	8-Ply Flat (J)	8-Ply Cyl. Curved (J)
1	1.510	1.610	0.269	3.120
2	1.060	0.879	0.327	1.370
3	0.697	0.726	0.302	0.842
4	1.950	1.913	0.286	0.545
5			0.285	0.505
6			0.300	0.829
7			0.316	1.460
8			0.269	3.200

In Table 3.7, the contact forces between the plies are compared. Contact forces can be effective on the delamination between the plies. If the forces are high, there could be an increase in the delamination. In the cylindrical panels, contact forces look higher than flat panels. In addition, Table 3.8 indicates that displacement values for cylindrical panels are higher than those for flat panels. The deformation of the thinner panel is higher than the thick panel. According to the reaction forces, vibration has more influence on the results. Another result is that residual velocities of the projectile are higher for cylindrical panels.

Table 3.7 : Max contact forces on the master surfaces.

Master	4-Ply Flat (N)	4-Ply Cyl. Curved (N)	8-Ply Flat (N)	8-Ply Cyl. Curved (N)
1	9952	19419	3269	29687
2	14118	20540	3394	42879
3	13158	9802	3405	68806
4			3380	110070
5			3271	103300
6			3272	47308
7			3210	25171

Table 3.8 : Displacement at the centre of backplane, reaction forces on the boundaries and residual velocities.

	Displacement (mm)	Reaction Force (N)	Residual Velocity (m/s)
4-Ply Flat CFRP	4.32	2782	0.87
4-Ply Curved CFRP	5.61	2015	0.49
8-Ply Flat CFRP	2.88	1542	0.83
8-Ply Curved CFRP	3.33	10283	0.52

3.5.4 Conclusion

In this study, the impact behavior of flat and cylindrical composite panels at the high-velocity impact of projectiles was compared for two different thicknesses. The results of analyses were compared and discussed in terms of absorbed energy, contact forces, reaction forces, backplane displacement and residual velocity of the panels.

The findings of this study can be summarized as the following:

- The absorbed energy of 4-ply flat and cylindrical panels are almost the same. On the other hand, the 8-ply cylindrical panel absorbs higher energy than the 8-ply flat panel. It results from the vibration of the cylindrical panel.
- The absorbed energy of the top and bottom plies are higher than those of interior plies except for the 8-ply flat panel.
- Contact forces of the cylindrical panels are higher than those for flat panels. Ply vibration leads to high contact force, especially for the 8-ply cylindrical panel.
- The deformed zone occurs at a local area for flat and cylindrical panels. Penetration values of the projectile for cylindrical panels are higher than those for flat panels.

3.6 Optimization of Cylindrical Curved Composite Panels Using Response Surface Methodology and Genetic Algorithm

In this study, a crashworthiness optimization study is carried out based on the Genetic Algorithm and Response Surface Method, which are used in the solution of this multi-objective optimization problem in order to determine the optimum designs of curved plates under high-velocity impact loading. SEA and backplane displacement are selected as objective functions for evaluating mechanical performance. Here CATIA, Ansys LS-DYNA and MATLAB software are used for design, FE modeling and optimization procedures, respectively

3.6.1 Problem definition

This study presents the effects of curvature and stacking sequences of composite panels under low-velocity impact loading by conducting multi-objective optimization

algorithms based on Response Surface Method and the Genetic Algorithm are developed. Best designs are determined according to the two objectives: higher energy absorption capacity and compressive strength. Cylindrical panels for clamped boundary conditions are analyzed at 10 m/s impact velocity of the projectile. The impacted projectile is a 10 mm diameter spherical steel. Panels are made of UD Hexcel S2 glass fiber prepreg composite material. For the cylindrical panel, the radius is 2000 mm, and the circumferential length is 400 mm. The thickness and surface area of 4-ply cylindrical panels are 2 mm and 400 x 400 mm.

3.6.2 Material properties of UD Hexcel S2 glass fiber prepreg composite

Material properties of UD Hexcel S2 glass fiber prepreg composite specimens have been determined following ASTM D3039/3039M-14, ASTM D6641/D6641M-14 and ASTM D3518/D3518M-13 test standards [151-153]. Tensile and compression tests were performed by using the MTS Universal test machine seen in Figure 3.41. According to the test results, the material properties were listed in Table 3.9.

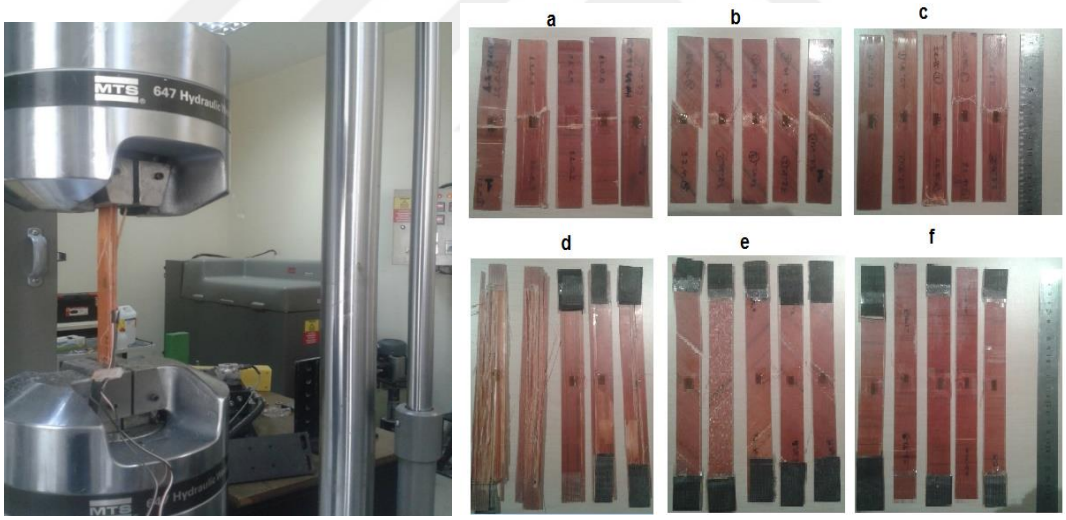

Figure 3.41 : Quasi static tensile and compression tests: a) 0^0 compression, b) 45^0 compression, c) 90^0 compression, d) 0^0 tension, e) 45^0 tension, f) 90^0 tension.

Table 3.9 : Properties of UD Hexcel S2 glass fiber prepreg composite.

Property	Value
Density, ρ (gr/cm^3)	1.85
Longitudinal stiffness, E_1 (MPa)	46120
Transverse stiffness, E_2 (MPa)	12960
Poisson's ratio, v_{12}	0.31
In-plane shear modulus, G_{12} (MPa)	9240
Longitudinal tensile strength, X_t (MPa)	865
Longitudinal compressive strength, X_c (MPa)	807
Transverse tensile strength, Y_t (MPa)	48
Transverse compressive strength, Y_c (MPa)	184
Transverse shear strength, S (MPa)	103

3.6.3 Formulation of the optimization problem

Here, the optimization of the cylindrical composite panel is formulated as a multi-objective constrained optimization problem. Backplane displacement and SEA criteria are used in expressing objective functions expressed as f_1 and f_2, respectively. For optimum crashworthiness design, SEA is increased for a high energy absorption capability, and backplane displacement is reduced for structural integrity and higher impact resistance. The optimization problem is formulated in equation (3.9):

Maximize $\quad F = -f_1 + f_2$

subject to

$$
\begin{aligned}
2 \leq = \frac{\mathrm{r}}{\mathrm{a}} = \leq 10 \\
0 \leq \theta_1 \leq 90 \\
0 \leq \theta_2 \leq 90 \\
0 \leq \theta_3 \leq 90 \\
0 \leq \theta_4 \leq 90
\end{aligned}
\tag{3.9}
$$

where r is the radius of curvature, a is side length, and θ is the angle of ply.

3.6.4 Response surface models for optimization criteria

In this study, RS models are used for backplane displacement and SEA criteria during optimization. In RSM, the polynomial model is selected first to approximate the actual

function. Then, the Design of Experiment (DOE) method is conducted considering the design variables and order of function that is fitted to the created data set. The steps of the RSM is summarized in Figure 3.42.

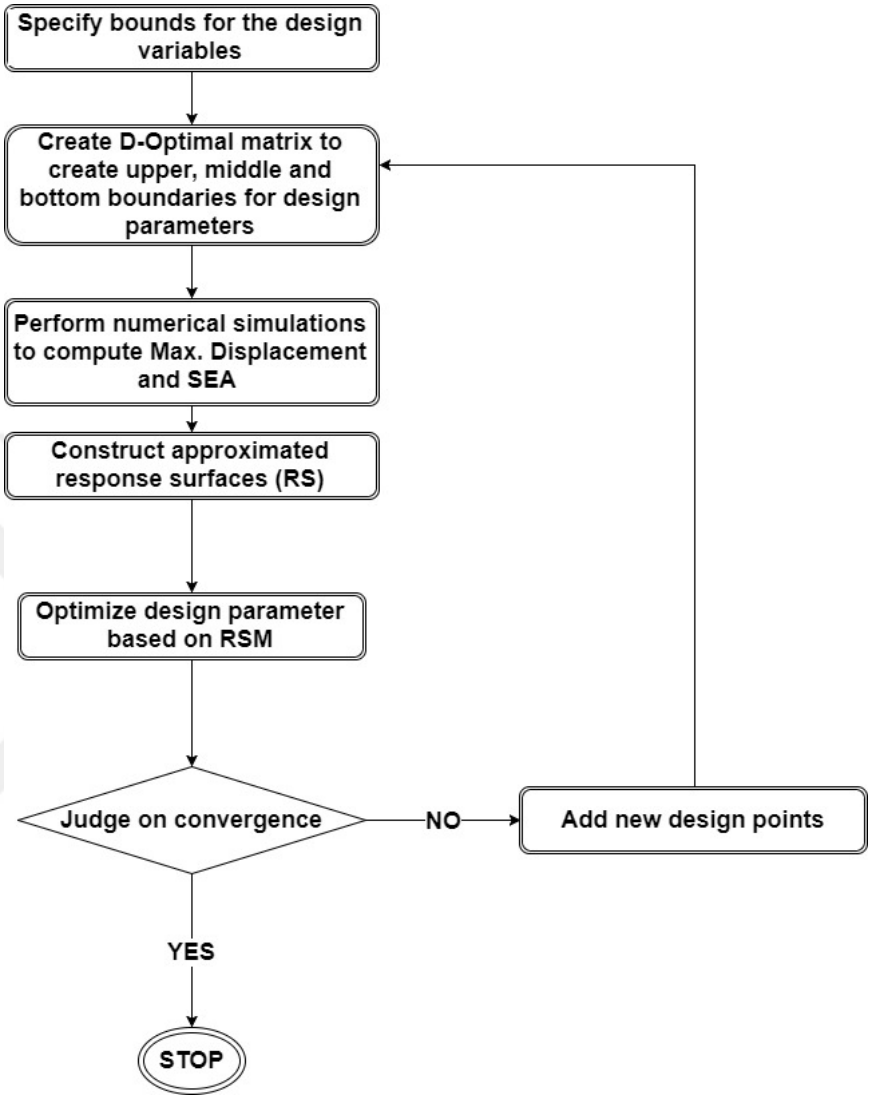

Figure 3.42 : Flowchart of the optimization process.

The subset includes 34 experiments, which is sufficient enough to fit a quadratic function for 5 variables. The ranges of design variables used in creating the DOE table and objective function values are shown in Table 10.

Table 3.10 : Ranges of design variables used in DOE table.

Design Number	r/a	θ1	θ2	θ3	θ4	SEA (J/kg)	Disp. (mm)
1	2	0	90	90	0	0.575	2.067
2	2	90	90	90	0	0.578	1.819
3	2	90	90	90	90	0.565	1.753
4	2	90	0	90	45	0.523	1.819
5	10	90	90	0	0	0.521	1.496
6	10	90	0	0	0	0.513	1.479
7	2	90	90	0	90	0.574	1.889
8	2	90	0	0	90	0.581	1.989
9	2	90	0	0	0	0.597	2.639
10	2	0	0	90	0	0.599	2.533
11	2	45	90	0	0	0.588	2.407
12	10	90	45	90	0	0.504	1.365
13	10	0	90	0	90	0.493	1.357
14	10	0	0	90	90	0.507	1.447
15	10	45	0	0	45	0.526	1.483
16	10	0	0	45	0	0.530	1.561
17	2	90	45	45	0	0.589	2.459
18	10	0	90	0	0	0.501	1.429
19	6	0	90	90	90	0.575	1.515
20	6	0	45	0	0	0.557	1.543
21	10	45	90	45	90	0.516	1.475
22	6	0	0	0	90	0.550	1.510
23	2	0	90	0	90	0.574	1.933
24	10	45	90	90	0	0.510	1.364
25	2	0	0	90	90	0.579	1.986
26	6	90	0	45	90	0.537	1.368
27	2	0	0	0	45	0.608	3.004
28	10	90	0	90	90	0.505	1.360
29	2	45	45	90	90	0.579	1.959
30	10	0	45	90	45	0.508	1.402
31	2	0	90	45	45	0.599	2.359
32	10	90	45	0	90	0.504	1.362
33	6	45	0	90	0	0.544	1.439
34	6	90	90	0	45	0.542	1.421

3.6.5 FE modeling and correlation of RSM and FE results

The FE models were developed by using the LS-DYNA software to simulate impact behavior of the curved specimens. 34 curved composite panels were modeled according to design variables in Table 3.10. A spherical steel projectile was impacted on the center of specimens with a speed of 10 m/s. The stress distribution of a set of selected specimens is indicated in Figure 3.43.

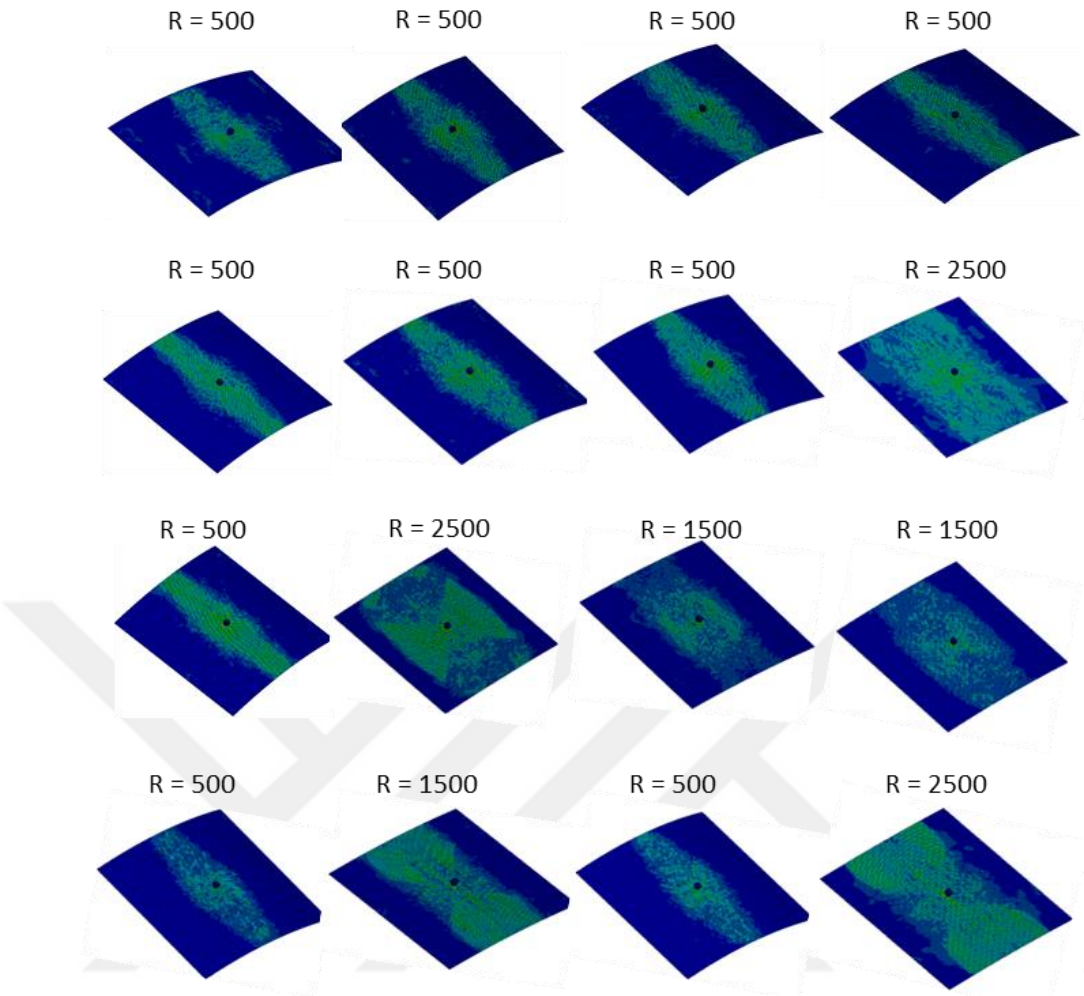

Figure 3.43 : FE analysis of a set of selected curved panels.

Fitted values and actual values for backplane displacement and SEA are compared in Figures 3.44 and Figure 3.5. The results show that there is a good correlation between the RS model and FE results.

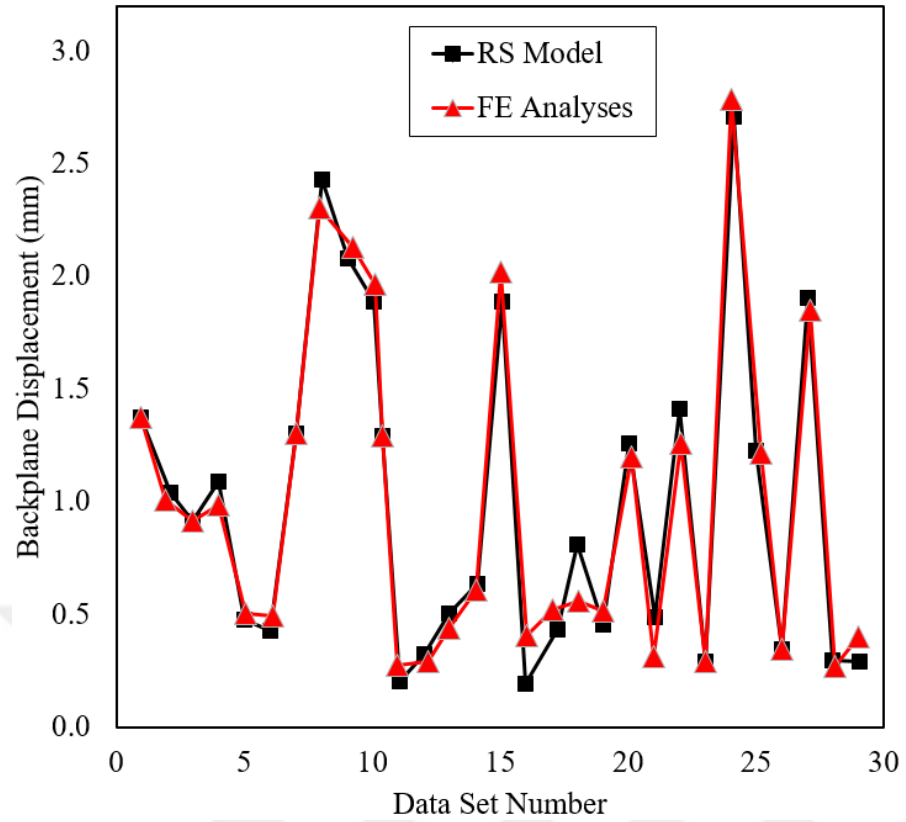

Figure 3.44 : Fitted and actual values for backplane displacement.

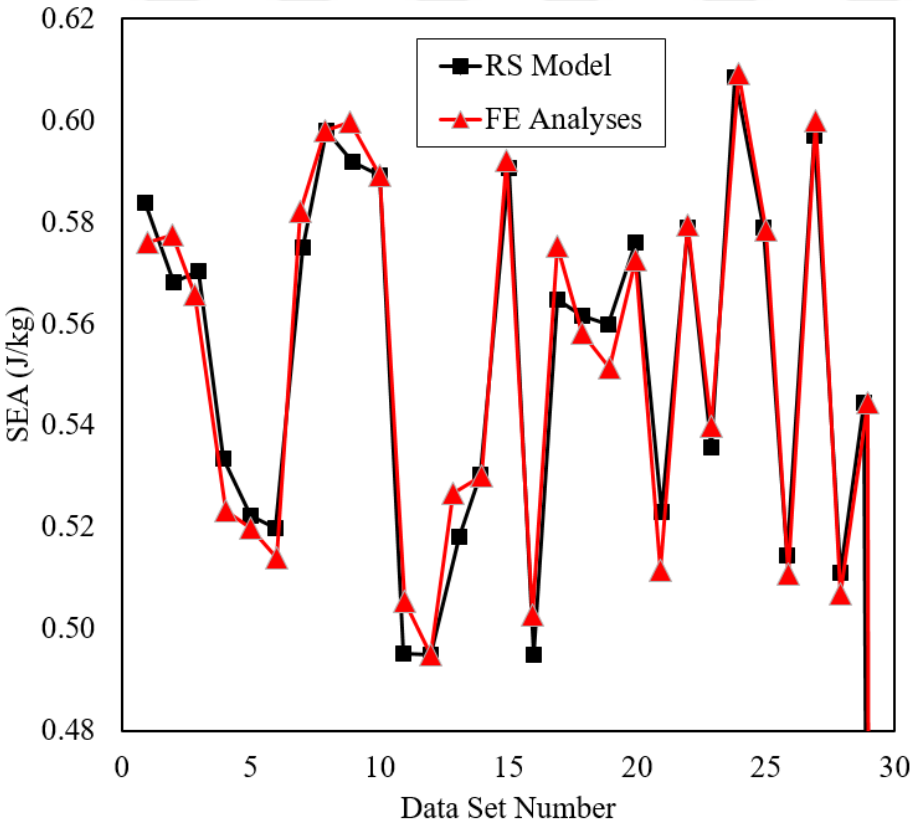

Figure 3.45 : Fitted and actual values for SEA.

3.6.6 Results and discussions

The Non-dominated Sorting Genetic Algorithm –II (NSGAII) is applied to obtain the Pareto optimal solutions. Then the objective functions were normalized, and multiobjective optimization functions are converted a single objective optimization function by the weighted-sum method in equation (3.10).

$$f = w1 * f1 + w2 * f2 \tag{3.10}$$

The stacking sequences and radius of curvature of the optimum design are [90/0/90/90] and 2500 mm, respectively. FE analysis of the best design was performed at the same impact conditions. Figure 3.46 indicates the stress distribution in FE analysis. Table 3.11 shows that there is good coherence between the FE and optimization results.

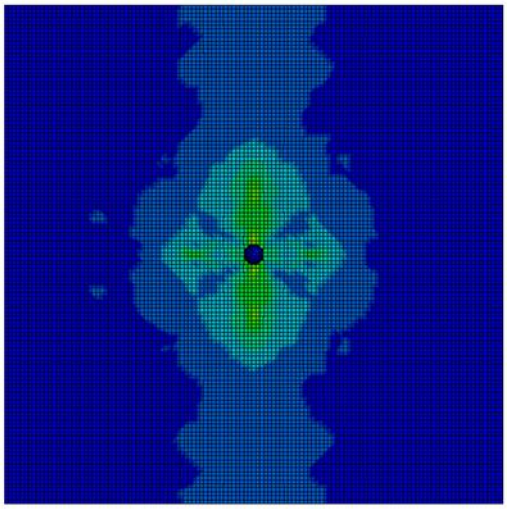

Figure 3.46 : Stress distribution in FE analysis of the best design.

Table 3.11 : Comparison of the FE and optimization results of the best design.

Backplane Displacement (mm)		SEA (J/kg)	
Optimization	Analysis	Optimization	Analysis
1.2686	1.3538	0.4742	0.5197

Overall, the results show that the reduction of the radius of curvature causes increasing SEA and maximum backplane displacement. By changing stacking sequences, the impact behavior of panels can be improved.

4. THIN WALLED CRASH TUBES

4.1 Purpose

This chapter consists of the studies on crash tubes subjected to axially quasi-static compression or low-velocity impact loading. Here we investigate the effects of filler types, curvature, tube numbers, cross-section and imperfection on the crashworthiness performance of the single and multi-tube systems. Re-entrant and hexagonal configurations are chosen as unit cell shapes of the filler. The numerical studies are conducted using LS-DYNA software.

In Section 4.2, the impact behavior of triggered and non-triggered tubes with and without auxetic fillers are examined by using numerical methods. In Section 4.3, circular aluminum tubes with auxetic filler were tested at quasi-static and low-velocity impact velocities. FE analyses were validated with the experimental results. In Section 4.4, the axial impact behavior of empty and filled nested tubular structures is parametrically investigated both experimentally and numerically. The experiments are conducted by a drop test machine. In Section 4.5, crashworthiness optimization of nested and concentric circular tubes under impact loading is performed by the coupling Finite Element model, Response Surface Models and Genetic Algorithm.

4.2 Impact Behavior of Triggered and Non-Triggered Crash Tubes with Auxetic Lattices

In this study, the impact behavior of triggered and non-triggered tubes with and without auxetic filler are examined by using numerical methods. Material properties of tubes made of aluminum alloy and auxetic lattices utilizing ABSplus plastics are determined by using tensile tests. Finite element analyses are performed by using LS-DYNA software at 5 m/s impact velocity. Two different trigger shapes are suggested and compared to each other and discussed the advantages and disadvantages over non-triggered tubes. For these loading conditions, the trigger mechanism provides lower peak forces and higher crash force efficiency (*CFE*), but lower specific energy

absorption (*SEA*). Also, the effects of using auxetic fillers in these triggered tubes are investigated in terms of crashworthiness characteristics.

4.2.1 Material properties of AL6063 aluminum alloy

The tubes considered here are made of aluminum alloy AA6063. Owing to insensitivity of aluminum on strain rate, tensile tests are carried out under quasi-static loading at 2 mm/min velocity. Six test specimens are cut by using the CNC machine according to ASTM E8/E8M test standard (see, in Figure 4.1) [156]. Biaxial strain gauges are stuck, and extensometers are located to define material properties. The material properties of each sample are determined and listed in Table 4.1. Random errors are calculated according to the average value of Young modulus, yield stress, and ultimate tensile strength, which are 67.69 GPa, 160 MPa, and 192 MPa, respectively. Poisson ratio and density are 0.3 and 2710 kg/m^3. No significant differences are observed between the stress and strain curves of tested specimens. The engineering stress and strain curve is plotted in Figure 4.2.

Figure 4.1 : Tensile test specimens of AL6063 aluminum alloy.

Table 4.1 : Mechanical properties and random errors of AL6063 aluminum alloy.

Specimen No	Young Modulus (GPa)	Random Error %	Yield Strength (MPa)	Error %	Ultimate Tensile Strength (MPa)	Random Error %
1	70.44	4.06	145	9.47	182	5.29
2	65.33	3.49	165	3.02	195	1.47
3	65.49	3.25	151	5.72	180	6.33
4	66.12	2.32	172	7.39	202	5.12
5	71.27	5.29	173	8.01	210	9.28
6	67.49	0.30	155	3.23	184	4.25
Average	67.69		160		192	

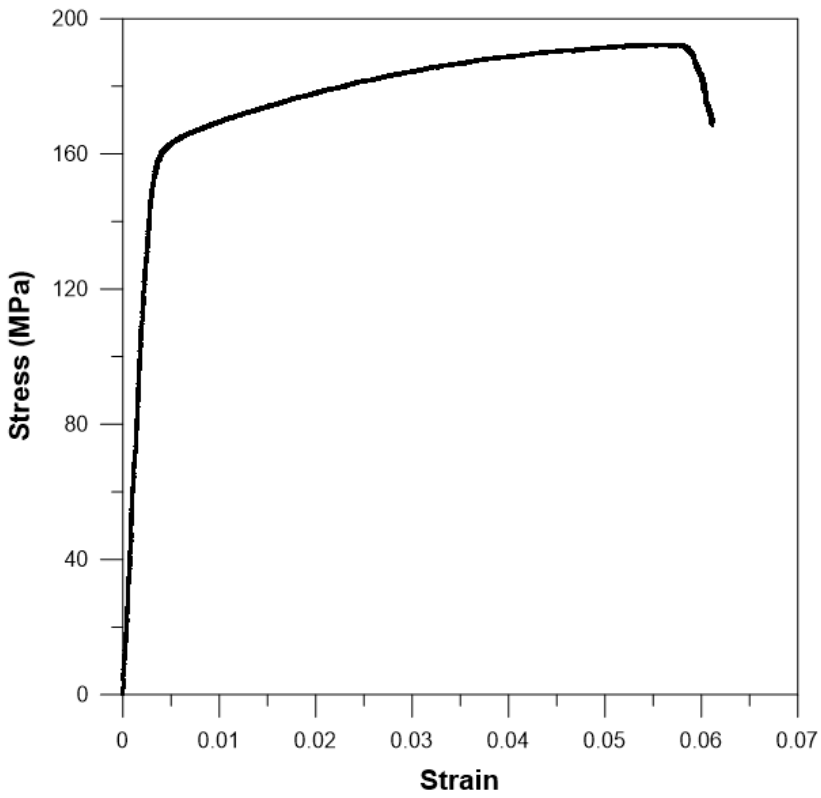

Figure 4.2 : Engineering stress and strain curve of AL6063 tube.

4.2.2 Material properties of ABSplus plastics

The auxetic lattice is made of ABSplus plastics. Strain rate has significant effects on the mechanical properties of ABSplus plastics [157]. In this study, tensile tests of ABSplus plastic are revealed under quasi-static loading due to having no possibility of a split Hopkinson pressure bar test system. Four test specimens are produced with FDM (fused deposition modeling) technology by using the Dimension Elite 3D printer

machine (see, Figure 4.3). Specimens are printed at room temperature (effective temperature range 15-30 ^{0}C), and the interior filling style is selected as solid, which provides more durable and stronger parts. After performing tension tests, the mechanical properties of each sample and random errors are determined (see, Table 4.2). Average Young modulus is 1.53 GPa, ultimate tensile strength is 23.25 MPa, the yield stress is 19.73 MPa, density is 1040 kg/m^{3,} and Poisson's ratio is 0.36. The engineering stress and strain curve are plotted in Figure 4.4.

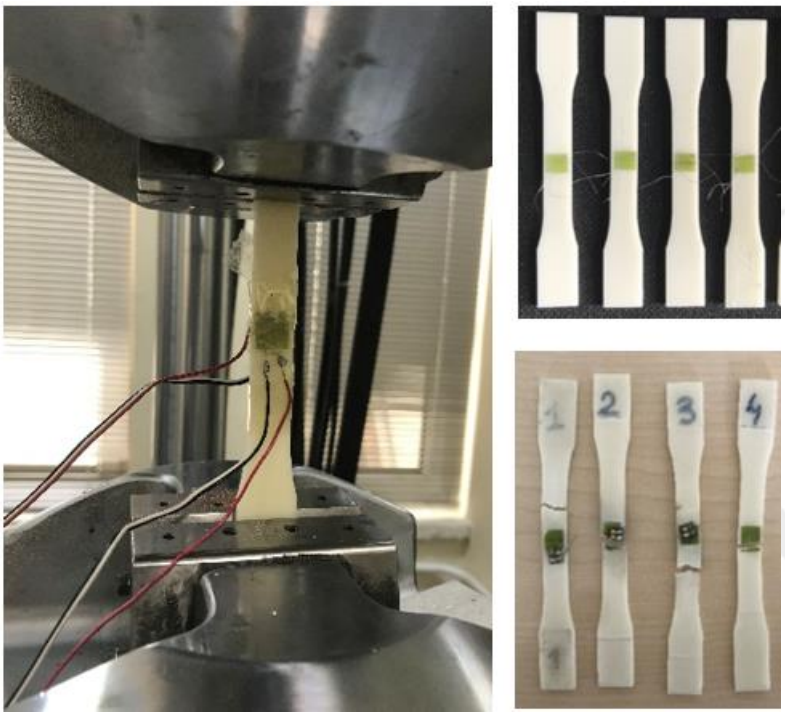

Figure 4.3 : Tensile test specimens of ABSplus plastics.

Table 4.2 : Mechanical properties and random errors of ABSplus plastics.

Specimen No	Young Modulus (GPa)	Random Error %	Yield Strength (MPa)	Error %	Ultimate Tensile Strength (MPa)	Random Error %
1	1.58	3.10	16.8	14.83	21.8	6.24
2	1.39	9.30	21.5	9.00	24.1	3.66
3	1.48	3.43	18.2	7.73	22.8	1.94
4	1.68	9.62	22.4	13.56	24.3	4.52
Average	1.53		19.73		23.25	

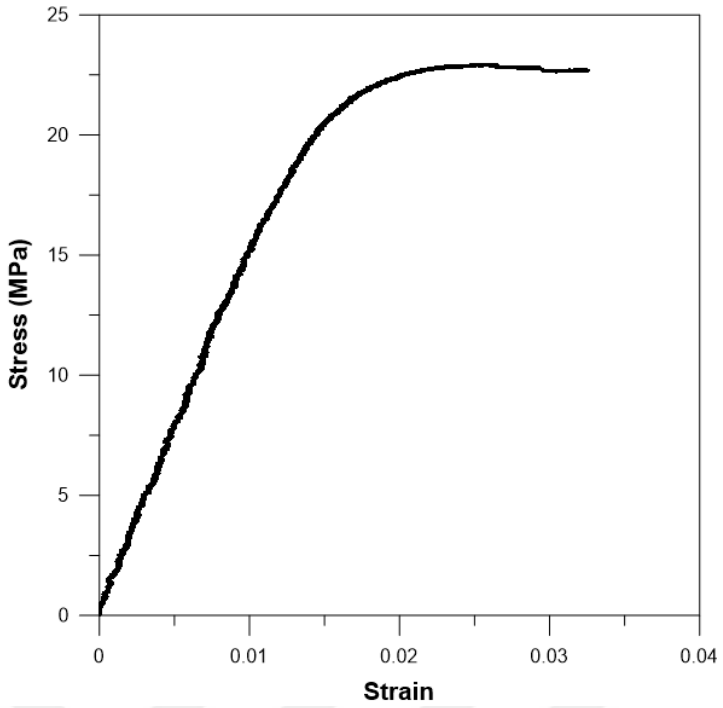

Figure 4.4 : Engineering stress and strain curve of ABSplus plastics.

4.2.3 Finite element modeling

A rigid mass is dropped on the tubes with a speed of 5 m/s. Rigidwall_Planar_Moving_Forces is used as an impactor to model the impact behavior. The nodes at the bottom of the tube structure are clamped. A schematic view of the tube and rigid impactor is plotted in Figure 4.5. Three different tube structures with and without re-entrant honeycomb structure are investigated. The diameter, length and thickness of the tubes are 70, 100 and 2 mm, respectively. Auxetic filler type is chosen as the re-entrant honeycomb owing to its wider capacity of negative Poisson ratio range in comparison with the other auxetic geometries [158]. Scarpa et al. [87] show that geometric cell parameters of reentrant honeycomb have significant effects on the mechanical properties such as in-plane Poisson ratio and Young modulus. The cell parameters of re-entrant honeycomb θ, h, l and t are 30^0, 10 mm, 10 mm and 1 mm.

Tubes and auxetic fillers are modeled by using Belytschko-Tsay shell elements. This element formulation gives greater computational efficiency compared with other shell element formulations [159]. Optimum element size is defined as 2 mm x 2 mm, after comparing the results of the analysis of crash tubes at different mesh qualities. Automatic single surface contact algorithms are identified for each specimen, because they have the possibility of lapping after deformation. Also, the automatic surface to

surface contact interface is defined between surfaces of tube and auxetic filler. The static and dynamic friction coefficients are chosen as 0.3 and 0.2, respectively for each contact definition.

The Material properties of aluminum tube and plastic auxetic lattice are defined with MAT24 (Piecewise Linear Plasticity) material model in LS-DYNA. Elastic material properties of the tube and auxetic lattice are used in this material model. True stress and effective plastic strain curve are embedded into this material model for the plasticity of this material. The effective plastic strain is derived from the difference of true strain and the ratio of true stress over Young modulus.

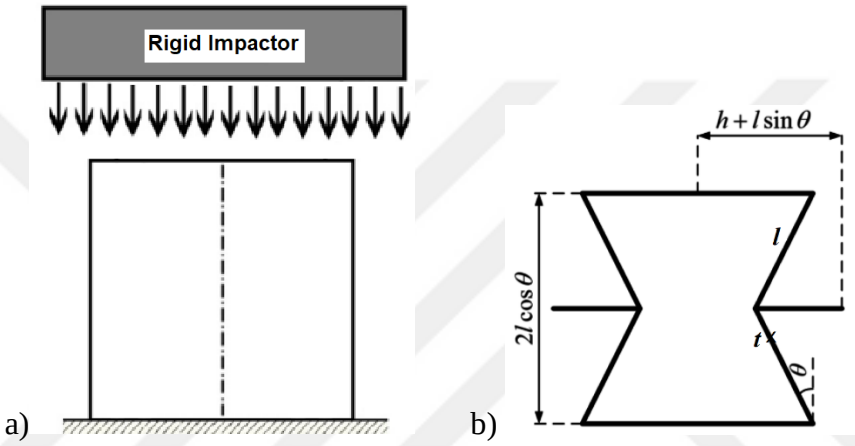

Figure 4.5: a) Schematic view of rigid impactor and tube, b) re-entrant honeycomb cell parameters.

4.2.4 Tube designs

The first model does not have any triggering on the tube structure so that it is abbreviated as NT (non-triggered) as shown in Figure 4.6. The empty tube is abbreviated as “E” and the auxetic filler is abbreviated as “A”. The number in the name of the model denotes tube length in terms of millimeter.

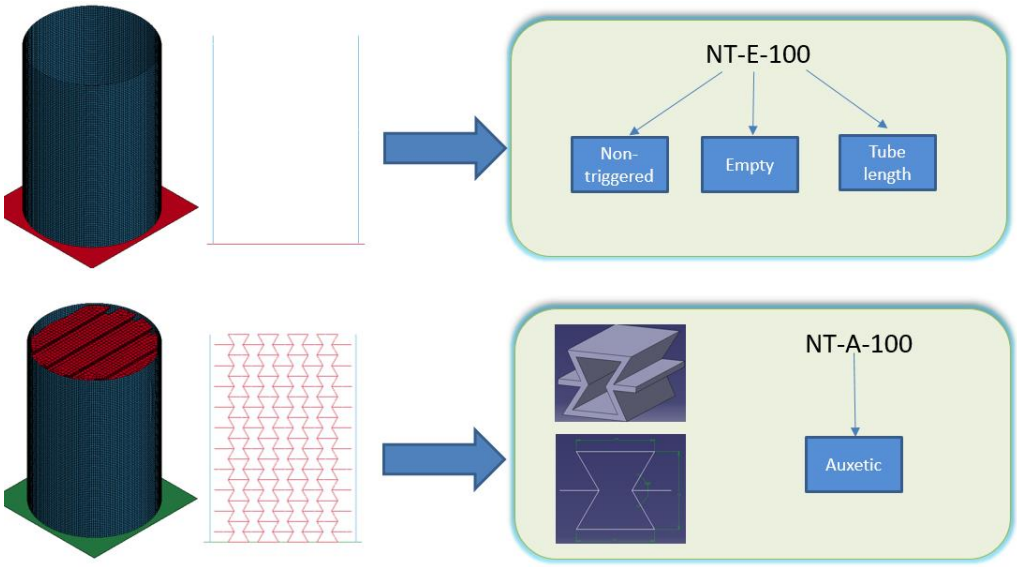

Figure 4.6 : NT-E and NT-A models.

The second and third models include imperfection on the tubes. The trigger mechanism of the second model is an arc, which is shown in Figure 4.7. Due to its circular shape, it is named as a circular trigger (CT). The trigger shape of the third model is like in zigzag geometry, which is shown in Figure 4.8. Because it consists of lines, it is named as Line Triggered (LT). It is aimed to control the crash stability and collapse modes and to increase crashworthiness characteristics of tubes by using these trigger shapes. The distance between two arcs and two zigzag lines are chosen as 10 mm, and the corner points of them are at the same level.

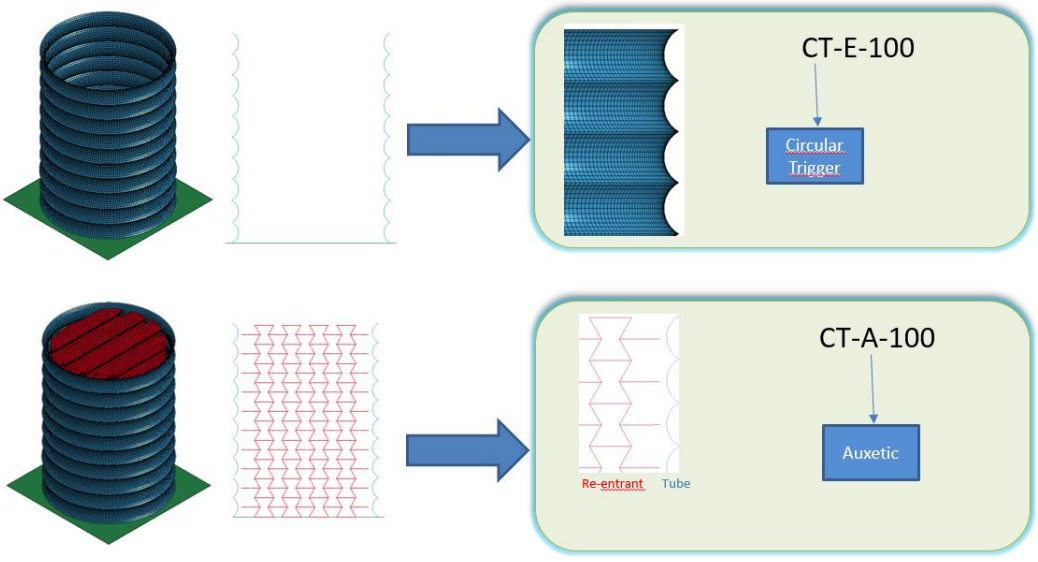

Figure 4.7 : CT-E and CT-A models.

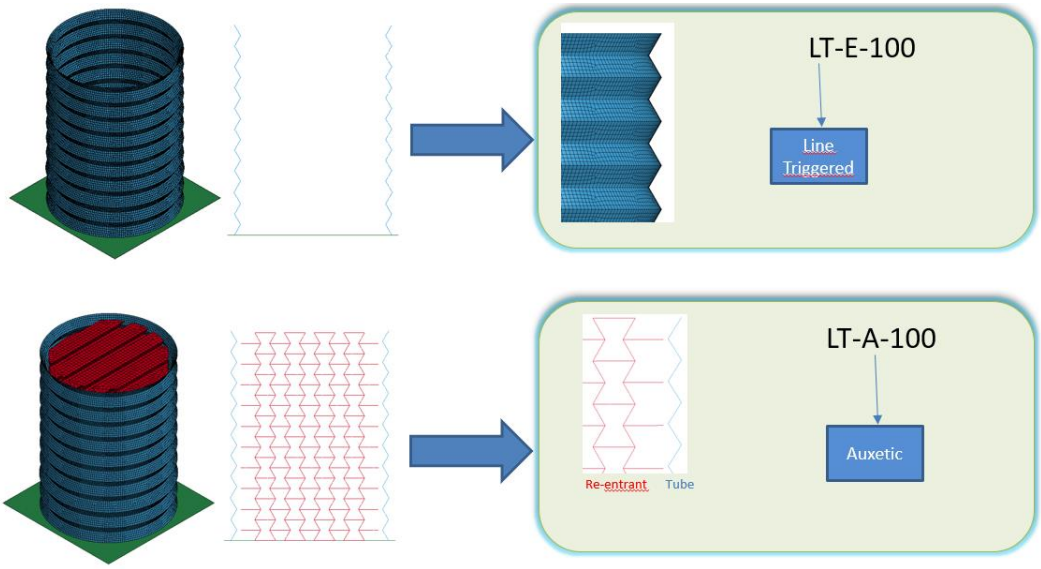

Figure 4.8 : LT-E and LT-A models.

4.2.5 Results and discussion

4.2.5.1 The effects of length of the tubes on crashworthiness

To investigate the effects of the length of the tubes on crashworthiness characteristics, all models are analyzed by changing tube length with a length of 100, 125 and 150 mm. The results are compared in terms of reaction force response in time and collapse mechanism. The results show that shorter tubes are better in terms of *SEA* and *MCF*, as shown in Table 3. Tube length has no remarkable effects on the crash force response as shown in Figure 4.9. The deformation of the re-entrant honeycomb of NT-A-100 begins to shrink initially at the bottom side. But for the most extended non-triggered model, collapse mechanism appears at the bottom and top surfaces together. Shorter tubes give better *SEA* and *MCF* values for CT and LT models. In comparison with CT and LT models with re-entrant structure, all tubes begin to collapse from top surfaces as shown in Figure 4.10 and Figure 4.11. In contrast to the Non-triggered model, the first buckling of CT and LT tubes reveal in the middle section. Therefore, it could be said that the trigger system may affect the deformation behavior of filler.

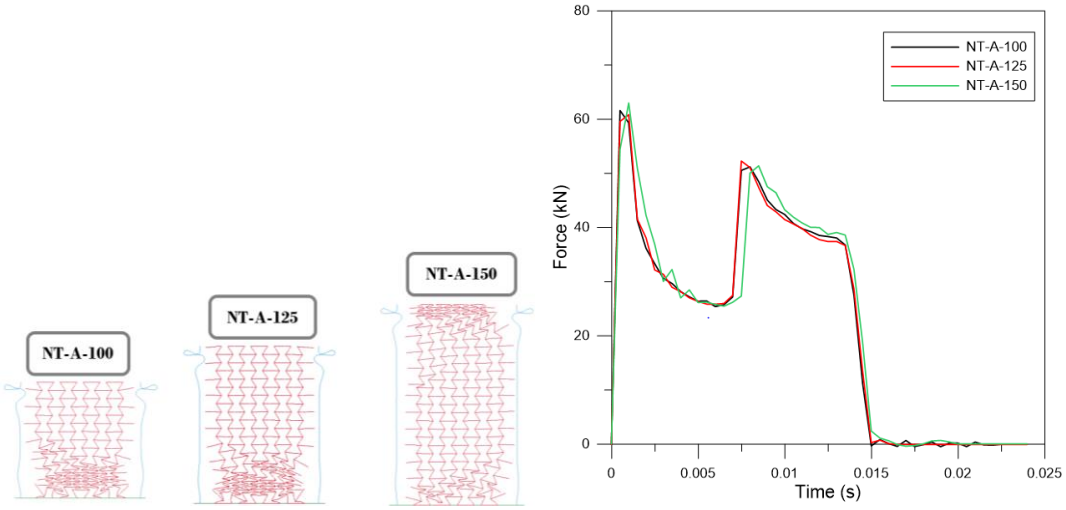

Figure 4.9 : Comparison of deformation and force response of NT-A models.

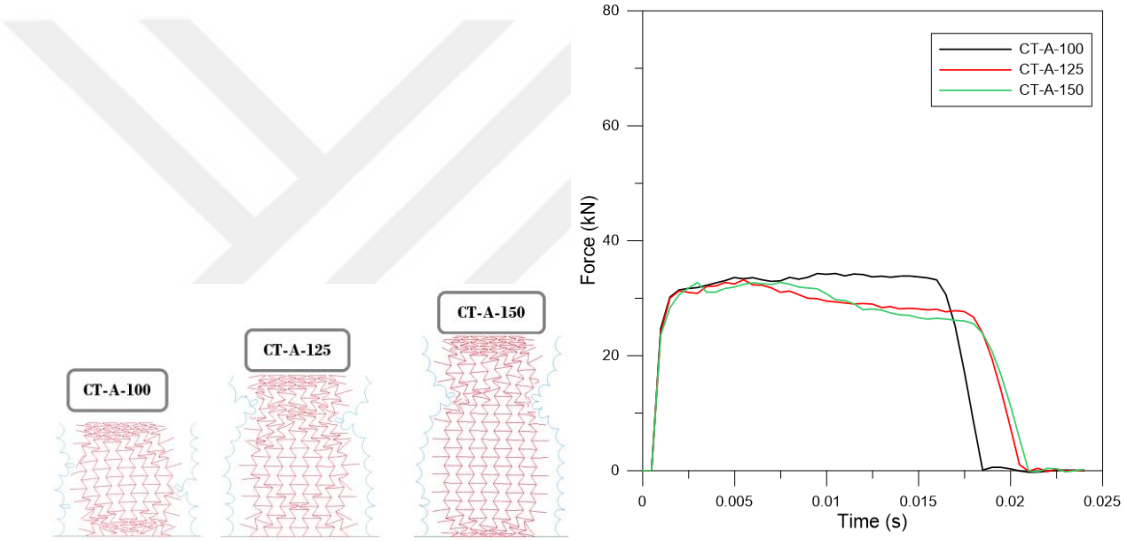

Figure 4.10 : Comparison of deformation and force response of CT-A models.

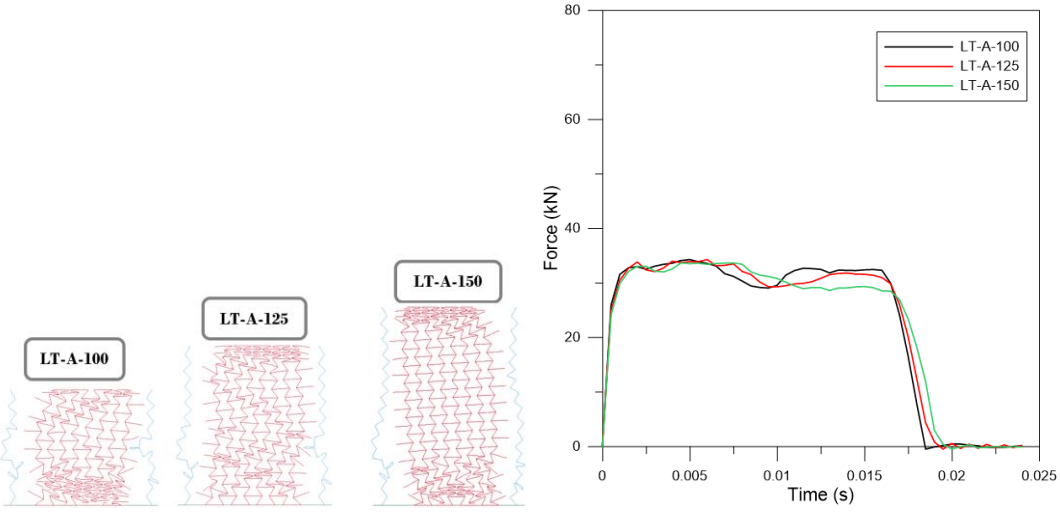

Figure 4.11 : Comparison of deformation and force response of LT-A models.

4.2.5.2 Comparison triggered and non-triggered tube designs

Another comparison is made between the impact behavior of the triggered and non-triggered tubes with auxetic lattice. Crash force response of NT-A-100, CT-A-100 and LT-A-100 models are plotted in Figure 4.12. There is a remarkable difference between the force response of non-triggered and triggered tubes. Initial peak crash forces are almost 62 kN and 34 kN, respectively. Although two different peak forces are observed for non-triggered tubes, initial and subsequent force values of triggered tubes become similar. It can be strictly effective on reducing the inertial effects of crash loads on the passenger. It is achieved a great reduction of these inertial loads owing to the small difference between subsequent forces of triggered tubes.

In Table 4.3, results show that Non triggered tubes have advantages over triggered tubes in terms of *MCF* and *SEA* due to higher durability under buckling and bending loads and lower mass. On the other hand, in terms of peak force and crush force efficiency, triggered tubes are obviously better than non-triggered tubes. *CFE* is the final decisive parameter to determine the most efficient tube design due to including three important results in one formulation. The triggering changes the deformation mode and increases the energy absorption capacity of the axially compressed tubes.

In comparison with the results of triggered tubes, and peak crash force change of CT tubes is smoother than LT tubes. Therefore it is more useful in terms of inertial loads. But CT tubes are deflected more than LT tubes in the axial direction, and also, its arc geometry causes higher mass. Therefore LT tubes are better than CT tubes in terms of *MCF* and *CFE*. Table 4.3 illustrates that LT-A-100/125/150 is superior to other types of tubes in terms of *CFE*.

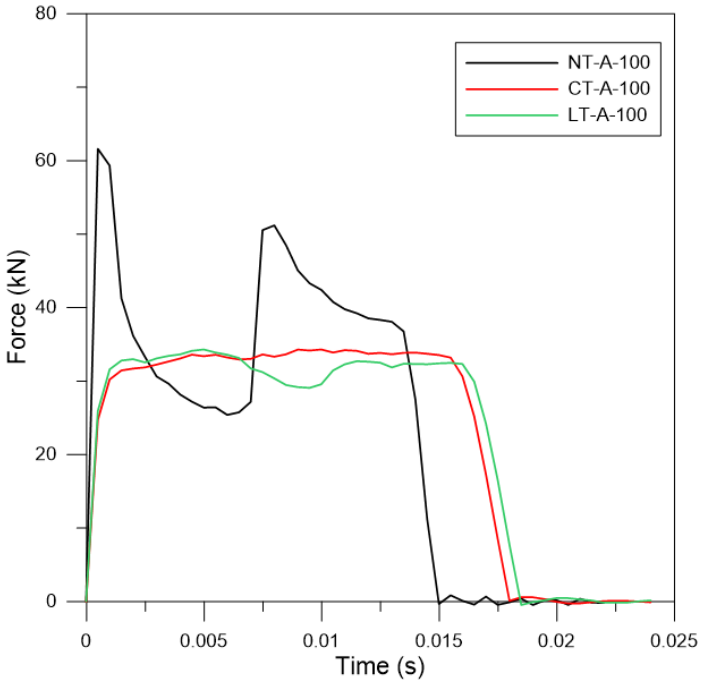

Figure 4.12 : Comparison of force response of different samples with auxetic filler.

Table 4.3 : Crashworthiness parameters of tubes with auxetic filler.

Models	PCF (kN)	Deflection (mm)	Mass (kg)	SEA (kJ/kg)	MCF (kN)	CFE
NT-A-100	61.62	32.70	0.2258	5.491	37.912	0.615
CT-A-100	34.35	39.78	0.2560	4.838	31.141	0.907
LT-A-100	34.28	39.32	0.2512	4.934	31.524	0.920
NT-A-125	60.89	32.74	0.2817	4.396	37.827	0.621
CT-A-125	33.22	41.13	0.3180	3.911	30.235	0.910
LT-A-125	34.29	39.46	0.3132	3.967	31.483	0.918
NT-A-150	62.97	33.55	0.3375	3.676	36.983	0.587
CT-A-150	32.75	41.22	0.3821	3.242	30.049	0.917
LT-A-150	33.73	39.73	0.3750	3.313	31.265	0.927

4.2.5.3 The effects of using auxetic lattices on crashworthiness

In Table 4.4, the last comparison is shown between empty and filled tubes. It is shown that using re-entrant honeycomb has small effects on the *PCF* values, axial deformation and efficiency. For example, *PCF* values of Non-triggered empty and auxetic filled tubes are 60.8 and 61.62 kN, crash force efficiency values are 0.614 and 0.615, respectively. Contrary to a conventional honeycomb, the cross-section area of

the re-entrant honeycomb reduces under compression loads due to its negative Poisson's ratio. Therefore, the contact surfaces could be reduced and contact forces between the aluminum tube and auxetic material are lower than between the tube and a traditional honeycomb folding. This contact tends to reduce the peak forces on the specimen. Besides, auxetic lattices tend to increase the stiffness of the tube structure during the compressive load phase and can absorb totally more energy than empty tubes. However, the re-entrant honeycomb structure can be easily deformed and have a smaller effect on the deflection and brings scarcely any improvement in terms of *MCF*. This improvement cannot visibly overcome the decline in *CFE* due to higher peak forces. Accordingly, *CFE* values of tubes with and without auxetic filler are close to each other.

In addition, it brings two times higher mass than empty tubes, which leads to lower *SEA* values, and there is a notable decline in energy absorption capability.

Table 4.4 : Crashworthiness parameters of tubes with and without auxetic filler.

Models	*PCF* (kN)	Deflection (mm)	Mass (kg)	*SEA* (kJ/kg)	*MCF* (kN)	*CFE*
NT-E-100	60.80	33.43	0.1187	10.513	37.333	0.614
NT-A-100	61.62	32.70	0.2258	5.491	37.912	0.615
CT-E-100	33.01	40.62	0.1490	8.366	30.686	0.929
CT-A-100	34.35	39.78	0.2560	4.838	31.141	0.907
LT-E-100	33.62	40.25	0.1442	8.664	31.038	0.923
LT-A-100	34.28	39.32	0.2512	4.934	31.524	0.920

4.2.5.4 Conclusion

In this study, triggered and non-triggered tubes with and without auxetic honeycomb structure are analyzed by using LS-DYNA software under dynamic impact loading. The ability of two different trigger systems according to non-triggered tubes is investigated, and the effects of using arc and line shape on triggered tubes are evaluated. Triggered tubes with auxetic honeycomb have not been studied before. This paper also focuses on the advantages and disadvantages of using auxetic honeycomb structure in the triggered tubes under crash load. The effects of the trigger mechanism,

auxetic lattice and length of the specimen are compared in terms of *PCF*, *SEA*, *MCF* and *CFE* values. The results are listed as follow:

- Shorter tubes can provide higher *SEA*, *MCF*.
- Triggered tubes are obviously better in terms of peak crash force and crush force efficiency. The trigger system affects the deformation behavior of the re-entrant structure. Peak crash force change of CT tubes is smoother than LT tubes. Therefore it is more useful in terms of inertial loads. On the other hand, LT tubes are better than CT tubes in terms of *MCF* and *CFE* due to lower deformation in the axial direction.
- *CFE* values of tubes with and without auxetic filler are close to each other. Re-entrant honeycomb brings two times the higher mass of specimens so that *SEA* values of specimens with auxetic lattices are lower than empty tubes.
- Table 3 illustrates LT-A-100/125/150 are superior to other types of tubes with auxetic filler in terms of *CFE,* which is our decisive parameters to choose the better design. This result indicates the Line triggering is the best choice according to our study. Desirable models can be obtained by changing the triggering shape of tube design and geometry of auxetic structures. By optimizing the geometry further, it is believed that the properties of auxetics can be exploited. A parametric optimization study on the lattices, changing the parameters (i.e., h, l, t, s and θ) could achieve this.

4.3 Crushing Behavior Of Circular Aluminum Tubes with Square Prism Auxetic Filler

In this work, circular crash tubes with and without auxetic lattices are examined under dynamic loads by using experimental and numerical techniques. The experiments are conducted by a drop test machine, and the numerical studies are conducted using LS-DYNA software. The tubes are made of AL6063 aluminum alloy and a re-entrant auxetic honeycomb filler of ABSplus plastics.

4.3.1 Manufacture of square prism auxetic filler

Gibson's and Masters' analytical formulation [85] was used to calculate the dimension of re-entrant lattice. Dimensions of L, H, θ, l and h are shown in Figure 4.13.

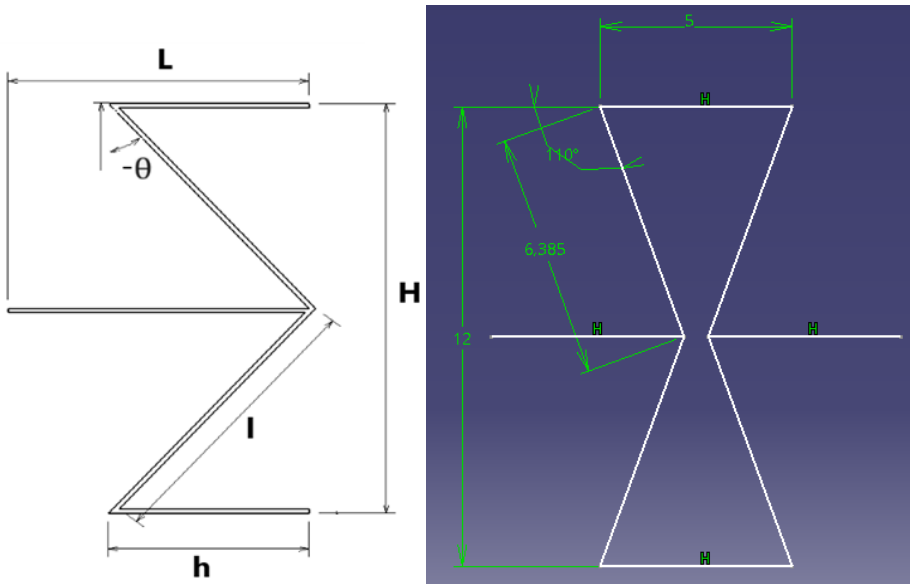

Figure 4.13 : Dimensions of re-entrant unit cell.

The diagonal of auxetic core could not exceed the internal clearence of tube which was 66 mm. Dimensions of auxetic core were selected as 40x40x150 mm applicable to the inner gap of the aluminum tube. In Figure 4.14, the design of the auxetic core in CATIA is shown.

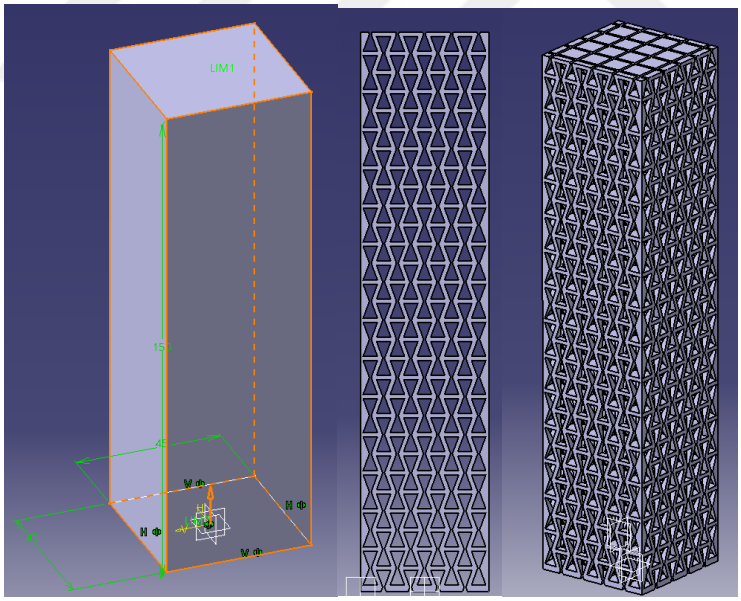

Figure 4.14 : Design of auxetic core in CATIA.

The effects of cell parameters on the deformation behavior of the auxetic core structure under axial loading were investigated by changing dimensions. The number of cells from the top to bottom and the cell angle did not change in the study (see, Figure 4.15). The dimension of L was reduced from Model 1 to 4.

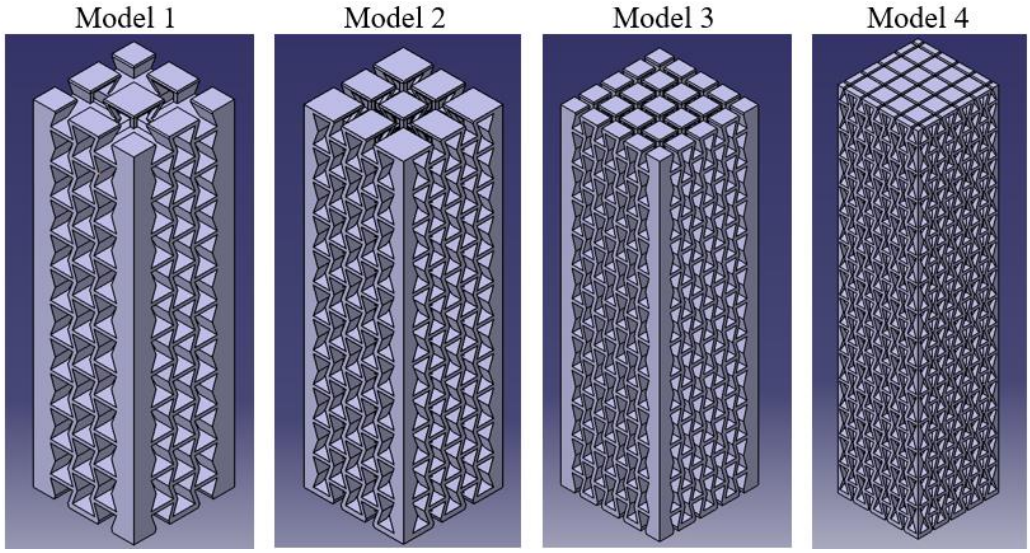

Figure 4.15 : Desing of auxetic core structure by changing lattice parameters.

In Figure 4.16, FE model and analysis of Model 1 are shown. ABSplus plastic core structure is fractured and scattered under impact loading.

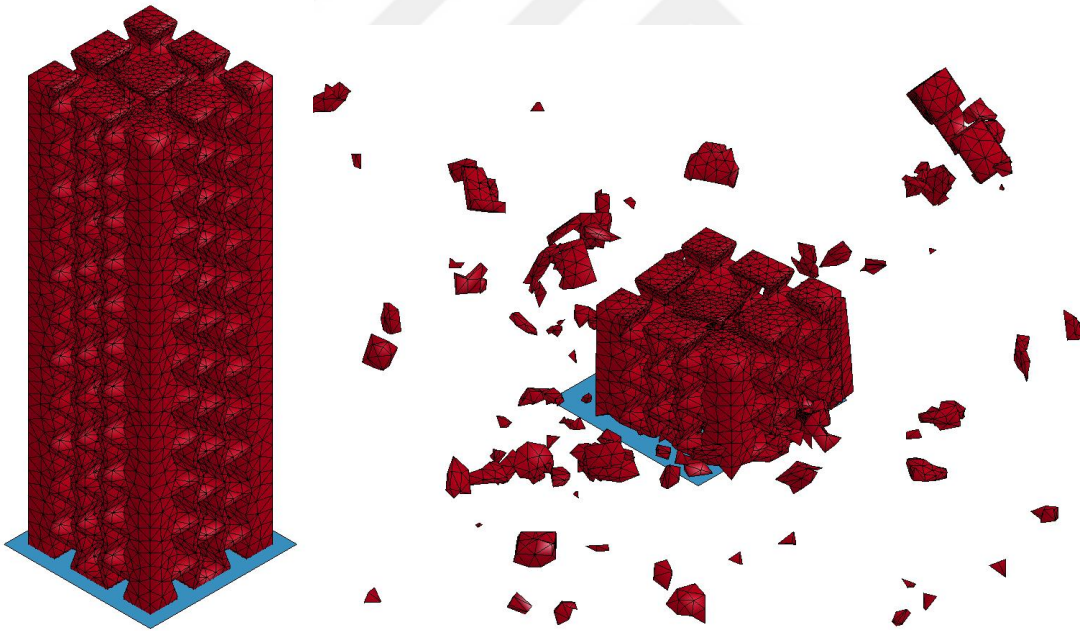

Figure 4.16 : FE model and analysis of Model 1.

In Figure 4.17, The FE model and analysis of Model 2 are shown. The auxetic core structure is fractured and scattered like Model 1, and it protects structural integrity due to the increase in auxetic behavior. In Figure 4.18 and Figure 4.19, The FE Models and deformed shapes of Model 3 and 4 are shown.

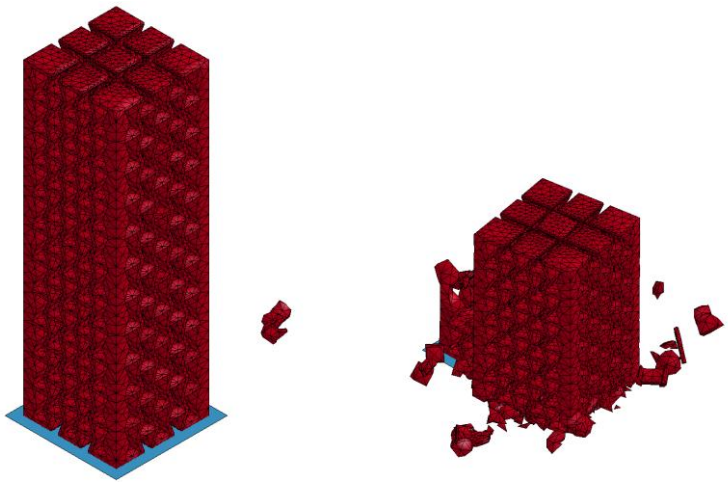

Figure 4.17 : FE model and analysis of Model 2.

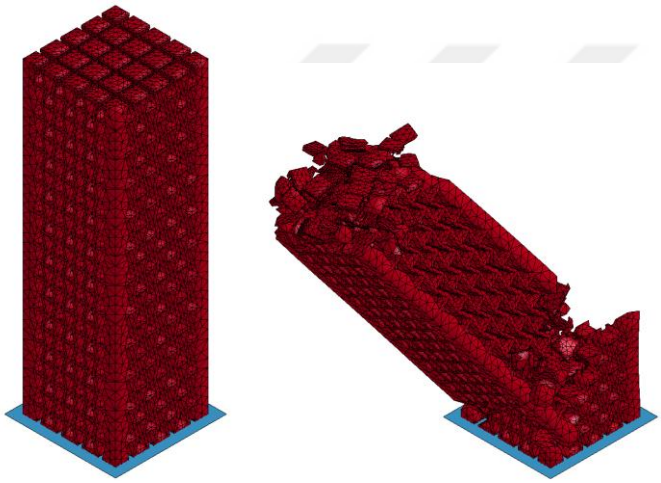

Figure 4.18 : FE model and analysis of Model 3.

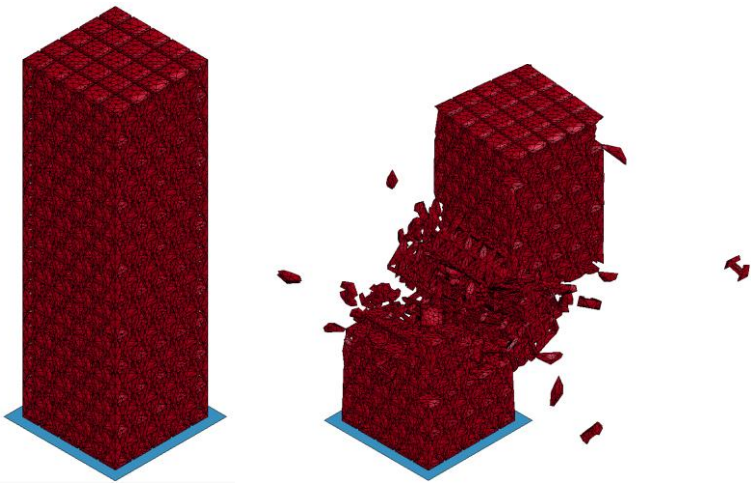

Figure 4.19 : FE model and analysis of Model 4.

The total mass and peak crash force of models are listed in Table 4.5. The deformation behavior of Model 4 in time is shown it Figure 4.20. The results show that Model 4 is

the most efficient model due to higher auxetic capacity, lower mass and lower peak force.

Table 4.5 : FE analyses results of auxetic core structures in tubes.

	Mass (g)	Peak Force (kN)
Model 1	99.432	6.9
Model 2	95.851	6.5
Model 3	100.248	9.6
Model 4	84.225	4.6

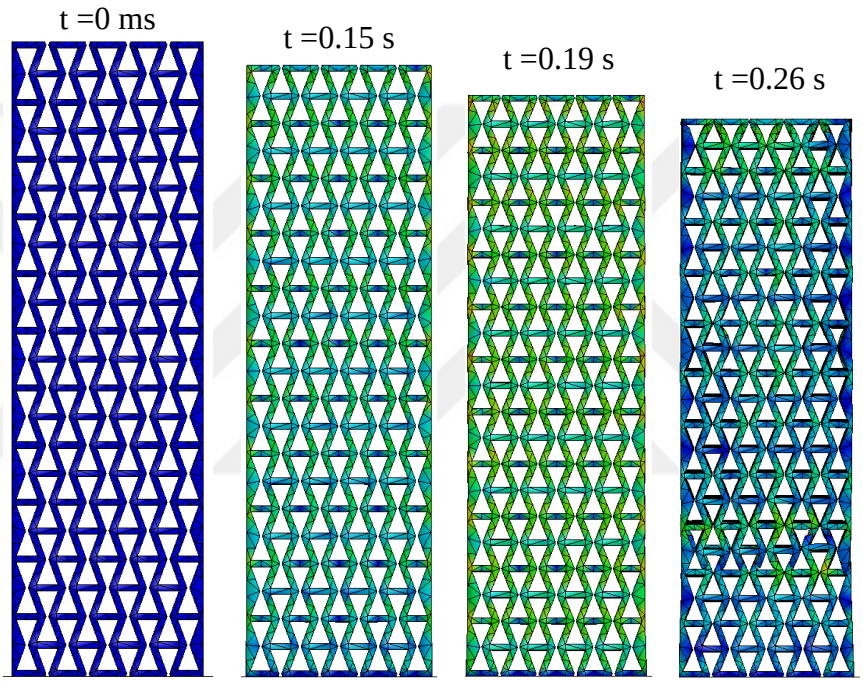

Figure 4.20 : Deformation behavior of Model 4 in time.

They have produced with FDM (fused deposition modeling) technology by using the Dimension Elite 3D printer machine. Specimens were printed at roam temperature (effective temperature range 15-30 ^{0}C), and the interior filling style was selected as solid, which provides more durable and stronger parts (see, Figure 4.21).

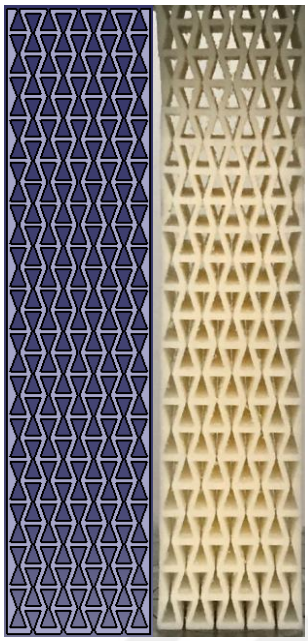

Figure 4.21 : Design and production of auxetic core.

4.3.2 Manufacture of aluminum tubes

The tube length was defined as 150 mm, and the outer tube diameter as 70 mm, the wall thickness was 2 mm. The tubes in the specified length were cut from the extruded cylindrical aluminum profiles. Then, they were placed in the special grooves made on an aluminum plate and bonded using an adhesive (see, Figure 4.22).

Figure 4.22: Manufacture of aluminum tubes.

4.3.3 Low-velocity impact tests

Impact tests were conducted by using INSTRON Drop Test Machine in TUBITAK. This machine is based on a maximum of 7 m/s impact velocity with 1132 kg mass (see, Figure 4.23). The moving rigid wall with 1132 kg was dropped on the specimens at 2.5 m/s initial velocity.

Figure 4.23 : INSTRON Drop Test Machine.

4.3.3.1 Impact tests and analysis of empty tubes

Three test specimen were produced and tested at the same conditions. They were named as E-1, E-2 and E-3. They were deformed 98.5, 100 and 99 mm in the axial direction, respectively. The deformation of the numerical model is 96 mm in the axial direction (see, Figure 4.24).

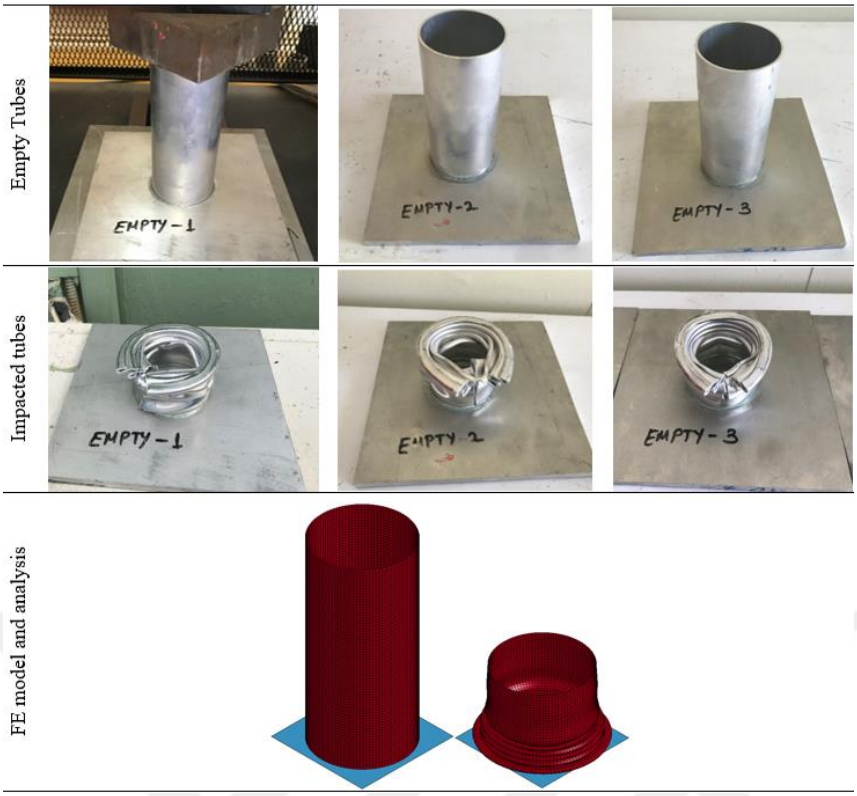

Figure 4.24 : E-1, E-2 and E-3 test specimens and FE analysis.

In Figure 4.25, force response of T-E-1, T- E-2 ve T-E-3, and numerical model are plotted. Initial peak crash force and subsequent forces are in coherence in comparison with the results of tests and analysis.

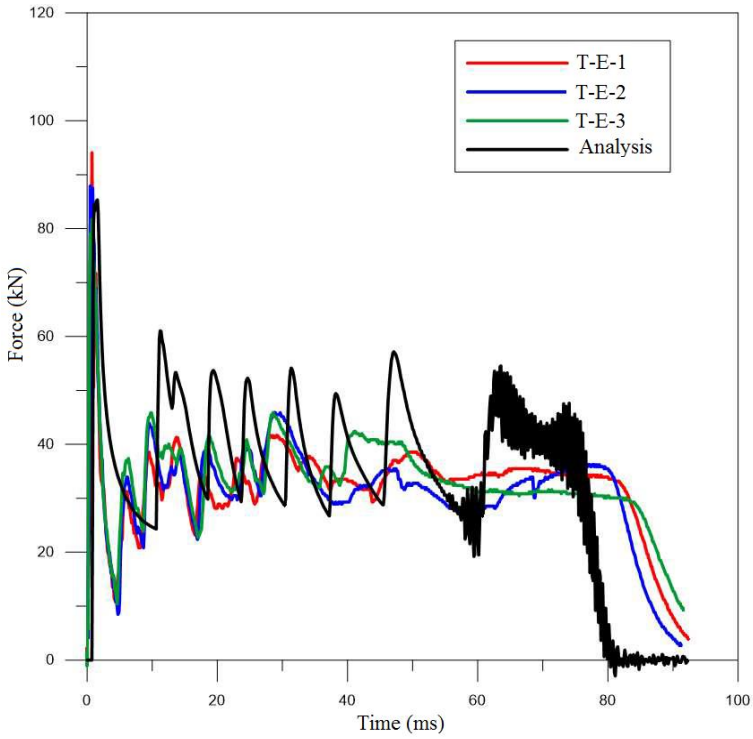

Figure 4.25 : Force-time response of E-1, E-2, E-3 test specimens and FE analyses.

4.3.3.2 Impact tests and FE analysis of auxetic core

In this study, 3D printed auxetic core was tested by using the drop test machine at the same conditions. In Figure 4.26, the test specimen and FE model are shown before and after impact loading. Both samples were broken, and their parts were scattered.

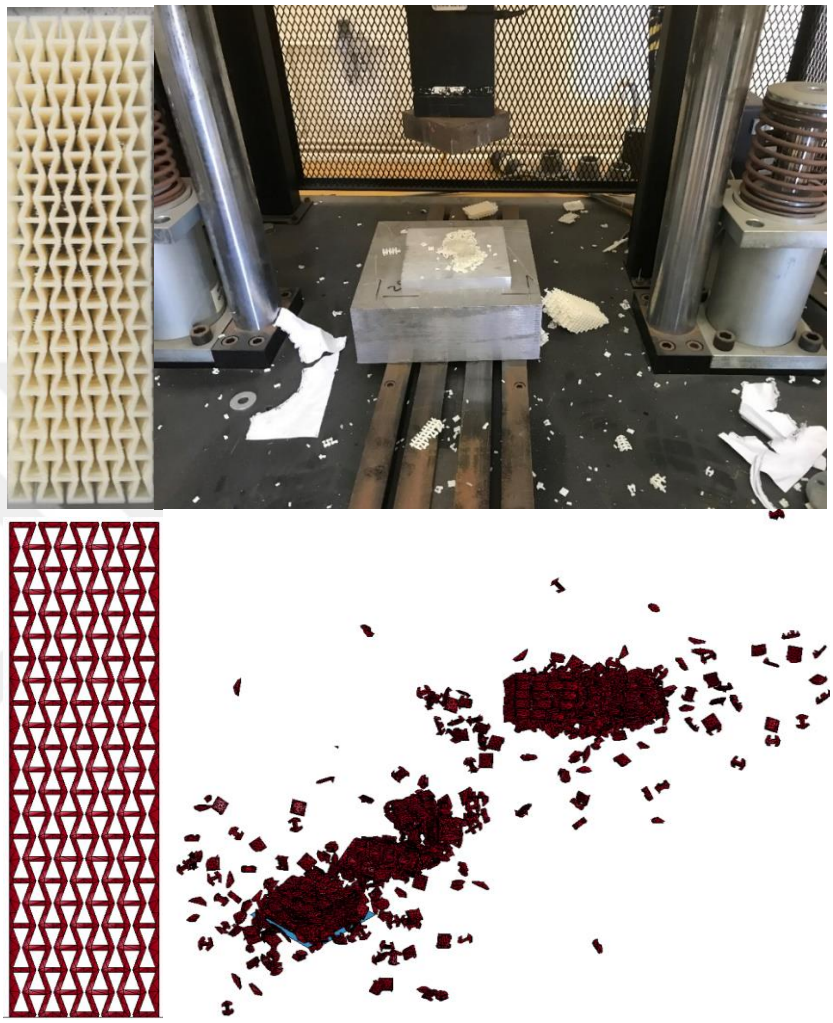

Figure 4.26 : AC (Auxetic core) impact test and analysis.

4.3.3.3 Impact tests and FE analysis of aluminum tubes with auxetic core

Three test specimens were produced and tested at the same conditions. They were named as T-AC-1, T-AC-2 and T-AC-3. They were deformed 93, 96 and 88 mm in the axial direction, respectively. The deformation of the numerical model is 86 mm in the axial direction (see, Figure 4.27).

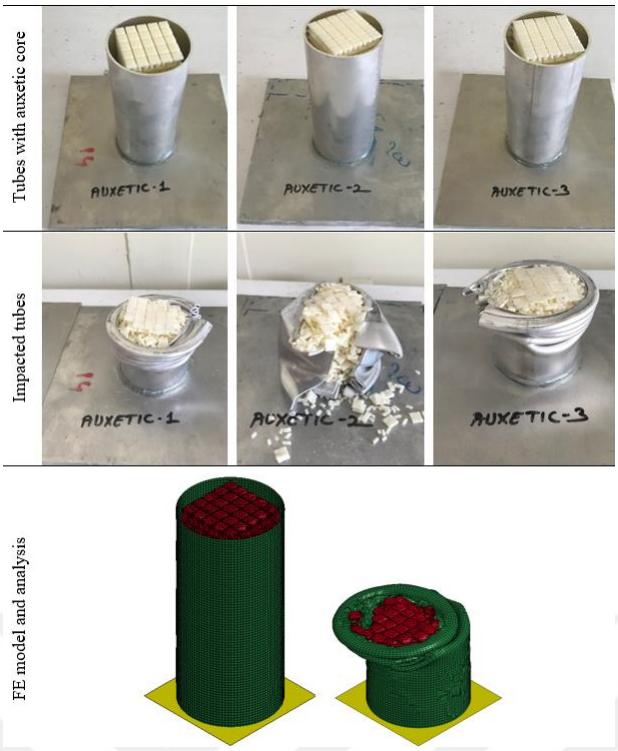

Figure 4.27 : T-AC-1, T-AC-2 and T-AC-3 test specimens and FE analysis.

In Figure 4.28, the force-time response of T-AC-1, T-AC-2 ve T-AC-3, and numerical model are plotted. Initial peak crash force and subsequent forces are in coherence in comparison with the results of tests and analysis.

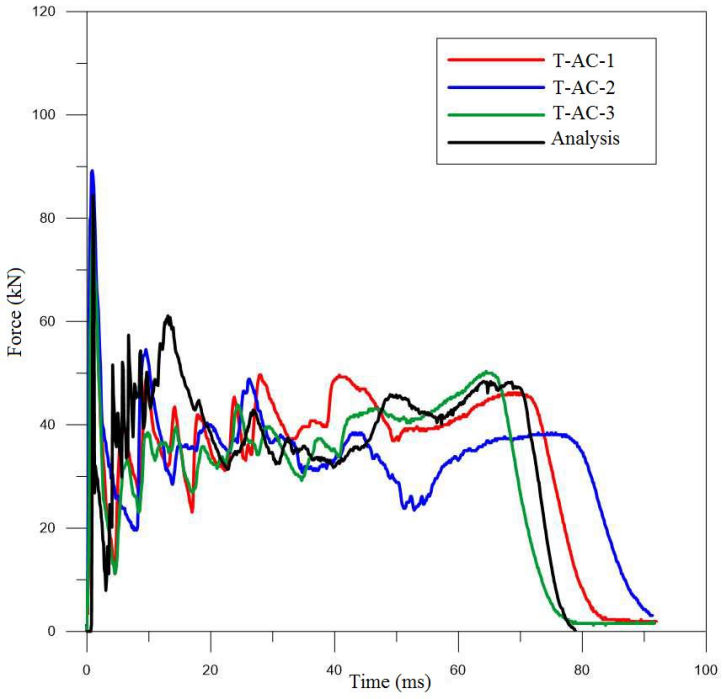

Figure 4.28 : Force-time response of T-AC-1, T-AC-2 ve T-AC-3 test specimens and FE analyses.

4.3.4 Results and discussions

The results of empty tubes, auxetic core and tubes with auxetic core are compared in Table 4.6. Empty tubes can provide higher SEA rather than tubes with the auxetic core. The reason is that both empty tubes and tubes with auxetic core absorb the same energy, although the auxetic core brings additional mass. On the other hand, tubes with auxetic core are more efficient in terms of MCF due to their higher stiffness. They were deformed less than empty tubes in the axial direction. Table 4.6 illustrates TC-A-3 is superior to other types of tubes with auxetic filler in terms of CFE, which is our decisive parameters to choose the better design. Results indicate the using auxetic core has advantages over empty tubes.

Table 4.6 : Comparison of the test results.

	Peak Force (kN)	Absorbed Energy (kJ)	Axial Deformaton (mm)	Mass (kg)	SEA (kj/kg)	MCF (kJ)	CFE
T-E-1	94.00	3.50	98.50	0.18	19.65	35.53	0.32
T-E-2	88.00	3.50	100.00	0.18	19.65	35.00	0.30
T-E-3	86.00	3.50	99.00	0.18	19.65	35.35	0.41
T-E-Analysis	85.31	3.50	92.41	0.18	19.44	37.88	0.44
T-AC-1	82.00	3.50	93.00	0.27	12.81	37.63	0.46
T-AC-2	92.00	3.50	96.00	0.27	12.81	36.46	0.40
T-AC-3	85.00	3.50	88.00	0.27	12.81	39.77	0.47
T-AC-Analysis	88.57	3.50	87.30	0.27	12.96	40..09	0.45
AC-1	4.50	0.10	147.00	0.10	1.05	0.68	0.15
AC- Analysis	4.43	0.07	147.00	0.10	0.70	0.48	0.11

4.4 Experimental and Numerical Investigation of Impact Behavior of Nested Tubes with and without Honeycomb Filler

In this study, the axial impact behavior of empty and filled nested tubular structures is parametrically investigated both experimentally and numerically. The experiments are conducted by a drop test machine, and the numerical studies are conducted using LS-DYNA software. The tubes are made of AL6063 aluminum alloy and a regular hexagonal honeycomb filler of ABSplus plastics. The external sizes of all specimens are held constant for meaningful comparisons. The primary objective of this study is

to investigate the effects of using a honeycomb filler, increasing the numbers of tubes, and changing the lengths of the tubes on the nested tube structures. The results of single, double, triple, quadruple, and quintuple tubular structures, with and without the honeycomb filler, are compared in terms of collapse mechanism and common crashworthiness indicators, namely, peak crash force, specific energy absorption, and crash force efficiency. The results indicate that the honeycomb filler has a significant effect on the collapse mechanism of single and nested tubular structures, and the filled nested tube systems with fewer tubes are better than empty ones in terms of specific energy absorption and crash force efficiency. In addition, the energy absorption of the nested tubes could be increased in certain cases with the increase in the number of tubes and tube lengths increasing from the innermost to outermost tubes. Therefore, the double nested tube structures with a honeycomb filler are recommended for crash box designs.

4.4.1 Nested tube structures and problem definition

Crash boxes are typically subjected to axial impact loads during accidents. Therefore, it is essential to investigate the deformation behavior of crash boxes under axial impact loading. Crash box tests could be performed by impacting a rigid impactor on the specimens, as illustrated in Figure 4.29, to investigate their deformation behavior. In this study, the deformation behavior of nested crash tubes with circular cross-sections is investigated. The effect of the number of tubes is investigated by testing double, triple, quadruple, and quintuple nested tubular structures, and the results are compared to a single tube. The mean diameter (D_m) and the length (L) of the longest tube are chosen as 120 mm and 100 mm, respectively. The radial gap and length difference between adjacent tubes are chosen as 10 mm. Two cases considering the sequence of tubes are studied. The lengths of the tubes decrease from the inner to outer tubes in case A and increase in case B. The wall thicknesses (t) of tubes are selected as 2 mm considering the standard aluminum profiles commercially available. Each tube in the nested tube designs is separately represented by a tube numbered from 1 to 5 according to the increasing diameter from inside to outside. The dimensions of the test specimens for both cases are presented in Tables 4.7 and 4.8.

Table 4.7 : Dimensions of single and nested tubes in case A (units: mm).

	Single			Nested-2A			Nested-3A			Nested-4A			Nested-5A		
Tube No.	D_m	L	t	D_m	L	t	D_m	L	t	D_m	L	t	D_m	L	t
1	120	100	1.90	60	100	2.47	80	100	1.86	60	100	2.47	40	100	1.91
2				120	90	1.90	100	90	1.81	80	90	1.86	60	90	2.47
3							120	80	1.90	100	80	1.81	80	80	1.86
4										120	70	1.90	100	70	1.81
5													120	60	1.90

Table 4.8 : Dimensions of nested tubes in case B (units: mm).

	Nested-2B			Nested-3B			Nested-4B			Nested-5B		
Tube No.	D_m	L	t	D_m	L	t	D_m	L	t	D_m	L	t
1	60	90	2.47	80	80	1.86	60	70	2.47	40	60	1.91
2	120	100	1.90	100	90	1.81	80	80	1.86	60	70	2.47
3				120	100	1.90	100	90	1.81	80	80	1.86
4							120	100	1.90	100	90	1.81
5										120	100	1.90

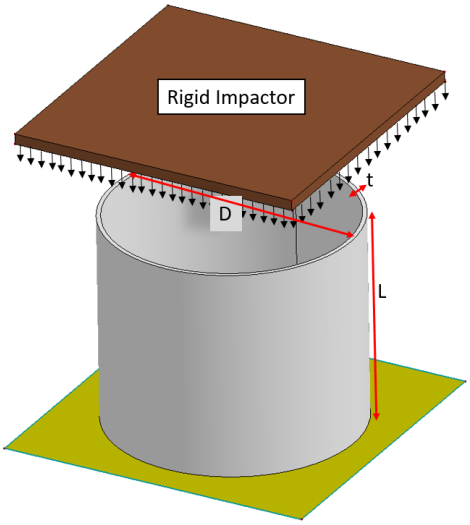

Figure 4.29 : Schematic representation of impact test.

The effect of using the conventional honeycomb filler, made of ABSplus plastic, in nested tubes is also investigated. The regular hexagonal unit cell geometry of the honeycomb filler is illustrated in Figure 4.30. The dimensions t_h, $l_h = h_h$, and θ are chosen as 1 mm, 10 mm, and 120°, respectively. The honeycomb fillers are designed in such a way that they can be inserted into the cylindrical gaps between the nested tubes. The innermost gap of the specimens is filled first with the honeycomb structure, and the next gap is not filled, as illustrated in Figure 4.31. The designs of the Nested-4A and the Nested-4B samples with honeycomb filler are illustrated in Figure 4.31.

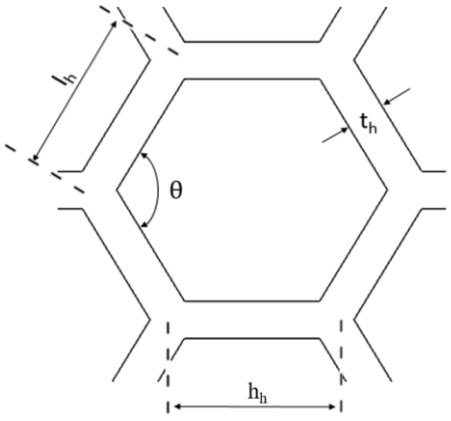

Figure 4.30 : Hexagonal unit cell of honeycomb filler.

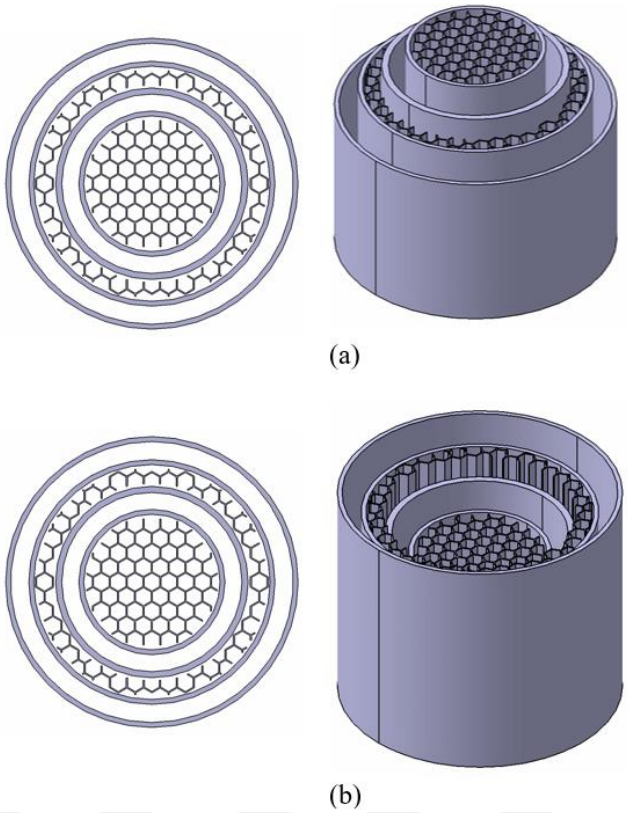

Figure 4.31 : a) Nested-4A and b) the Nested-4B samples with honeycomb filler.

4.4.2 Finite element modeling

A rigid mass is dropped on the tubes at an axial speed of 2.75 m/s, as illustrated in Figure 4.32. The Rigidwall_Planar_Moving_Forces software package is used as an impactor to model the impact test. The nodes at the bottom of the tube structure are fixed. Tubes and honeycomb fillers are modeled by Belytschko–Tsay explicit shell elements, which are the most computationally cost-effective elements and comprise 5-DOF in the local coordinate system, which yields 6-DOF globally. A mesh convergence study is performed to demonstrate the mesh quality. It is found that the optimum element size is 2 mm × 2 mm according to the results of FE analyses that are performed by changing mesh qualities parametrically. The tubes and honeycomb filler could have mutual-interaction during crushing; therefore, automatic single surface contact algorithms are identified for each individual part. In addition, automatic surface-to-surface contact interfaces are defined between surfaces of the tubes and honeycomb filler.

The MAT24 piecewise linear plasticity material model is used to define the material properties of the aluminum tube and honeycomb filler in LS-DYNA. The elastic

material properties of the tube and honeycomb filler, which were calculated from the tension tests, are introduced into this material model. True stress vs. effective plastic strain curves are determined by using engineering stress-strain curves and embedded into the MAT24 material model for defining the plastic behavior of this material.

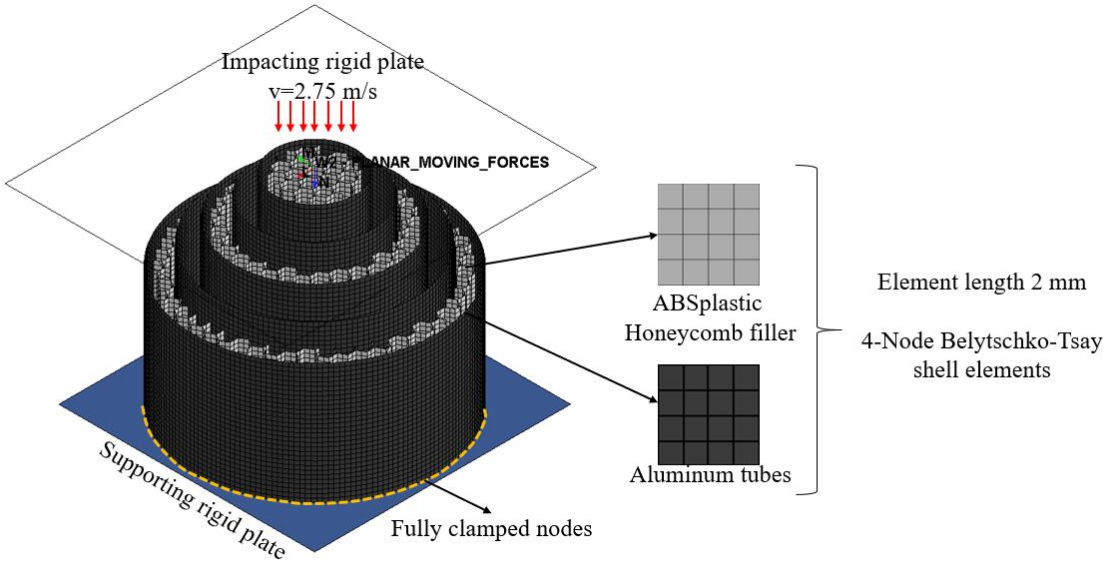

Figure 4.32 : FE model of nested aluminum tube with honeycomb filler with labeling mesh types, mesh sizes, boundaries, material types, impact velocity, and impact direction.

4.4.3 Results

4.4.3.1 Single tube

A single tube can be considered as the simplest crash box. Therefore, an empty single tube is tested and analyzed at 2.75 m/s impact velocity to better understand the advantages of nested tube structures (Figure 4.33). The tube collapsed an average of 87 mm in the concertina deformation mode (axisymmetric folding mechanism) in the three tests. The initial collapse mechanism begins from the bottom section of the tube. The reaction force variation over time obtained from the experimental and numerical results are illustrated in Figure 4.33. The FE results are in good agreement with the experimental results. Contrary to expectations, the initial *PCF* is not the maximum force in the plot. This is because the kinetic energy of the rigid impactor exceeds the energy absorbing capacity of the single tube so that the reaction force reaches a maximum value, between 35 ms and 45 ms, as illustrated in Figure 4.33.

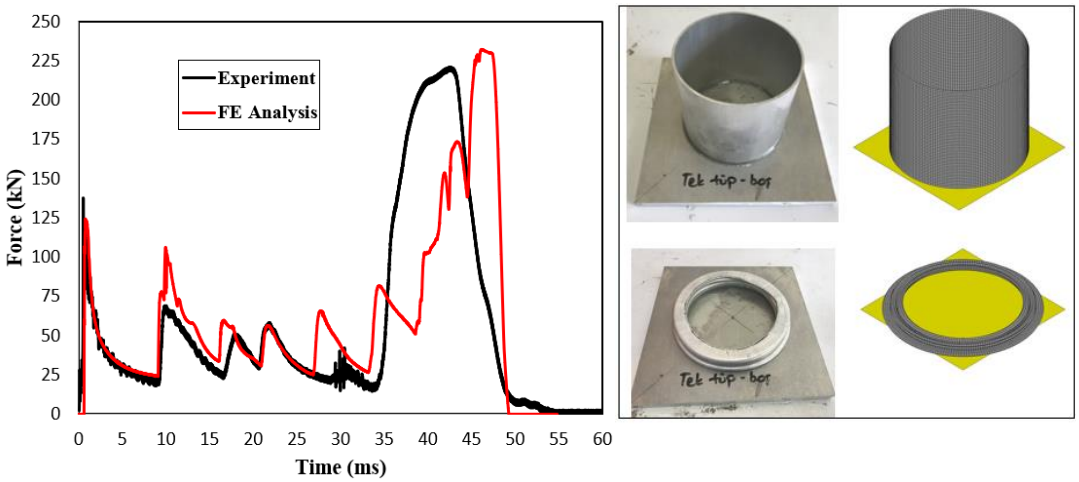

Figure 4.33 : Single tube test and FE analysis results.

4.4.3.2 Nested tubes (case A)

Double, triple, quadruple, and quintuple nested tubular structures, with and without honeycomb filler, are tested and analyzed under the same conditions as the single tube case. In the experimental study, the Nested-2A sample collapses 37 mm axially with a progressive axisymmetric folding mechanism (concertina), and deformation begins from the top section of the tubes. In the FE analyses, the outermost tube begins to deform from the bottom edge. Therefore, a slight discrepancy can be observed between the FE and the experimental results after 15 ms in Figure 4.34.a. However, in general, the results are in good agreement. In addition, the FE results of the Nested-2A sample with honeycomb filler are in good agreement with the experimental results, as illustrated in Figure 4.34b. The collapse mechanism and number of folds are similar. The maximum peak forces of the bi-tubular structures indicate that, at the time of impacting the rigid wall, with the outer tube and using honeycomb filler results in higher peak forces and less deformation.

The FE and experimental results of the first three peak forces of the innermost, middle, and outermost tubes of the Nested-3A sample, with and without honeycomb filler, are also in good agreement, as illustrated in Figure 4.35a and Figure 4.35b, respectively. The empty Nested-3A sample deforms 56 mm axially in the concertina deformation mode, and with honeycomb filler the test sample deforms 28 mm in axisymmetric deformation mode (single barreling).

The peak force levels of the Nested-4A sample, with and without honeycomb filler, increase over time, and four different peak forces related to tubes from the innermost

to the outermost can be seen in Figure 4.36 a Figure 4.36b. One axisymmetric folding deformation mode appears. The force-time history obtained from the FE analysis is in good agreement with the results obtained from tests until the end of the third peak, as illustrated in Figure 4.36a; however, the subsequent force-time history is not in agreement. Similarly, the force response of the Nested-4A sample with honeycomb filler was different from the experimentally obtained force response after the third peak force, as illustrated in Figure 4.36b. These differences also indicate the complexity of estimated contact force responses because of increasing tube numbers. These reasonable local differences do not invalidate the correlation of numerical and experimental studies.

The Nested-5A samples, with and without honeycomb fillers, are investigated under the same impact loading. The FE results are in good agreement with the experimental results in Figure 4.37a Figure 4.37b. The empty Nested-5A sample collapses 43 mm axially in axisymmetric deformation mode, and five noticeable peak forces, which are related to tubes from the innermost to the outermost, are observed. In addition, the force response of the Nested-5A sample with honeycomb filler exhibits four separate peak forces. This is because the outermost tube is not deformed, and the fifth peak force is not initiated. The Nested-5A sample with honeycomb filler deforms 38 mm axially. The honeycomb filler absorbs the excessive impact energy without causing any peak force by the outermost tube. Therefore, the outermost tube is not useful in this nested tube structure. The results indicate that using the honeycomb filler could be an effective method for reducing the number of tubes.

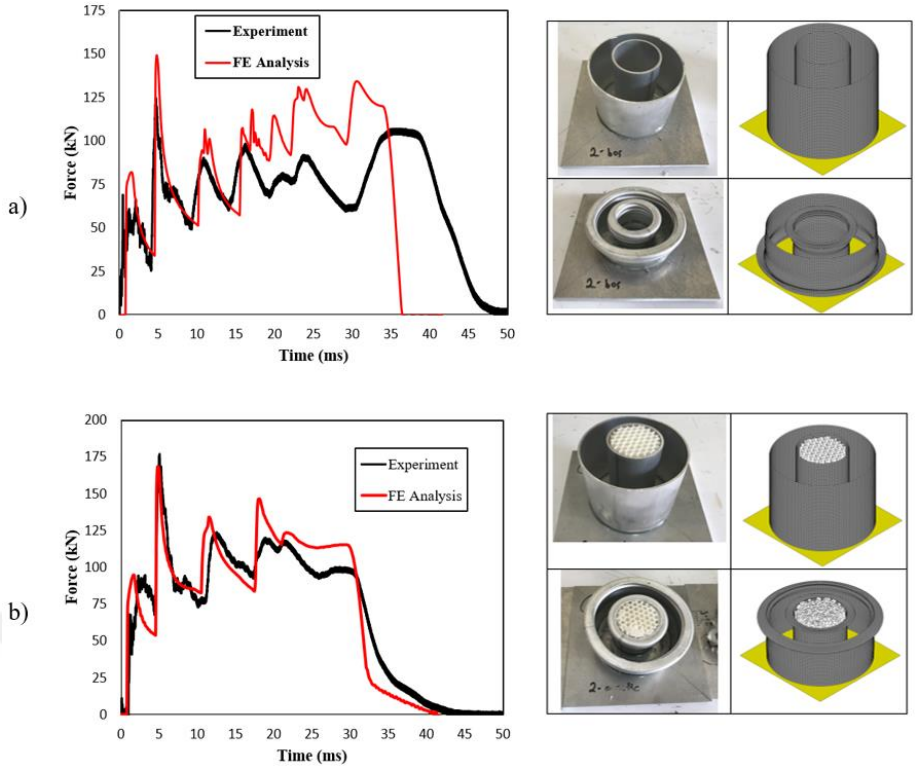

Figure 4.34 : Experiment and FE analysis results: a) empty Nested-2A and b) Nested-2A samples with honeycomb filler.

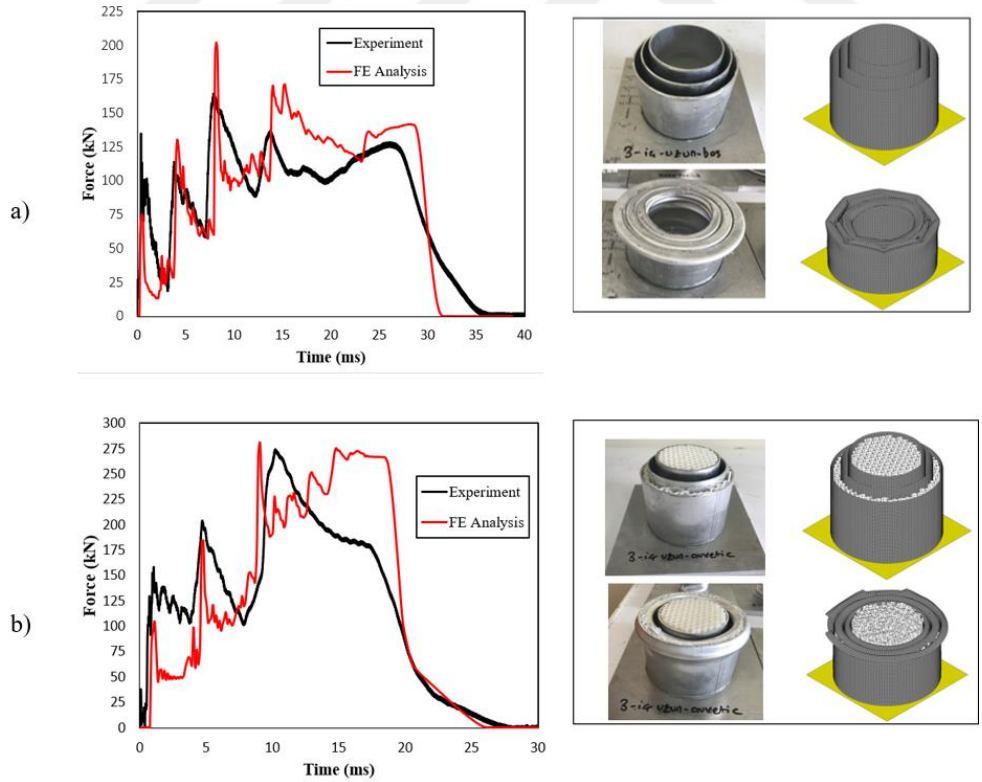

Figure 4.35 : Experiment and FE analysis results: a) empty Nested-3A and b) Nested-3A samples with honeycomb filler.

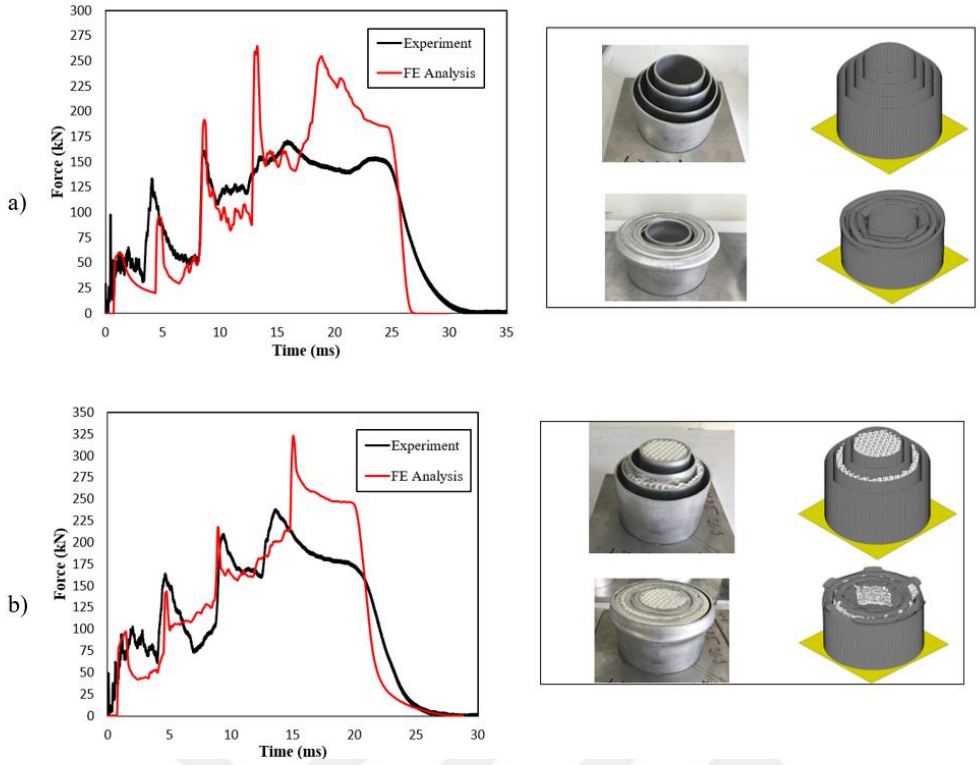

Figure 4.36 : Experiment and FE analysis results: a) empty Nested-4A and b) Nested-4A samples with honeycomb filler.

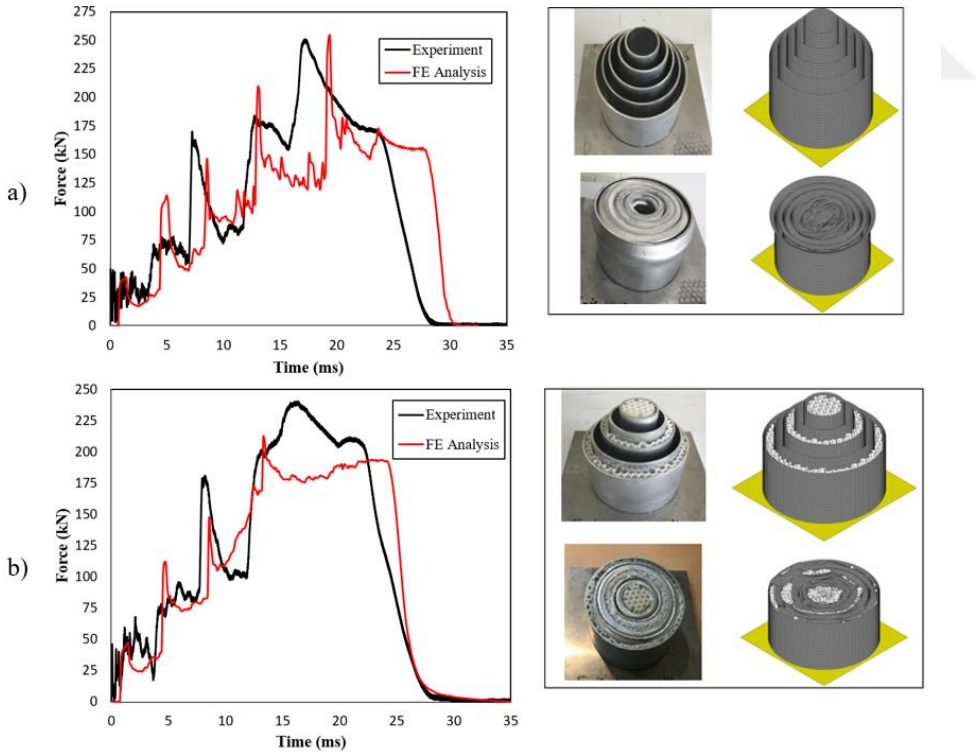

Figure 4.37 : Experiment and FE analysis results: a) empty Nested-5A and b) Nested-5A samples with honeycomb filler.

4.4.3.3 Nested tubes (case B)

For case B, the maximum length and diameter of nested tubular systems are chosen as 100 mm and 120 mm, respectively. The outermost tube is the longest and the tube lengths decrease by 10 mm each from the outermost to the innermost tubes. In this case, the effects of the tube length on the deformation behavior are investigated by testing triple, quadruple, and quintuple tubular nested tube systems.

The force response and deformation mode of empty and filled Nested-3B samples obtained from numerical and experimental studies were observed to be similar. The collapse mechanism of the empty Nested-3B sample begins from the bottom surface, as opposed to the Nested-3B sample with honeycomb filler, as illustrated in Figure 4.38 a and Figure 4.38b. The innermost and middle tubes of the empty Nested-3B sample collapse in diamond mode, and the outermost tube collapses in concertina mode in the experiment; however, they all collapse in concertina mode in the numerical analysis. These differences in mode shapes have an influence on the force response during deformation in the numerical and experimental analyses. Three peak forces can be observed in Figure 4.38a and Figure 4.38b. As opposed to case A, the initial peak force is higher, and the subsequent peak forces are close to each other. The Nested-3B with honeycomb filler collapses in mixed modes (concertina and single barreling). The third peak force becomes excessive, and a single barreling mode shape is exhibited because of the honeycomb filler in Figure 4.38b. The Nested-3B samples, with and without honeycomb filler, are axially deformed by 32 mm and 40 mm, respectively.

In Figure 4.39a, the deformation of the empty Nested-4B sample initiates from the top surfaces of the tubes, and the nested tubes collapse in the diamond mode in the experiment. The deformation and force response in the experiment and numerical analysis are similar. Using the honeycomb filler changes the collapse mechanisms, which are concertina and single barreling mode shapes, and increases the maximum peak force of the Nested-4B samples, as illustrated in Figure 4.39b. The Nested-4B samples, with and without honeycomb filler, are axially deformed by 34 mm and 37 mm, respectively.

The FE results of the Nested-5B samples, with and without honeycomb filler, are in good agreement with the experimental results. The empty Nested-5B sample collapses

in a mixed type of mode shapes (concertina and diamond modes) in Figure 4.40a. The Nested-5B sample with honeycomb filler collapses in axisymmetric folding followed by single barreling, as illustrated in Figure 4.40b. The Nested-5B samples, with and without honeycomb filler, are axially deformed by 31 mm and 37 mm, respectively. The first four tubes absorb the total kinetic energy; therefore, the fifth tube becomes redundant as an energy absorber.

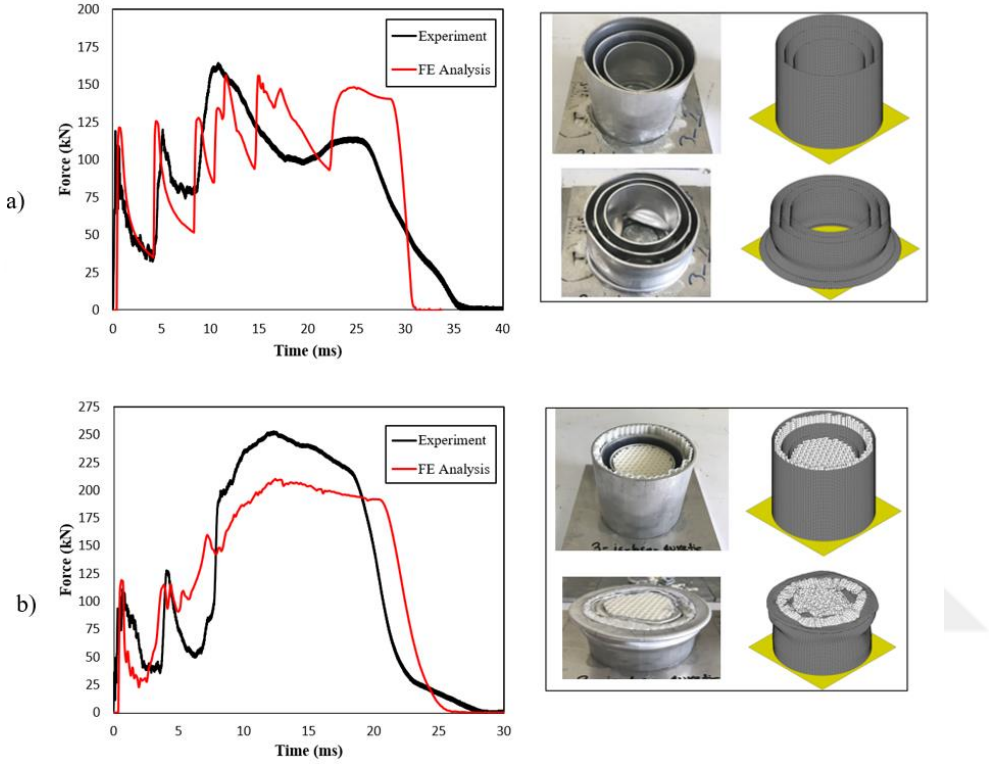

Figure 4.38 : Experiment and FE analysis results: a) empty Nested-3B and b) Nested-3B samples with honeycomb filler.

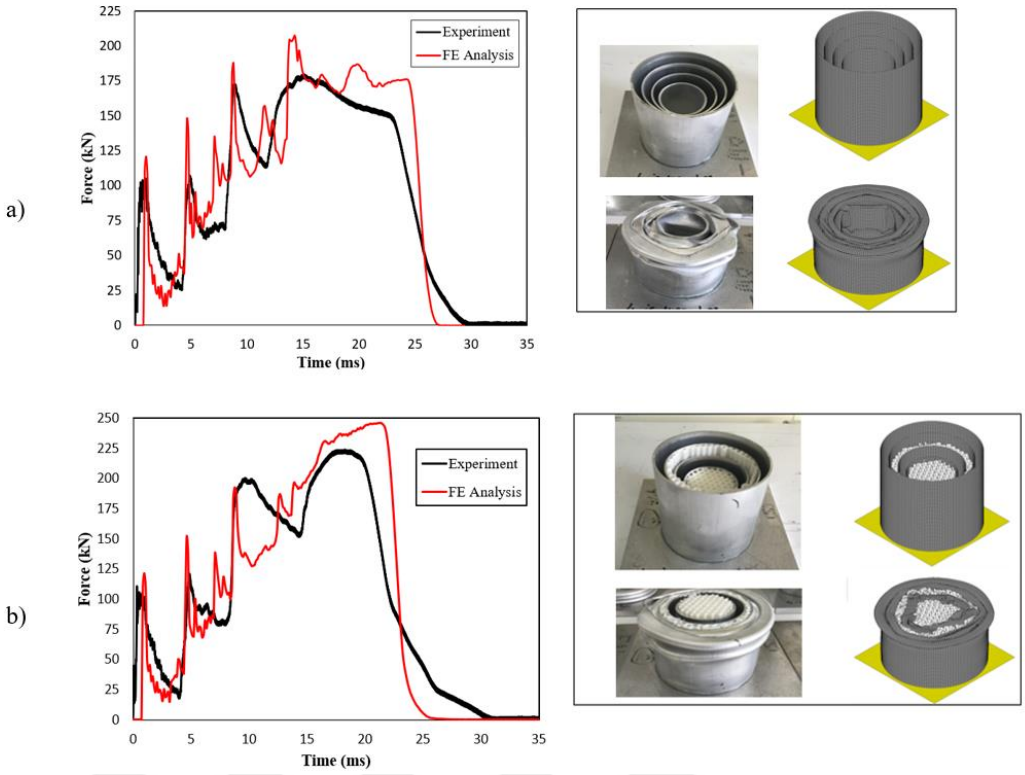

Figure 4.39 : Experiment and FE analysis results: a) empty Nested-4B and b) Nested-4B samples with honeycomb filler.

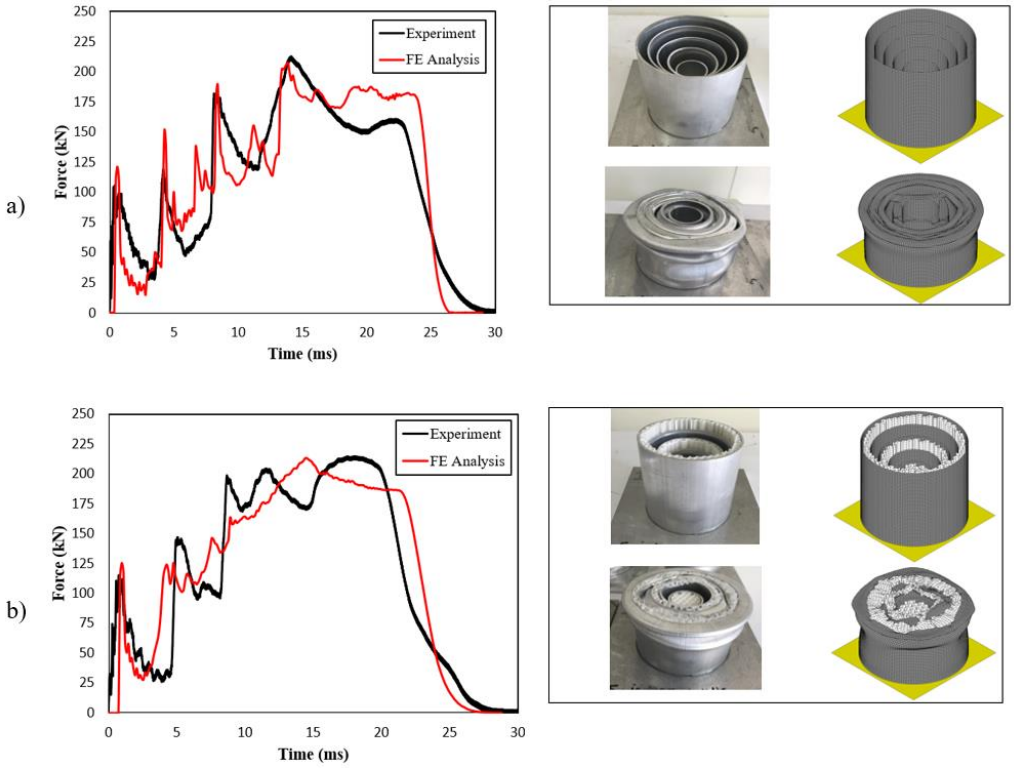

Figure 4. 40 : Experiment and FE analysis results: a) empty Nested-5B and b) Nested-5B samples with honeycomb filler.

4.4.4 Discussion

The results of the experimental and numerical studies are evaluated in terms of crashworthiness indicators, and collapse mechanisms of samples obtained from numerical simulation are discussed. The single tube test specimens with honeycomb filler, and the Nested-2B samples, with and without honeycomb filler, were not manufactured because of the lack of materials. The FE analyses of these samples are performed initially under the same conditions as the experiments, and the impactor is then dropped with higher energy at the same velocity to obtain the maximum energy absorption capacity of each sample. The results of the crashworthiness indicators for these models are illustrated in Figures 4.42-4.44.

4.4.4.1 Collapse mechanism of samples

A two-dimensional view of each crashed specimen after being cut in half is obtained from the FE analyses and presented in Figure 4.41. The empty single tube folds completely from the top to the bottom surface in a progressive folding mechanism. A critical parameter is that the width ($w = D_{m\_outer}$) to wall thickness (t) ratio of the empty tubes are in the range of $12.1 \leq w/t \leq 62.8$ mm. The radial gap between the adjacent tubes in Nested-2A and -2B samples is 20 mm, whereas it is 10 mm for other nested tubes. In particular, it was observed in the empty tubes of both cases A and B that increasing the number of tubes changes the location of the folding from the bottom to top surfaces of the specimens. This could result from both the interactions of the nested tube and increasing width to wall thickness ratios. This result indicates that the location of deformation initiation could be predicted and controlled because of the increasing number of tubes in nested tube structures, and more stabilized tubes can be obtained with the same width to wall thickness ratios in a future study.

The stress-strain relationship of foams typically has three primary regions: linear elastic, plastic collapse plateau, and densification region [160]. Honeycomb filler used in a single tube is analyzed under compressive load. The mean plateau stress is calculated as approximately 9.24 MPa between strains of 0.2 and 0.3 [161]. The compaction between the honeycomb filler and aluminum tubes begins at a strain of 0.08. The honeycomb filler in single and nested tubes increases the width to weight ratio and stiffness and limits the inward folds of aluminum tubes because of its lateral extension, which is typical behavior of other types of foams, such as aluminum foams,

in cylindrical tubes [161, 162]. In addition, gradual changes in tube lengths and using honeycomb filler have a significant influence on the deformation shape of the samples. It appears that the top points of the tubes in Nested-A samples tend to deform outward, as opposed to the inward folds in Nested-B samples. Because of its negative Poisson's ratio, auxetic cellular structures could be used as a filler to reduce the interaction between aluminum tubes and filler in a future study.

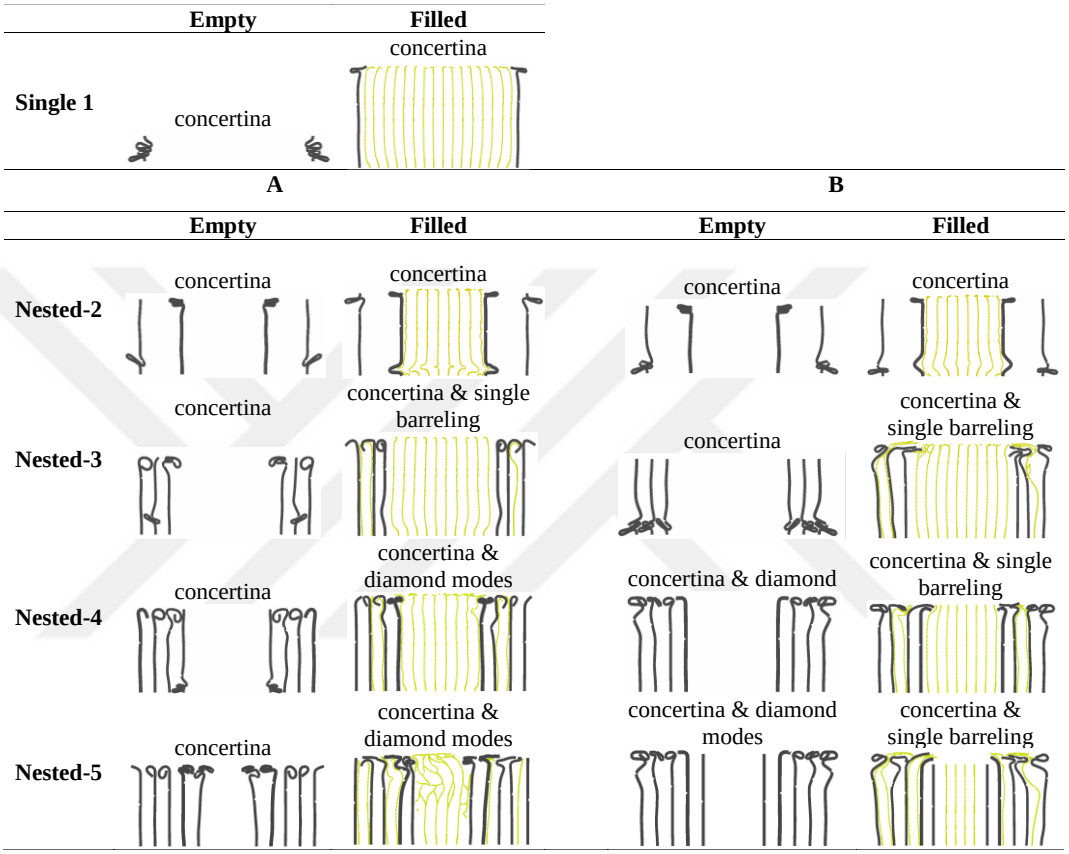

Figure 4.41 : Comparison of crashed specimens obtained from FE analyses.

4.4.4.2 Effect of honeycomb filler

Figure 4.42 illustrates the effects of using honeycomb filler on the crash behavior of nested tube structures. It can be clearly shown that using the honeycomb filler increases the peak force. This is because using honeycomb filler increases the amount of material in nested tube systems, which increases the lateral stiffness of the tube systems, and a greater force response is required. Figure 4.43 illustrates that the *SEA* values of tubes with honeycomb filler are greater than those of empty ones for Single and Nested-2A and -2B samples, which is anticipated as it was reported in similar studies in the literature [58-60]. On the other hand, using honeycomb filler in triple,

quadruple, and quintuple tubular structures for both cases A and B is approximately inefficient in increasing the *SEA* over those of empty ones. Therefore, using honeycomb filler in stepped and nested tubes comprising more than two tubes might not be recommended in terms of energy absorption capacity. The *CFE* values of nested tube structures with honeycomb filler are greater than empty tube structures in all cases except for Nested-5B samples (cases A and B). When the percentage change in *CFE* values of empty and filled tubes are compared, it can be seen that there is a decreasing trend as the number of tubes increases. This indicates that using honeycomb filler could effectively increase the *CFE* of nested tube systems comprising fewer tubes.

4.4.4.3 Effect of the number of tubes

The effect of varying the number of tubes from one to five is investigated for single and nested tube systems by choosing a constant maximum diameter of 120 mm and the maximum length of 100 mm. The *PCF* values of the double nested tube combinations (Nested-2A and -2B) are lower than single and other nested tube structures in all scenarios: case A empty tubes, case A tubes with honeycomb filler, case B empty tubes, and case B tubes with honeycomb filler.

The *SEA* values of tube structures exhibit an increasing trend as the number of tubes is increased in case A empty tubes, as illustrated in Figure 4.43. It can be concluded that nested tubes comprising gradually increased lengths of tubes from outermost to innermost can be capable of having greater *SEA* as the number of tubes is increased. When comparing the filled tubes in case A, there is a decreasing trend as the number of tubes is increased. However, it appears that it resulted primarily from the effects of using honeycomb filler in nested tubes. In addition, there is no clear trend for both empty and filled tubes in case B. In this comparison, the *SEA* values of both empty and filled Nested-2B samples are greater than those of the other examples in case B.

Figure 4.44 illustrates that the bulk of cases of the nested tubes, with and without honeycomb filler, have greater *CFE* values than single ones. In both cases A and B, the *CFE* values of empty nested tubes are approximately identical. As opposed to the filled ones, the *CFE* values decrease as the number of tubes is increased. The Nested-2A and -2B samples with honeycomb filler are the most effective models. Therefore, double nested tube combinations can be recommended by considering *CFE* values.

4.4.4.4 Effect of tube lengths

Nested tube structures in the clusters of cases A and B are compared to evaluate the effects of tube length sequence on the crash behavior. Initial *PCF*s of all tube structures in case A are lower than for case B. This is because the first impacted tube is the outermost tube with a diameter of 120 mm in case B. On the other hand, the diameters of the first impacted tubes are 40, 60, and 80 mm in case A. An increase in the diameter of the tube results in an increase in peak force. In addition, subsequent peak forces increase gradually in case A and are similar to each other in case B. Figure 4.42 illustrates that the *PCF* of the double, triple, quadruple, and quintuple nested tubular structures in case A are greater than that for case B. Even though the *SEA* values of Nested-2A and -2B samples are similar for both the empty and filled structures. It can be seen in Figure 4.43 that the *SEA* values of triple, quadruple, and quintuple nested tubular structures in case A are greater than in case B. The *CFE* values of the double, triple, quadruple, and quintuple nested tubular structures in case B are greater than those of case A, as illustrates in Figure 4.44. The results indicate that choosing tube lengths that gradually increase from the innermost to the outermost tube are better in terms of *PCF* and *CFE*.

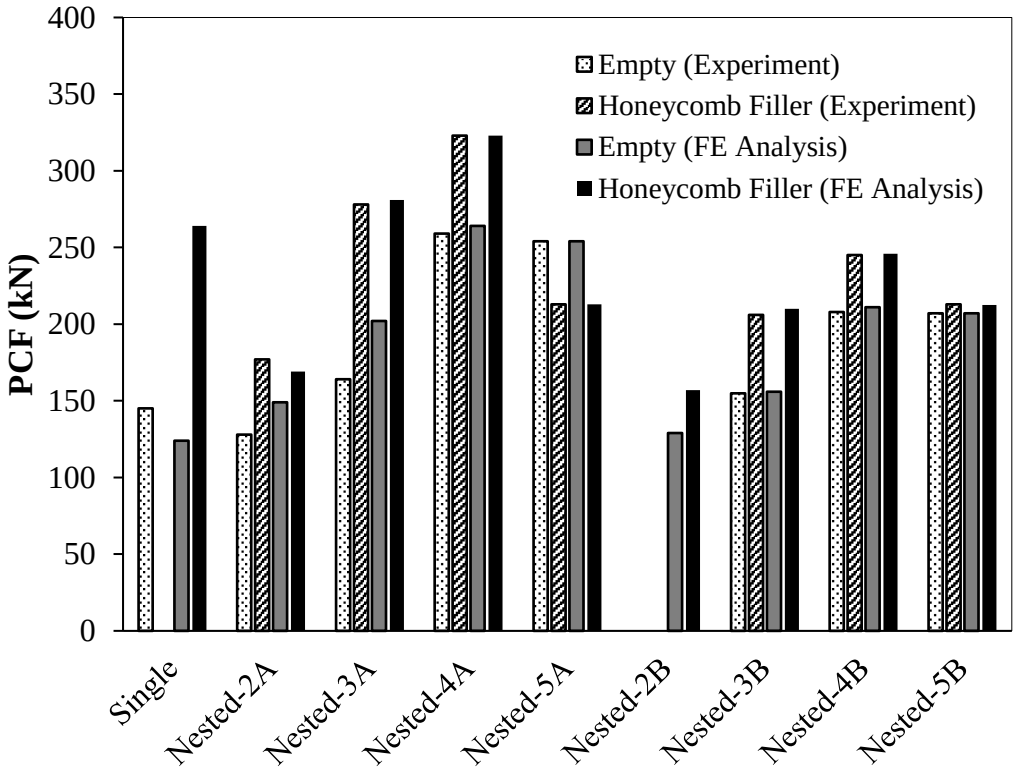

Figure 4.42 : PCF values for all cases.

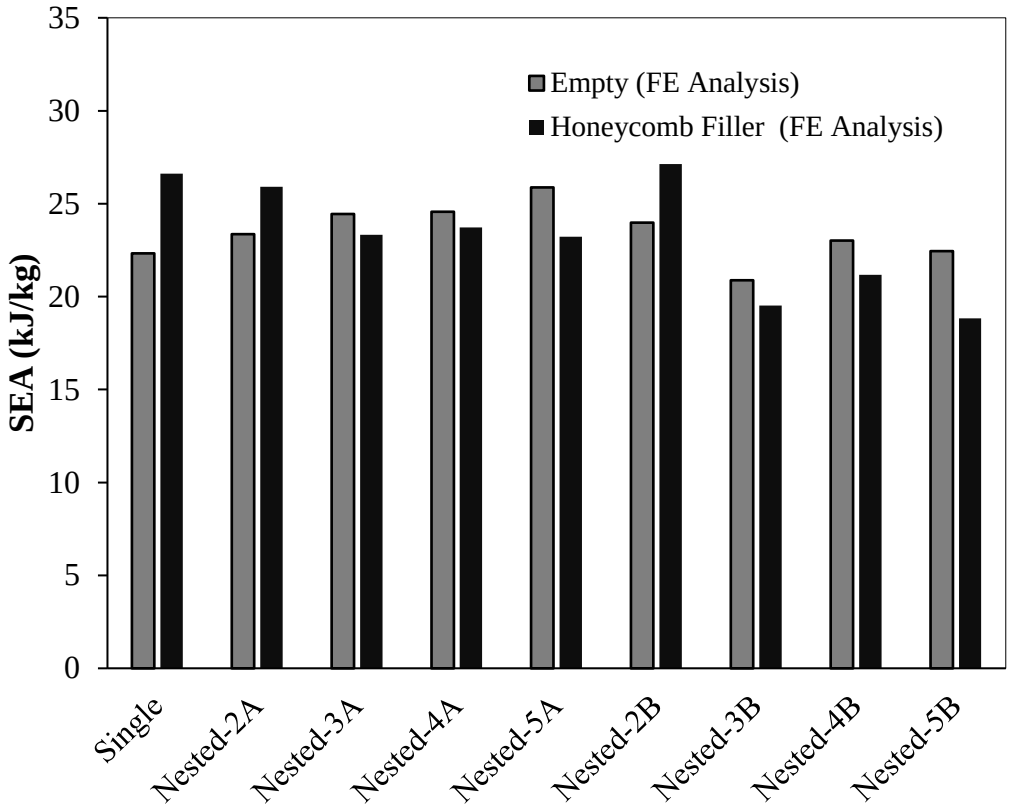

Figure 4.43 : SEA values for all cases.

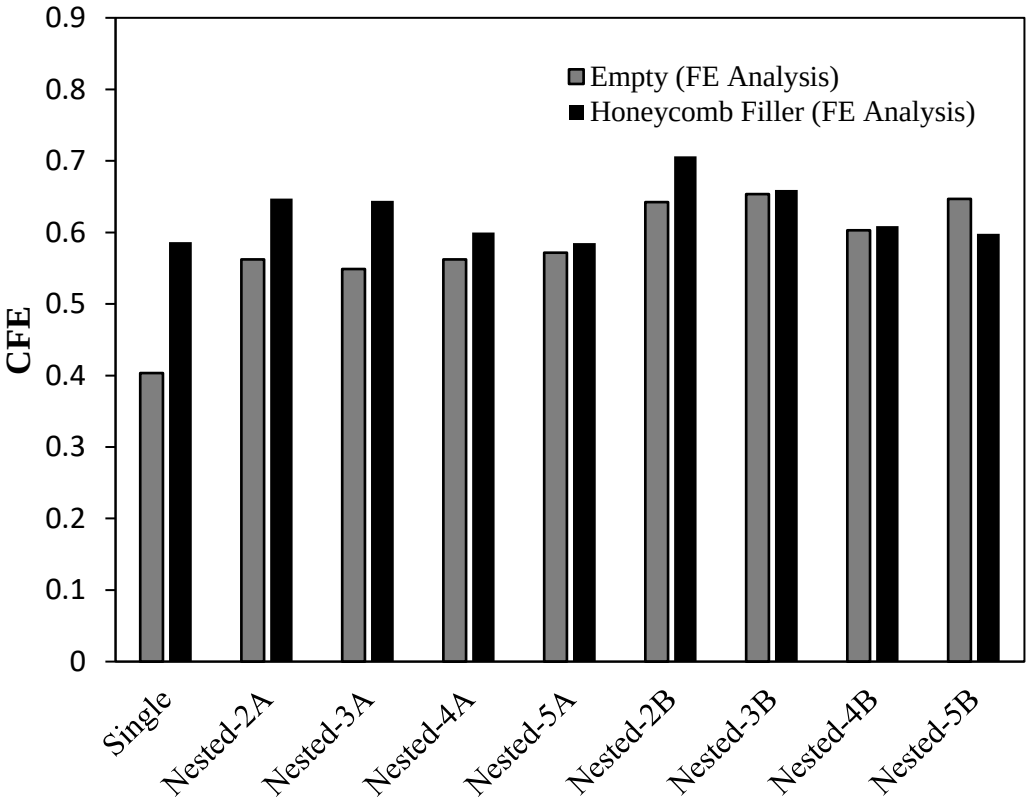

Figure 4.44 : CFE values for all cases.

4.4.5 Conclusion

In this study, the crashworthiness characteristics of axially loaded nested crash tubes made of aluminum alloy were investigated experimentally and numerically. In the experimental study, a mass was dropped at 2.75 m/s impact velocity onto the multi-tubular crash tubes by a drop test machine. Finite element analyses were performed using LS-DYNA software to investigate the design cluster and to discuss the absorbed energy, which could not be obtained from experimental results. The deformation mode and force response of one single and fourteen nested tube structures predicted by the FE code were compared and validated with those obtained from the experimental studies under dynamic loading. It was indicated that the FE models were in good agreement with the experimental results. The effects of using honeycomb filler, number of tubes, and tube lengths were evaluated from the results of the analyses, and the samples were compared in terms of common crashworthiness indicators: *PCF*, *SEA*, and *CFE*. The external dimensions of all specimens were held constant for meaningful comparisons.

Using honeycomb filler in nested tube structures affected the deformation shapes of the aluminum tubes and added mass and greater stiffness, which required greater force to collapse. Therefore, they exhibited no advantages over empty nested tubes in terms of the *PCF* indicator, as anticipated. Using honeycomb filler increased the energy absorption capabilities in all scenarios of the nested tube systems. However, it appeared that the *SEA* values of all samples with honeycomb filler were lower than for the empty samples, with the exception of the Single, Nested-2A and -2B tubular structures. Therefore, using honeycomb filler might not be recommended in nested and stepped tubular structures with increased numbers of tubes. In addition to these, the *CFE* results indicated that more efficient nested tubes could be designed by using honeycomb filler.

Results indicated that the location of deformation initiation could be controlled by increasing the number of tubes in nested tube structures, and more stabilized tubes could be provided with the same width to wall thickness ratios in a future study. The *SEA* values of tube structures exhibited an increasing trend with increasing numbers of tubes in case A for empty tubes. Empty nested tubes comprising gradually increased tube lengths from outermost to innermost tubes was recommended because of the capability of greater *SEA*s as the number of tubes was increased. All the nested tube

designs exhibited greater *CFE*s than single tubes. There was a decreasing trend in the variations in *CFE* values of nested tubes with foam filler with increasing numbers of tubes for both cases A and B. Double nested tube structures with honeycomb filler exhibited a significant amount of *CFE* and lower *PCF* values in all scenarios. Therefore, double nested tube combinations could be the best choices when considering all crashworthiness indicators simultaneously.

With the length of tubes decreasing gradually from the innermost to the outermost tubes (case A), a lower initial peak force and a gradual increase in force response was observed. However, this resulted in a higher maximum crash force (*PCF*) than the nested tubes in case B. The results indicated that the *SEA* values of the triple, quadruple, and quintuple nested tubular structures in case A were greater than in case B for both empty and filled samples. The *CFE* values of nested tubes in case B were greater than the nested tubes in case A. It could be concluded that choosing the tube length to gradually increase from the outermost to the innermost tubes had greater advantages in nested tube designs in terms of *SEA*, in particular for greater numbers of tubes, but was less efficient than tube lengths increasing gradually from the innermost to the outermost tube.

Compared to the results of nested tube structures and single tubes, providing an optimum design depended on the simultaneous evaluation of *PCF*, *SEA*, and *CFE* indicators. Overall, double nested tube structures with honeycomb filler could be the optimal choice for crash box designs.

4.5 Impact Behavior of Tapered Nested Tube Structures with and without Imperfection

In this study, the impact behavior of the tapered nested crash tube structures is examined with and without imperfection according to different cross-section types. Crash boxes are used as passive energy absorbers generally in the automotive industry. This study contributes to the literature that the comparison of different cross-section types of tapered nested tube structures. Numerical analyses are performed by using LS-DYNA, and numerical results are validated with experimental results of a nested tube structure. All specimens are made of aluminum alloy. Square, pentagon, hexagon, heptagon, octagon, nonagon, decagon, and circular cross-sectional tube structures are investigated by giving circular impactions and without imperfections. The

crashworthiness of the samples is discussed in terms of peak crash force, mean crash force, and crush force efficiency.

4.5.1 Problem definition

The number of nested tubes are selected as three tubular systems. For a good comparison, the outer radii of innermost, middle, outmost tubes are kept the same for all types of polygons and circular tubes. The outmost radius is 45 mm. The slope of the frustums is 85^{o}. In addition, the thickness of the plates and the height of the tubes are equal. Besides, the total mass of one nested tube structure is same for each sample. In Figure 4.45, it is seen that schematic views of the square tapered nested tube structure.

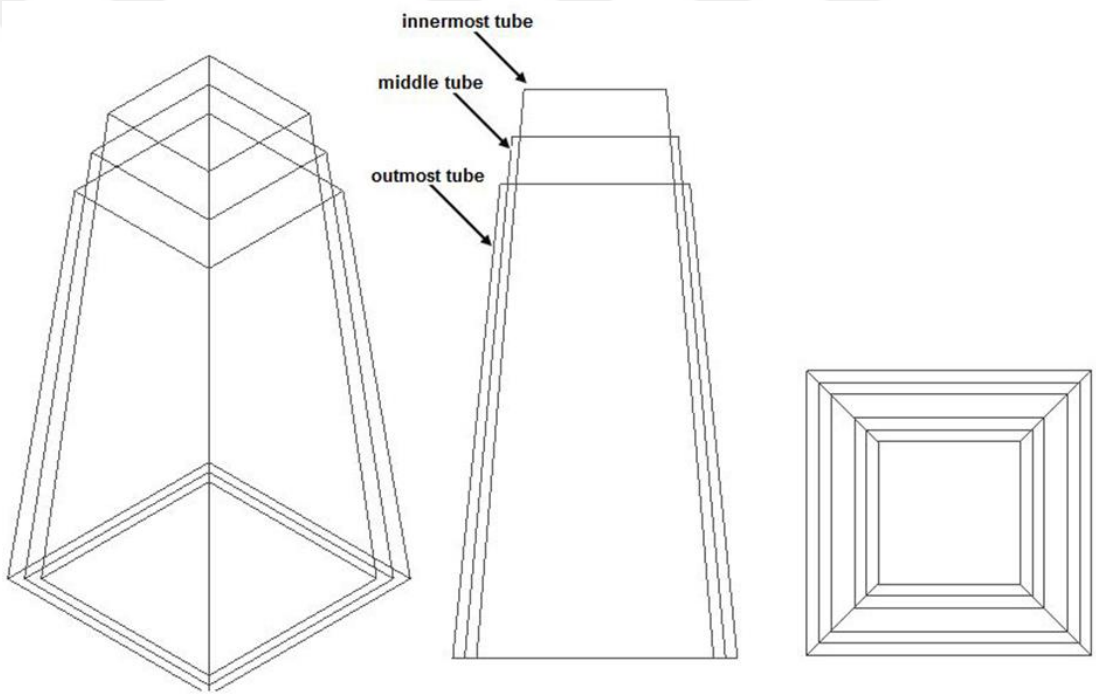

Figure 4.45 : Schematic of the square tapered nested tube structure.

In Table 4.9, the dimensions of each model are listed. There are eight different cross-section types of tapered nested tube structures. The first seven samples have cornered cross-sections, and the number of corners changes from 4 to 10. The eighth sample is selected as circular cross-section. For the cornered tubes, the parameter of ‘a’ in the table represents the length of the one side of the regular polygonal cross-section, and parameter ‘L’ represents the length of the tubes.

Table 4.9 : Dimensions of samples.

Cross section	Location	a	L	t	**Cross section**	Location	a	L	t
Square	Innermost	90	100	2	Octagon	Innermost	37.3	100	2
	Middle	80	110	2		Middle	33.1	110	2
	Outmost	70	120	2		Outmost	29	120	2
Pentagon	Innermost	65.4	100	2	Nonagon	Innermost	32.8	100	2
	Middle	58.1	110	2		Middle	29.1	110	2
	Outmost	50.9	120	2		Outmost	25.5	120	2
Hexagon	Innermost	52	100	2	Decagon	Innermost	29.2	100	2
	Middle	46.2	110	2		Middle	26	110	2
	Outmost	40.4	120	2		Outmost	22.7	120	2
Heptagon	Innermost	43.3	100	2	Circular (a=r)	Innermost	45	100	2
	Middle	38.4	110	2		Middle	40	110	2
	Outmost	33.6	120	2		Outmost	35	120	2

4.5.2 Finite element modeling

Tubes are modeled by using Piecewise_Linear_Plasticity in LS-DYNA. The rigid mass, which is defined as Rigidwall_Planar_Moving_Forces, is impacted axially to the tube structures. The nodes at the bottom of the specimens are clamped. Tubes are modeled by using Belytschko-Lin-Tsay-4-node-thin shell elements. During crushing, tube structures interact with each other or expose to the self-folding mechanism. Therefore, Automatic_Single_Surface and Automatic_Surface_to_Surface contact types are defined.

4.5.3 Results and discussion

The deformed and undeformed shapes of eight different tapered nested tube structures are demonstrated in Figure 4.46.

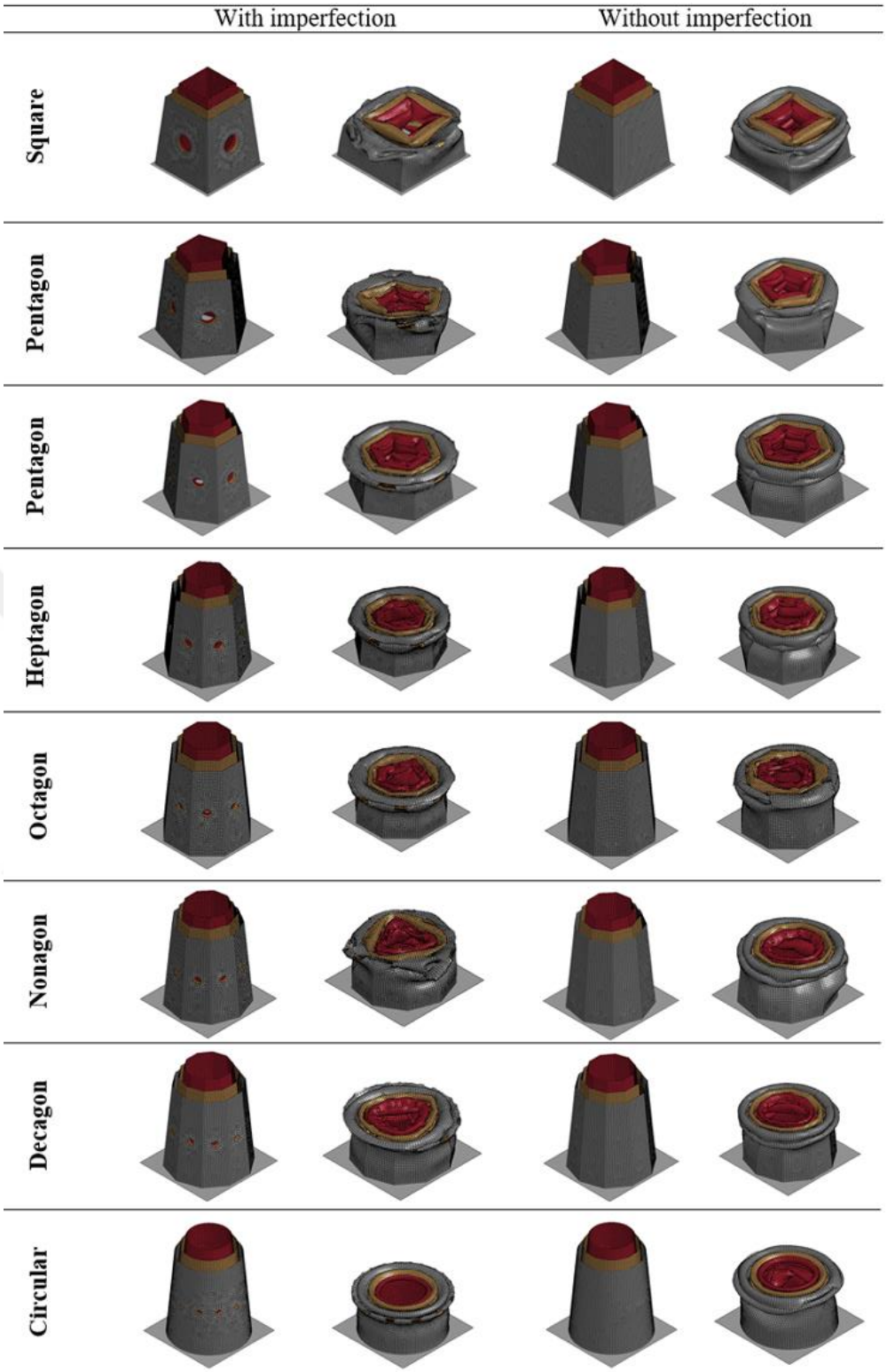

Figure 4.46 : Undeformed and deformed the shape of optimum tube systems for different weight functions.

In Table 4.10, it is denoted that when the number of corner increases, SEA and CFE increase and PCF values reduce, although a few results cause a violation. Besides, the nested and tapered circular tube gives a remarkably higher SEA and CFE and lower

peak values than the nested and tapered box with square cross-section. These results show that increasing the number of the corner has advantages over square cross-sectional nested and tapered tubes in terms of energy absorption capacity and peak forces.

PCF and CFE values of tubes with imperfection are lower, and SEA values are higher than the tubes without imperfection. SEA values depend on the total mass of the tube structure. Imperfection reduces the total mass of the structures; therefore, they can give higher SEA values. CFE values of the tube with imperfection are lower due to reducing the stiffness of the structure.

Table 4.10 : Results of FE analyses.

	PCF (kN)		**SEA (J/kg)**		**CFE**	
	a	b	a	b	a	b
Square	147.75	163.63	12.760	12.045	0.531	0.535
Pentagon	143.28	154.00	13.772	13.152	0.572	0.584
Hexagon	141.30	150.97	14.133	13.770	0.586	0.624
Heptagon	144.02	150.47	14.384	14.208	0.565	0.634
Octagon	146.06	147.86	14.649	14.360	0.558	0.659
Nonagon	136.44	152.48	14.898	14.600	0.610	0.607
Decagon	140.57	149.82	14.776	14.727	0.569	0.622
Circular	136.37	142.83	15.588	15.263	0.614	0.644

As a result, the effects of the number of corners and the imperfections to the frustums on the CFE, MFC and PFC values are investigated. The results show that increasing the number of the corner has advantages in terms of energy absorption capacity and peak forces. Besides, the imperfection method can reduce the initial peak force, but still, it can reduce the energy absorption capacity due to reducing the stiffness of tube structures.

4.6 Crashworthiness Optimization of Nested and Concentric Circular Tubes Using Response Surface Methodology and Genetic Algorithm

In this study, crashworthiness optimization of nested and concentric circular tubes under impact loading is performed by the coupling Finite Element model, Response

Surface Models and Genetic Algorithm. Specific Energy Absorption (SEA) and Crash Force Efficiency (CFE) are used in crashworthiness optimization since these criteria are important indicators for evaluating crashworthiness performance. The length and thickness of three concentric tubes as well as the radius of one tube, are adopted as design variables, which are effective parameters on SEA and CFE. To reduce the computational cost of the optimization procedure, simple and computationally cheap Response Surface Models are created to replace finite element analyses in further calculations. The Non-dominated Sorting Genetic Algorithm –II (NSGAII) is applied to obtain the Pareto optimal solutions. Optimization results are presented for different selected designs that indicate the relative importance of multi-objective functions. Results show that the total weight of the vehicles can be reduced by using nested tubes comparing to single tubes with identical masses. These designs can be adapted for use in practice.

4.6.1 Finite element model

In this study, the Finite Element model of the nested and concentric circular tri-tubular system is used in obtaining SEA and CFE responses required in optimization. Nested and concentric circular tri-tubular system employed is shown in Figure 4.47. L_1, L_2 and L_3 indicate the length of tubes, t_1, t_2 and t_3 denote the thickness of tubes, and r_2 indicates the radius of the middle tube. A nested and concentric circular tri-tubular system is crushed in the axial direction by an 1132 kg rigid mass with a 4.22 m/s initial velocity. The bottom line nodes of all tri-tubes are clamped, while top nodes of the three tubes are constrained except axial direction due to provide deformation behavior. Tubes are modeled by using Belytschko-Lin-Tsay-4-node thin shell elements with three integration points through the thickness and one integration point in the element plane. The element size of 2 x 2 mm is found to be sufficient and suitable to simulate the crushing deformation of tubes (29160 elements, 29491 nodes). Automatic contact algorithms are activated to prevent penetration of tube surfaces after deformation. The static and dynamic friction coefficients are chosen as 0.2 and 0.3, respectively. In FE analysis, the tube system is considered made of Aluminum 6063. The following material properties for Aluminum 6063 is used in this study. Density is $\rho = 2700$ kg/m^3, Young's modulus is E = 68.2 GPa, initial yield stress is σ_y= 80 MPa, ultimate stress is σ_u= 173 MPa, and Poisson's ratio is υ = 0.3.

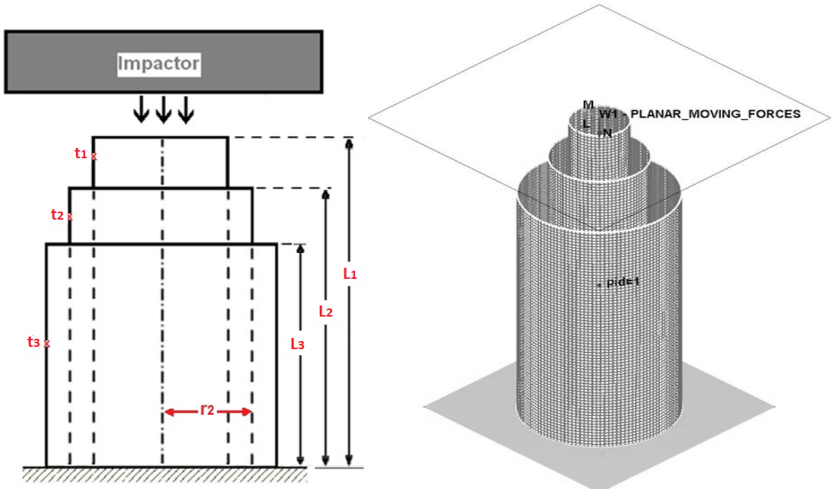

Figure 4.47 : Concentric circular tri-tubular structure and FE model.

In order to validate the FE model, the FE analysis result of the tri-tubular circular tubes under axial dynamical loading is compared with experimental results as shown in Figure 4.48. The experiment is conducted by using the drop-tower test facility of the Scientific and Technological Research Council of Turkey (TUBITAK). 1132 kg drop weight is released from a height that provides approximately 10 kJ. From the comparison, it is seen that the FE response is very close to the experimental result, and therefore it can be concluded that the FE model can be used in producing crush responses used in optimization.

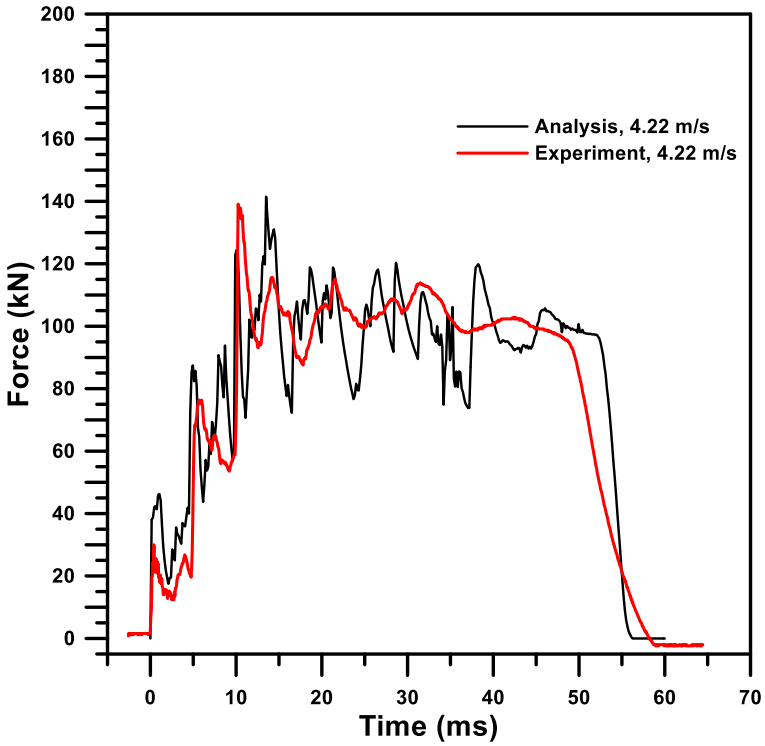

Figure 4.48 : Comparison of experiment and numerical analysis (V = 4.22 m/s).

4.6.2 Optimization procedure

In order to evaluate the crashworthiness of the thin-walled structures, it is essential to define crashworthiness indicators. Energy Absorption (EA), Specific Energy Absorption (SEA), Mean Crushing Force (MCF), and Crash Force Efficiency (CFE) are usually used as the important indicators for evaluating crashworthiness performance [163]. Energy absorption of a structure subjected to the axial loading can be expressed as:

The flowchart of the optimization procedure adopted in this study is shown in Figure 4.49. Details of optimization steps are explained in the following sections.

4.6.3 Formulation of the optimization problem

In this study, optimization of the tri-tubular nested and concentric circular tube system is formulated as a multi-objective constrained optimization problem. CFE and SEA criteria are used in expressing objective functions expressed as f_1 and f_2 successively. For optimum crashworthiness design, objective functions are desired to be maximized.

In the multi-objective optimization procedure adopted in this study, multi-objective particle swarm optimization (MOPSO) method is used. Considering multi-objective and constraint functions, the optimization problem is formulated in equation (4.1).

Maximize $F = f_1 + f_2$

subject to

$$\begin{gathered} 150 \leq L_1 \leq 200 \\ 150 \leq L_2 \leq 200 \\ 150 \leq L_3 \leq 200 \\ 1 \leq t_1 \leq 3 \\ 1 \leq t_2 \leq 3 \\ 1 \leq t_3 \leq 3 \\ 23 \leq r_2 \leq 32 \end{gathered} \tag{4.1}$$

4.6.4 Response surface models for optimization criteria

In order to reduce the computational cost of the optimization problem with many design variables, simple approximate models are used to replace the costly original objective and constraint functions, which are calculated using expensive FE analysis. Simple approximate models are often referred to as Response Surface (RS) models and are obtained using Response Surface Method (RSM). In this study, RS models are used for SEA and CFE criteria during optimization. RSM was originally developed for the model fitting of physical experiments by Box and Draper [164] and later adopted in other fields.

In RSM, the polynomial model is selected first to approximate the actual function. Often quadratic polynomial models are selected. Quadratic models can be written in equation (4.2).

$$f = c_0 + \sum_{i=1}^{n} c_i x_i + \sum_{i=1}^{n}\sum_{j=1}^{n} c_{ij} x_i x_j + \cdots \tag{4.2}$$

where x_i is variables that the function depends on. c_0, c_i, and c_{ij} are tuning parameters, and n is the number of variables. Then, the Design of Experiment (DOE) method is selected according to the order of polynomial function and the number of design variables. Full Factorial DOE is a good choice for a few design variables. For large number of design variables, often a subset of Full Factorial DOE is selected using a suitable selection criterion such as the D-optimality selection criterion. Then, FE analyses corresponding to the DOE table are conducted to calculate function values. Finally, the polynomial model is fitted to the created data set corresponding to DOE table using the least-squares method. The steps of the RSM is summarized in Figure 4.50.

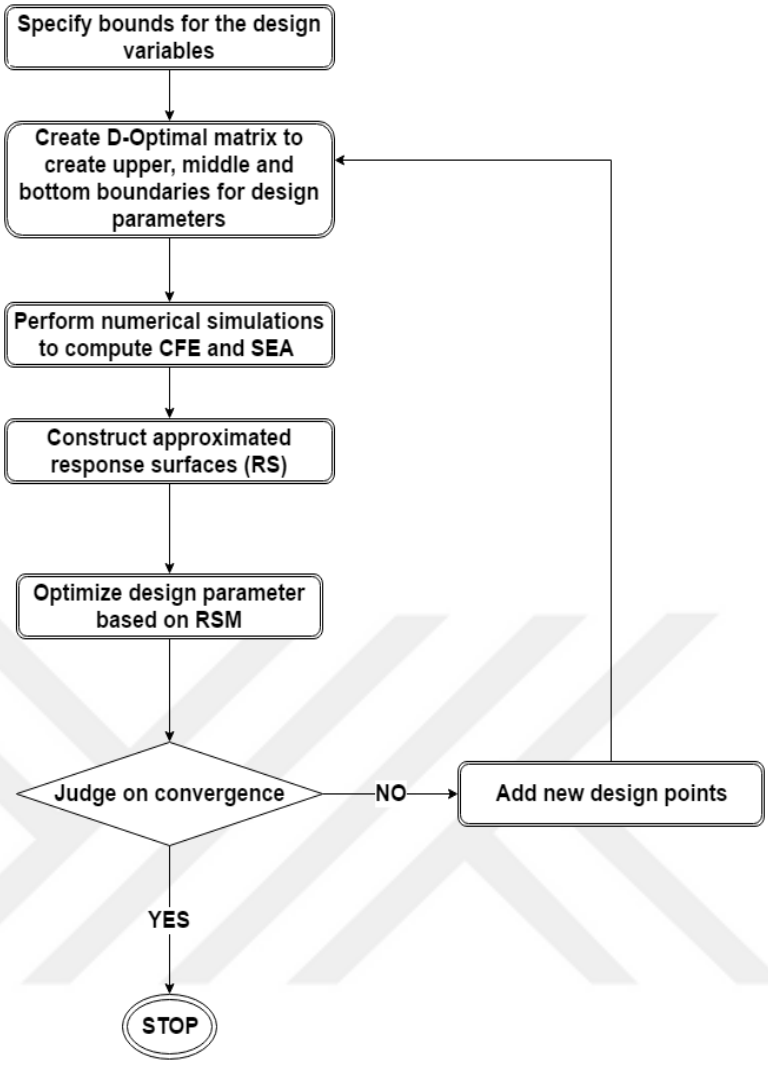

Figure 4.49 : Flowchart of the optimization process.

In this study, a subset of a three-level Full Factorial DOE is selected using the D-optimality criterion. The subset includes 45 experiments, which is sufficient enough to fit a quadratic function for 7 variables. To implement RSM, a MATLAB code is written.

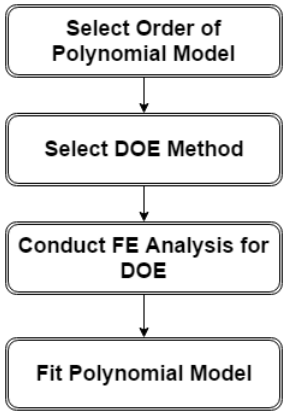

Figure 4.50 : Steps of RSM.

The ranges of design variables used in creating the DOE table are shown in Table 4.11. Resulting in the DOE table and corresponding function values for SEA and CFE criteria are given in Table 4.12.

Table 4.11 : Ranges of design variables used in the DOE table.

		Lower (mm)	Upper (mm)
Parameter 1	Length of the innermost tube, L_1	150	200
Parameter 2	Length of middle tube, L_2	150	200
Parameter 3	Length of the outmost tube, L_3	150	200
Parameter 4	Thickness of the innermost tube, t_1	1	3
Parameter 5	Thickness of the middle tube, t_2	1	3
Parameter 6	Thickness of the outmost tube, t_3	1	3
Parameter 7	Radius of middle tube, r_2	23	32

Table 4.12 : DOE table used in creating RS models.

Design No.	L_1 (mm)	L_2 (mm)	L_3 (mm)	t_1 (mm)	t_2 (mm)	t_3 (mm)	r_2 (mm)	SEA (kJ/kg)	F_{max} (kN)	CFE
1	150	175	150	2	1	2	27.5	27.67	157	0.42
2	200	150	150	3	3	1	23	23.26	130	0.60
3	200	150	150	3	1	3	32	18.54	144	0.50
4	200	150	200	1	3	3	32	14.24	188	0.57
5	150	150	150	3	1	3	23	20.91	169	0.69
6	150	150	200	3	1	1	23	32.40	142	0.40
7	150	150	150	1	1	3	32	23.54	140	0.61
8	175	150	150	1	1	1	23	48.83	123	0.49
9	200	200	150	3	3	3	32	12.76	208	0.66
10	200	150	200	3	3	3	23	13.60	196	0.67
11	150	200	150	1	3	3	32	14.94	174	0.64
12	200	200	200	1	1	1	23	37.80	333	0.16
13	200	200	200	1	3	3	23	14.45	193	0.68
14	200	150	150	1	3	1	32	25.20	127	0.50
15	150	200	150	3	1	3	32	18.93	173	0.45
16	200	175	150	1	2	3	23	20.30	157	0.47
17	200	200	150	3	1	1	23	30.09	78	0.79
18	150	150	200	1	1	1	32	39.18	430	0.12
19	150	200	150	1	2	1	23	33.79	165	0.34
20	200	200	150	1	3	1	23	16.89	185	0.54
21	200	200	150	1	1	3	27.5	22.25	133	0.48
22	150	200	175	1	1	3	23	21.17	124	0.57
23	200	150	200	3	1	1	32	27.05	103	0.54
24	175	150	200	3	1	3	27.5	16.38	165	0.59
25	150	150	200	1	2	3	23	17.79	148	0.59
26	150	200	150	3	3	1	32	18.45	134	0.68

Table 4.12 (continued) : DOE table used in creating RS models.

27	150	175	175	3	3	3	27.5	13.98	228	0.70
28	200	175	200	1	1	3	32	18.08	126	0.64
29	175	200	175	1	2	2	32	20.04	123	0.55
30	200	200	200	3	3	1	32	16.29	154	0.71
31	175	150	150	2	3	3	32	15.66	205	0.56
32	200	200	200	3	1	3	23	14.97	168	0.64
33	150	150	200	3	3	2	32	15.87	169	0.54
34	200	200	150	1	1	1	32	38.29	235	0.23
35	200	150	175	2	1	2	23	25.14	98	0.62
36	150	200	200	3	1	1	32	27.88	130	0.44
37	175	200	150	3	3	3	23	14.86	214	0.53
38	150	150	175	2	3	1	23	26.99	118	0.64
39	200	150	200	1	2	1	27.5	30.63	101	0.56
40	150	150	150	3	2	1	32	26.38	121	0.71
41	150	150	150	1	3	2	23	23.97	147	0.68
42	150	200	200	3	3	2	23	16.13	156	0.72
43	150	200	200	1	3	1	32	20.02	110	0.72
44	175	175	200	1	3	1	23	25.97	106	0.62
45	10	200	200	2	2	3	32	14.28	169	0.68

RS models for f_1=SEA and f_2=CFE are given as follows:

$$
\begin{aligned}
f_1 = {} & 231.889010 + 0.571470 * L_1 - 0.476764 * L_2 - 1.168656 * L_3 \\
& - 15.072271 * t_1 - 17.153109 * t_2 - 32.213825 * t_3 \\
& - 1.857914 * r_2 - 0.002040 * {L_1}^2 - 0.000330 * L_1 * L_2 \\
& + 0.000389 * L_1 * L_3 - 0.001148 * L_1 * t_1 - 0.013376 * L_1 * t_2 \\
& + 0.019219 * L_1 * t_3 + 0.003070 * L_1 * r_2 + 0.000325 * L_2^2 \\
& + 0.001060 * L_2 * L_3 + 0.014181 * L_2 * t_1 - 0.020717 * L_2 \\
& * t_2 + 0.037345 * L_2 * t_3 + 0.004300 * L_2 * r_2 \\
& + 0.002253 * {L_3}^2 + 0.004103 * L_3 * t_1 + 0.037217 * L_3 * t_2 \\
& - 0.002252 * L_2 * t_3 - 0.000068 * L_3 * r_2 + 0.887080 * {t_1}^2 \\
& + 1.346279 * t_1 * t_2 + 1.014347 * t_1 * t_3 + 0.049750 * t_1 * r_2 \\
& + 0.862942 * {t_2}^2 + 2.462641 * t_2 * t_3 + 0.032040 * t_2 * r_2 \\
& + 1.918523 * t_3^2 + 0.082639 * t_3 * r_2 + 0.000140 * r_2^2
\end{aligned}
\tag{4.3}
$$

$$f_2 = -0.965422 + 0.006601 * L_1 - 0.020759 * L_2 + 0.021284 * L_3 - 0.091727 * t_1 - 0.011542 * t_2 - 0.145493 * t_3 + 0.076866 * r_2 - 0.000025 * L_1^2 + 0.000016 * L_1 * L_2 + 0.000022 * L_1 * L_3 + 0.000791 * L_1 * t_1 - 0.001449 * L_1 * t_2 - 0.000548 * L_1 * t_3 - 0.000063 * L_1 * r_2 + 0.000000 * L_2^2 + 0.000047 * L_2 * L_3 + 0.000999 * L_2 * t_1 + 0.001299 * L_2 * t_2 + 0.000335 * L_2 * t_3 + 0.000161 * L_2 * r_2 - 0.000116 * L_3^2 - 0.000293 * L_3 * t_1 + 0.001403 * L_3 * t_2 + 0.001347 * L_3 * t_3 + 0.000088 * L_3 * r_2 + 0.034847 * t_1^2 - 0.040104 * t_1 * t_2 - 0.049482 * t_1 * t_3 - 0.002872 * t_1 * r_2 - 0.017323 * t_2^2 - 0.029434 * t_2 * t_3 + 0.002706 * t_2 * r_2 + 0.026728 * t_3^2 + 0.001158 * t_3 * r_2 - 0.002054 * r_2^2 \quad (4.4)$$

Fitted values and actual values (FE results) for SEA and CFE are compared in Figure 4.51 and Figure 4.52. It is seen that a good correlation exists between the RS model and FE results. Therefore, RS models can be used in the optimization of concentric circular tri-tubular systems.

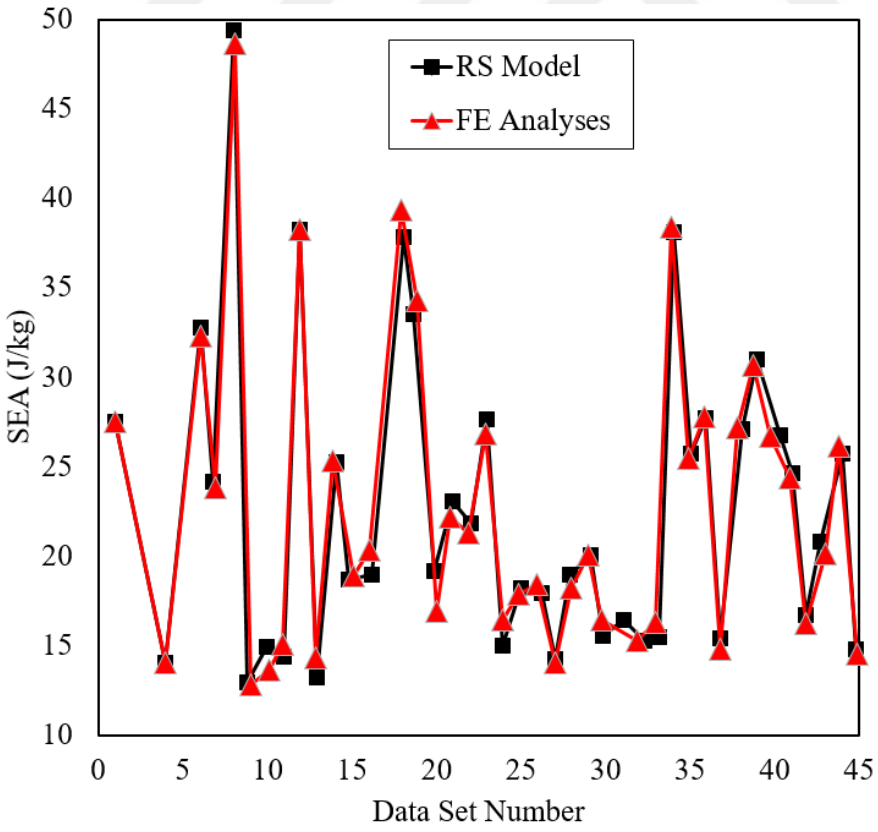

Figure 4.51 : Fitted and actual values for SEA.

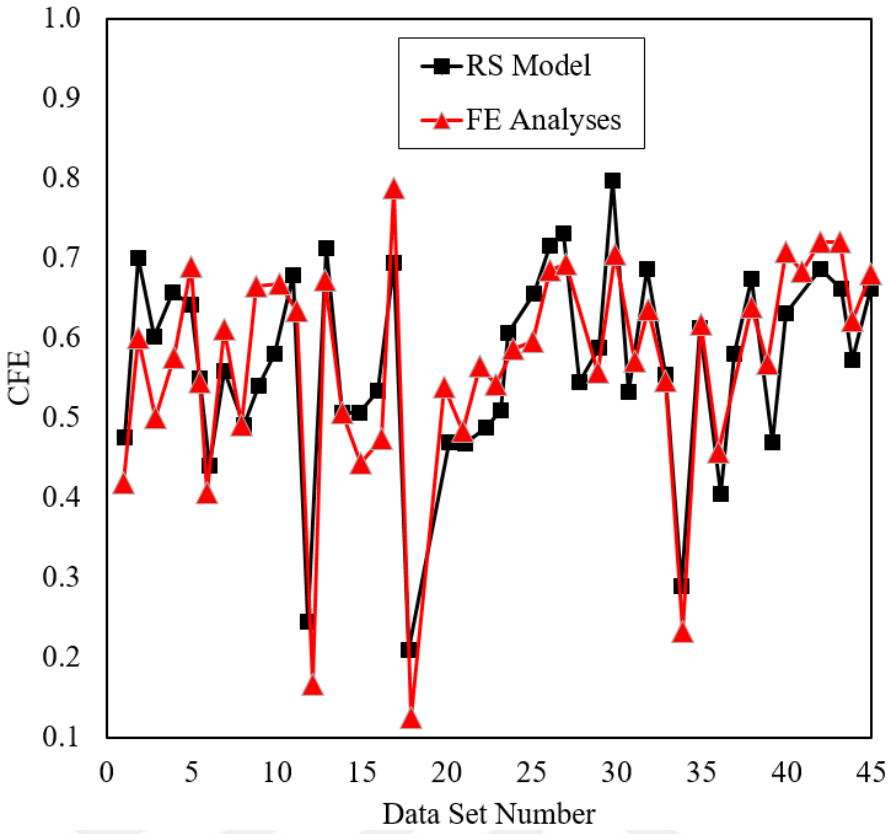

Figure 4.52 : Fitted and actual values for CFE.

4.6.5 Solution of optimization problem

The optimization problem formulated in equations (4.1)-(4.2) is solved using Genetic Algorithm (GA).

GA is coupled with the RS models to yield a global optimum as shown in Figure 4.53. The GA solves the optimization problem by simulating the biological evolution process based on Darwin's theory of survival of the fittest. First, a set of potential solutions referred to as population or chromosomes is selected. New and improved solutions are then generated using the previous solutions based on the crossover and mutation technique. This process repeats until optimum values are reached. The critical parameters in GAs are the size of the population, cross over rate, mutation rate and the number of generations. Detailed information about GA can be found in the [165].

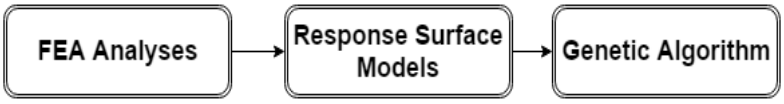

Figure 4.53 : Coupling of FE Analyses, RS models and GA for crashworthiness optimization.

The Non-dominated Sorting Genetic Algorithm –II (NSGAII) is applied to obtain the Pareto optimal solutions [166]. Table 4.13 indicates the values of NSGAII parameters for the considered problem, which provides results with good repeatability.

Table 4.13 : Parameter specifications for the NSGA-II.

Population size	200
Repository size	25
Number of generation	1000
Crossover probability	%80
Mutation probability	%20

In this section, multi-objective optimization results of the concentric circular tri-tubular system are presented for different CFE and SEA values. The multi optimization method provides Pareto optimal sets for nested and concentric circular tubes. The Pareto optimal frontier provides a set of solutions according to CFE and SEA values, shown graphically in Figure 4.54.

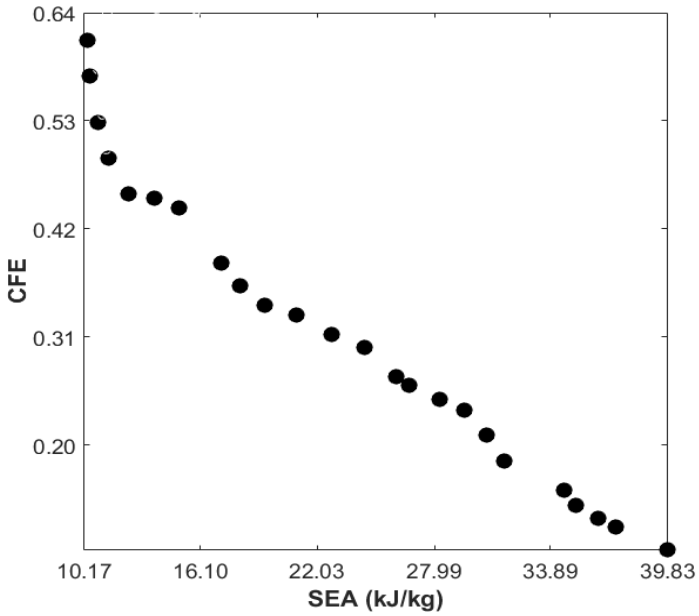

Figure 4.54 : Pareto frontier for nested and concentric circular tubes.

The solution of the optimization problem expressed in equations (4.1)-(4.2) is conducted with GA. Optimum values of design variables found are shown in Table 4.14. SEA and CFE values at optimum are compared for the RS model and FE analysis. Undeformed and deformed shapes of optimum tube structures under impact for different SEA and CFE values are demonstrated in Figure 4.55.

Table 4.14 : Optimum values of design variables for concentric circular tubes.

Design no	L1 (mm)	L2 (mm)	L3 (mm)	t1 (mm)	t2 (mm)	t3 (mm)	r2 (mm)	SEA Opt. (kJ/kg)	SEA FE (kJ/kg)	CFE Opt.	CFE FE
1	150.00	200.00	200.00	1.00	1.00	1.00	23.00	39.83	39.70	0.09	0.16
2	151.25	200.00	198.24	1.00	1.03	1.05	23.00	38.91	38.50	0.12	0.18
3	150.00	200.00	200.00	1.00	1.00	1.30	23.00	36.09	34.20	0.13	0.25
4	150.00	200.00	199.55	1.00	1.00	1.39	23.00	35.05	32.93	0.14	0.28
5	150.00	198.49	200.00	1.14	1.00	1.41	23.00	34.07	32.08	0.16	0.29
6	150.72	197.19	200.00	1.00	1.00	1.62	23.00	32.61	29.87	0.18	0.33
7	150.32	197.10	199.53	1.30	1.03	1.49	23.00	32.09	30.25	0.19	0.41
8	150.00	200.00	200.00	1.26	1.00	1.75	23.00	29.75	27.55	0.20	0.38
9	150.00	198.75	198.45	1.39	1.00	1.76	23.23	28.89	27.19	0.23	0.45
10	152.11	199.00	198.68	1.41	1.06	1.87	23.23	27.36	25.85	0.27	0.43
11	150.00	188.51	200.00	1.26	1.00	1.92	32.00	25.29	24.33	0.29	0.53
12	150.00	200.00	199.50	1.38	1.05	2.25	23.08	24.37	22.79	0.30	0.73
13	150.00	198.10	200.00	1.61	1.00	2.29	23.00	23.42	22.25	0.31	0.70
14	150.91	151.84	200.00	2.21	1.00	1.89	32.00	21.66	23.62	0.32	0.50
15	150.00	150.00	200.00	2.25	1.00	1.98	32.00	20.61	22.97	0.33	0.72
16	150.00	151.25	199.83	2.56	1.00	1.99	32.00	19.54	22.25	0.35	0.62
17	152.56	151.37	199.85	2.31	1.00	2.30	31.94	17.97	20.66	0.37	0.72
18	150.19	150.16	200.00	2.38	1.05	2.45	32.00	16.24	19.64	0.39	0.71
19	151.08	150.00	199.46	2.03	1.00	2.70	32.00	15.77	19.04	0.42	0.62
20	200.00	200.00	150.00	1.37	3.00	2.52	23.00	11.53	17.86	0.46	0.68
21	200.00	199.30	150.00	1.62	3.00	2.43	32.00	11.22	15.29	0.49	0.62
22	200.00	200.00	153.97	1.86	3.00	2.63	31.78	10.76	14.44	0.54	0.64
23	200.00	199.23	158.92	1.95	3.00	2.06	31.14	10.74	15.70	0.59	0.72
24	200.00	200.00	162.26	1.85	3.00	2.51	31.99	10.30	14.37	0.60	0.75
25	200.00	200.00	163.72	2.39	3.00	2.44	26.17	10.12	15.19	0.66	0.75

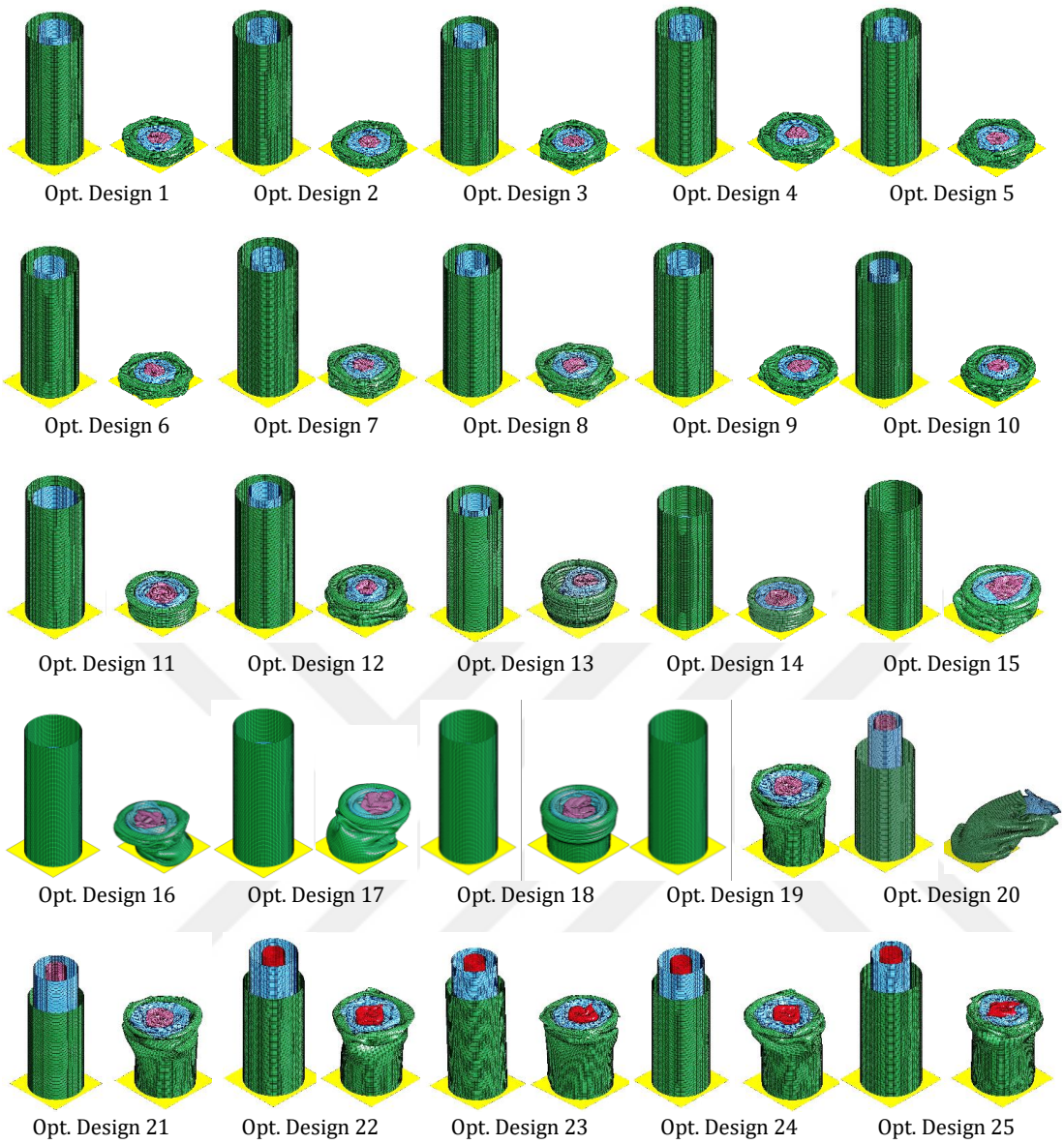

Figure 4.55 : Undeformed and deformed shape of optimum tube systems for different SEA and CFE values.

Results show that SEA and CFE values obtained from optimization models and FE analyses are sufficiently close. It indicates that quadratic polynomial function is accurate enough for concentric circular tri-tubular structures. CFE values from optimization results are lower than the values from FE analyses, and SEA values are similar for all optimum designs.

In Table 4.15, it is seen that the values of optimum design lengths, thicknesses and radius change according to SEA and CFE values. The innermost tube tends to increase with the higher SEA and lower CFE from 150 to 200 mm. On the other hand, the length of the outmost tube becomes lower for higher SEA and lower CFE. Besides, the

thicknesses of every tube become higher values with the increase of SEA and reduction of CFE. The results prove that optimum designs show a tendency to reduce the weight of the tube systems due to obtaining better SEA results. The radius of the middle tube, which is another design parameter becomes nearly at limit values 23 and 32 mm for each design.

Table 4.15 : Comparison of single and optimum nested tube results.

	SEA (kJ/kg)			CFE		
Design no	Single Tube Type 1	Single Tube Type 2	Nested Tube	Single Tube Type 1	Single Tube Type 2	Nested Tube
1	37.99	39.51	39.70	0.70	0.44	0.16
2	36.70	38.30	38.50	0.24	0.55	0.18
3	32.38	33.94	34.20	0.66	0.39	0.25
4	31.03	32.66	32.93	0.53	0.41	0.28
5	30.19	31.84	32.08	0.67	0.48	0.29
6	27.94	29.58	29.87	0.48	0.42	0.33
7	28.35	30.01	30.25	0.48	0.40	0.41
8	25.67	27.28	27.55	0.46	0.60	0.38
9	25.27	26.93	27.19	0.50	0.55	0.45
10	23.68	25.35	25.85	0.46	0.62	0.43
11	22.80	23.97	24.33	0.49	0.62	0.53
12	20.80	22.51	22.79	0.53	0.64	0.73
13	20.26	21.99	22.25	0.61	0.64	0.70
14	22.09	23.44	23.62	0.76	0.63	0.50
15	21.42	22.79	22.97	0.62	0.63	0.72
16	20.75	22.12	22.25	0.79	0.64	0.62
17	19.07	20.45	20.66	0.86	0.60	0.72
18	18.02	19.43	19.64	0.85	0.61	0.71
19	17.36	18.78	19.04	0.85	0.62	0.62
20	15.98	17.77	17.86	0.79	0.68	0.68
21	13.73	14.97	15.29	0.87	0.75	0.62
22	12.85	14.11	14.44	0.70	0.83	0.64
23	14.18	15.42	15.70	0.24	0.75	0.72
24	12.83	14.03	14.37	0.66	0.75	0.75
25	13.44	15.01	15.19	0.53	0.71	0.75

Crash tubes are used traditionally as single tube structures in the automotive industry. Therefore, the results of optimum designs of nested tubes structures are compared with the results of two different types of single tube structures in Table 4.15. In Table 5,

single tubes corresponding to a design have no identical mass values. In Single Tube Type 1, radius and length values correspond to average values in those of nested tubes shown in Figure 4.56. In Single Tube Type 2, radius and length values correspond to maximum values in those of nested tubes.

In comparison with the results, nested tubes give higher CFE values only for a few designs. The axial displacement and peak crash force values should be lower to obtain higher CFE values. It can be said that the stiffness of nested tubes should be increased to prevent more deflection in the axial direction and the gaps between the tubes should be increased to reduce contact forces.

On the other hand, the SEA values of each type are similar. SEA values of Nested Tubes are higher than Single Tube Type 1 and 2. The results show that nested tubes have more advantages in terms of SEA values. Therefore, the total weight of the structure can be reduced by using nested tube structures.

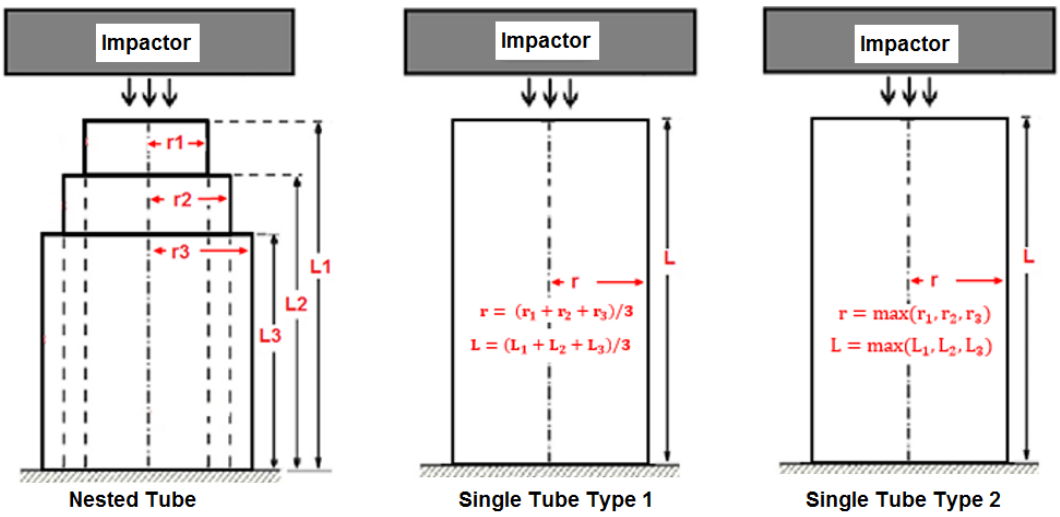

Figure 4.56 : Schematic views of nested and single tube structures.

4.6.6 Conclusion

In this study, optimization was carried out in order to improve the crashworthiness performance of nested and concentric circular tubes. SEA and CFE were considered as a performance measure for crashworthiness. Specific Energy Absorption and Crash Force Efficiency were calculated using Explicit Finite Element analysis. For further calculations in the optimization procedure, FE Analyses were replaced with RS models in order to reduce the computational cost. RS models for SEA and CFE were coupled with the Genetic Algorithm to find optimum design variables, and the multi-objective

optimization procedure was performed to maximize the objective function of SEA and CFE. NSGAII was applied to obtain the Pareto optimal solutions, and the Pareto optimal frontier was plotted. The length and thickness of three concentric tubes as well as the radius of one tube were considered as design variables.

25 different optimum crash tube models were obtained by using a multi-objective optimization method. Peak force and SEA values of optimum designs of nested tube structures were compared with the results of two different types of circular tube structures having identical masses. From the design point of view, it was observed that nested tubes had no advantages according to single tubes for the CFE criterion. To increase the CFE values of nested tube structures, the stiffness of each tube and the gaps between nested tubes should be increased.

On the other hand, optimum designs gave better results than the single tube types in terms of SEA values. Therefore, nested tubes could provide lower weight to the vehicles.

5. CONCLUSIONS

Sandwich panels and thin-walled tubes have a large use in engineering applications ranging from transportation vehicles to storage vessels thanks to the lightweight, energy dissipation capacity, tailorability, etc. Panels and tubular structures studied here are widely used as a member of air vehicles. From an engineering perspective, in this thesis, we have focused on integrated structures, e.g., sandwich panels and filled tubes with auxetic and non-auxetic core structures in order to improve crashworthiness and energy absorption capacity. Some novel designs of auxetic lattice have been developed, and then mainly the effects of curvature and unit cell geometry of the sandwich panels and filled tubes have been investigated by using experimental and numerical techniques under low and high-velocity impact loads.

First, we focused on the development of novel auxetic lattices as the core structure of sandwich panels and crash tubes. We introduce a novel type of auxetic open cell assembly with asymmetrical unit cells along the two edge sides and a new architectural design with the modified thickness of unit cells. This study also introduces a novel type of composite open cells honeycombs with the PLA plastic reinforcements, hydrogel and polyurethane rigid (PUR) foam over a hierarchical cellular platform. Overall, this study has shown that strength, stiffness and energy absorption of cellular metamaterials can be increased by using slotted unit cells and asymmetric cells along the edge of the lattice assemblies and composite open cells honeycombs with the PLA plastic reinforcements, hydrogel and polyurethane rigid (PUR) foam. Our new designs also contribute to tailor the deformation mechanism of the lattices under compression and provide more stable and predictable deformation patterns under crushing.

Second, we mainly focused on the effects of different types of auxetic and non-auxetic core structures and curvature of panels on the composite sandwich panels. In addition, effects of thickness and curvature on the composite plates are examined, and an optimization study of curved plates has been performed based on these objectives. The principal results of these studies are summarized below:

- The study of low-velocity impact resistance of the flat composite sandwich panels indicates that composite sandwich panels with PUR foam core could be a good choice considering their lightweight especially for the lower impact energy cases. However, it could not withstand without full perforation as the increase of impact energies due to very low impact resistance of foam core. In the case of higher impact, sandwich panels with auxetic structures provided great resistance under large deformation thanks to increasing the amount of material flowing into the impact region and material concentration. Double arrowhead and hexachiral core composite sandwiches are highly recommended over re-entrant, hexagonal and PUR foam core ones.
- The study of the high-velocity impact on the doubly curved sandwich panels indicates that the penetration depth of the re-entrant core doubly curved sandwich panel is greater than flat re-entrant sandwich panel, unlike flat foam core sandwich core are fully perforated and doubly curved foam core sandwich panels are not.
- The study of single and doubly curved sandwich panels indicates that the increase of the radius of curvature of these structures brings a higher resistance against the damage from a projectile impact. A selected toroidal sandwich panel is then parametrically analyzed by impacting the projectile on different points of its surface. The results show that the indentation resistance of the impacted location is lower on the center point and on locations close to the clamped edges. Most of the impact energy is absorbed by the auxetic core rather than by the composite face sheets.
- The impact behavior of flat and cylindrical composite panels at the high-velocity impact of projectiles was compared for two different thicknesses. The results of analyses were compared and discussed in terms of absorbed energy, contact forces, reaction forces, backplane displacement and residual velocity of the panels. The absorbed energy of the top and bottom plies are higher than those of interior plies. Contact forces of the cylindrical panels are higher than those for flat panels. Ply vibration leads to high contact force. The deformed zone occurs at a local area for flat and cylindrical panels. Penetration values of the projectile for cylindrical panels are higher than those for flat panels.

- The results of the multiobjective optimization study show that reduction of the radius of curvature causes increasing SEA and maximum backplane displacement. By changing stacking sequences, the impact behavior of panels can be improved.

Third, we have conducted studies on crash tubes subjected to axially quasi-static compression or low-velocity impact loading. The effects of filler types, curvature, tube numbers, cross-section and imperfection on the crashworthiness performance of the single and multi-tube systems are examined and the results from experiments, FE analyses and optimization are provided in order to get better designs in terms of crashworthiness indicators. The unit cell of 3D printed fillers is composed of re-entrant and hexagonal configurations. In addition to traditional tube structures, nested tube structures, which I have also studied in my MSc thesis, are investigated by implementing fillers. The principal results of these studies are summarized as below:

- Comparing to single triggered and non-triggered tubes with and without auxetic honeycomb structure under low-velocity impact loading, triggered tubes are obviously better in terms of peak crash force and crush force efficiency, and re-entrant honeycomb brings two times the higher mass of specimen so that *SEA* values of specimens with auxetic lattices are lower than empty tubes.
- The results of the impact tests on single circular tubes with and without auxetic lattices show that using auxetic core has advantages over empty tubes in terms of MCF and CFE, but empty tubes can provide higher SEA rather than tubes with the auxetic core.
- The results of single, double, triple, quadruple, and quintuple tubular structures with and without honeycomb filler indicate that using honeycomb filler in nested tube structures affected the deformation shapes of the aluminum tubes and increases energy absorption capabilities but reduces SEA due to higher mass. Deformation initiation can be controlled by increasing the number of tubes in nested tube structures. The nested tubes possessing gradually increased tube length from the outermost to the innermost tubes has greater advantages in nested tube designs in terms of *SEA*, in particular for greater numbers of

tubes unlike having less efficiency. Overall, double nested tube structures with honeycomb filler could be the optimal choice for crash box designs.

- The study of tapered and imperfect nested tubes shows that the imperfection method reduces the peak load, increases stability and achieves uniform responses, but, still, it has a disadvantage that can reduce the energy absorption capacity by reducing the stiffness of the energy absorber.
- In addition, optimum nested tubes designs having advantages over the single tube types are obtained by performing the multi-objective optimization method algorithm.

5.1 Recommendations and Suggestions for Future Research

The activities related to novel auxetic hierarchical lattices will be conducted by theoretical, numerical and experimental methods. The hierarchies used here in re-entrant auxetic cells will also apply to the chiral, arrowhead and missing rib auxetic cellular structures. Multi-objective optimization algorithms based on the Response Surface Method and Genetic Algorithm are developed. Best designs are determined according to the two objectives: higher energy absorption capacity and compressive strength. Optimal designs will be printed by using the 3D printer machine with ABS or PLA plastic filament. Composite auxetic structures will be manufactured by inserting polyurethane foam into the slots of 3D printed cellular structures. All specimens are tested under quasi-static compression and impact loading.

Additionally, to the best of the authors' knowledge, the high-velocity impact behavior of composite doubly curved sandwich panels with foam core and auxetic honeycomb core have not been presented yet in the open literature. We will conduct a parametric FE analysis study performing in order to search the effects of curvature and impact angle of doubly curved sandwich panels studied in this thesis.

REFERENCES

[1] **Hedayati, R. & Sadighi, M.** (2015). *Bird strike: an experimental, theoretical and numerical investigation.* Woodhead Publishing.

[2] **Goraj, Z. J., and Kustron, K**. (2018). Review of current research trends in bird strike and hail impact simulations on wing leading edge, *Aircraft Engineering and Aerospace Technology*, *90*(4).

[3] **Neidigk, S. (2013).** Detection and characterization of impact damage in carbon fiber aircraft fuselage structure. (Master Thesis). The University of New Mexico, Albuquerque, New Mexico.

[4] **Fatt, M.S.H., and Park, K.S.** (2001). Dynamic models for low-velocity impact damage of composite sandwich panels – Part A: Deformation, *Composite Structures*, *52*(3), 335–351.

[5] **Gustin, J., Joneson, A., Mahinfalah, M., and Stone, J.** (2005). Low velocity impact of combination Kevlar/carbon fiber sandwich composites, *Composite Structures*, *69*(4), 396-406.

[6] **Hosur, M. V., Mohammed, A. A., Zainuddin, S., and Jeelani, S.** (2008). Impact performance of nanophased foam core sandwich composites, *Materials Science and Engineering: A*, *498*(1-2), 100-109.

[7] **Caprino, G., and Teti, R.** (1994). Impact and post-impact behavior of foam core sandwich structures, *Composite Structures*, *29*(1), 47-55.

[8] **Sharma, S. C., Narasimha Murthy, H. N., and Krishna, M.** (2004). Low-velocity impact response of polyurethane foam composite sandwich structures, *Journal of Reinforced Plastics and Composites*, *23*(17), 1869-1882.

[9] **Zhang, G., Wang, B., Ma, L., Wu, L., Pan, S., and Yang, J.** (2014). Energy absorption and low velocity impact response of polyurethane foam filled pyramidal lattice core sandwich panels, *Composite Structures*, 108, 304-310.

[10] **Njuguna, J., Michałowski, S., Pielichowski, K., Kayvantash, K., and Walton, A. C**. (2011). Fabrication, characterization and low-velocity impact testing of hybrid sandwich composites with polyurethane/layered silicate foam cores, *Polymer Composites*, *32*(1), 6-13.

[11] **Vinson, J. R.** (1989). *The behavior of thin walled structures: beams, plates, and shells*. Kluwer Academic Publishers.

[12] **Altenbach, H., and Eremeyev, V.** (2017). *Thin-walled structural elements: Classification, classical and advanced theories, new applications*, In Shell-like Structures, pp.1-62.

[13] **Cantwell, W. J., and Morton, J.** (1989). Comparison of the low and high velocity impact response of CFRP, *Composites*, *20*(6), 545-551.

[14] **Nettles, A. T., and Douglas, M. J.** (2000). A comparison of quasi-static indentation to low-velocity impact, (Report no: TP--2000-210481), NASA report.

[15] **Sjoblom, P. O., Hartness, J. T., and Cordell, T. M.** (1988). On low-velocity impact testing of composite materials, *Journal of Composite Materials*, *22*(1), 30-52.

[16] **Lee, M., and Cho, Y. J.** (2011). Characterization of the ballistic limit curve for hypervelocity impact of sphere onto single plate, *Journal of mechanical science and technology*, *25*(9), 2457.

[17] **Richardson, M. O. W., and Wisheart, M. J.** (1996). Review of low-velocity impact properties of composite materials, C*omposites Part A: Applied Science and Manufacturing*, *27*(12), 1123-1131.

[18] Besant, T., Davies, G. A. O., and Hitchings, D. (2001). Finite element modelling of low velocity impact of composite sandwich panels, *Composites Part A: Applied science and manufacturing*, *32*(9), 1189-1196.

[19] **Strait, L. H., Karasek, M. L., and Amateau, M. F.** (1992). Effects of stacking sequence on the impact resistance of carbon fiber reinforced thermoplastic toughened epoxy laminates, *Journal of Composite Materials*, *26*(12), 1725-1740.

[20] **Wang, S. X., Wu, L. Z., and Ma, L.** (2010). Low-velocity impact and residual tensile strength analysis to carbon fiber composite laminates, *Materials & Design*, *31*(1), 118-125.

[21] **Ghelli, D., and Minak, G**. (2011). Low velocity impact and compression after impact tests on thin carbon/epoxy laminates, *Composites Part B: Engineering*, *42*(7), 2067-2079.

[22] **López-Puente, J., Zaera, R., and Navarro, C.** (2008). Experimental and numerical analysis of normal and oblique ballistic impacts on thin carbon/epoxy woven laminates, *Composites Part A: Applied Science and Manufacturing*, *39*(2), 374-387.

[23] **Wambua, P., Vangrimde, B., Lomov, S., and Verpoest, I.** (2007). The response of natural fibre composites to ballistic impact by fragment simulating projectiles, *Composite Structures*, *77*(2), 232-240.

[24] **Gower, H. L., Cronin, D. S., and Plumtree, A.** (2008). Ballistic impact response of laminated composite panels, *International Journal of Impact Engineering*, *35*(9), 1000-1008.

[25] **Ahmadi, H., Liaghat, G. H., Sabouri, H., and Bidkhouri, E.** (2013). Investigation on the high velocity impact properties of glass-reinforced fiber metal laminates, *Journal of Composite Materials*, *47*(13), 1605-1615.

[26] **Naik, N. K., Shrirao, P., & Reddy, B.C.K.** (2006). Ballistic impact behaviour of woven fabric composites: Formulation, *International Journal of Impact Engineering*, *32*(9), 1521-1552.

[27] **Vlot, A.** (1996). Impact loading on fibre metal laminates, *International Journal of Impact Engineering*, *18*(3), 291-307.

[28] **Okafor, A.C., Otieno, A. W., Dutta, A., and Rao, V.S.** (2001). Detection and characterization of high-velocity impact damage in advanced composite plates using multi-sensing techniques, *Composite Structures*, *54*(2-3), 289-297.

[29] **Aktay, L., Johnson, A.F., and Holzapfel, M**. (2005). Prediction of impact damage on sandwich composite panels, *Computational Materials Science*, *32*(3-4), 252-260.

[30] **Sun, C.T., and Potti, S.V.** (1996). A simple model to predict residual velocities of thick composite laminates subjected to high velocity impact, *International Journal of Impact Engineering*, *18*(3), 339-353.

[31] **Mouritz, A. P.** (2001). Ballistic impact and explosive blast resistance of stitched composites, *Composites Part B: Engineering*, 32(5), 431-439.

[32] **Caprino, G., Lopresto, V., and Santoro, D.** (2007). Ballistic impact behaviour of stitched graphite/epoxy laminates, *Composites Science and Technology*, *67*(3-4), 325-335.

[33] **Sheikh, A.H., Bull, P.H., and Kepler, J.A.** (2009). Behaviour of multiple composite plates subjected to ballistic impact, *Composites Science and Technology*, *69*(6), 704-710.

[34] **Bland, P.W., and Dear, J.P.** (2001). Observations on the impact behaviour of carbon-fibre reinforced polymers for the qualitative validation of models, *Composites Part A: Applied Science and Manufacturing*, *32*(9), 1217-1227.

[35] **Olson, M. D., and Lindberg, G. M.** (1971). Dynamic analysis of shallow shells with a doubly-curved triangular finite element, *Journal of Sound and Vibration*, *19*(3), 299-318.

[36] **Ahmad, S., Irons, B.M., and Zienkiewicz, O.C.** (1970). Analysis of thick and thin shell structures by curved finite elements, *International Journal for Numerical Methods in Engineering*, *2*(3), 419-451.

[37] **Chakravorty, D., Bandyopadhyay, J.N., and Sinha, P**. (1996). Finite element free vibration analysis of doubly curved laminated composite shells, *Journal of Sound and Vibration*, *191*(4), 491-504.

[38] **Reddy, J.N., and Chandrashekhara, K**. (1985). Geometrically non-linear transient analysis of laminated, doubly curved shells, *International Journal of Non-Linear Mechanics*, *20*(2), 79-90.

[39] **Kapania, R.K., and Yang, T.Y.** (1986). Formulation of an imperfect quadrilateral doubly curved shell element for postbuckling analysis, *AIAA Journal*, *24*(2), 310-311.

[40] **Ganapathy, S., and Rao, K.P.** (1998). Failure analysis of laminated composite cylindrical/spherical shell panels subjected to low-velocity impact, *Computers & Structures*, *68*(6), 627-641.

[41] **Tornabene, F., and Ceruti, A.** (2013). Mixed static and dynamic optimization of four-parameter functionally graded completely doubly curved and

degenerate shells and panels using GDQ method, *Mathematical Problems in Engineering*, 2013.

[42] **Tornabene, F., Fantuzzi, N., and Bacciocchi, M.** (2014). Free vibrations of free-form doubly-curved shells made of functionally graded materials using higher-order equivalent single layer theories, *Composites Part B: Engineering*, *67*, 490-509.

[43] **Tornabene, F., Fantuzzi, N., Viola, E., and Batra, R.C.** (2015). Stress and strain recovery for functionally graded free-form and doubly-curved sandwich shells using higher-order equivalent single layer theory, *Composite Structures*, *119*, 67-89.

[44] **Tornabene, F., Liverani, A., and Caligiana, G.** (2011). FGM and laminated doubly curved shells and panels of revolution with a free-form meridian: a 2-D GDQ solution for free vibrations, *International Journal of Mechanical Sciences*, *53*(6), 446-470.

[45] **Tornabene, F., Liverani, A., and Caligiana, G.** (2012). General anisotropic doubly-curved shell theory: a differential quadrature solution for free vibrations of shells and panels of revolution with a free-form meridian, *Journal of Sound and Vibration*, *331*(22), 4848-4869.

[46] **Nothard, S., McKenzie, D., Haines, J., and Jackson, J.** (1996). Gaussian curvature and the relationship between the shape and the deformation of the Tonga slab, *Geophysical Journal International*, *127*(2), 311-327.

[47] **World Health Organization**. (2013). *Global status report on road safety 2013: supporting a decade of action: summary* (No. WHO. NMH. VIP 13.01). World Health Organization.

[48] **Usta, F., and Türkmen, H.S.** (2017). Crash behavior of nested tube structures with various cross sections. *In 2017 8th International Conference on Recent Advances in Space Technologies (RAST)*, IEEE, (pp. 23-27).

[49] **Usta, F., Türkmen, H.S., Kazancı, Z., and Mecitoğlu, Z.** (2015). Numerical investigation of stepped concentric crash tubes subjected to axial impact: The effects of number of tubes. *In 2015 7th International Conference on Recent Advances in Space Technologies (RAST)*, IEEE, (pp. 39-43).

[50] **Eyvazian, A., Habibi, M.K., Hamouda, A.M., and Hedayati, R.** (2014). Axial crushing behavior and energy absorption efficiency of corrugated tubes, *Materials & Design*, *54*, 1028-1038.

[51] **Lee, S., Hahn, C., Rhee, M., and Oh, J.E.** (1999). Effect of triggering on the energy absorption capacity of axially compressed aluminum tubes, *Materials & Design*, *20*(1), 31-40.

[52] **Marsolek, J., and Reimerdes, H. G.** (2004). Energy absorption of metallic cylindrical shells with induced non-axisymmetric folding patterns, *International Journal of Impact Engineering*, *30*(8-9), 1209-1223.

[53] **El-Hage, H., Mallick, P. K., and Zamani, N.** (2005). A numerical study on the quasi-static axial crush characteristics of square aluminum tubes with chamfering and other triggering mechanisms, *International Journal of Crashworthiness*, *10*(2), 183-196.

[54] **Ashby, M. F., & Gibson, L. J.** (1997). Cellular solids: structure and properties. *Press Syndicate of the University of Cambridge*, Cambridge, UK.

[55] **Duarte, I., Krstulović-Opara, L., Dias-de-Oliveira, J., and Vesenjak, M**. (2019). Axial crush performance of polymer-aluminium alloy hybrid foam filled tubes, *Thin-Walled Structures*, *138*, 124-136.

[56] **Googarchin, H. S., Pasandidehpoor, M., Mahmoodi, A., and Shojaeefard, M. H.** (2019). Energy absorption analysis for tapered multi-cell tubes improved by foams: theoretical development and numerical simulation, *Composite Structures*, *207*, 213-222.

[57] **Liu, W., Huang, J., Deng, X., Lin, Z., and Zhang, L.** (2018). Crashworthiness analysis of cylindrical tubes filled with conventional and negative Poisson's ratio foams, *Thin-Walled Structures*, *131*, 297-308.

[58] **Li, Z., Chen, R., and Lu, F.** (2018). Comparative analysis of crashworthiness of empty and foam-filled thin-walled tubes, *Thin-Walled Structures*, *124*, 343-349.

[59] **Taherishargh, M., Vesenjak, M., Belova, I. V., Krstulović-Opara, L., Murch, G. E., and Fiedler, T.** (2016). In situ manufacturing and mechanical properties of syntactic foam filled tubes, *Materials & Design*, *99*, 356-368.

[60] **Hussein, R.D., Ruan, D., Lu, G., Guillow, S., and Yoon, J.W.** (2017). Crushing response of square aluminium tubes filled with polyurethane foam and aluminium honeycomb, *Thin-Walled Structures, 110,* 140-154.

[61] **Usta, F., Ertaş, O.F., Ataalp, A., Türkmen, H.S., Kazancı, Z., and Scarpa, F**. (2019). Impact behavior of triggered and non-triggered crash tubes with auxetic lattices, *Multiscale and Multidisciplinary Modeling, Experiments and Design*, *2*(2), 119-127.

[62] **Luo, Y., and Fan, H.** (2018). Energy absorbing ability of rectangular self-similar multi-cell sandwich-walled tubular structures, *Thin-Walled Structures*, *124*, 88-97.

[63] **Nia, A. A., and Parsapour, M.** (2014). Comparative analysis of energy absorption capacity of simple and multi-cell thin-walled tubes with triangular, square, hexagonal and octagonal sections, *Thin-Walled Structures*, *74*, 155-165.

[64] **Tran, T., and Baroutaji, A.** (2018). Crashworthiness optimal design of multi-cell triangular tubes under axial and oblique impact loading, *Engineering Failure Analysis*, *93*, 241-256.

[65] **Fang, J., Gao, Y., Sun, G., Qiu, N., and Li, Q.** (2015). On design of multi-cell tubes under axial and oblique impact loads, *Thin-Walled Structures*, *95*, 115-126.

[66] **Xie, S., Yang, W., Wang, N., and Li, H**. (2017). Crashworthiness analysis of multi-cell square tubes under axial loads, *International Journal of Mechanical Sciences*, *121*, 106-118.

[67] **Chen, S., Yu, H., and Fang, J.** (2018). A novel multi-cell tubal structure with circular corners for crashworthiness, *Thin-Walled Structures*, *122*, 329-343.

[68] **Usta, F., Eren, Z., Kurtaran, H., Türkmen, H.S., Kazancı, Z., and Mecitoglu, Z.** (2018). Crashworthiness optimization of nested and concentric circular tubes using response surface methodology and genetic algorithm, *Latin American Journal of Solids and Structures, 15*(5).

[69] **Niknejad, A., and Orojloo, P.H.** (2016). A novel nested system of tubes with special cross-section as the energy absorber, *Thin-Walled Structures, 100*, 113-123.

[70] **Tasdemirci, A., Akbulut, E. F., Guzel, E., Tuzgel, F., Yucesoy, A., Sahin, S., and Guden, M.** (2018). Crushing behavior and energy absorption performance of a bio-inspired metallic structure: Experimental and numerical study, *Thin-Walled Structures, 131*, 547-555.

[71] **Altin, M., Acar, E., and Güler, M.A**. (2018). Foam filling options for crashworthiness optimization of thin-walled multi-tubular circular columns, *Thin-Walled Structures, 131*, 309-323.

[72] **Wang, H., Yang, J., Liu, H., Sun, Y., and Yu, T.X.** (2015). Internally nested circular tube system subjected to lateral impact loading, *Thin-Walled Structures, 91*, 72-81.

[73] **Nia, A.A., and Chahardoli, S.** (2016). Mechanical behavior of nested multi-tubular structures under quasi-static axial load, *Thin-Walled Structures, 106*, 376-389.

[74] **Nia, A.A., and Chahardoli, S.** (2016). Optimizing the layout of nested three-tube structures in quasi-static axial collapse, *Thin-Walled Structures, 107*, 169-181.

[75] **Esa, M., Xue, P., Zahran, M., Abdelwahab, M., and Khalil, M.** (2017). Novel strategy using crash tubes adaptor for damage levels manipulation and total weight reduction, *Thin-Walled Structures, 111*, 176-188.

[76] **Baroutaji, A., Gilchrist, M.D., and Olabi, A.G.** (2016). Quasi-static, impact and energy absorption of internally nested tubes subjected to lateral loading. *Thin-Walled Structures, 98*, 337-350.

[77] **Morris, E., Olabi, A.G., and Hashmi, M.S.J.** (2006). Analysis of nested tube type energy absorbers with different indenters and exterior constraints, *Thin-walled structures, 44*(8), 872-885.

[78] **Tran, T., Le, D., and Baroutaji, A.** (2019). Theoretical and numerical crush analysis of multi-stage nested aluminium alloy tubular structures under axial impact loading, *Engineering Structures, 182*, 39-50.

[79] **Crupi, V., Epasto, G., and Guglielmino, E**. (2013). Comparison of aluminium sandwiches for lightweight ship structures: Honeycomb vs. foam, *Marine structures, 30*, 74-96.

[80] **Jiang, L., and Hu, H.** (2017). Low-velocity impact response of multilayer orthogonal structural composite with auxetic effect, *Composite Structures, 169*, 62-68.

[81] **Gibson, L.J., Ashby, M.F., Schajer, G.S., and Robertson, C.I.** (1982). The mechanics of two-dimensional cellular materials. *Proceedings of the Royal Society of London. A. Mathematical and Physical Sciences, 382*(1782), 25-42.

[82] **Ingrole, A., Hao, A., and Liang, R.** (2017). Design and modeling of auxetic and hybrid honeycomb structures for in-plane property enhancement, *Materials & Design, 117*, 72-83.

[83] **Lakes, R.** (1987). Foam structures with a negative Poisson's ratio, *Science*, *235*, 1038-1041.

[84] **Choi, J.B., and Lakes, R.S**. (1992). Non-linear properties of polymer cellular materials with a negative Poisson's ratio, *Journal of Materials Science*, *27*(17), 4678-4684.

[85] **Masters, I.G., and Evans, K.E.** (1996). Models for the elastic deformation of honeycombs, *Composite Structures*, *35*(4), 403-422.

[86] **Evans, K.E., and Alderson, A.** (2000). Auxetic materials: functional materials and structures from lateral thinking!, *Advanced Materials, 12*(9), 617-628.

[87] **Scarpa, F., Panayiotou, P., and Tomlinson, G.** (2000). Numerical and experimental uniaxial loading on in-plane auxetic honeycombs, *The Journal of Strain Analysis for Engineering Design*, *35*(5), 383-388.

[88] **Scarpa, F., and Tomlinson, G**. (2000). Theoretical characteristics of the vibration of sandwich plates with in-plane negative Poisson's ratio values, *Journal of Sound and Vibration*, *230*(1), 45-67.

[89] **Grima, J.N., Alderson, A., and Evans, K.E.** (2005). Auxetic behaviour from rotating rigid units, *Physica Status Solidi (b), 242*(3), 561-575.

[90] **Bezazi, A., Scarpa, F., and Remillat, C.** (2005). A novel centresymmetric honeycomb composite structure, *Composite Structures*, *71*(3-4), 356-364.

[91] **Simpson, J., and Kazancı, Z.** (2020). Crushing investigation of crash boxes filled with honeycomb and re-entrant (auxetic) lattices, *Thin-Walled Structures*, *150*, 106676.

[92] **Hu, L. L., and Deng, H.** (2015). Indentation resistance of the re-entrant hexagonal honeycombs with negative poisson's ratio, *Materials Research Innovations*, *19*(sup1), S1-442.

[93] **Lira, C., and Scarpa, F.** (2010). Transverse shear stiffness of thickness gradient honeycombs, *Composites Science and Technology*, *70*(6), 930-936.

[94] **Easey, N., Chuprynyuk, D., Musa, W.M., Bangs, A., Dobah, Y., Shterenlikht, A., and Scarpa, F.** (2019). Dome-shape auxetic cellular metamaterials: manufacturing, modeling, and testing, *Frontiers in Materials*, *6*, 86.

[95] **Alderson, K., Alderson, A., Anand, S., Simkins, V., Nazare, S., and Ravirala, N.** (2012). Auxetic warp knit textile structures, *Physica Status Solidi (b), 249*(7), 1322-1329.

[96] **Mohsenizadeh, M., Gasbarri, F., Munther, M., Beheshti, A., and Davami, K.** (2018). Additively-manufactured lightweight Metamaterials for energy absorption, *Materials & Design*, *139*, 521-530.

[97] **Rayneau-Kirkhope, D.** (2018). Stiff auxetics: Hierarchy as a route to stiff, strong lattice based auxetic meta-materials, *Scientific Reports*, *8*(1), 1-10.

[98] **Grima, J.N., and Evans, K.E.** (2006). Auxetic behavior from rotating triangles. *Journal of Materials Science, 41*(10), 3193-3196.

[99] **Grima, J. N., Farrugia, P. S., Gatt, R., and Attard, D**. (2008). On the auxetic properties of rotating rhombi and parallelograms: A preliminary investigation, *Physica Status Solidi (b), 245*(3), 521-529.

[100] **Attard, D., and Grima, J. N.** (2008). Auxetic behaviour from rotating rhombi, *Physica Status Solidi (b), 245*(11), 2395-2404.

[101] **Grima, J.N., Gatt, R., Ellul, B., and Chetcuti, E.** (2010). Auxetic behaviour in non-crystalline materials having star or triangular shaped perforations, *Journal of Non-Crystalline Solids, 356*(37-40), 1980-1987.

[102] **Wang, Z.P., Poh, L.H., Zhu, Y., Dirrenberger, J., and Forest, S.** (2019). Systematic design of tetra-petals auxetic structures with stiffness constraint, *Materials & Design, 170*, 107669.

[103] **Sarvestani, H.Y., Akbarzadeh, A.H., Niknam, H., and Hermenean, K.** (2018). 3D printed architected polymeric sandwich panels: Energy absorption and structural performance, *Composite Structures, 200*, 886-909.

[104] **Yang, L., Harrysson, O. A., West II, H. A., Cormier, D. R., Park, C., and Peters, K.** (2015). Low-energy drop weight performance of cellular sandwich panels. *Rapid Prototyping Journal*, *21*(4), 433–442.

[105] **Qi, C., Remennikov, A., Pei, L.Z., Yang, S., Yu, Z.H., & Ngo, T.D**. (2017). Impact and close-in blast response of auxetic honeycomb-cored sandwich panels: experimental tests and numerical simulations, *Composite Structures, 180*, 161-178.

[106] **Xiao, D., Chen, X., Li, Y., Wu, W., and Fang, D.** (2019). The structure response of sandwich beams with metallic auxetic honeycomb cores under localized impulsive loading-experiments and finite element analysis, *Materials & Design, 176*, 107840.

[107] **Larsen, U. D., Signund, O., and Bouwsta, S**. (1997). Design and fabrication of compliant micromechanisms and structures with negative Poisson's ratio, *Journal of Microelectromechanical Systems, 6*(2), 99-106.

[108] **Wang, X.T., Wang, B., Wen, Z.H., and Ma, L.** (2018). Fabrication and mechanical properties of CFRP composite three-dimensional double-arrow-head auxetic structures, *Composites Science and Technology, 164*, 92-102.

[109] **Qiao, J., and Chen, C.Q.** (2015). Analyses on the in-plane impact resistance of auxetic double arrowhead honeycombs, *Journal of Applied Mechanics, 82*(5), 1-9.

[110] **Gao, Q., Wang, L., Zhou, Z., Ma, Z.D., Wang, C., and Wang, Y**. (2018). Theoretical, numerical and experimental analysis of three-dimensional double-V honeycomb, *Materials & Design, 139*, 380-391.

[111] **Lim, T.C.** (2016). A 3D auxetic material based on intersecting double arrowheads, *Physica status solidi (b), 253*(7), 1252-1260.

[112] **Prall, D., and Lakes, R.S.** (1997). Properties of a chiral honeycomb with a Poisson's ratio of—1, *International Journal of Mechanical Sciences*, *39*(3), 305-314.

[113] **Alderson, A., Alderson, K.L., Attard, D., Evans, K.E., Gatt, R., Grima, J.N., ... & Zied, K.** (2010). Elastic constants of 3-, 4-and 6-connected chiral and anti-chiral honeycombs subject to uniaxial in-plane loading, *Composites Science and Technology*, *70*(7), 1042-1048.

[114] **Scarpa, F., Blain, S., Lew, T., Perrott, D., Ruzzene, M., and Yates, J.R.** (2007). Elastic buckling of hexagonal chiral cell honeycombs, *Composites Part A: Applied Science and Manufacturing*, *38*(2), 280-289.

[115] **Spadoni, A., Ruzzene, M., and Scarpa, F.** (2005). Global and local linear buckling behavior of a chiral cellular structure, *Physica Status Solidi (b)*, *242*(3), 695-709.

[116] **Abramovitch, H., Burgard, M., Edery-Azulay, L., Evans, K.E., Hoffmeister, M., Miller, W., ... & Tee, K.F**. (2010). Smart tetrachiral and hexachiral honeycomb: sensing and impact detection, *Composites Science and Technology*, *70*(7), 1072-1079.

[117] **Airoldi, A., Crespi, M., Quaranti, G., and Sala, G.** (2012). Design of a morphing airfoil with composite chiral structure, *Journal of Aircraft*, *49*(4), 1008-1019.

[118] **Dirrenberger, J., Forest, S., and Jeulin, D.** (2012). Elastoplasticity of auxetic materials. *Computational Materials Science*, *64*, 57-61.

[119] **Lorato, A., Innocenti, P., Scarpa, F., Alderson, A., Alderson, K.L., Zied, K.M., ... & Evans, K.E.** (2010). The transverse elastic properties of chiral honeycombs, *Composites Science and Technology*, *70*(7), 1057-1063.

[120] **Tan, H.L., He, Z.C., Li, K. X., Li, E., Cheng, A.G., and Xu, B.** (2019). In-plane crashworthiness of re-entrant hierarchical honeycombs with negative Poisson's ratio, *Composite Structures*, *229*, 111415.

[121] **Chen, Y., Li, T., Jia, Z., Scarpa, F., Yao, C. W., and Wang, L**. (2018). 3D printed hierarchical honeycombs with shape integrity under large compressive deformations, *Materials & Design*, *137*, 226-234.

[122] **Alomarah, A., Masood, S. H., Sbarski, I., Faisal, B., Gao, Z., and Ruan, D.** (2020). Compressive properties of 3D printed auxetic structures: experimental and numerical studies, *Virtual and Physical Prototyping*, *15*(1), 1-21.

[123] **Hou, Y., Neville, R., Scarpa, F., Remillat, C., Gu, B., and Ruzzene, M.** (2014). Graded conventional-auxetic Kirigami sandwich structures: Flatwise compression and edgewise loading, *Composites Part B: Engineering*, *59*, 33-42.

[124] **Ge, Z., Hu, H., and Liu, Y.** (2013). A finite element analysis of a 3D auxetic textile structure for composite reinforcement, *Smart Materials and Structures*, *22*(8), 084005.

[125] **Jayanty, S., Crowe, J., and Berhan, L.** (2011). Auxetic fibre networks and their composites, *Physica Status Solidi (b)*, *248*(1), 73-81.

[126] **Jopek, H., and Strek, T.** (2015). Thermal and structural dependence of auxetic properties of composite materials, *Physica Status Solidi (b)*, *252*(7), 1551-1558.

[127] **Scarpa, F., Remillat, C., Landi, F.P., and Tomlinson, G.R.** (2000). Damping modelization of auxetic foams, *In Smart Structures and Materials 2000: Damping and Isolation*, volume 3989, pp.336-343.

[128] **Murray, G.J., and Gandhi, F.** (2013). Auxetic honeycombs with lossy polymeric infills for high damping structural materials, *Journal of Intelligent Material Systems and Structures*, *24*(9), 1090-1104.

[129] **Barbarino, S., Pontecorvo, M. E., and Gandhi, F.S.** (2012). Cellular honeycomb-like structures with internal buckling and viscous elements for simultaneous load-bearing and dissipative capability, *In Smart Materials, Adaptive Structures and Intelligent Systems*, volume 45103, pp. 395-405.

[130] **Aumjaud, P., Smith, C.W., and Evans, K.E.** (2015). A novel viscoelastic damping treatment for honeycomb sandwich structures, *Composite Structures*, *119*, 322-332.

[131] **Boucher, M.A., Smith, C.W., Scarpa, F., Rajasekaran, R., and Evans, K.E.** (2013). Effective topologies for vibration damping inserts in honeycomb structures. *Composite Structures*, *106*, 1-14.

[132] **Sloan, M.R., Wright, J.R., and Evans, K.E.** (2011). The helical auxetic yarn–a novel structure for composites and textiles; geometry, manufacture and mechanical properties, *Mechanics of Materials*, *43*(9), 476-486.

[133] **Quan, C., Han, B., Hou, Z., Zhang, Q., Tian, X., and Lu, T.J.** (2020). 3D printed continuous fiber reinforced composite auxetic honeycomb structures. *Composites Part B: Engineering*, *187*, 107858.

[134] **Subramani, P., Rana, S., Oliveira, D.V., Fangueiro, R., and Xavier, J.** (2014). Development of novel auxetic structures based on braided composites, *Materials & Design*, *61*, 286-295.

[135] **Xu, W., Yan, B., Hu, D., and Ma, P.** (2020). Preparation of auxetic warp-knitted spacer fabric impregnated with shear thickening fluid for low-velocity impact resistance, *Journal of Industrial Textiles*, 1528083720927013.

[136] **Fu, K., Wang, H., Chang, L., Foley, M., Friedrich, K., and Ye, L.** (2018). Low-velocity impact behaviour of a shear thickening fluid (STF) and STF-filled sandwich composite panels, *Composites Science and Technology*, *165*, 74-83.

[137] **Armstrong, J.P., Burke, M., Carter, B. M., Davis, S.A., and Perriman, A.W.** (2016). 3D bioprinting using a templated porous bioink, *Advanced Healthcare Materials*, *5*(14), 1724-1730.

[138] **ASTM International** (2004). Standard Test Method for Tensile Properties of Plastics (ASTM D638-14).

[139] **ASTM International** (1991). ASTM D1621-91 Standard test method for compressive properties of rigid cellular plastics (ASTM D1621-91).

[140] **Toksoy, A.K.** (2003). Quasi-static axial compression behavior of empty and polystyrene foam filled aluminum tubes (Master thesis). Izmir Institute of Technology.

[141] **Yin, H., Huang, X., Scarpa, F., Wen, G., Chen, Y., and Zhang, C**. (2018). In-plane crashworthiness of bio-inspired hierarchical honeycombs, *Composite Structures*, *192*, 516-527.

[142] **Chen, J., Chen, W., Hao, H., Huan, S., and Tao, W.** (2020). Mechanical behaviors of 3D re-entrant honeycomb polyamide structure under compression, *Materials Today Communications*, *24*, 101062.

[143] **Zhou, Z., Zhou, J., and Fan, H.** (2017). Plastic analyses of thin-walled steel honeycombs with re-entrant deformation style, *Materials Science and Engineering: A*, *688*, 123-133.

[144] **Xiao, D., Kang, X., Li, Y., Wu, W., Lu, J., Zhao, G., and Fang, D.** (2019). Insight into the negative Poisson's ratio effect of metallic auxetic reentrant honeycomb under dynamic compression, *Materials Science and Engineering: A*, *763*, 138151.

[145] **Tatlier, M.S.** (2019). A numerical study on energy absorption of re-entrant honeycomb structures with variable alignment, *International Journal of Crashworthiness*, 1-9.

[146] **Li, D., Yin, J., Dong, L., and Lakes, R.S.** (2016). Numerical analysis on mechanical behaviors of hierarchical cellular structures with negative Poisson's ratio, *Smart Materials and Structures*, *26*(2), 025014.

[147] **Hou, J., Li, D., and Dong, L.** (2018). Mechanical behaviors of hierarchical cellular structures with negative Poisson's ratio, *Journal of Materials Science*, *53*(14), 10209-10216.

[148] **Hou, X., Deng, Z., and Zhang, K**. (2016). Dynamic crushing strength analysis of auxetic honeycombs, *Acta Mechanica Solida Sinica*, *29*(5), 490-501.

[149] **Sharma, D.S.** (2012). Stress distribution around polygonal holes, *International Journal of Mechanical Sciences*, *65*(1), 115-124.

[150] **ASTM International** (2013). Standard Test Method for Measuring the Damage Resistance of a Fiber-Reinforced Polymer Matrix Composite to a Drop-Weight Impact Event (ASTM D7136/D7136M).

[151] **ASTM International** (2008). Standard Test Method for Tensile Properties of Polymer Matrix Composite Materials (ASTM D3039/D3039M-14).

[152] **ASTM International** (2009). Standard Test Method for Compressive Properties of Polymer Matrix Composite Materials Using a Combined Loading Compression (CLC) Test Fixture (ASTM D6641/D6641M-14).

[153] **ASTM International** (2013). Standard Test Method for In-Plane Shear Response of Polymer Matrix Composite Materials by Tensile Test of a ±45° Laminate (ASTM D3518/D3518M-13).

[154] **Chang, F.K., and Chang, K.Y.** (1987). A progressive damage model for laminated composites containing stress concentrations. *Journal of Composite Materials, 21*(9), 834-855.

[155] **Kayya, R.** (2012). Numerical Modelling of Impact Damage on Carbon Fiber Reinforced Polymer Laminates (Master thesis). Ryerson University, Toronto, Ontario, Canada.

[156] **ASTM International** (2011). Standard test methods for tension testing of metallic materials (ASTM E8/E8M).

[157] **Rodríguez, J.F., Thomas, J.P., and Renaud, J.E.** (2003). Mechanical behavior of acrylonitrile butadiene styrene fused deposition materials modeling, *Rapid Prototyping Journal*, *9*(4), 219–230.

[158] **Elipe, J.C.Á., and Lantada, A.D.** (2012). Comparative study of auxetic geometries by means of computer-aided design and engineering, *Smart Materials and Structures*, *21*(10), 105004.

[159] **Hallquist, J.O.,** (2006). *LS-DYNA Theory Manual*, Livermore Software Technology Corporation.

[160] **Duarte, I., Vesenjak, M., and Krstulović-Opara, L.** (2014). Variation of quasi-static and dynamic compressive properties in a single aluminium foam block, *Materials Science and Engineering: A, 616*, 171-182.

[161] **Duarte, I., Vesenjak, M., Krstulović-Opara, L., and Ren, Z.** (2015). Static and dynamic axial crush performance of in-situ foam-filled tubes, *Composite Structures*, *124*, 128-139.

[162] **Mohsenizadeh, S., Alipour, R., Rad, M.S., Nejad, A.F., and Ahmad, Z.** (2015). Crashworthiness assessment of auxetic foam-filled tube under quasi-static axial loading, *Materials & Design*, *88*, 258-268.

[163] **Guler, M.A., Cerit, M.E., Bayram, B., Gerceker, B., and Karakaya, E.** (2010). The effect of geometrical parameters on the energy absorption characteristics of thin-walled structures under axial impact loading, *International Journal of Crashworthiness*, *15*(4), 377-390.

[164] **Box, G.E., and Draper, N.R**. (1987). *Empirical model-building and response surfaces*. New York: Wiley.

[165] **Golberg, D.E.** (1989). *Genetic algorithms in search, optimization, and machine learning*. Addison Wesley Publishing.

[166] **Deb, K., Pratap, A., Agarwal, S., and Meyarivan, T**. (2002). A fast and elitist multiobjective genetic algorithm: NSGA-II, *IEEE Transactions on Evolutionary Computation*, *6*(2), 182-197.

CURRICULUM VITAE

Name Surname **:** Fatih Usta

Place and Date of Birth **:**

EDUCATION **:**

- **B.Sc. :** 2013, Istanbul Technical University, Faculty of Aeronautics and Astronautics, Aeronautical Department
- **M.Sc. :** 2015, Istanbul Technical University, Graduate School of Science Engineering and Technology, Aeronautics and Astronautics Department

PROFESSIONAL EXPERIENCE AND REWARDS:

- 2019-2021, Teaching Assistant, Department of Aeronautical Engineering, Istanbul Technical University.
- 2019, Visiting Postgraduate Researcher, Aerospace Engineering, Bristol Composite Institute, University of Bristol.
- 2018-2021, The Scientific and Technological Research Council of Turkey (TUBITAK) 2211/C Domestic Priority Doctoral Fellowship.
- 2018-2019, TUBITAK 2214-A International Doctoral Research Fellowship.
- 2017-2019, Council of Higher Education (YOK) 100/2000 Domestic Priority Doctoral Fellowship.
- 2017-2018, TUBITAK 1001-The Scientific and Technological Research Projects Funding Program, Scholarship for Ph.D. Student.
- 2015-2017, Turkish Aerospace Industries (TAI) & ITU Industrial Research Projects, Project Engineer.
- 2013-2015, TUBITAK 1001-The Scientific and Technological Research Projects Funding Program, Scholarship for M.Sc. Student.

PUBLICATIONS, PRESENTATIONS AND PATENTS ON THE THESIS:

Journal Papers

- **Usta, F.,** Turkmen, H.S., Scarpa, F. 2021. Low-velocity impact resistance of composite sandwich panels with various types of auxetic and non-auxetic core structures, *Thin-Walled Structures*.
- **Usta, F.,** Scarpa, F., Johnson P., Perriman A.W., Turkmen, H.S. 2021. Multiphase lattice metamaterials with enhanced mechanical performance, *Smart Materials and Structures*, 30(2), 025014.
- **Usta, F.,** Scarpa, F., Turkmen, H.S. 2020. Edgewise compression of novel hexagonal hierarchical and asymmetric unit cells honeycomb metamaterials, *Materials Today Communications*, 24, 101102.
- **Usta, F.**, Türkmen, H. S. 2019. Experimental and numerical investigation of impact behavior of nested tubes with and without honeycomb filler. *Thin-Walled Structures*, 143, 106256.
- **Usta, F.,** Ertaş, O. F., Ataalp, A., Türkmen, H. S., Kazancı, Z., & Scarpa, F. 2019. Impact behavior of triggered and non-triggered crash tubes with auxetic lattices. *Multiscale and Multidisciplinary Modeling, Experiments and Design*, 2(2), 119-127.
- **Usta, F.,** Eren, Z., Kurtaran, H., Türkmen, H. S., Kazancı, Z., & Mecitoglu, Z. (2018). Crashworthiness optimization of nested and concentric circular tubes using response surface methodology and genetic algorithm. *Latin American Journal of Solids and Structures*, 15(5).
- **Usta, F.,** Mullaoglu, F., Türkmen, H. S., Balkan, D., Mecitoglu, Z., Kurtaran, H., & Akay, E. (2016). Effects of Thickness and Curvature on Impact Behaviour of Composite Panels. *Procedia engineering*, 167, 216-222.

Conference Papers

- **Usta F.,** Turkmen H.S., Ökzetik dolgulu tüplerin statik ezme yükü altında deformasyon davranışının incelenmesi. 8. Ulusal Havacılık ve Uzay Konferansı (UHUK'2020). Ankara, Turkey, 2020.
- **Usta F.,** Turkmen H.S., Ökzetik dolgulu tüplerin çarpma yükleri altında deneysel ve sayısal olarak incelenmesi. 8. Ulusal Havacılık ve Uzay Konferansı (UHUK'2020). Ankara, Turkey, 2020.
- **Usta F.,** Turkmen H.S., Scarpa F. Toroidal Sandwich Panels with Auxetic Core under Impact Loads: Numerical simulations. *9th International Conference on Recent Advances in Space Technologies (RAST 2019)*. June 11-14, Istanbul, Turkey, 2019.
- **Usta F.,** Ataalp A., Turkmen H.S. Crushing Behavior of Nested Composite Crash Tubes. 9th International Conference on Recent Advances in Space Technologies (RAST 2019). June 11-14, Istanbul, Turkey, 2019
- **Usta F.,** Eren Z., Kurtaran H., Turkmen H.S., Kazancı Z., Mecitoğlu Z. Numerical and Experimental Impact Analysis of Stepped and Concentric Crash Tubes.

International Symposium on Dynamic Response and Failure of Composite Materials-DRAF2018. Naples, Italy, 2018.

- **Usta F.,** Kurtaran H., Turkmen H.S. Optimization of Cylindrical Curved Composite Panels Using Response Surface Methodology and Genetic Algorithm. 20th International Conference on Composite Structures (ICCS20). Paris, France, 2017.
- **Usta F.,** Turkmen H.S. Crash Behavior of Nested Tube Structures with Various Cross Sections. 8th International Conference on Recent Advances in Space Technologies (RAST 2017). Istanbul, Turkey, 2017.
- **Usta F.,** Turkmen H.S., Kurtaran H. Numerical and Experimental Investigation of Curved Sandwich Panels and Plates. International Conference on Mechanics of Composites-(MECHCOMP3), Bologna, Italy, 2017.
- **Usta F.,** Eren Z., Turkmen H.S., Kazancı Z., Mecitoğlu Z. Crash Response of Composite Multitubular Structures: The Effects of Wall Thickness. 19th International Conference on Composite Structures (ICCS19), Porto, Portugal, 2016.
- **Usta F.,** Eren Z., Turkmen H.S., Kazancı Z., Mecitoğlu Z. Numerical Investigation of Foam Filled Axially Loaded Multitubular Structures. 1st International Conference on Impact Loading of Structures and Materials-ICILSM2016, Turin, Italy, 2016.

OTHER PUBLICATIONS, PRESENTATIONS AND PATENTS:

Patent

- Eren Z., Kazancı Z., Mecitoğlu Z., Turkmen H.S., **Usta, F.,** 2020 Araçlarda Pasif Güvenlik Bileşeni Olarak İç İçe Çarpışma Kutusu, *Patent numarası*: TR 2015-10333-A2.

Journal Papers

- Mullaoğlu, F., **Usta, F.,** Türkmen, H. S., Kazancı, Z., Balkan, D., & Akay, E. (2016). Deformation behavior of the polycarbonate plates subjected to impact loading. Procedia engineering, 167, 143-150.

Conference Papers

- Ataalp A., **Usta F.,** Turkmen H.S., Scarpa F., Doltsinis I., Kazancı Z. Impact Response of Sandwich Structures with Auxetic and Honeycomb Core. 9th International Conference on Recent Advances in Space Technologies (RAST 2019), Istanbul, Turkey, 2019.
- **Usta F.,** Eren Z., Turkmen H.S., Kazancı Z., Mecitoğlu Z. Numerical Investigation of Stepped Concentric Crash Tubes Subjected to Axial Impact: The Effects of Number of Tubes. 7th International Conference on Recent Advances in Space Technologies (RAST 2015). Istanbul, Turkey, 2015.
- Eren Z., **Usta F.,** Turkmen H.S., Kazancı Z., Mecitoğlu Z. Axial Crash and Crush Response of Novel Nested Tube Designs. 12th International Conference on the Mechanical Behaviour of Materials (ICM 12), Karlsruhe, Germany, 2015.